Observation of atmospheric greenhouse gas abundances on regional scales in boreal areas using portable FTIR Spectrometers

Zur Erlangung des akademischen Grades einer
DOKTORIN DER NATURWISSENSCHAFTEN
von der Fakultät für Bauingenieur-, Geo- und Umweltwissenschaften
des Karlsruher Instituts für Technologie (KIT)

genehmigte

DISSERTATION

von

Qiansi Tu

aus Jian'ou, China

Referent:	Prof. Dr. Thomas von Clarmann
Korreferent:	Prof. Dr. Stefan Hinz
Korreferent:	Prof. Dr. André Butz
Tag der mündlichen Prüfung:	14 May 2019

Abstract

Carbon dioxide (CO_2) and methane (CH_4) are the most important greenhouse gases (GHGs) in terms of anthropogenic activities. The investigation of GHGs' sources and sinks is critical in order to understand climate change and global warming.

The Total Carbon Column Observing Network (TCCON) is a worldwide network for long-term measurement of trace gases. However, its sparse distribution and considerable infrastructure requirements hinder the study of GHG sources/sinks, especially at remote sites and in the context of mobile applications. Recently, a new prototype FTIR spectrometer (EM27/SUN) with high stability, accuracy and portability was developed at KIT (Karlsruhe Institute of Technology) in cooperation with Bruker Optics, Ettlingen. Such instruments are promising complements to the TCCON for observations on regional-scale and short-term campaigns.

This work presents the application of two EM27/SUN spectrometers in measuring GHG emissions from wetlands near the Arctic Circle in Sodankylä (Finland), Kiruna (Sweden) and Fairbanks (Alaska). The Finland campaign was performed in the framework of ESA's (European Space Agency) Fiducial Reference Measurements for Ground-Based Infrared Greenhouse Gas Observations (FRM4GHG) project which aimed at the intercomparison of different compact low-resolution instruments with respect to TCCON measurements.

To minimize the errors and biases in the retrievals, different optimization strategies are discussed using one day of measurements as an example. Instrumental line shape (ILS) is an important characteristic for assessing the instrumental performance and stability, and the modulation efficiency is the main factor influencing the retrievals. In addition, pressure and temperature show certain impact on the retrievals, so as the a-priori VMR (volume mixing ratio) profiles.

To ensure high accuracy of retrievals from the EM27/SUN observations, the results are compared to the co-located TCCON observations at the Finnish Meteorological Institute (FMI) in Sodankylä. The overall biases compared to the reference TCCON results are approximately (0.28 ± 0.64) ppm in XCO_2, (1.99 ± 5.76) ppb in XCH_4 and (1.72 ± 2.48) ppb in case of XCO over the year. The a-priori VMR profiles have a significant impact on the retrieval results, especially in XCH_4 during spring. The biases for CH_4 profiles were larger in spring when comparing the modeled daily-variable profiles (MAP) used in TCCON to the realistic profiles measured by the AirCore soundings. This difference is mainly due to the influence of the polar vortex which consequently results in the difference in the retrieved column abundances. In addition, the application of measured ILS parameters helps to reduce

the relative bias by approximately 0.33 % and 0.30 % in XCO_2 and XCO, respectively, while it increases the bias in XCH_4 by 0.17 %.

The gradient studies for GHGs surface flux estimates were performed between Kiruna and Sodankylä in 2017, and in the Fairbanks region in Alaska in 2016 by using two EM27/SUN instruments located at two sites. The area between Kiruna and Sodankylä is likely to be a GHG sink, absorbing CO_2 on the order of 10^{18} molec. $m^{-2}\,s^{-1}$ and CH_4 on the order of 10^{17} molec. $m^{-2}\,s^{-1}$. The wetland between Nenana and Anderson in Fairbanks tends to be a CH_4 source with an emission rate on the order of 10^{17} molec. $m^{-2}\,s^{-1}$.

This work demonstrates that the EM27/SUN FTIR spectrometer is accurate and stable enough to observe the dedicated sources/sinks on regional scales and to validate satellite data, e.g., the recently launched Sentinel-5P satellite.

Zusammenfassung

Kohlendioxid (CO_2) und Methan (CH_4) sind die wichtigsten anthropogenen Treibhausgase (GHGs). Die Untersuchung der Quellen und Senken von GHGs ist wichtig, um den Klimawandel und die globale Erwärmung zu verstehen.

Das Total Carbon Column Observing Network (TCCON) ist ein weltweites Netzwerk zur Messung von langlebigen Spurengasen. Ihre spärliche Verteilung behindert jedoch das Studium der Quellen/Senken von GHGs, insbesondere an abgelegenen Standorten und im Zusammenhang mit mobilen Anwendungen. Kürzlich wurde am KIT (Karlsruher Institut für Technologie) in Zusammenarbeit mit Bruker Optics, Ettlingen, ein neuer portabler Prototyp eines FTIR Spektrometers (EM27/SUN) für die Messung von GHGs mit hoher Stabilität und Genauigkeit und entwickelt. Solche Instrumente sind vielversprechende Ergänzungen des bestehenden Netzwerkes TCCON, insbesondere für regionale und kurzfristige Kampagnen.

Diese Arbeit präsentiert die Anwendung von EM27/SUN-Spektrometern zur Messung der Treibhausgasemissionen aus Feuchtgebieten in der Nähe des Polarkreises in Sodankylä (Finnland), Kiruna (Schweden) und Fairbanks (Alaska). Die Kampagne in Finnland wurde im Rahmen des "Fiducial Reference Measurements for Ground-Based Infrared Greenhouse Gas Observations (FRM4GHG)" Projektes der ESA (European Space Agency) durchgeführt, bei dem verschiedene kompakte FTIR Instrumente mit niedriger Auflösung verglichen werden.

Um die Fehler und den Bias des Retrievals zu minimieren, werden verschiedene Optimierungsstrategien am Beispiel eines Messetages diskutiert. Die instrumentelle Linienform (ILS) ist ein wichtiges Merkmal zur Beurteilung der instrumentellen Leistung. Zusätzlich beeinflussen der Bodendruck und das atmosphärische Temperaturprofil die abgeleiteten Spurengaskonzentrationen.

Um die hohe Genauigkeit der EM27/SUN-Spektrometer sicherzustellen, werden die Ergebnisse mit den in-situ und TCCON Beobachtungen am Finnischen Meteorologischen Institut (FMI) verglichen. Der Bias bezüglich der TCCON Ergebnisse beträgt ungefähr $(0{,}28 \pm 0{,}64)$ ppm für XCO_2, $(1{,}99 \pm 5{,}76)$ ppb für XCH_4 und $(1{,}72 \pm 2{,}48)$ ppb für XCO über das Jahr. Die Wahl der a-priori VMR (Volumenmischungsverhältnis) Profile spielen bei den Retrievals ebenfalls eine wichtige Rolle, insbesondere bei XCH_4 im Frühjahr. Für die Abweichungen gegenüber der TCCON-Referenz ergaben sich im Frühling größere Werte, wenn in der Auswertung anstelle der von TCCON verwendeten aus klimatologischen Schätzungen abgeleiteten täglich variablen Profile (MAP) die aktuellen mit AirCore Systemen gemessenen Profile verwendet wurden. Dieser Unterschied ist hauptsächlich auf den in der TCCON-Auswertung nicht berücksichtigten Einfluss des Polarwirbels auf die Spurengasprofile zurückzuführen.

Zusätzlich reduziert die Anwendung von gemessenen ILS Parametern die Abweichung in XCO_2 und XCO um etwa 0,33 % und 0,30 %, während sie die Abweichung in XCH_4 um 0,17 % leicht erhöht.

Die Gradientenstudie zur Ableitung von Treibhausgasemissionen wurde zwischen Kiruna und Sodankylä und in der Region Fairbanks in Alaska durchgeführt. Das Gebiet zwischen Kiruna und Sodankylä ist wahrscheinlich eine Senke für CO_2 und CH_4 in der Größenordnung von 10^{18} bzw. 10^{17} molec. $m^{-2}\,s^{-1}$. Während die Regionen in Fairbanks eine komplexere Struktur aufweisen, ist das Feuchtgebiet zwischen Nenana und Anderson wahrscheinlich eine Quelle für CH_4 mit einer Emission in der Größenordnung von 10^{17} molec. $m^{-2}\,s^{-1}$.

Die in dieser Arbeit erzielten Ergebnisse weisen darauf hin, dass mit dem EM27/SUN FTIR Spektrometer gewonnene Messungen genau genug sind, um Quellen und Senken von GHGs auf regionaler Ebene zu quantifizieren und weltraumgestützte Sensoren für die Messung von GHGs zu validieren, z.B. den kürzlich gestarteten Satelliten Sentinel-5P der ESA.

Contents

Introduction

Greenhouse gases (GHGs) trap heat in the atmosphere which thereby warms the atmosphere, so called the greenhouse effect. The main GHGs are water vapor (H_2O), carbon dioxide (CO_2), methane (CH_4), nitrous oxide (N_2O) and ozone (O_3). Among the GHGs, CO_2 is the most common gas emitted by anthropogenic activities and has the greatest impact on global warming. The atmospheric CO_2 levels increased from 280 ppm (parts per million) in the pre-industrial period in the later 1700s [Joos and Spahni, 2008] to over 400 ppm nowadays recorded at Mauna Loa Observatory[1], corresponding to an approximate increase of 40 %. CH_4 is a far more active greenhouse gas with 25 times higher global warming potential (GWP) than CO_2 over 100 years. Moreover, the globally averaged CH_4 shows a stronger relative growth. It has increased by a factor of 2.5 from an annual average of 720 ppb (parts per billion) to approximately 1800 ppb within the same period [Dlugokencky et al., 2011; Etheridge et al., 1998]. The pronounced increase in GHGs largely contributes to the greenhouse effect caused by human activities and has led to the rise of the global mean temperatures by about 1 °C [Hansen et al., 2010].

The importance of reducing GHGs emissions has been considered by different international parties and organizations. Nearly 200 countries have signed the 1997 Kyoto Protocol with the objective to reduce the global warming by decreasing the atmospheric concentrations of GHGs[2]. Later, the Paris Agreement[3] was adopted in 2015 and 196 state parties agreed on the central aim to hold the increase in the global average temperature in this century to less than 2 °C above pre-industrial levels and to attempt to limit the increase to 1.5 °C[4]. A special report has been published by the Intergovernmental Panel on Climate Change (IPCC) in October, 2018 as part of the decision to adopt the Paris Agreement (SR15[5]). The report focuses on the effects of global warming if the temperature would increase by 1.5 °C over pre-industrial levels. Additionally, global GHG emission pathways are discussed in the report.

Different measurement programs are implemented for observing atmospheric trace gases to improve the scientific understanding of the change in climate connected with the increasing GHGs and to support environmental treaty programs. Generally, three methods are used to monitor trace gas concentrations and long-term trends in the atmosphere. In-situ measure-

[1] https://www.esrl.noaa.gov/gmd/obop/mlo/

[2] https://unfccc.int/process/the-kyoto-protocol

[3] http://unfccc.int/paris_agreement/items/9485.php

[4] http://www.documentcloud.org/documents/2647638-ParisAgreemen-tOnClimateChange2015.html#document/p22

[5] http://www.ipcc.ch/report/sr15/

ments mostly aim at surface observations and characterize individual sources and sinks of GHGs, e.g., from plants and cattle and on a local scale. However, the variable exchange between the planetary boundary layer and the free troposphere introduces errors in simulating vertical mixing ratios in transport models [Gurney et al., 2004; Yang et al., 2007]. The second method, based on satellite measurements provides coverage on a global scale but is limited by its precision and temporal resolution. Its high efficiency in collecting data is accompanied with additional uncertainties because accumulated data do not always reflect accurately local sources and sinks [Nicholls et al., 2015]. The third method is the ground-based remote sensing technique, detecting the total column abundances of atmospheric gases at the observer position. Based on this technique a worldwide network named as the Total Carbon Column Observing Network (TCCON) has been developed. It aims at providing accurate and precise measurements of total columns of GHGs for understanding the global carbon cycle and for validation of satellite observations [Oshchepkov et al., 2013; Wunch et al., 2011]. However, gaps in global coverage exist, especially in remote regions because this network uses logistically demanding high-resolution laboratory Fourier-Transform Infrared (FTIR) spectrometers. Additionally, the costs for new stations limit further expansion of the network. Infrastructure, internet, dedicated power, etc. are required and at least one trained person is needed for operation and maintenance on site. In addition, relocation of a TCCON station, often built into 2500 kg shipping containers, is a major effort, requiring heavy equipment such as cranes and semi-trailer trucks.

Therefore, these disadvantages limit the study of local- to regional-scale sources and sinks of GHGs in interesting regions. A portable spectrometer offering high stability, precision, robustness, portability and easy operability is desirable. Recently, a ground-based solar absorption FTIR spectrometer was developed at Karlsruhe Institute of Technology (KIT) [Gisi et al., 2012; Hase et al., 2016], which offers the aforementioned advantages. The EM27/SUN spectrometer has been available from Bruker as a commercial item since 2014. EM27/SUN instruments have been operated in various field campaigns and allow characterization of local sources and sinks, such as GHGs emission from metropolitan regions or from volcano plumes, and are capable of detecting sub percent enhancement over the background concentration [Butz et al., 2017; Frey et al., 2015; Klappenbach et al., 2015]. In addition, this promising instrument has the potential to complement the TCCON network, especially at remote sites, and to intercompare GHGs retrievals among different TCCON sites [Hedelius et al., 2017].

This thesis aims at performing highly accurate ground-based remote sensing measurements of GHGs and at estimating the emission from boreal wetland with two mobile EM27/SUN spectrometers. This work is organized in 6 chapters. The instruments used in this thesis are introduced in Chapter 2, including the general introduction of the TCCON network, the two high resolution Bruker FTIR 125HR spectrometers at Karlsruhe and Sodankylä sites and the low resolution EM27/SUN instruments. Additionally, the important instrumental characteristics (instrumental line shape) of the EM27/SUN spectrometer are described. Two different

retrieval algorithms—GGG2014 [Wunch et al., 2015] and PROFFIT V9.6 [Hase et al., 2004] used for retrieving column abundances from spectra or rather interferograms measured with high and low resolution instruments are introduced subsequently.

In Chapter 3 a more detailed description of the optimization of the retrievals is provided. Several possible error sources in the retrieval procedure within the PROFFIT software are analyzed and the resulting level of uncertainty is quantified. An optimized retrieval strategy for column-average dry-air mole fraction of trace gases in the atmosphere is applied to minimize the errors and to achieve the desired accuracy.

Chapter 4 deals with the ground-based GHG measurements performed at the Sodankylä and Kiruna stations. First, the complete set of measurements collected with the EM27/SUN instrument in Sodankylä, 2017 with and without optimized approaches are analyzed. The optimized retrievals are compared to the in-situ observations at the Finnish Meteorological Institute (FMI), Sodankylä. Furthermore, a more detailed comparison with the TCCON high-resolution and 125HR low-resolution results used as reference is presented respectively. Finally, the gradients observations between Kiruna and Sodankylä are discussed. Emission rates from the area are estimated afterwards.

Results from the Alaska campaign performed in 2016 are discussed in Chapter 5. Two EM27/SUN instruments from KIT and LANL (Los Alamos National Laboratory) were used to study the emissions of XCO_2 and XCH_4 from the boreal wetland near Fairbanks. In Chapter 6 the summary of the work and an outlook on further research topics are given.

Chapter 1

Theoretical Background

1.1 The Earth's atmosphere

This section summarizes the relevant properties and processes of the Earth's atmosphere. First the composition and vertical structure are described. After that the carbon cycle and its changes due to anthropogenic activities are outlined, while the last section discusses the greenhouse effect, including its basic physical principles and important greenhouse gases. The content of this section is mostly based on Le Quéré et al. [2015], the latest IPCC report [IPCC, 2013], Archer [2012], Schlager et al. [2012] and Davis et al. [2001].

1.1.1 Composition and structure of the atmosphere

The atmosphere of Earth contains various gases. The dominant constituents are nitrogen (N_2), oxygen (O_2) and the inert gas Argon (Ar), assuming dry air. By volume, the fractional concentration is about 78.09 % for N_2, 20.95 % for O_2 and 0.93 % for Ar, all of which account for almost 99.96 % in total. However, these gases have negligible impacts on the climate system because they interact only weakly with infrared radiation. In addition N_2 and O_2 absorb in the shortwave ultraviolet region which is less important in the lower atmosphere. Conversely, the so-called trace gases like carbon dioxide (CO_2), methane (CH_4), nitrous oxide (N_2O) and ozone (O_3) play key roles in the Earth's climate system due to their radiative forcing impact, even though they only contribute 0.04 % by volume in dry air.

Gaseous water (H_2O) is by definition not included in dry air. It is a major greenhouse gas with highly variable tropospheric concentrations from less than 100 to over 10 thousand ppm, and is of particular importance for the Earth's energy balance in the atmosphere [Bengtsson, 2010]. Approximately 90 % of the H_2O molecules are concentrated in the lower atmosphere (troposphere) and the H_2O distribution is regulated by Earth's hydrological cycle. Water vapor condensates to the liquid or solid phase by forming clouds, rain, snow and other precipitation. The transitions among these three phases are shaping our climate and weather and affect the Earth's energy budget because H_2O is an effective GHG and heat is absorbed

or released during the phase changes.

The volume mixing ratio of a trace gas can vary dramatically, ranging from a few parts per trillion (ppt) to several hundred parts per million (ppm). The trace gases emitted to the atmosphere depend on two possible kinds of sources—natural or anthropogenic. Natural emissions encompass biogenic processes at the Earth's surface (e.g. photosynthesis, wetlands) or release from solid Earth (e.g. volcanoes) and from the oceans (in particular sulfur-containing gases). In addition to the natural sources, many trace gases are directly emitted into the atmosphere by human activities. The anthropogenic sources include fossil fuel mining and combustion (CO, CO_2, NO_x, SO_2), biomass burning (CO, CO_2, NO_x, SO_2), agriculture (CH_4, N_2O, NH_3), and industrial activity (CO_2, CH_4, N_2O). The residence time of a trace gas in the atmosphere depends on its concentration and the rate of elimination. Some trace gases are characterized by high chemical reactivity and ability to influence the oxidation processes in the atmosphere, resulting in short lifetimes of these molecules.

Two major layers can be distinguished in the Earth's atmosphere according to the homogeneity of atmospheric composition. The lower layer, the homosphere, reaches up to a height of 100 km, where the atmosphere is well mixed due to the continuous convection. Above the homosphere lies the heterosphere, where molecular diffusion dominates. The atmospheric constituents are stratified and vary according to the molecular mass in this upper layer. The heavier molecules like N_2 and O_2 are concentrated in the lower heterosphere, while the lighter gases dominate the higher layers.

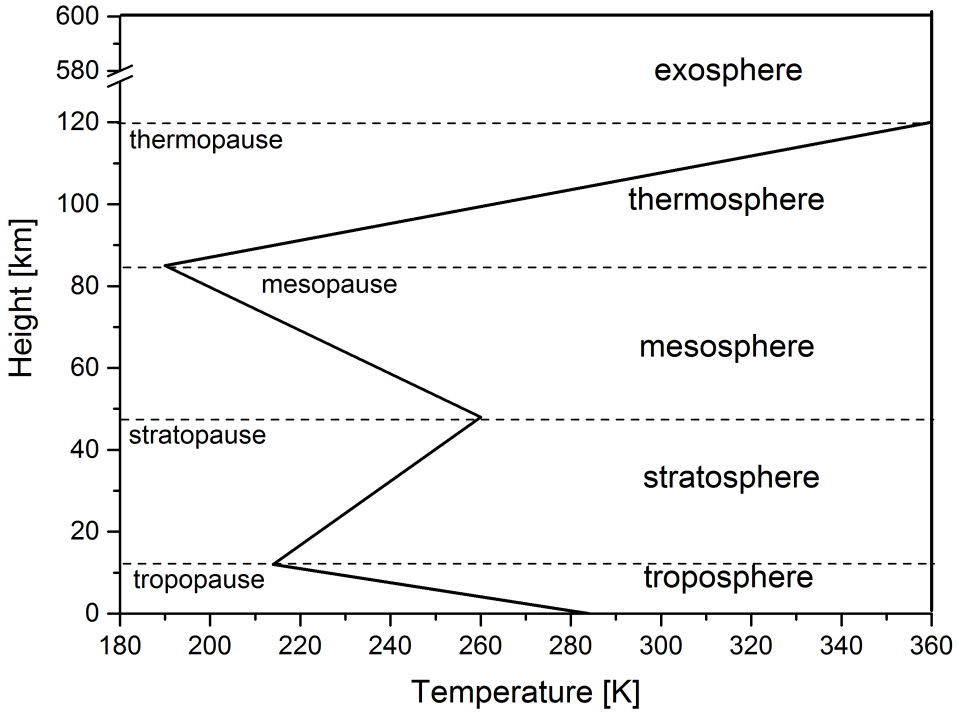

Figure 1.1: Schematic depiction of vertical structure of the Earth's atmosphere.

Another way to classify the atmosphere is based on the variation of temperature with height. The atmosphere can be divided to several layers: troposphere, stratosphere, mesosphere, thermosphere and exosphere. A schematic depiction of the vertical temperature structure of the Earth's atmosphere is presented in Figure 1.1. The lowest layer is the troposphere and it reaches up to 8–9 km in the regions nearest the two poles and up to about 18 km over the equator, resulting in an average value of 12 km. In the troposphere nearly 80 % of the atmospheric mass and essentially all the water vapor and the primary greenhouse gases are concentrated. This layer is characterized by a decreasing temperature with height with an average lapse rate of $6.5\,\mathrm{K\,km^{-1}}$. In this layer, convective exchange and almost all weather phenomena as well as cloud formation occur here. The stratosphere lies above the troposphere, extending from about 10–18 km to 50–55 km. In contrast to the troposphere, the stratosphere is a relatively stable layer, highly stratified and poorly mixed. It contains approximately 19 % of total mass of the atmosphere and has only traces of water vapor. In this layer the temperature increases with height due to the ozone layer. O_3 molecules strongly absorb most of the ultraviolet radiation (UV) from the Sun, which in consequence heats the atmosphere. The stratopause separates the stratosphere from the mesosphere. The mesosphere reaches up to 85–100 km above the Earth's surface. In the mesosphere, temperature decreases with increasing altitude because the absorption of solar radiation is decreasing. The thermosphere lies above the top of mesosphere, separated by the mesopause. The temperature in this layer rises rapidly where the molecular constituents (O_2 and N_2) are easily ionized by the solar radiance. The thermopause is highly dependent on solar activity. It can extend to 400 km during the low sun activity and reach around 500 km when the sun is active. Above approximately 500–1000 km the exosphere is located, which steadily looses molecules to space and gradually merges into interplanetary space.

1.1.2 The carbon cycle

Carbon is found in various chemical forms and oxidation states. The most stable forms are the gaseous CO_2 and solid $CaCO_3$ on Earth. The carbon cycle describes the exchange of carbon among the atmosphere, oceans, biosphere and geosphere (see Figure 1.2). A reservoir releasing a larger amount of carbon than absorbing is called a net carbon source, while a net carbon sink absorbs more carbon than it emits.

In general, the carbon cycle can be divided into two components depending on the time scale. The fast carbon cycle is usually related with biological processes, including photosynthesis and respiration. Through the process of photosynthesis, algea and terrestrial green plants convert the atmospheric CO_2 to a higher-energy reduced form (carbohydrates) by using solar energy (forward direction of reaction (1.1)). The reverse process of photosynthesis is called respiration which uses these carbohydrates in metabolism by plants and animals

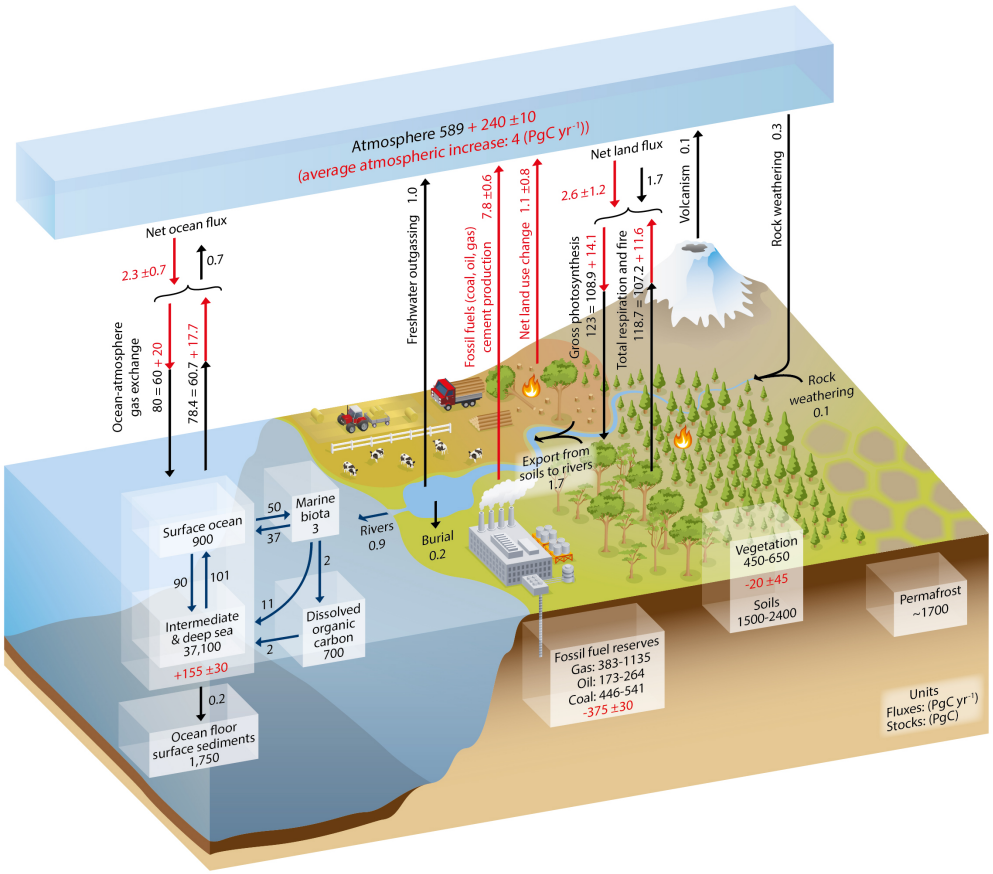

Figure 1.2: Simplified schematic depiction of the global carbon cycle. Numbers denote reservoir mass in PgC ($1\,\mathrm{PgC} = 10^{15}\,\mathrm{gC}$) and annual carbon exchange fluxes in PgC/year. Image taken from IPCC [2013].

and in turn releases CO_2 back to the atmosphere (backward direction of reaction (1.1)).

$$6CO_2 + 6H_2O + \text{energy} \rightleftharpoons C_6H_{12}O_6 + 6O_2 \tag{1.1}$$

In addition, photosynthesis and respiration largely influence the annual and intraday fluctuation of CO_2 concentrations in the atmosphere. When plants are in the growing season, photosynthesis outweighs respiration, absorbing more CO_2 from the atmosphere than they release. This leads to decreasing atmospheric CO_2 concentrations. When respiration dominates, more CO_2 is released to the atmosphere, resulting in increasing CO_2 levels.

The atmospheric CO_2 is only the tiniest reservoir of carbon in the terrestrial system. Carbon is also stored for long periods of time at the land surface, in the oceans, in sedimentary rocks, and in the Earth's interior. Carbon exchange among these reservoirs usually takes millions of years, much longer than the fast carbon cycle. This slow carbon cycle is also known as geological carbon cycle. The movement of carbon from the atmosphere to the lithosphere (rocks) starts with rain, where atmospheric CO_2 is dissolved in water and reacts

with water molecules to form carbonic acid (H_2CO_3):

$$CO_2 + H_2O \rightleftharpoons H_2CO_3 \rightleftharpoons HCO_3^{-1} + H^+ \rightleftharpoons CO_3^{2-} + 2H^+ \tag{1.2}$$

Via chemical weathering, H_2CO_3 reacts with minerals at the Earth's surface and slowly dissolves them into their component ions. These component ions are carried by rivers eventually to the ocean, where the dissolved carbonate (CO_3^{2-}) combines with Ca^{2+} ions to build calcium carbonate ($CaCO_3$). $CaCO_3$ is a key component to form the shell building of marine organisms. When the organisms die, a part of $CaCO_3$ from their remains sink and eventually deposit at the ocean floor as sediments. On geological time scales, the ocean sediments are converted into rocks called limestone. CO_2 is released back into the atmosphere through volcanoes. The Earth's land and the whole sea floor are located above moving crustal plates. If the tectonic plates collide, one moves under another (called subduction), and the sinking plate is pushed deeper into the Earth. The rocks melt under the extreme heat and pressure, and release CO_2 mostly via volcanic eruption back into the atmosphere.

In addition, the slow carbon cycle has a slightly faster component—the ocean which is a larger reservoir than the land surface or the atmosphere. CO_2 is slowly exchanged between the ocean and atmosphere through dissolution and evaporation at the ocean surface. The ocean's carbon exists in the forms of CO_2, H_2CO_3, HCO_3^{-1}, CO_3^{-2}, all of which are called dissolved inorganic compounds.

1.1.3 The greenhouse effect

The greenhouse effect describes a natural or man-made process that warms the Earth's surface and lower atmosphere. When the solar radiation strikes the Earth's atmosphere, about 30 % of the radiation is reflected back to space by clouds and by the Earth's surface. Most of the remaining radiation is absorbed in terms of shortwave radiation and re-emitted as longwave radiation by the atmosphere. The solar power flux density at the top of the atmosphere is about $1372\,\mathrm{W\,m^{-2}}$ and is called the solar constant S. Therefore, the Earth receives an influx of solar energy for its cross section given as:

$$P = \pi R_E^2 S = 175\,\mathrm{PW} \tag{1.3}$$

where $R_E = 6378\,\mathrm{km}$ is the Earth's radius. When the infrared light leaves the warm Earth, it emitted by the whole surface area of the Earth ($4\pi R_E^2$). In equilibrium between shortwave intake and outgoing infrared radiation (IR), the averaged radiant power for the whole surface needs to be:

$$p = \frac{P}{4\pi R_E^2} = \frac{S}{4} = 343\,\mathrm{W\,m^{-2}} \tag{1.4}$$

The Earth's surface absorbs the radiation and re-emits the radiation as a black body in order to keep thermal balance. The emission spectrum can be described by Planck's law:

$$B_\lambda(T,\lambda) = \frac{2hc^2\lambda^{-5}}{\exp(\frac{hc}{\lambda k_B T}) - 1} \tag{1.5}$$

here k_B is the Boltzmann constant, h is the Planck's constant, and c is the speed of light. λ represents the wavelength of the spectral radiance. When integrating the black body spectral flux over all wavelengths, the total power emitted per unit area at the surface of a black body can be determined using the Stefan-Boltzmann law:

$$I = \varepsilon\sigma T^4 \tag{1.6}$$

where ε is the emissivity, a value between 0 and 1, describing how efficient the emitting surface is. It equals to 1 for a perfect black body. σ is the Stefan-Boltzmann's constant ($\sigma = 5.67 \times 10^{-8}\,\mathrm{W\,m^{-2}\,K^{-4}}$) and T is the temperature in Kelvin. In thermal balance, the energy fluxes in and out are equal to each other. When no atmosphere exists and therefore, no radiation interacts between the Earth and the atmosphere, the radiation balance can be defined as:

$$\varepsilon_{earth}\sigma T_{earth}^4 = (1-\alpha)\frac{S}{4} \tag{1.7}$$

the α represents the Earth's albedo, which is approximately 30 % on average. Assuming the Earth's emissivity $\varepsilon_{earth} = 0.95$, it yields a surface temperature of $T_{earth} = 258\,\mathrm{K}$ in the absence of an atmosphere (one-layer system, see Figure 1.3, left panel). However, an approximately 30 K difference exists between the theoretical earth-surface temperature and the real measured mean value of 288 K [Hansen et al., 2010]. This discrepancy is caused by the interaction of longwave radiation with the Earth's atmosphere, called greenhouse effect. Some minor trace gases (e.g. GHGs) in the atmosphere are transparent for visible light. However, they are strongly absorbing in the thermal IR spectral range, and they re-emit longwave radiation in all directions, resulting in an increase of the Earth's surface temperature. The main GHGs are CO_2, CH_4, N_2O and H_2O.

The existence of the atmosphere containing GHGs is essential for the Earth's radiation budget and makes the Earth habitable. For estimating the greenhouse effect, an additional atmosphere layer is added to the previous one-layer model. The new two-layer system consists of the Earth's surface and an atmospheric layer (see Figure 1.3, right panel). The radiative budget of this simple system can be defined as:

$$\varepsilon_{earth}\sigma T_{earth}^4 = (1-\alpha)\frac{S}{4} + \varepsilon_{atm}\sigma T_{atm}^4 \tag{1.8}$$

$$\varepsilon_{earth}\sigma T_{earth}^4 = (1-\alpha_{atm})\varepsilon_{earth}\sigma T_{earth}^4 + 2\varepsilon_{atm}\sigma T_{atm}^4 \tag{1.9}$$

The Equation (1.8) is based on the radiative balance at the Earth's surface, and Equation (1.9) represents the atmospheric radiative balance. The subscript 'atm' denotes the atmosphere. Assuming $\varepsilon_{atm} = 0.75$ leads to a surface temperature T_{earth} of 287 K which is in good agreement with the aforementioned actually measured Earth's surface temperature.

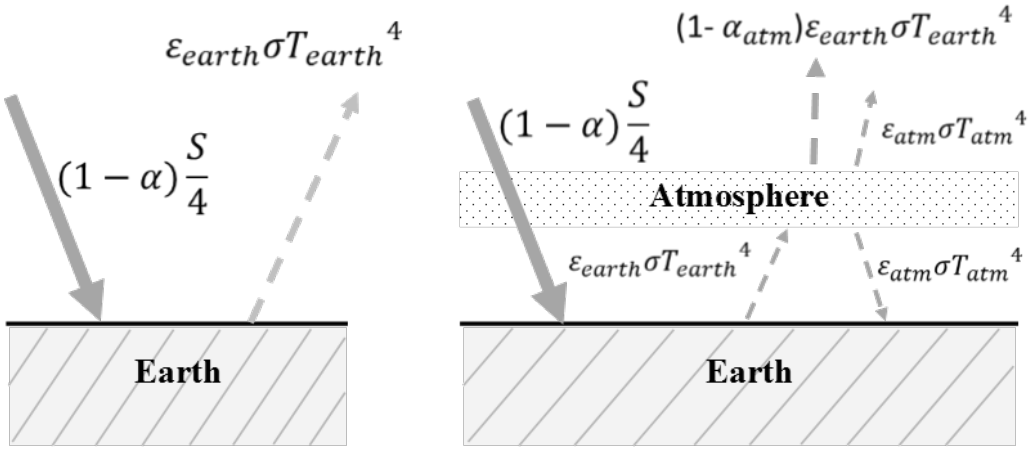

Figure 1.3: Schematic depiction of the simplified model of the Earth's radiation budget. Left panel: one-layer system without the Earth's atmosphere; right panel: two-layer system including the atmosphere as an absorbing and re-emitting medium.

The strength of the Earth's greenhouse effect is determined by the GHGs concentrations in the atmosphere. Besides the natural greenhouse effect, human activities have caused a pronounced rise in the concentrations of GHGs in the atmosphere since the start of the industrial revolution in the mid-eighteenth century. The main sources of GHGs due to the anthropogenic activities include burning of fossil fuels (principally coal, oil and natural gas), deforestation, land use change and agriculture (e.g. rice paddles and livestock).

The Intergovernmental Panel on Climate Change (IPCC) is an intergovernmental body established by the United Nations Environmental Programme (UNEP) and the World Meteorological Organization (WMO) in 1988. It provides assessments of scientific and technical results on climate change that is induced by human-related activities. IPCC uses the concept of radiative forcing (RF) to provide a measure for how various factors contribute to the greenhouse effect. RF describes the net change in the energy balance of the Earth system influenced by a given climatic factor, e.g. a GHG. A positive value represents an increase in the Earth's energy balance, resulting in the warming of the Earth's surface, while a negative value describes a decrease in the energy balance, resulting in the cooling of the Earth's surface. RF is usually presented for the changes relative to the pre-industrial conditions in 1750. Generally, it is expressed in Watts per square meter (Wm^{-2}).

The CO_2 RF is $(1.82 \pm 1.90)\,\mathrm{Wm}^{-2}$ [IPCC, 2013]. Atmospheric CO_2 is currently rising by about 2 ppm/year. Its concentration has increased approximately by 40 %, from 280 ppm in the middle 1700s to over 400 ppm that has been observed at the Mauna Loa Observatory in early 2017. This growth is mainly due to the continuously increasing use of fossil fuels.

Other anthropogenic activities, e.g. deforestation, industrial processes and biomass burning also emit CO_2 to the atmosphere. CO_2 accounts for $\sim$20 % of the total greenhouse effect [Schmidt et al., 2010].

Global warming potential (GWP) describes a metric to determine the ability of a GHG for trapping heat in the atmosphere during a certain period, normalized to CO_2 by mass. CH_4 is a far more active greenhouse gas and its GWP is 25 times higher than CO_2 over 100 years. Additionally, it shows a stronger growth than carbon dioxide, rising from about 722 ppb (parts per billion) in 1750 to about 1800 ppb by 2011 [IPCC, 2013]. This increase by approximately 150 % over that time scale is mostly due to human-related activities. Anthropogenic sources (e.g. landfills, agriculture, livestock raising) contribute about 65 % of the total atmospheric methane emissions. The RF assigned to the excess atmospheric methane is $(0.48 \pm 0.05)\,\mathrm{Wm}^{-2}$ [IPCC, 2013].

CO is not a direct GHG. However, it influences the global warming indirectly due to its reaction with hydroxyl (OH) radicals in the atmosphere, because OH radicals help to reduce the lifetimes of some GHGs. Natural sources of CO include emissions from vegetation and oceans. In addition, considerable amounts of CO are due to the oxidation of CH_4 and other hydrocarbons [Daniel and Solomon, 1998].

1.2 IR absorption spectroscopy

In the following section, the interaction of molecules with infrared electromagnetic radiation is described. Atoms or molecules absorb, emit or scatter electromagnetic radiation and in consequence, their electronic, vibrational, rotational and translational states are changed. Concerning the atmosphere, its major constituents O_2 and N_2 are essentially transparent in the infrared spectral range, and hence are called infrared inactive. Other trace gases, such as CO_2, H_2O and CH_4 are infrared active gases, because they can effectively absorb infrared light. A molecule is an efficient absorber if the molecular dipole moment is changing during transition. For convenience, only a short and simplified introduction is given in this section. First, the formation of IR spectra is discussed for diatomic molecules, followed by the polyatomic molecules using CO_2 as an example.

1.2.1 Diatomic molecules

The vibration of a diatomic molecule can be described as quantum-mechanical oscillation, consisting of two atoms with masses m_1 and m_2, and a massless spring connecting the two atoms. This system is known as harmonic oscillator and can be described as:

$$E(\upsilon) = (\upsilon + \frac{1}{2})\frac{h}{2\pi}\omega, \quad \upsilon = 0, 1, 2, ... \quad \text{with} \quad \omega = (\frac{k_f}{\mu})^{\frac{1}{2}} \tag{1.10}$$

here, h denotes the Planck constant, k_f the force constant and ω the angular frequency. υ represents the vibrational quantum number and $\upsilon = 0$ level is the vibrational ground state. The effective mass μ is given by:

$$\mu = \frac{m_1 m_2}{m_1 + m_2} \tag{1.11}$$

The vibrational energy $G(\upsilon)$ can be written in terms of wavenumbers $\tilde{\nu}$:

$$G(\upsilon) = \frac{E_\upsilon}{hc} = \tilde{\nu}(\upsilon + \frac{1}{2}) \quad \text{with} \quad \tilde{\nu} = \frac{\omega}{2\pi c} \tag{1.12}$$

According to the harmonic oscillator selection rule, $\Delta\upsilon = \pm 1$ is required. $\Delta\upsilon = +1$ represents absorption of radiation, while $\Delta\upsilon = -1$ represents emission. At room temperature (T $\sim$300 K), $k_B T$ is about one order of magnitude smaller than the energy difference and almost all molecules stay at the ground state. Therefore, the transitions from $\upsilon = 0$ to $\upsilon = 1$ dominate.

However, the harmonic oscillation can only partly describe the diatomic molecular vibration. For lower energy states the harmonic oscillation can be approximated with a parabolic function. For internuclear separation $r \gg r_e$, dissociation happens and the real molecular potential differs from a parabolic shape. Therefore, an anharmonic potential (Morse potential) is used for the higher energy states, modifying the harmonic potential by an additional different potential. The Morse potential is a better inter-atomic interaction model for the diatomic molecular potential energy, because it accounts for the effects of bond breaking, the anharmonicity of real bonds, and the non-zero transition probability for overtone and combination bands. A schematic depiction of the harmonic potential together with the Morse potential is given in Figure 1.4. The energy levels of the anharmonic vibrational terms by using the Morse potential can be expressed as:

$$G(\upsilon) = \tilde{\nu}(\upsilon + \frac{1}{2}) - x_e\tilde{\nu}(\upsilon + \frac{1}{2})^2 \quad \text{with} \quad x_e = \frac{\tilde{\nu}}{4D_e} \tag{1.13}$$

here x_e is the anharmonicity constant and D_e the dissociation energy. The first part is identified as the energy levels of the harmonic oscillation, while the second part represents the anharmonic potential. Compared to the harmonic oscillation, the selection rule has to be modified for the anharmonic vibrational energy levels, i.e. $\Delta\upsilon = \pm 1, \pm 2, \pm 3, ...$ is allowed.

Besides vibration, a molecule also rotates. Only one line is generated due to every single vibrational transition. However, a highly resolved spectrum of a molecular gas reveals patterns of closely-spaced lines (10 cm^{-1} difference). These lines form a band caused by rovibrational transitions. For diatomic molecules, a simple system of the rigid rotor is used to describe the rotational energy levels, assuming that only orthogonal rotations about the molecular axis occur and the centrifugal force is neglected. The rotational potential in terms

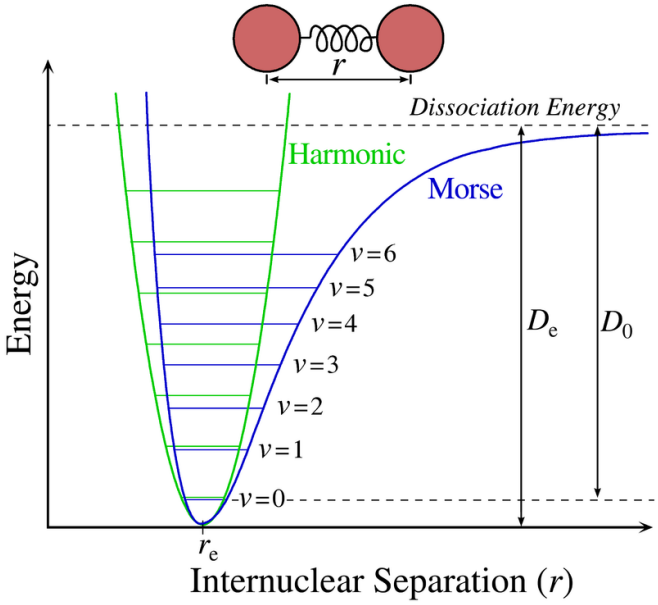

Figure 1.4: Schematic depiction of the harmonic oscillation (green) and anharmonic oscillation (Morse potential, blue). The harmonic potential shows a parabolic shape and the energy differences are equidistant, whereas the Morse potential has an asymmetric shape, with non-equidistant energy differences. Meanwhile, higher energy levels in the Morse potential are lower than the harmonic potential. Image taken from Wikipedia (https://en.wikipedia.org/wiki/File:Morse-potential.png).

of the rotational quantum number J is given:

$$F(J) = BJ(J+1), \quad J = 0, 1, 2... \quad \text{with} \quad B = \frac{h}{8\pi^2 \Theta} \tag{1.14}$$

where B represents the rotational constant. Θ is the moment of inertia and R the bond length of the molecule. However, the centrifugal force affects the molecules in reality which results in a change of the inertial moment. Thus, it is necessary to also take it into account. The inter-nuclear distance expands with increasing rotational frequencies. It leads to a higher angular momentum, which in turn results in a lower energy value:

$$F(J) = BJ(J+1) - D_J J^2 (J+1)^2 \quad \text{with} \quad D_J = \frac{4B^3}{\tilde{\nu}^2} \tag{1.15}$$

D_J is the centrifugal distortion constant. The selection rule $\Delta J = \pm 1$ is required for the rotational transition of diatomic molecules. Transitions for $\Delta J = 0$ are only allowed for molecules when their angular momentum is parallel to the symmetry axis. According to the Born-Oppenheimer approximation, the energy levels of a diatomic molecule consist of rotational and vibrational energy, called rovibrational energy:

$$S(\upsilon, J) = G(\upsilon) + F(J) \tag{1.16}$$

Assuming no anharmonicity and centrifugal forces, S can be expressed as:

$$S(\upsilon, J) = \tilde{\nu}(\upsilon + \frac{1}{2}) + BJ(J+1) \tag{1.17}$$

Energy required for transitions between the rovibrational states is provided by absorbed or emitted photons. Typically, vibrational transitions need more energy and are about two orders of magnitude larger than the rotational transitions. An energy level scheme is illustrated in Figure 1.5.

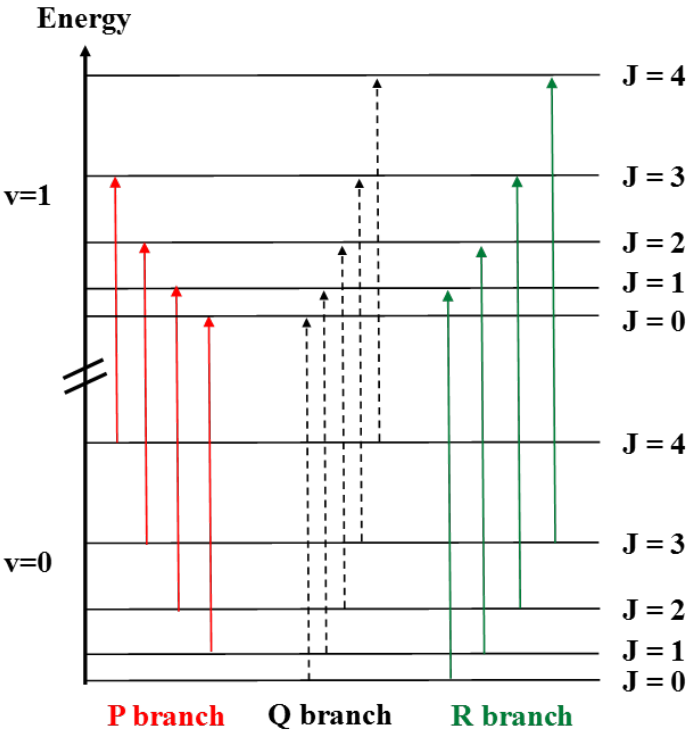

Figure 1.5: Schematic depiction of the rovibrational energy level transitions for different vibrational and rotational quantum numbers—υ, J. Transitions with $\Delta J = -1$ are called the P-branch, while $\Delta J = +1$ transitions build the R-branch. Q-branch denotes the transitions with the same rotational quantum number ($\Delta J = 0$) at ground and excited states. Only vibrational transitions occur when the molecular angular momentums is parallel to the molecular symmetry axis.

According to the Boltzmann distribution, individual line intensities vary with different J due to different populations N_i at states i:

$$\frac{N_J}{N_0} = (2J+1)\exp\left(\frac{-h\nu}{k_B T}\right) \tag{1.18}$$

where k_B is the Boltzmann constant and T the absolute temperature. $(2J+1)$ represents the degeneracy of the rotational states. For a J starting from the middle of the transition band, the term $(2J+1)$ dominates and the line strength increases linearly with increasing J. At

margins of the band, the line strength decreases with increasing J caused by the dominant thermal distribution of the molecular states ($\exp(\frac{-h\nu}{k_B T})$).

1.2.2 Polyatomic molecules

Polyatomic molecules like CO_2, have much more complicated energy transitions and hence much more complicated spectra. To locate a molecule with N atoms, $3N$ coordinates are required, as each atom moves in three dimensions. The $3N$ is also known as the number of degrees of freedom (DOF) of the system due to translations, vibrations and rotations. The translational motion describes the position of the center mass for a molecule, and every molecule has three translational DOF. For rotational motion, a linear molecule has two angular coordinates, i.e. two rotational DOF, while a nonlinear molecule has three angular coordinates, i.e. three DOF. Therefore, a linear molecule contains $3N$-5 ($3N$-3-2) normal vibration DOF, and a nonlinear molecule has $3N$-6 ($3N$-3-3) vibrational DOF.

This thesis mainly deals with the linear molecule CO_2, consisting of one carbon atom and two oxygen atoms and containing $3N$-5 = 4 vibrational DOF. These four vibrational normal modes are presented in Figure 1.6. The symmetric stretching vibration with $\tilde{\nu}_1 = 1388\,\mathrm{cm}^{-1}$ is infrared inactive because of an unchanged dipole moment. The asymmetric stretching and both bending vibrations are infrared active and the corresponding wavenumbers are $\tilde{\nu}_1 = 2349\,\mathrm{cm}^{-1}$ and $\tilde{\nu}_3 = 667\,\mathrm{cm}^{-1}$, respectively. For the stretching vibrations the $\Delta J = 0$ is not allowed because the changing dipole moment is parallel to the molecular axis. However, $\Delta J = 0$ can exist in the bending vibrations when CO_2 becomes a nonlinear molecule and its dipole moment change is perpendicular to the molecular axis. A schematic depiction of the structure of a CO_2 band is presented in Figure 1.7 where spectral lines are caused by combinations of four different vibrational modes.

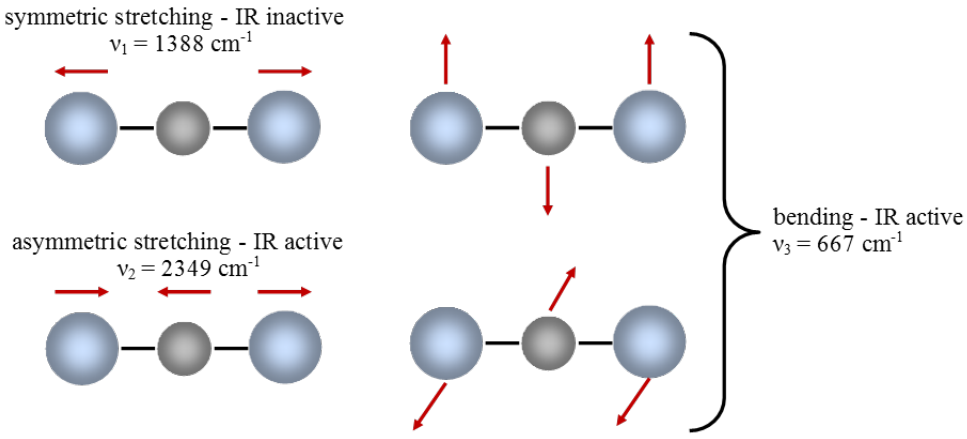

Figure 1.6: The four vibrational modes of a linear polyatomic molecule, using CO_2 as an example, including symmetric stretching (IR inactive), asymmetric stretching (IR active) and two bending vibrations (IR active) [Atkins and De Paula, 2006].

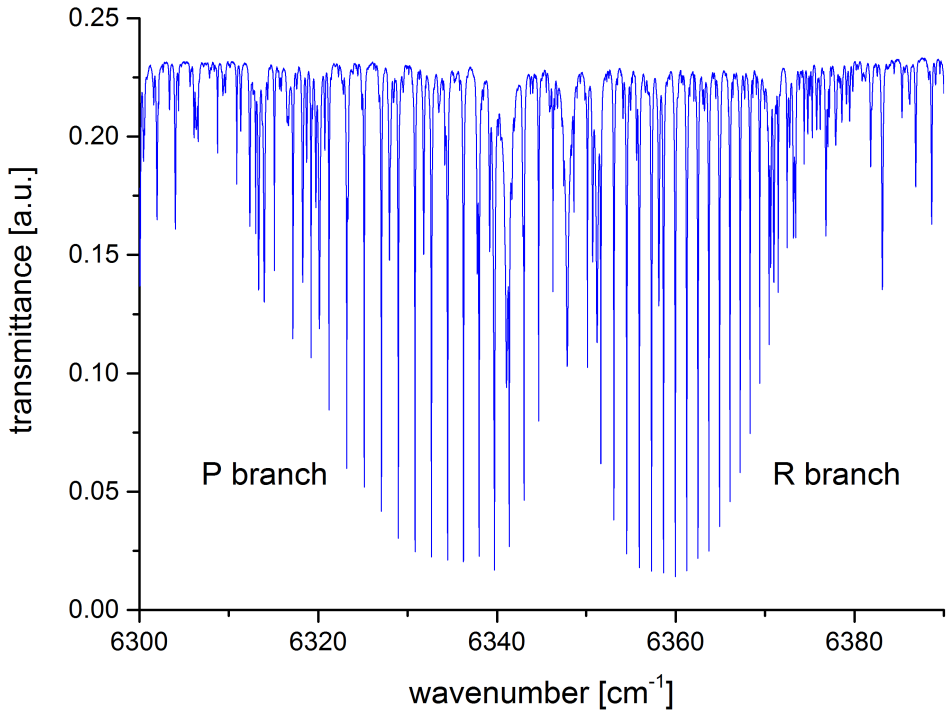

Figure 1.7: Atmospheric transmission spectrum of CO_2 recorded with the 125HR FTIR spectrometer in Karlsruhe, including the P and R branches of CO_2 with some interferring water lines.

1.3 Spectral line shapes

Absorption or emission line profiles observed in spectra are not infinitely narrow but have specific shapes and widths. Various physical mechanisms can lead to the broadening of spectral lines. According to the uncertainty principle, the lifetime of an excited state is related with the uncertainty of its energy:

$$\Delta E \Delta t \approx \frac{h}{4\pi} \tag{1.19}$$

Typically, the spectral line width is limited to the finite lifetime of molecular excited states and a shorter lifetime has a higher energy uncertainty and a spectrally broader emission. Broadening due to this effect is called the natural linewidth, producing a spectral line with Lorentzian shape. In general, a full width at half maximum (FWHM) is on the order of $\Delta\tilde{\nu}$ $\approx 10^{-8}\,\mathrm{cm}^{-1}$ [Hase, 2000]. However, this broadening can be neglected compared to other effects (Doppler broadening or pressure broadening) for atmospheric spectra.

1.3.1 Doppler broadening

The Doppler broadening is also known as thermal broadening. The atoms or molecules are constantly and randomly in motion with velocities depending on the temperature. The thermal velocity distribution for a gas relative to the observer can be described with a Maxwell-Boltzmann distribution:

$$\frac{n(\upsilon)}{N}d\upsilon = \sqrt{\frac{m}{2\pi k_B T}}\exp\Big(\frac{-mv^2}{2k_B T}\Big)dv \tag{1.20}$$

here $\frac{n(\upsilon)}{N}$ is the fraction of particles with a thermal speed υ, i.e. a probability density function of the particle energy distribution. In consequence, Doppler broadened spectral lines have a Gaussian distribution:

$$f_D(\tilde{\nu}) = \frac{1}{\sigma\sqrt{2\pi}}\exp\Big(-\frac{1}{2}\big(\frac{\tilde{\nu}-\tilde{\nu}_0}{\sigma}\big)^2\Big)d\upsilon \quad \text{with} \quad \sigma = \sqrt{\frac{k_B T\tilde{\nu}_0^2}{mc^2}} \tag{1.21}$$

The FWHM of the Doppler line shape is:

$$\Delta\tilde{\nu}_D = \tilde{\nu}_0\sqrt{\frac{8k_B T ln\,2}{mc^2}} \tag{1.22}$$

$\Delta\tilde{\nu}_D$ increases with higher temperature, higher wavenumber, and lower molecular mass. Typically, for CO_2 the Doppler broadening is $\Delta\tilde{\nu}_D \approx 7\times10^{-3}\,\mathrm{cm}^{-1}$ at 270 K.

1.3.2 Pressure broadening

The pressure broadening is caused by the collision between atoms or molecules, resulting in shorter lifetime of excited states and broader line shapes. Higher pressure, i.e. higher molecular number density leads to higher probability of collisions. Therefore, the pressure broadening effect is stronger at lower atmospheric levels. Similar to the natural lifetime broadening, the profile of the collision broadening lines follows a Lorentzian distribution:

$$f_P(\nu) = \frac{1}{\sqrt{\pi}}\frac{\Delta\nu_P}{(\nu-\nu_0)^2+\Delta\nu_P^2} \tag{1.23}$$

The FWHM depends on the mean time $\tau_{coll}=\frac{\sqrt{mkT}}{4\sqrt{\pi}d^2p}$:

$$\Delta\nu_P = \frac{1}{2\pi\tau_{coll}c} \sim p \tag{1.24}$$

$\Delta\nu_P$ show a positive correlation to the pressure p and therefore, the pressure broadening is the dominating factor contributing to the line shape in the troposphere up to the middle stratosphere. The Doppler broadening is the dominant effect in the middle stratosphere and upwards. Assuming $p = 1000$ hPa, $\Delta\nu_P$ reaches approximately $0.01\,\mathrm{cm}^{-1}$.

1.3.3 The Voigt function

In order to determine an atmospheric spectral line shape, both Doppler and pressure broadening are needed. The resulting shape of the observed spectral line profile can be expressed as the Voigt profile, the convolution of a Gaussian with a Lorentzian distribution:

$$f(\nu) = \int_{-\infty}^{\infty} f_P(\tilde{\nu}) f_D(\nu - \tilde{\nu}) d\tilde{\nu} \tag{1.25}$$

The above equation is analytically unsolvable. However, various approximations can be used to numerically solve the convolution [Liu et al., 2001]. Due to the computational expense of the convolution operation, the Voigt profile is often handled by assuming a pseudo-Voigt profile which uses different approximative methods instead of a direct convolution.

1.4 Fourier transform infrared spectroscopy

Fourier transform infrared (FTIR) spectroscopy is an analytic technique, measuring the absorption or emission of infrared radiation by gaseous, liquid and solid constituents versus wavelength. It helps to qualitatively and quantitatively identify the chemical bonding and molecular components and structures. This powerful technique is often used in the remote sensing of GHGs in the atmosphere for measuring trace gas abundances. In the following section, the principles of FTIR spectroscopy are introduced, together with the principles and setup of an FTIR spectrometer. In addition, the mathematical procedure is described for deriving a spectrum from an interferogram (IFG) recorded with the FTIR spectrometer.

1.4.1 The FTIR spectrometer

Generally, the core component of an FTIR spectrometer is a Michelson interferometer (see Figure 1.8), including a semi-transparent beam splitter, a fixed mirror and a moving mirror. Incoming radiation from the external light source is collimated and directed to the beam splitter, which divides the radiation ideally half to a fixed mirror and the other half to a moving mirror. The optical path difference (x) between the partial beams is thereby determined by the position of the moving mirror. Both mirrors reflect the radiation back through the beam splitter acting as a recombiner. The recombined beam is directed to a photo diode detector, where the fluctuating intensity is measured as a function of the optical path difference.

According to the principle of superposition when two or more waves travel through the same medium at the same time, the resulting electric field is determined by the sum of each wave vector. Considering the two beams from a common source with different distance of

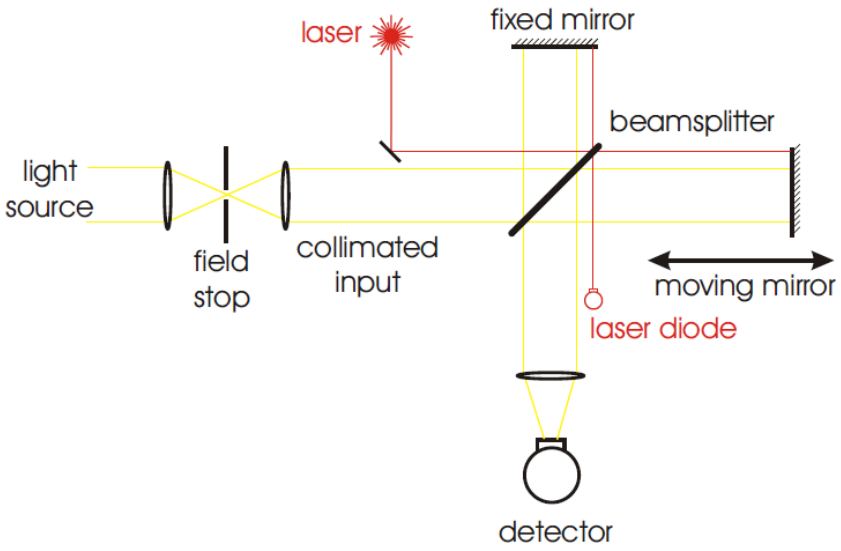

Figure 1.8: Schematic depiction of a Michelson interferometer. The laser beam is used to determine the precise position of the moving mirror that helps to generate the path difference. Image taken from Gisi [2012].

propagation x_1 and x_2, the superposition of two monochromatic waves is given by:

$$\begin{aligned} a &= A\cos(2\pi x_1\tilde{\nu}) + A\cos(2\pi x_2\tilde{\nu}) \\ &= 2A\cos(\pi\tilde{\nu}x)\cos\left(2\pi\tilde{\nu}\left(\frac{2x_2+x}{2}\right)\right) \end{aligned} \tag{1.26}$$

here A denotes the amplitude and x the optical path difference between x_1 and x_2. The measured intensity of the interferogram $I(x)$ is connected to the temporal average of the square of the superimposed wave amplitudes:

$$I(x) \approx a^2 = I(\tilde{\nu})[1+\cos(2\pi\tilde{\nu}x)] \tag{1.27}$$

The beams interfere constructively when the optical path difference is $x = \frac{n}{\tilde{\nu}}$ with n = 0,1,2,... while the beams interfere destructively when n = $\frac{1}{2}$,$\frac{3}{2}$,$\frac{5}{2}$,... When the light radiates from a polychromatic source instead of a monochromatic one, the superimposed intensity has to be integrated over all wavenumbers:

$$\begin{aligned} I(x) &= \int_{-\infty}^{\infty} I(\tilde{\nu})[1+\cos(2\pi\tilde{\nu}x)]d\tilde{\nu} \\ &= \int_{-\infty}^{\infty} I(\tilde{\nu})d\tilde{\nu} + \int_{-\infty}^{\infty} I(\tilde{\nu})\cos(2\pi\tilde{\nu}x)d\tilde{\nu} \\ &= I_{DC}(x) + I_{AC}(x) \end{aligned} \tag{1.28}$$

The resulting interferogram $I(x)$ comprises a constant term ($I_{DC}(x)$) and a modulated fluctuating term ($I_{AC}(x)$). The latter is generally referred to as the interferogram:

$$I(x) = \int_{-\infty}^{\infty} I_{AC}(x)\cos(2\pi\tilde{\nu}x)dx \tag{1.29}$$

1.4.2 The Fourier transformation

To determine the spectrum $S(\tilde{\nu})$ from the interferogram $I(x)$, the Fourier transformation is used:

$$S(\tilde{\nu}) = FT(I(x)) = \int_{-\infty}^{\infty} I(x)\exp(-i2\pi\tilde{\nu}x)dx \tag{1.30}$$

$$I(x) = FT^{-1}(S(\tilde{\nu})) = \int_{-\infty}^{\infty} S(\tilde{\nu})\exp(i2\pi\tilde{\nu}x)d\tilde{\nu} \tag{1.31}$$

The above mentioned case is assuming that the measured interferogram is continuous. However, the practically recorded interferogram is finite, consisting of N equally spaced discrete sampling points with distance Δx. Therefore, Equations (1.30) and (1.31) can be written as:

$$S(\tilde{\nu}_m) = \sum_{n=1}^{N} I(x_n)\exp(-i2\pi\tilde{\nu}_m x_n) \tag{1.32}$$

$$I(x_n) = \frac{1}{N}\sum_{m=1}^{N} S(\tilde{\nu}_m)\exp(i2\pi\tilde{\nu}_m x_n) \tag{1.33}$$

The sampling interval Δx needs to satisfy the Nyquist-Shannon sampling theorem with a band limitation of ($\tilde{\nu}_{max}$-$\tilde{\nu}_{min}$):

$$\frac{1}{\Delta x} > 2(\tilde{\nu}_{max} - \tilde{\nu}_{min}) \tag{1.34}$$

The Nyquist sampling theorem links the continuous-time signals and discrete-time signals. For recording a useful interferogram, it is necessary to appropriately choose the optical path difference sampling interval Δx. The spectrum frequency is not allowed to be outside the range. Otherwise, the contributions from the out-of-range spectrum will be folded back into the observed range, resulting in a systematic distortion, called aliasing. For the FTIR spectrometers used in this work, a reference Helium-Neon (HeNe) laser (632.988 nm) is used to determine the sampling interval Δx. The high folding limit (HFL) is set to $\tilde{\nu}_{max} = 15\,798\,\mathrm{cm}^{-1}$. Ideally, the reference laser passes through the interferometer and the interferogram is sampled at every zero crossing of the laser AC interferogram. However, to reduce ghosting for some setups it is only sampled on the rising edge and interpolated in between using the XSM[1] parameter [Hedelius et al., 2016].

[1] XSM: Bruker code for interpolation during acquisition

1.4.3 Apodisation and instrumental line shape

In practice, the maximum optical path difference (MOPD) is limited due to the limited path length of the moving mirror. Therefore, the size of the interferogram is finite and a realistic interferogram is truncated at MOPD. The truncated interferogram is mathematically equivalent to the convolution of the infinite interferogram ($I_{inf}(x)$) and a Boxcar function ($B(x)$):

$$I_{AC}(x) = I_{inf}(x) \otimes B(x) \tag{1.35}$$

where $B(x) = 1$ for $|x| \leq$ MOPD and 0 for $|x| >$ MOPD. The resultant measured spectrum $S_{meas}(\tilde{\nu})$ is derived from the Fourier transform of $I_{inf}(x)$ and $B(x)$:

$$S_{meas}(\tilde{\nu}) = S_{inf}(\tilde{\nu}) \otimes \frac{\sin(2\pi \text{MOPD}\tilde{\nu})}{2\pi\tilde{\nu}} \tag{1.36}$$

The spectral resolution is defined by the width of the sinc function with the FWHM of $\Delta\tilde{\nu} = \frac{0.6035}{\text{MOPD}}$.

However, the sinc function shows pronounced non-physical negative side lobes, which leads to unrealistic values in the measured spectrum. To eliminate this impact, another function (e.g. a triangular or Gaussian function) is introduced and multiplied with the Boxcar function, called apodization. This method dampens the negative side lobes but also reduces the spectral resolution. In this thesis the Norton-Beer-Medium apodization is applied to the interferograms recorded with the EM27/SUN spectrometer to obtain sufficient suppression of the side lobes and acceptable resolution. The spectral resolution of an Fourier transform spectrometer (FTS) can not be defined unambiguously because different resolution criteria can be applied. In this work the FTS resolution is defined as:

$$\Delta(\tilde{\nu}) = \frac{0.9}{\text{MOPD}} \tag{1.37}$$

The sinc function is also part of the instrumental line shape (ILS), which is an important factor to characterize the shape of a spectral line. More detail about the ILS is provided in section 2.2.

1.5 Inversion theory

The scientific inversion problem describes the mathematical process of calculating the target variables $\mathbf{x}$ from a set of observations $\mathbf{y}$. It is the inverse of a forward problem, which sets the $\mathbf{y}$ value as a function of $\mathbf{x}$, using a function $\mathbf{F}$. In the atmospheric remote sensing FTIR spectroscopy, in general a measured transmission spectrum is considered as $\mathbf{y}$. The inversion calculation of this atmospheric spectrum is performed to determine the amounts of trace gas concentrations, $\mathbf{x}$. In this section, vectors are denoted by bold lower case symbols, e.g. $\mathbf{x}$ and matrices by the bold upper case symbols, e.g. $\mathbf{A}$.

In general, the inverse model starts with the forward calculation. Assuming no measured signal error, a simple forward model is written:

$$\mathbf{y} = \mathbf{F}(\mathbf{x}, \mathbf{u}) \tag{1.38}$$

here $\mathbf{x}$ is the state vector of length n, containing independent unknown variables, e.g. volume mixing ratio, while $\mathbf{u}$ includes fixed parameters, e.g. pressure, temperature. The measured signal is denoted by a measurement vector $\mathbf{y}$, of size m. In general, $\mathbf{F}$ is not linear and has to be adequately linearized for the inversion within the range of the comparison ensemble:

$$\mathbf{y} - \mathbf{y}_0 = \mathbf{K}(\mathbf{x} - \mathbf{x_0}) \tag{1.39}$$

where $\mathbf{K} = \frac{\Delta F}{\Delta x}$ is the $m \times n$ Jacobian matrix. $\mathbf{x}_0$ represents a linearization point with only local permission, and $\mathbf{y}_0 = \mathbf{F}(\mathbf{x}_0)$. When n > m, the inversion problem is overdetermined, i.e. more measurements exist than unknowns, otherwise it is underdetermined in case of m > n. To minimize the difference $\Delta\mathbf{y}$ between the measured signal ($\mathbf{y}_{meas}$) and the synthetic signal ($\mathbf{y}$), the square norm is applied:

$$|\Delta\mathbf{y}|^2_{\mathbf{S_y}^{-1}} = |\mathbf{y_{meas}} - \mathbf{y}|^2_{\mathbf{S_y}^{-1}} = (\mathbf{y_{meas}} - \mathbf{y(x)})^{\mathbf{T}}\mathbf{S_y}^{-1}(\mathbf{y_{meas}} - \mathbf{y(x)}) \tag{1.40}$$

where $\mathbf{S_y}$ denotes the covariance matrix of the retrieved state. The superscript T represents the transpose of matrices and vectors. To solve the nonlinearity least-squares problem, the Gauss-Newton algorithm is used to estimate the state vector after $i + 1$ iterations:

$$\mathbf{x}_{i+1} = \mathbf{x}_i + (\mathbf{K}_i^{\mathbf{T}}\mathbf{S_y}^{-1}\mathbf{K}_i)^{-1}\mathbf{K}_i^{\mathbf{T}}\mathbf{S_y}^{-1}(\mathbf{y_{meas}} - \mathbf{y(x_i)}) \tag{1.41}$$

In case of remote sensing measurements, the knowledge from the experiment is insufficient for the inversion of trace gas profiles, resulting in unrealistic oscillations. To solve the ill-posed inverse problem, either a constrained profile retrieval or a simple scaling of the a-priori profile is used. One of the common regularization methods called Tikhonov-Philips [Phillips, 1962; Tikhonov, 1963] is frequently applied. Equation (1.40) after regularization is given by:

$$|\mathbf{y_{meas}} - \mathbf{y}|^2_{\mathbf{S_y}^{-1}} + \gamma|\mathbf{B}(\mathbf{x} - \mathbf{x_a})|^2 \tag{1.42}$$

The above term should be minimized. $\mathbf{x_a}$ denotes an a-priori set of state variables, $\mathbf{B}$ the regularization matrix. γ represents the regularization parameter, ranging from 0 to ∞. A larger γ depicts higher strictness of the constraint. Therefore, the iterative solution is:

$$\mathbf{x}_{i+1} = \mathbf{x}_i + (\mathbf{K}_i^{\mathbf{T}}\mathbf{S_y}^{-1}\mathbf{K}_i + \gamma\mathbf{B}^{\mathbf{T}}\mathbf{B})^{-1}\left[\mathbf{K}_i^{\mathbf{T}}\mathbf{S_y}^{-1}(\mathbf{y_{meas}} - \mathbf{y(x_i)}) + \gamma\mathbf{B}^{\mathbf{T}}\mathbf{B}(\mathbf{x_a} - \mathbf{x_i})\right] \tag{1.43}$$

The altitude resolution of a measurement is described by the resolution matrix $\mathbf{R}$:

$$\mathbf{R} = (\mathbf{K^T S_y^{-1} K} + \gamma \mathbf{B}^T \mathbf{B})^{-1} \mathbf{K^T S_y^{-1} K} \tag{1.44}$$

where the trace of the matrix determines the number of degrees of freedom for the signal.

In this work, the simple approach of scaling the a-priori profile is applied. This strategy is also used by TCCON and is even more justified when working with low-resolution spectrometers. The applied retrieval equation for the scalar scaling factor is equivalent to Equation (1.41).

Chapter 2

Instruments and retrieval method

This chapter first introduces the Total Carbon Column Observing Network (TCCON) and the 125HR FTIR spectrometer used by the network, mainly focusing on the Karlsruhe, Germany and Sodankylä, Finland sites. The FTS primarily used in this work is the EM27/SUN FTIR spectrometer. It is a new kind of a mobile solar absorption spectrometer, developed by KIT (Karlsruhe Institute of Technology) in cooperation with Bruker Optics GmbH. A brief outline of the EM27/SUN spectrometer characteristics is given. In order to take into account the performance of an individual spectrometer, the instrumental line shape is used as an important assessment and should be considered in the retrieval procedure. Therefore, a simple open-path measurement is used to obtain the ILS parameters of the EM27/SUN spectrometer. Additionally, two types of retrieval software, GGG for the official TCCON retrievals and PROFFIT for the EM27/SUN retrievals are introduced.

2.1 Instrumentation

2.1.1 TCCON Network

Established in 2004, the TCCON[1] had the initial purpose of acquiring precise and accurate column abundance of CO_2 [Wunch et al., 2011]. It has been gradually extended to the detection of more species (e.g. CH_4, CO, N_2O, HF, HDO) and expanded all over the world. Currently there are 26 TCCON stations in service and some potential sites are planned (see Figure 2.1).

The Bruker 125HR instrument (Bruker Optics GmbH, Germany) is a well-developed commercial FTIR spectrometer. It is characterized as a stable, robust and high-resolution instrument and is so far the only accepted instrument for TCCON measurements [Wunch et al., 2011]. In order to obtain comparable and accurate data within the network, instrumental settings are officially specified, as is the data retrieval approach. The standard TCCON instrument measures column-averaged abundances of trace gases, like CO_2, CH_4, CO and

[1] https://tccon-wiki.caltech.edu

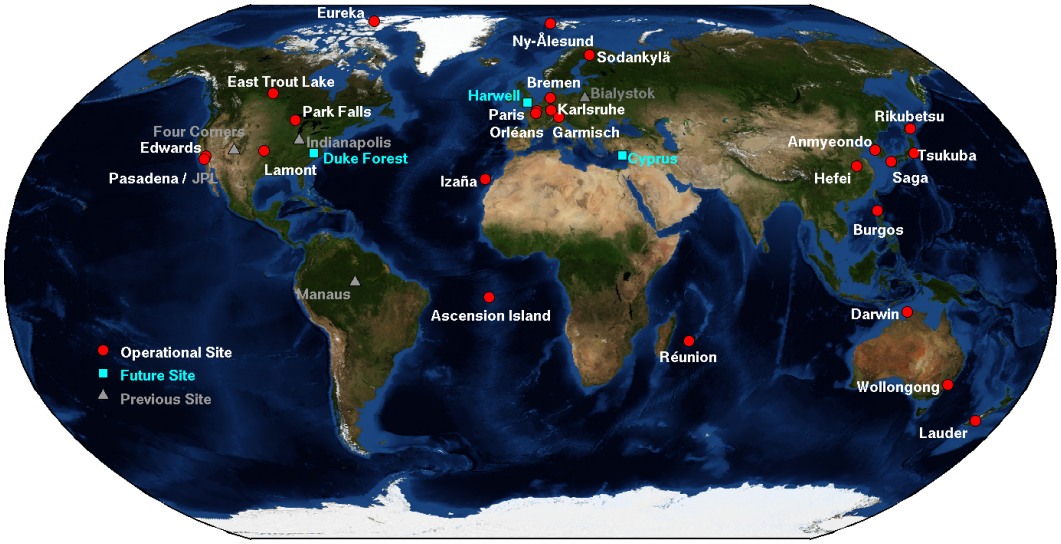

Figure 2.1: TCCON site map, showing the operational, future and previous sites. Image taken from https://tccondata.org/.

N_2O in the near-infrared (NIR) spectral window by recording solar-absorption spectra. The MOPD is 45 cm, resulting in a spectral resolution of 0.02 cm^{-1}. Spectral coverage from 3800 to 15 500 cm^{-1} is achieved by simultaneous operation of two detectors at room temperature. One is an indium gallium arsenide (InGaAs) detector, covering a spectral range from 3800 to 12 000 cm^{-1}. A dichroic optic is used to define a cutoff at wavenumbers of 10 000 cm^{-1}. The other official detector is the silicon diode (Si) detector, originally covering a spectral range from 9500 to 30 000 cm^{-1}. A cut-off filter is applied to discard the visible spectra with wavenumbers larger than 15 500 cm^{-1}. Additionally, similar optical elements, like beam splitters, band filters, etc. are applied to further fulfill the standardization.

The standardization decreases the site-to-site bias and improves the comparability within the network. It also satisfies the requirements for the global-scale satellite validation studies, like the OCO-2 satellite (Orbiting Carbon Observatory 2), GOSAT (Greenhouse Gases Observing Satellite), SCIAMACHY (Scanning Imaging Absorption Spectrometer for Atmospheric Chartography) and others. A consistent comparison of XCO_2 for GOSAT, SCIAMACHY, CarbonTracker and MACC (Monitoring Atmospheric Composition and Climate) with TCCON observations was performed by Kulawik et al. [2016]. The recent work by Wunch et al. [2017] compared measurements of XCO_2 from different TCCON sites around the world to XCO_2 retrievals from the OCO-2 satellite (version B7), based on three kinds of viewing modes (nadir, glint and target modes). Moreover, TanSat (Chinese Carbon Dioxide Observation Satellite Mission, also known as CarbonSat) was launched in December, 2016 which carries the Carbon Dioxide Spectrometer (CDS). This high-resolution grating spectrometer measures CO_2 absorption in the NIR spectral range. The validation projects for CDS are ongoing including comparisons with TCCON data [Lu et al., 2017].

2.1.1.1 The Karlsruhe site

The Ground-based Remote Sensing group of the Institute of Meteorology and Climate Research at KIT has been operating a TCCON site at Campus North since 2009. Karlsruhe, located in the Rhine valley is a urban sprawled city (population: ca. 440 000), and is characterized by a mild oceanic climate, with rare extreme temperatures or precipitation year around. However, it is one of the cities with the highest number of sunshine hours in Germany.

The Karlsruhe FTIR station is located in the central west part of Europe (49.10 °N, 8.44 °E, 110 m a.s.l.) with a rather flat topography, extending northward to the foothills of the Black Forest, which is a large forested mountain range. It provides useful data for understanding the emission of GHGs in Central Europe and is an excellent place for validating satellite measurements, like the OCO-2 satellite, GOSAT, SCIAMACHY, TROPOMI, etc. because of its relatively flat topography.

Figure 2.2: Shipping container (left panel) and TCCON FTIR spectrometer (right panel) at KIT - Campus North, Karlsruhe, Germany. Figures were taken by Dr. Thomas Blumenstock.

The Karlsruhe FTIR instrument is settled in climate controlled container to keep a steady lab environment year around (see Figure 2.2). The Bruker IFS 125HR spectrometer is operated remotely and performs the measurements semi automatically. In addition to the standard NIR spectral range covered by the InGaAs detector, the Karlsruhe instrument extends the measuring region to the mid-infrared (MIR) band, down to 1900 cm^{-1}. A dichroic optical element with a cut-off wavenumber at 5250 cm^{-1} is installed in front of the InGasAs detector, defining a spectral coverage from 5250 to 11 000 cm^{-1}. An indium antimonide (InSb) detector together with a cut of narrowband spectral filter covers the spectral region from 3800 to 5250 cm^{-1}. The target gases relevant with the context of this work are CH_4, O_2, CO_2 measured with InGaAs detector while CO is measured with the InSb detector [Kiel, 2016].

2.1.1.2 The Sodankylä site

The Sodankylä FTIR instrument is located at the Finnish Meteorological Institute (FMI), Arctic Research Center (67.37 °N, 26.63 °E, 188 m a.s.l.), and is about 7 km away from the low-population-density city center (population: ca. 8500). This area represents a typical northern boreal forest/taiga environment, surrounded predominantly by coniferous forest withh some mixed/deciduous forest (see Figure 2.3). The FTIR spectrometer was established in early 2009 and has been part of the TCCON since then. Inside the Arctic Circle, Sodankylä experiences a subarctic climate, with mild temperature and long sunshine hours in summer. Around the summer solstice (around June 21), the sun shines for a full 24 hours everyday. Measurements during summer daylight therefore offer a good temporal coverage for the study of intraday changes.

The Sodankylä FTIR instrument records interferograms from which total columns of CO_2, O_2, CH_4, CO, N_2O, H_2O, HDO and HF can be retrieved. These spectra are recorded with the TCCON official 125HR spectrometer. This instrument is located in a laboratory and a solar tracker (type Bruker A457N) is mounted on the roof of the building. Since July 2013 the FTIR spectrometer has been operated automatically with the help of a self-controlled cover for the solar tracker which reads and analyzes weather radar forecast data, along with rain and direct solar radiation for opening and closing the cover [Kivi and Heikkinen, 2016]. The instrument employs the standard TCCON setting of InGaAs and Si detectors. Spectral coverage from 4000 to 15 000 cm^{-1} is achieved by simultaneous operation of two detectors at room temperature as used by the majority of TCCON sites: an indium gallium arsenide (InGaAs), covering from 4000 to 11 000 cm^{-1} and a silicon diode (Si), covering from 9000 to 15 000 cm^{-1}. Two kinds of resolution settings are used for the 125HR instrument during the campaign. The TCCON official measurements with a high resolution of 0.02 cm^{-1} is used as a reference to the retrievals of the EM27/SUN instruments and other portable FTIR instruments. Lower resolution scans are also recorded with 0.5 cm^{-1} resolution to mimic the EM27/SUN instrument using similar measurement parameters (double sided, 4 scans at 20 kHz). The measurements with lower resolution are considered as an additional kind of comparison reference with matched sensitivity.

2.1.2 The KIT EM27/SUN instruments in Sodankylä and Kiruna

The high-resolution TCCON sites are distributed globally, however, many of these are concentrated in Europe, Northern America and eastern Asia. The costs and heavy equipment being required to move it on site have hindered the expansion of the network to the African continent, South America and central Asia [Wunch et al., 2015]. Remote sites and regions with high or low surface albedo are generally poorly covered by the TCCON network. Recently, cheaper and portable spectrometers have been developed and are now available for GHG measurements, with the potential to complement the TCCON network. The EM27/SUN

Figure 2.3: TCCON station (right) and the EM27/SUN spectrometer (lower left) at FMI, Sodankylä, Finland.

spectrometer was developed by KIT [Gisi et al., 2012], in cooperation with Bruker Optics GmbH, Ettlingen, Germany. It has been offered by Bruker as a commercial device since spring 2014. The EM27/SUN instrument is a portable ground-based FTIR spectrometer, consisting of a spectrometer body with dimensions of $35 \times 40 \times 27\,\mathrm{cm}$ and a solar tracker which is directly mounted on the spectrometer. The whole weight is approximately 25 kg and can be carried by one person.

The EM27/SUN employs the Bruker's RockSolid$^{\mathrm{TM}}$ pendulum interferometer with paired retroreflecting cube corner mirrors and a CaF_2 beam splitter. The 1.8 cm MOPD is generated by a balanced wear-free pivot mechanism, corresponding to a spectral resolution of $0.5\,\mathrm{cm}^{-1}$. To reach this, the two gimbal-mounted retroreflectors move a geometrical distance of 0.45 cm. This creative design achieves high stability and is resistant to thermal influences and mechanical disturbances. A 90° off-axis parabolic mirror is used for centering the solar beam on the detector and it has a focal length of 127 mm. Together with a 0.6 mm aperture, this defines a semi-FOV (field of view) of 2.36 mrad. An external FOV of around 56 % of the solar disc diameter is used. Double-sided DC coupled interferograms are recorded with an InGaAs detector at ambient temperature. The detector is a photodiode type HAMAMATSU$^{\mathrm{TM}}$ G12181-010K with a size of $1 \times 1\,\mathrm{mm}$, covering the spectral range from 5500 to $12\,000\,\mathrm{cm}^{-1}$. Total columns of CO_2, O_2, CH_4 and H_2O can be retrieved from this spectral range. The target gases and corresponding spectral windows for the TCCON and EM27/SUN spectrometers retrievals are listed in Table 2.1.

Recently, a second DC-coupled InGaAs detector has been added to additionally cover the spectral region from 4000 to $5500\,\mathrm{cm}^{-1}$ [Hase et al., 2016] (see Figure 2.4). The dual-channel EM27/SUN instrument covers the same spectral range used by the TCCON and TROPOMI (TROPOspheric Monitoring Instrument) short-wave band used for CO and CH_4 retrievals.

Target gas	Spectral window [cm^{-1}]	
	TCCON	EM27/SUN
O_2	7765.00-8005.00	7765.00-8005.00
CO_2	6180.00-6260.00 6297.00-6382.00	6173.00-6390.00
CH_4	5880.00-5996.00 5996.45-6007.55 6007.00-6145.00	5897.00-6145.00
CO	4208.70-4257.30 4262.00-4318.80	4210.00-4320.00

Table 2.1: Various target gases and spectral windows for the TCCON and EM27/SUN spectrometers.

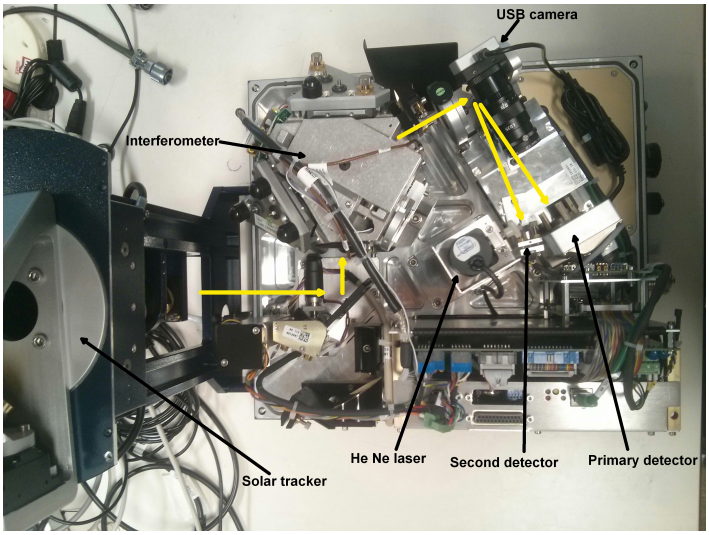

Figure 2.4: The open EM27/SUN instrument with a second CO channel [Hase et al., 2016]. The yellow arrows depict the light path. This figure is adapted from Frey [2018].

This extension enables the observation of CO, N_2O and HDO. To achieve this, a plane mirror of $10 \times 20\,mm^2$ is located directly behind the off-axis parabolic mirrors for the partial decoupling of the beam. This method avoids readjustment of the optical alignment. Nearly 40 % of the incoming beam is reflected to the additional detector. The reflected beam to the second detector forms approximately a 25° intersection angle with the primary reflected beam going into the first detector. The secondary aperture stop in front of the detector element has a larger diameter (0.80 mm) than the primary one. The detector element has $1\,mm^2$ sensitive area. A wedged Germanium long-pass filter is mounted between the secondary field stop and the additional InGaAs diode in order to suppress the spectral range which is already covered by the primary detector and hence to increase the signal to noise ratio.

The excellent robust and reliable characteristics of the EM27/SUN instrument have been demonstrated in several successful field campaigns [Butz et al., 2017; Frey et al., 2015; Klappenbach et al., 2015]. The EM27/SUN instrument was also used for the observation of GHGs in Sodankylä with ambient temperature in the range between −15 to 30 °C, see Figure 2.5. These measurements were performed in the framework of the Fiducial Reference Measurements for Ground-Based Infrared Greenhouse Gas Observations campaign (FRM4GHG). This project was funded by European Space Agency (ESA), focusing on the intercomparison of different compact low-resolution instruments.

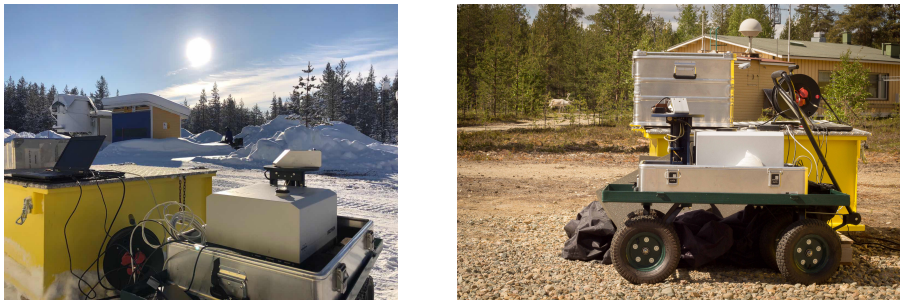

(a) Spring (b) Summer

Figure 2.5: The EM27/SUN spectrometer operated at FMI, Sodankylä in early spring (a) and summer (b). The right figure was taken by Dr. Friedrich Wilhelm Klappenbach.

Another EM27/SUN spectrometer (without the secondary channel) was installed at the Swedish Institute of Space Physics (IRF), Kiruna, northern Sweden (67.84 °N, 20.41 °E, 419 m a.s.l.) to study GHG gradients between Kiruna and Sodankylä. As part of the NDACC network, a Bruker 120 HR FTIR spectrometer has been operated at IRF since 1996 by KIT in cooperation with IRF and Nagoya University. The EM27/SUN spectrometer co-uses the solar beam of the Bruker 120HR interferometer. The solar tracker of the HR instrument is controlled with a camera and camtracker software, see Figure 2.6 (a). The tracker mirror of the EM27/SUN instrument is pointed to a fixed position, towards the mirror coupling out a part of the solar beam, see Figure 2.6 (b).

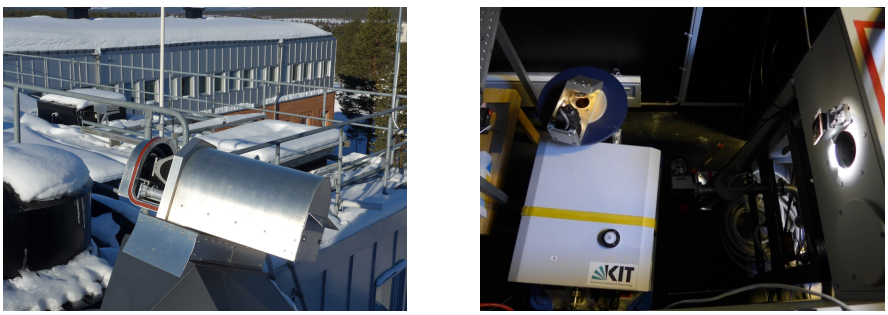

(a) Sun tracker on the roof (b) Sunbeam sharing in the lab

Figure 2.6: Sun tracker and the EM27/SUN spectrometer at IRF, Kiruna. The EM27/SUN instrument shares the solar beam with the NDACC instrument.

2.2 Instrument characterization-instrumental line shape

Properly characterizing the instrumental line shape (ILS) is of utmost important, because systematic biases are introduced into the trace gas retrievals when assuming an incorrect ILS. Hase et al. [1999] developed the LINEFIT algorithm to characterize the ILS referencing an ideal instrument in the form of two parameters—modulation efficiency (ME) and phase error (PE). These two characterizing parameters describe the modulation loss as a function of optical path difference with respect to an ideal spectrometer [Hase et al., 1999]. The ME describes the ratio between normalized modulation of actual observed interferogram signal and that of nominal FTS [Hase, 2012]. A modulation loss (ME < 1.0) indicates a broadening of the ILS at MOPD, while the ME larger than 1 indicates a narrower ILS. The optical path dependent phase error measures the degree of the asymmetry of the ILS and a zero value depicts a symmetric ILS shape.

Low-pressure ($\sim$5 hPa) gas cell measurements of HCl or HBr are normally used in TCCON and NDACC to retrieve the ILS [Hase et al., 2013]. However, to avoid the requirement of a gas cell, an open-path observation of a few meters of lab air is sufficient for retrieving the ILS of the low resolution (0.5 cm^{-1}) EM27/SUN instrument [Frey et al., 2015], see Figure 2.7. An external light source and ambient pressure, temperature, and humidity sensors are required. An Osram Halogen Display/Optic lamp 64602 (50 W, 12 V) is used as the radiation source. A stabilized digital laboratory DC power supply is used to obtain a constant and lower voltage than the nominal one. Here, a voltage of 11 V is used. An aspherical collimation lens with a diameter of about 2 inches is used for collimating the lamp's light. The system of the lamp and the collimation lens is mounted on a stable photographic tripod which allows simple and accurate adjustment of the height and direction of the lamp, to obtain an even illumination on the tracker mirror and a uniform image of the light source on the field stop. The bulb is slightly tilted to the lens which prevents multiple reflections. Finally, the tracker mirrors are adjusted manually to achieve a fully illuminated image of the lamp on the field stop.

Figure 2.7: Open-path measurement of a few meters of air in the KIT lab.

The instrument and light source are powered up two hours prior to the actual experiment. This ensures operation of the non-stabilized reference laser at a constant temperature and ensures emission of a constant wavelength. This experiment measures a few meters of lab air and the water column inside the instrument cannot be neglected. Hence, the two venting holes of the EM27/SUN are opened to allow ventilation, ensuring an equilibrated H_2O mixing ratio inside and outside the spectrometer (see Figure 2.8). Additionally, the ILS measurements are performed in a reasonably clean and controlled surrounding to avoid condensation and to obtain a stable thermal and clean condition inside the spectrometer [Frey et al., 2015]. It is not recommended to open the apertures when the surrounding humidity is too high or the instrument is colder than the environment.

Figure 2.8: Two apertures located on the top and lower side of the EM27/SUN instrument are open for the ventilation.

The distance between the spectrometer and the light source should be in a reasonable range. Too short of a distance might bring in systematic errors due to the non-negligible heat effect from the lamp on the section of the open-path near the lamp. A longer distance reduces the impact of the hot air surrounding the light bulb and leads to stronger water vapor absorption. However, this results in a smaller image on the field view, which makes it harder to ensure an even illumination. Typically, a distance of 4–5 m between the lamp to the first mirror of the solar tracker is used in this experiment. An environment with a room temperature around 20 °C and relative humidity between 30 % and 60 % is suggested.

The Bruker software OPUS is used to operate the spectrometer and to record both solar and laboratory spectra. The settings used in the open-path measurement are almost the same as those used in the solar observations and only the preamplifier gain which amplifies the analog signal before digitalization is set to a higher value. Thirty sets of 5 forward and 5 backward scans at full resolution are recorded of the lamp measurement. These 30 interferograms are averaged, DC corrected and fast Fourier transformed, along with applying a medium Norton-Beer apodization function at a limited resolution of $0.5\,\mathrm{cm}^{-1}$ in order to obtain the final spectrum for the LINEFIT analysis.

Several parameters are needed for retrieving the ILS parameters with the LINEFIT: the total optical path length (L), the air temperature and the pressure in the lab. L is comprised of the external distance from the very front of the collimator lens to the first tracking mirror

of the spectrometer (d, normally 4–5 m), the distance between the light bulb and the lens (5 cm), the distance between the first tracking mirror and the entrance window (38 cm), and the distance inside the spectrometer housing (58 cm). A Lutron MHB-383SD data logger is used for measuring both the temperature and the pressure in Karlsruhe, while a VAISALA PTB220ACA2A3 device records the pressure and a VAISALA HM40 with a HMP113 probe records the temperature in Sodankylä.

A simple two-parameter model (ME and PE) is obtained with the LINEFIT algorithm and is sufficient for the EM27/SUN instrument, because the ILS shape is close to the nominal expectation for a Fourier transform interferometer. The H_2O line list is required because this open-path experiment measures the absorption of the water column in the room. The H_2O line list is based on the HITRAN 2009 database with slight empirical modifications. Before retrieving the measured and final ILS, a precalculation of the H_2O column should be performed in the LINEFIT software based on the measured spectrum. This total column value of H_2O, together with the total optical path length of L (L=d+5 cm+38 cm+58 cm), and the air temperature are used to calculate the partial pressure of H_2O. The partial pressure is then used for the final retrieval run of the ILS parameters.

The ILS was first measured in February at KIT before the EM27/SUN instrument was shipped to Sodankylä. Several ILS characterization experiments were performed in the FRM4GHG project container on a regular schedule (see Figure 2.9). The values of the modulation efficiency at MOPD are shown in Figure 2.10.

Figure 2.9: Open-path measurement in the container of the FRM4GHG campaign at FMI, Sodankylä.

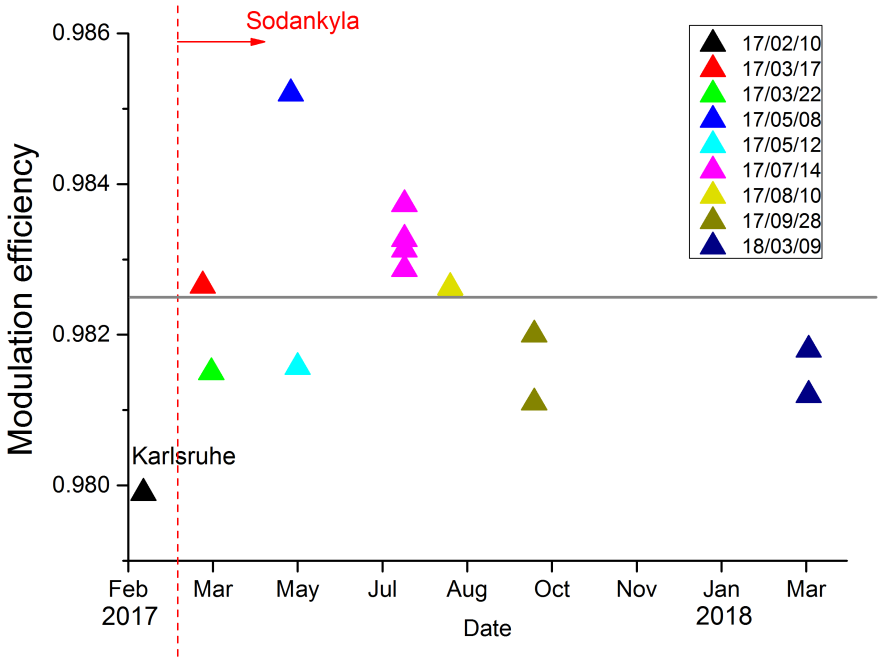

Figure 2.10: The results of the modulation efficiency at MOPD obtained with the LINEFIT software at KIT and FMI. EM27/SUN instrument was transported from Karlsruhe to Sodankylä in late February.

Compared to the experiment done at KIT (black triangle), the modulation efficiency recorded at FMI increased by about 0.27 %. This small change is probably due to the mechanical impacts and vibrations during the shipment from Germany to Finland. The ME results measured during the campaign varied within 0.14 %, showing no clear indication for a significant drift of the ILS parameters. This tiny variation is mainly caused by e.g. various surroundings, the lamp situation, everyday carrying in the early period of the campaign and manual errors during the characterization (e.g. alignment error, and error in the external distance measurement). The sudden increase of the modulation efficiency on May 8, 2017 is probably due to the use of the air conditioner in the lab which blew cold air directly through the path between the lamp and the instrument. This bias indicates that the open-path experiment requires stable ambient conditions. To study the effect of the length of the air column, an experiment testing three different distances was performed. Figure 2.11 shows the ME parameters and the water column as a function of the distance. No obvious change of ILS parameters occurs when the distance changes. The ME values are between 0.9918 and 0.9929, with a 0.06 % standard deviation (Figure 2.11, left panel). The abundances of the water column show an excellent linear correlation with distance (Figure 2.11, right panel). The ME and PE for the two EM27/SUN instrument located in Sodankylä and Kiruna are listed in table 2.2.

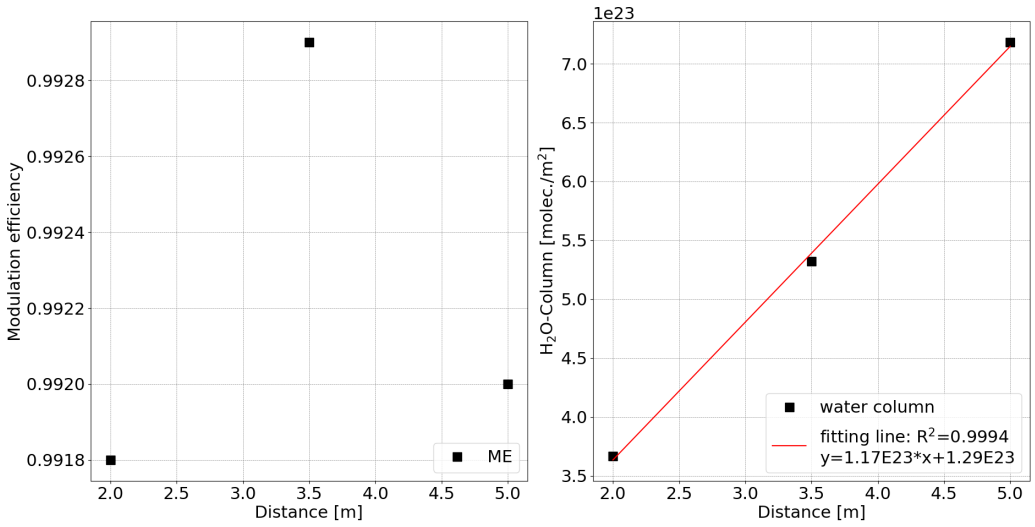

Figure 2.11: Open-path measurements for the EM27/SUN instrument on May 12, 2017 when ILS characterization of the instrument at three different locations was performed. The left panel shows the modulation efficiency with respect to the distance; the right panel shows the measured water column with respect to the distance and a linear fitting line.

EM27/SUN	ME	PE
Sodankylä	0.9825	-0.001
Kiruna*	0.9862	0.0034

Table 2.2: Average ILS parameters at MOPD for the EM27/SUN instruments located in Sodankylä and Kiruna (*: ILS parameters for the Kiruna instrument are taken from Frey [2018]).

2.3 Retrieval software

2.3.1 GGG for TCCON retrievals

The official TCCON retrieval algorithm is GGG, which is used for obtaining the total column abundances of the target species from the spectra [Wunch et al., 2011]. GGG is an open-source software package, including a nonlinear least-squares spectral fitting and the retrieval program named GFIT. The latest released suite is GGG2014 which offers the option of correcting the laser sampling errors detected on several TCCON spectrometers [Wunch et al., 2015]. To maintain consistency, official TCCON data require processing of the measured interferograms with the GGG algorithm. The prescription of a common retrieval method for all TCCON measurements decreases the computational errors among different stations and ensures a consistent TCCON database in long-term.

The GFIT algorithm consists of two models, a forward and an inverse model. The forward model computes an atmospheric transmittance spectrum for prescribed atmospheric

conditions. The inverse model employs the comparison between the observed spectrum and the calculated one from the forward model. The retrieved parameters are adjusted during the inversion model to achieve the best spectral fit. The treatment of the fit parameters, e.g. the continuum level, the frequency shift, etc. are user defined. Common predefined settings for the standard TCCON data products helps to ensure a high level of consistency between sites [Wunch et al., 2011].

The GFIT program does not execute a profile retrieval. The amount of gases at every altitude level is not scaled independently to obtain the best match to the spectrum. Instead, a faster and much simpler approach is used which also reduced the effects of certain systematic errors. An a-priori VMR (volume mixing ratio) profile is scaled, assuming a known shape of the gas profile because the VMR profile shapes of the most important TCCON target gases (e.g. CO_2 and O_2) are well known and fairly constant in the troposphere [Wunch et al., 2011].

The concentrations of some gases (e.g. CO and CH_4) vary strongly with altitude. As the a-priori knowledge of the VMR profile shape is important, a set of empirical functions are used to generate them. Most of the a-priori VMR profiles (e.g. CO) are derived from solar occultation measurements of the space-based Atmospheric Chemistry Experiment (ACE) interferometer [Bernath et al., 2005] and the balloon-borne Jet Propulsion Laboratory MkIV interferometer [Toon, 1991]. The relationship between the profiles of HF and those of CH_4 and N_2O is well studied and shows a nearly inverse trend in the stratospheric layer [Luo et al., 1996; Saad et al., 2014; Washenfelder et al., 2003]. A constant value of N_2O with 320 ppb, and HF with approximately 0.1 ppt and a secular decrease of 1% per year are assumed in the troposphere [Wunch et al., 2011, 2015]. The CO_2 a-priori profiles are derived from the GLOBALVIEW dataset [GLOBALVIEW-CO_2, 2013] and are variable depending on the time of year and the latitude of the site. In addition, the research conducted by Andrews et al. [2001] helps to derive the stratospheric CO_2 a-priori profiles from the age of air relationship.

In addition to the aforementioned a-priori VMR profiles, other main inputs for the GFIT algorithm are the profiles of daily pressure, temperature and humidity which can alter the spectral line shape. These daily profiles are generated from the NCEP/NCAR (National Centers for Environmental Prediction/National Center for Atmospheric Research) daily analysis data [Kalnay et al., 1996]. However, these profiles only represent the vertical atmospheric conditions during noon time but not the intraday variation. Accurate in-situ measurements of the ground pressure at TCCON sites are also required to obtain a better prior estimate of the total column mass corresponding to each spectrum. Here, they are taken from the local automatic weather station (AWS) at FMI for the Sodankylä TCCON station or from the meteorological tall tower (200 m) at KIT - Campus North for the Karlsruhe TCCON station.

For the forward calculation of the radiation transfer, trace gas abundance and spectral data (e.g. line intensities, self-broadening coefficients) are needed in the GFIT algorithm and generally derived from the HITRAN database [Rothman et al., 2013]. HITRAN is the

acronym for the High Resolution Transmission Molecular Absorption Database, supporting various algorithms to predict and simulate the atmospheric transmission and emission of light[1].

Several researches noted that the atmospheric trace gases retrieved from spectra in the near-infrared region are affected by the solar zenith angle (SZA) because of the spectroscopic inadequacies and instrumental problems [Deutscher et al., 2010; Wunch et al., 2011]. This airmass-dependent artifact adds approximately an extra 1 % for XCO_2 retrievals at low SZA around noon as compared to high SZA around sunrise or sunset. Therefore, the airmass-dependent bias must be taken into account as an additional post correction to meet the accuracy requirements for TCCON. Wunch et al. [2011] suggested an empirical correction scheme, using several years of data from remote sites and assuming that on a given day, any XCO_2 variation symmetrical around noon is a bias, and that any anti-symmetrical variation is real. The statistical estimate of the symmetrical variation is combined for the remote sites and used for the entire network.

In addition, airmass independent calibration factors (AICF) are needed for performing a post processing of the trace gases retrievals tie measurements to the WMO scale. These factors are achieved by comparing the highly accurate in-situ vertical gas profiles from aircraft or balloon experiments with TCCON data [Geibel et al., 2012; Messerschmidt et al., 2011; Wunch et al., 2010]. Such a scaling is required due to spectroscopic inaccuracies, especially in the O_2 band.

2.3.2 PROFFIT for EM27/SUN retrievals

PROFFIT (latest version is 9.6) is an algorithm package developed and maintained by Dr. Frank Hase at KIT and is available for the Windows environment [Hase et al., 2004]. The code is well developed and has been validated for retrieving dry-air mole fractions (DMF) of trace gases in the NDACC FTIR measurements [Kiel et al., 2016; Schneider et al., 2008, 2010] and in the EM27/SUN low-resolution measurements [Frey et al., 2015; Gisi et al., 2012; Klappenbach et al., 2015].

Before retrieving the total amounts of species with the PROFFIT V9.6, a preprocessing is performed by using the CALPY program. This preprocessor includes the quality check and the calculation of the solar absorption spectrum from the raw interferograms [Kiel, 2016]. A constant solar intensity during the interferogram recording is a precondition to obtain the most accurate and precise trace gas concentrations. However, source brightness fluctuations (SBF) due to clouds, multiplicatively disturb the interferograms and distort the derived spectra [Keppel-Aleks et al., 2007]. This impact cannot be neglected and needs to be corrected. Normally, the SBF generates low-frequency variation while the expected inteferograms reveal relatively higher frequency, containing the useful spectral information [Keppel-Aleks et al., 2007]. With this knowledge, DC interferograms are acquired for the SBF correction in order

[1] https://www.cfa.harvard.edu/hitran/

to reduce the SBF-incurred errors. The EM27/SUN instrument is operated in DC mode and therefore, the SBF correction can be applied directly. TCCON instruments are operated in a similar manner, and the SBF correction is applied post-acquisition in GGG.

A reweighting procedure is performed by dividing the raw interferogram (I_{raw}) with the smoothed one (I_{smooth}) [Kiel, 2016; Ridder et al., 2011]. The correction is then applied using the function below:

$$I_{corr} = \left(\frac{I_{raw}}{I_{smooth}} - 1\right) \cdot DC_{offset} \tag{2.1}$$

The smoothed interferogram is obtained from the raw one by applying a moving average 5 times over 61 sampling points. This method suppresses the spectral information with high frequency and averages out the centerbursts of the interferogram (see Figure 2.12).

However, this SBF correction does not cancel out the DC variation perfectly well, especially when the intensity is too weak or the IFG has too strong of variations during a single scan. Therefore, two more parameters for quality checks are introduced. One is the "offset", defined by the absolute value of the maximum signal strength. It was set as 0.05 and -0.05 here separately because the two-channel EM27/SUN instrument generates both positive and negative signals. When the minimum absolute value of the IFG signal is below 0.05, the measurement is considered bad and discarded. The other quality criteria is the "Threshold", describing how variable the IFG is allowed to be and whether it can be determined as a good IFG. An empirical value is 0.1, i.e. when the variability of a IFG is larger than 10 %, this IFG is defined as poor and discarded [Frey et al., 2015; Kiel, 2016]. The "Threshold" is defined as:

$$\text{Threshold} = \frac{|I_{smooth}|_{max} - |I_{smooth}|_{min}}{|I_{smooth}|_{max}} \tag{2.2}$$

The quality-filter-passed IFGs are fast Fourier transformed with the Sande-Tukey algorithm along with Norton-Beer-Medium apodization, and the resulting spectra are stored as binary files (*.BIN). These files include additional measurement information, like a location description, coordinates, azimuth degree, spectra information, ILS, etc. and are used as input files in the PROFFIT software package.

The PROFFIT is a non-linear least-squares fitting algorithm and analyzes spectra based on inversion methods. The low-resolution spectra measured with the EM27/SUN instrument are fitted by scaling a-priori profiles, similar to GGG.

Normally, the a-priori VMR profiles are derived from the WACCM (Whole Atmospheric Chemistry Climate Model). The latest version is WACCM Version 6[1]. This numerical model encompasses the entire atmosphere, ranging from the Earth's surface to the thermosphere [Marsh et al., 2013] and has been applied for the analysis of previous EM27/SUN measurements [Frey et al., 2015]. However, here we use the same VMR profiles from the GGG as used in the TCCON to avoid that systematic errors which are caused by different a-priori VMR profiles. The same pT profiles from the NCEP/NCAR are used in the PROFFIT. Addition-

[1] https://www2.acom.ucar.edu/gcm/waccm

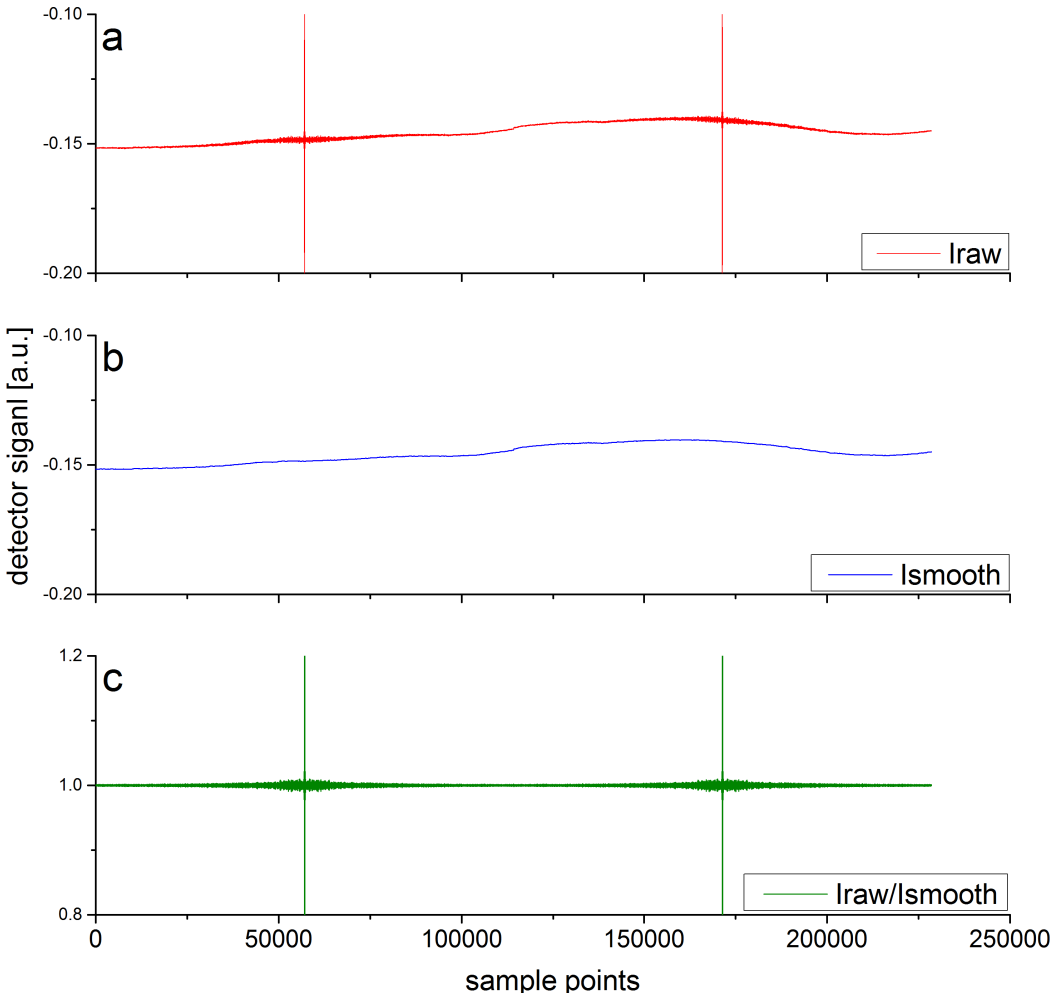

Figure 2.12: DC correction for a raw EM27/SUN interferogram as an example. (a) I_{raw}; (b) I_{smooth}; (c) DC corrected IFG.

ally, the intraday variable ground pressure at the TCCON site are used and interpolated to the EM27/SUN instrument's observatory height.

The same O_2 and CH_4 line lists, based primarily on HITRAN 2012, and as applied in the TCCON analysis are used in the PROFFIT algorithm. The CO_2 line list used by PROFFIT is slightly different. It applys the modified HITRAN 2008 line list to which Dr. Frank Hase added line-mixing parameters based on J.-M Hartmann's code [Lamouroux et al., 2010]. The CO line list is essentially derived from HITRAN 2008 [Hase et al., 2016]. For H_2O the updated HITRAN 2009 line list with empirical corrections is used [Wunch et al., 2010].

Figure 2.13 shows the processing flow chart. The CALPY-filtered and Fourier-transformed binary files (*.BIN) are imported into the required folder. The pressure and temperature information, a-priori VMR profiles of the trace gases and line lists are also used as inputs. The batched code "BAT-SU96.EXE" is used to create the required file structures and input files, then the batch code "BAT-EX96.EXE" (or BAT-EX96PP.EXE for parallel operation)

is started for executing a sequence of PROFFIT jobs, including the radiative transfer and retrieval calculations. PROFFIT creates result files containing the total column amounts of the target gases. Empirical solar zenith angle corrections can also be applied as a post-processing step based on the work of Klappenbach et al. [2015] and Frey et al. [2015] to reduce airmass-dependent artefacts. This will be discussed in Chapter 3.

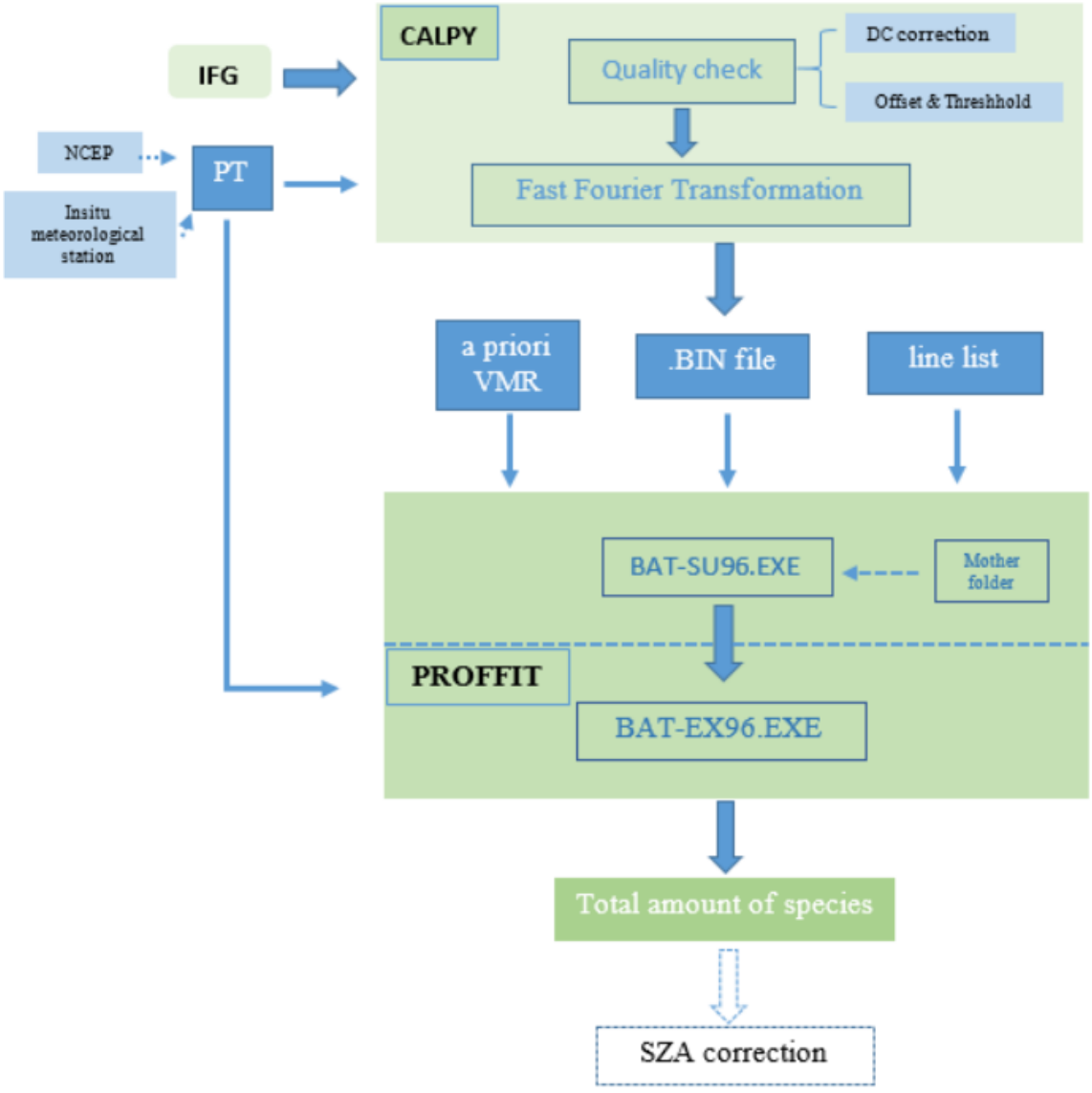

Figure 2.13: Processing flow chart including pre-processing with CALPY and the retrieving package PROFFIT.

Chapter 3

Characterization and optimization of retrievals

Trace gas retrievals are subject to numerous error sources. The uncertainties of the measurements are mainly caused by the complex measurement environment, uncertainties in the retrieval algorithms such as spectroscopy and the components of the instrument itself. These error sources must be quantified and, if possible reduced in order to increase the accuracy and quality of the retrieved column-averaged amounts of atmospheric trace gases, and to understand their limitations. Therefore, main error sources are investigated in the following sections. Moreover, solutions are introduced to minimize them and to obtain retrievals with optimal accuracy and precision.

To ensure accuracy of trace gas results derived from spectra recorded with the EM27/SUN spectrometer, each instrument is characterized with open-path measurements. These laboratory measurements are used for the determination of the ILS parameters, i.e. the modulation efficiency amplitude and the phase error at MOPD. The high-resolution spectra recorded with the ground-based TCCON 125HR FTIR spectrometer at KIT are in the same near-infrared spectral range as used by the EM27/SUN instrument. Therefore, co-located measurements are performed before the EM27/SUN spectrometer is transported to field campaigns in order to obtain the instrument-specific airmass independent calibration factors. Furthermore, for each species airmass dependent calibration factors are also applied to minimize errors that vary with solar zenith angle.

The first section contains the fundamental equations for the calculation of the column-averaged dry-air mole fraction of a trace gas (X_{Gas}). Then, in the second section, the empirical corrections are presented, both for the airmass independent and the airmass dependent corrections.

In section 3.3 the effects of intraday variable pressure and temperature are studied, which turns out to be an important impact factor on the trace gases retrieval. Since the ILS slightly deviates from the nominal expectation for each spectrometer, the use of instrument-

specific measured ILS parameters is required in the trace gases retrieval, which is presented in section 3.4.

Three different a-priori VMR profiles are investigated for one sample measurement day. This sensitivity study with respect to the different VMR profiles is presented in section 3.5. The results of the investigation highlight the importance of the use of realistic VMR profiles, which helps to minimize the bias of the retrieved total column amounts.

3.1 Column-averaged dry-air mole fraction

The variable surface pressure affects the column amount of atmospheric molecules. Thus, the column-averaged dry-air mole fraction (DMF) is used to reduce the ground pressure effect. With this method, the dependency of derived abundances on surface pressure variations is largely reduced. The column-averaged DMF can be computed by dividing the column abundances of a gas by the total column of dry air:

$$X_{Gas} = \frac{Column_{Gas}}{Column_{dryair}} \tag{3.1}$$

The column of dry air is a function of the surface pressure and the atmospheric humidity. The equation is then:

$$Column_{dryair} = \frac{P_{gr}}{g \cdot m_{dryair}} - Column_{H_2O} \frac{m_{H_2O}}{m_{dryair}} \tag{3.2}$$

where P_{gr} is the ground pressure, g represents the gravitational acceleration. m_{H_2O}, m_{dryair} and $Column_{H_2O}$ are the mean molecular mass of water and dry air, and the total column of water, respectively.

The calculation of the ratio of the target gas and the column amount of O_2 retrieved from the same spectrum is an alternative and superior method. The volume mixing ratio of O_2 in the atmospheric altitude range up to 100 km is nearly constant at approximately 20.95 %. Therefore, the total column of dry air based on the retrieved O_2 column is:

$$Column_{dryair} = \frac{Column_{O_2}}{0.2095} \tag{3.3}$$

By this approach, the systematic errors that affect both the O_2 bands and bands of target gases like CO_2, CH_4 and CO can be largely reduced. These include, for example, the deviation in the pointing of the solar position, the offset of the spectral zero level, or errors in the surface pressure due to the measurement inaccuracy of the data logger [Wunch et al., 2011]. In addition, for the calculation of the DMFs, it is not necessary to use the water column to correct the ground pressure. With these advantages, it is therefore the official method used in TCCON.

Insertion of Equation (3.3) into Equation (3.1) yields the following expression for the column-averaged DMF of a target trace gas:

$$X_{Gas} = \frac{Column_{Gas}}{Column_{O_2}} \cdot 0.2095 \tag{3.4}$$

3.2 Empirical corrections

Empirical corrections are necessary to match unites defined by the assumed spectroscopic line contributes with in-situ/WMO units. In addition, airmass dependent correction removes residual artificial airmass dependency of retrieved X_{Gas} due to spectroscopic inaccuracies (mainly incorrect line shapes and pressure broadening parameters). In this subsection, empirical airmass independent and airmass dependent corrections are introduced.

3.2.1 Airmass independent (AI) correction

The main bias between the retrieved column-averaged DMFs from TCCON and EM27/SUN measurements is mostly induced by the different spectrometer resolutions. The instrument-specific deviations from the nominal behavior can be diminished by applying scaling factors to the trace gas abundances derived from long-term observations. Frey et al. [2018] have studied nearly four years of measurements from a selected EM27/SUN reference instrument with respect to the TCCON 125HR high-resolution instrument at KIT. The average bias between EM27/SUN and TCCON retrievals amounts to approximately 0.20 ppm for XCO_2 and 0.80 ppb for XCH_4. Meanwhile, an ensemble of 30 EM27/SUN instruments has been studied to investigate and quantify the variance of the EM27/SUN instruments with respect to the reference EM27/SUN instrument. Therefore, comparison measurements are required to ensure that the results measured with the EM27/SUN spectrometers are comparable to each other and to the TCCON retrievals. Before the EM27/SUN spectrometers are sent out for campaigns, they are operated on the roof of the institute's building (49.09 °N, 8.43 °E, 133 m a.s.l.) together with the co-located reference TCCON instrument for side-by-side measurements. Additionally, it is advisable to perform another comparison measurement after the campaigns in order to verify the instrumental stability.

The correction of the spectroscopic differences is carried out by multiplying the dry-air mole fraction of the particular trace gas by an airmass independent correction factor (f_{AI}). This factor is deduced by side-by-side measurements over several days. The following example describes the practical approach of this procedure on the basis of the campaigns in Sodankylä and Kiruna. Side-by-side measurements were performed in Karlsruhe from February 13 to 15, 2017 before 2 EM27/SUN spectrometers were transported to Sodankylä and Kiruna. XCO_2, XCH_4 and XCO from the co-located reference 125HR measurements were retrieved following the TCCON protocol with the officially recommended GGG2014 package [Wunch et al., 2011]. The retrievals from the EM27/SUN measurements were instead

performed with the PROFFIT V9.6 software. The solar zenith angle dependent corrections for target gases were applied afterwards in the post-processing step (see section 3.2.2). The measured ILS (see section 3.4) and the a-priori VMR profiles used in GGG2014 were applied in the retrieval. The results from the TCCON and the EM27/SUN measurements recorded at the same time (1 minute) were selected for the generation of a paired dataset. Finally, the scaling factors were derived from this dataset. We find that a nearly 1 % change of XCO_2 can be observed when measurements recorded at noon and sunset are compared [Wunch et al., 2011]. Therefore, an SZA filter was here applied to eliminate the measurement errors derived from high solar zenith angles. Only the results with SZA less than 75° were used. The scaling factor is computed as follows:

$$f_{AI} = \left\langle \frac{X_{TCCON,paired}}{X_{EM27/SUN,paired}} \right\rangle \tag{3.5}$$

where the terms in the angle brackets indicate the slope of the linear regression line. This correction function between the TCCON data and the EM27/SUN data with the SZA dependency correction is forced to go through the point of origin. Figure 3.1 shows the linear relation corresponding to the TCCON retrievals for XCO_2, XCH_4 and XCO. The obtained scaling factors for both EM27/SUN spectrometers are shown in Table 3.1 where the error margins are the standard deviation from the calibration dataset. The very close scaling factors between these two instruments verify for all XCO_2 and XCH_4 the high degree of instrument-to-instrument consistency. Note that the XCO retrieved from the EM27/SUN measurements had no empirical SZA dependent correction, and the Kiruna instrument does not have external CO channel.

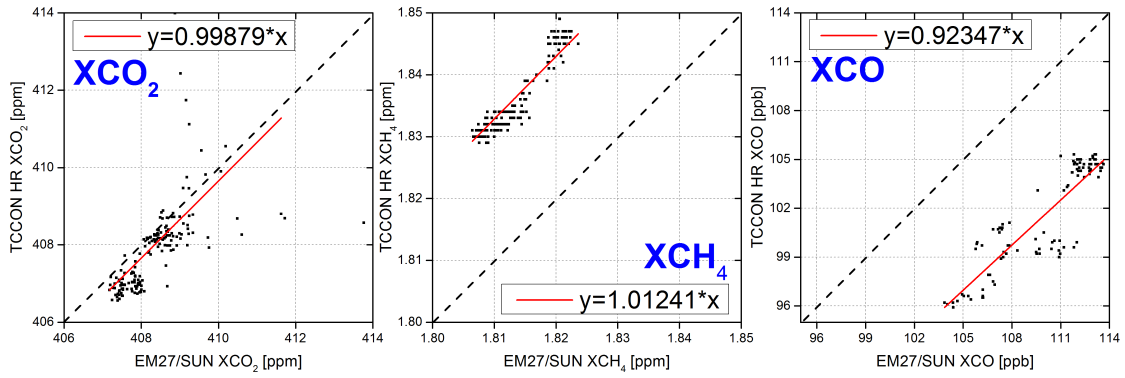

Figure 3.1: Correlation between the EM27/SUN that went to Sodankylä and the reference TCCON data for XCO_2, XCH_4 and XCO for 1 minute paired averages. The red line denotes the linear regression line through the origin. The data recorded with the Sodankylä EM27/SUN are used as an example here. Measurements were performed in Karlsruhe from February 13 to 15, 2017.

EM27/SUN	XCO_2	XCH_4	XCO
Sodankylä	0.99879±1.7E-4	1.01241±9.1E-5	0.92347±1.3E-3
Kiruna	0.99871±2.2E-4	1.01250±1.2E-4	–*

Table 3.1: Airmass independent correction factors of XCO_2, XCH_4 and XCO for the two EM27/SUN spectrometers deployed to Sodankylä and Kiruna, with the TCCON data as a reference (*: No CO channel in the Kiruna instrument.)

The entire EM27/SUN dataset is scaled to the TCCON reference with the global scaling factor $f_{AI,Gas}$ for specific species, which can be calculated by using the formula below:

$$X_{Gas,EM27/SUN,corr} = X_{Gas,EM27/SUN} \cdot f_{AI,Gas} \tag{3.6}$$

3.2.2 Airmass dependent (AD) correction

The impact of the SZA dependency on the spectroscopic trace gas measurements in the NIR is not negligible. This, in particular, affects all the measurements with large SZA in the early spring and winter time. Such problems are mainly introduced by the insufficient accuracy of the spectroscopic data, i.e. the line positions, the line widths, etc. The GGG package includes an empirical ad-hoc SZA correction. A similar correction is applied for the PROFFIT retrievals as an external post processing based on the research from Klappenbach et al. [2015]. The applied polynomial correction is defined as:

$$X_{Gas,corr} = X_{Gas} \cdot \left\{ 1 + a \cdot \left[\left(\frac{SZA + b}{90° + b} \right)^2 - \left(\frac{45° + b}{90° + b} \right)^2 \right] \right\} \tag{3.7}$$

here the parameters a and b are free fitting factors. $X_{Gas,corr}$ and X_{Gas} represent the column-averaged DMF of one species with and without SZA dependent correction. The dataset is referenced to SZA=45° as the neutral angle, where $X_{Gas,corr}$ equals to X_{Gas}.

The TCCON 125HR spectrometer in Karlsruhe provides high-resolution data as a reference. It is, however, not well suited for determining the correction parameters due to the actual intraday variability of the trace gases and the unknown local sources and sinks. To determine the SZA correction parameters, a scientific campaign covering a wide range of latitudes was performed [Klappenbach et al., 2015]. In this campaign, an EM27/SUN spectrometer was operated on the research ship "Polarstern". The ship departed from the port Cape Town, south Africa (34 °S) on March 4, 2014. The route over the Atlantic Ocean along the west coast of Africa was far away from local sources and sinks which contribute to CO_2 or CH_4. The travel ended at the port Bremerhaven, Germany (54 °N) on April 14, 2014. The measured data clearly showed the intraday variability which was only affected by the solar zenith angle dependency. In contrast to GGG retrievals, the O_2 column-averaged DMFs retrieved with the PROFFIT algorithm from the EM27/SUN spectra do not show a

significant SZA dependency when angles are less than 80°. There is an airmass dependency detectable for the CO_2 and CH_4 retrievals. The fitting parameters are a=6.296×10^{-3} and b=1.291 for XCO_2; and a=3.796×10^{-3} and b=16.04 for XCH_4.

Finally, these corrections are applied to the raw EM27/SUN retrievals. Figure 3.2 shows different EM27/SUN time series datasets with different corrections: without any correction (pink squares), with only AI correction (green crosses), with both AI and AD correction (blue dots), and the reference TCCON data (black triangles) for (a): XCO_2, (b): XCH_4 and (c): XCO. The difference between the EM27/SUN and TCCON datasets is also shown in the second figure of every panel to quantify the impact of the airmass independent and dependent correction factor for the target gases. The difference between these three EM27/SUN measurements in XCO_2 was close to zero over the whole time series. After the correction, the offset slightly increased and less change happened around noon because the AD correction used a diurnal-neutral angle of 45° as the reference. The mean offset before was (-0.16 ± 0.87) ppm and after the correction was $(-6.2 \times 10^{-4} \pm 0.89)$ ppm. For XCH_4 the mean offset decreased to (1.7 ± 1.2) ppb after AD and AI corrections, comparing with the uncorrected mean offset of (24.0 ± 2.0) ppb. The agreement of XCO measurements between EM27/SUN and TCCON reference improved from (8.4 ± 1.5) ppb to (0.002 ± 1.4) ppb after applying the AI correction. Note that the TCCON data incorporated an AD correction for XCO, while no AD correction for XCO was applied in EM27/SUN data processing.

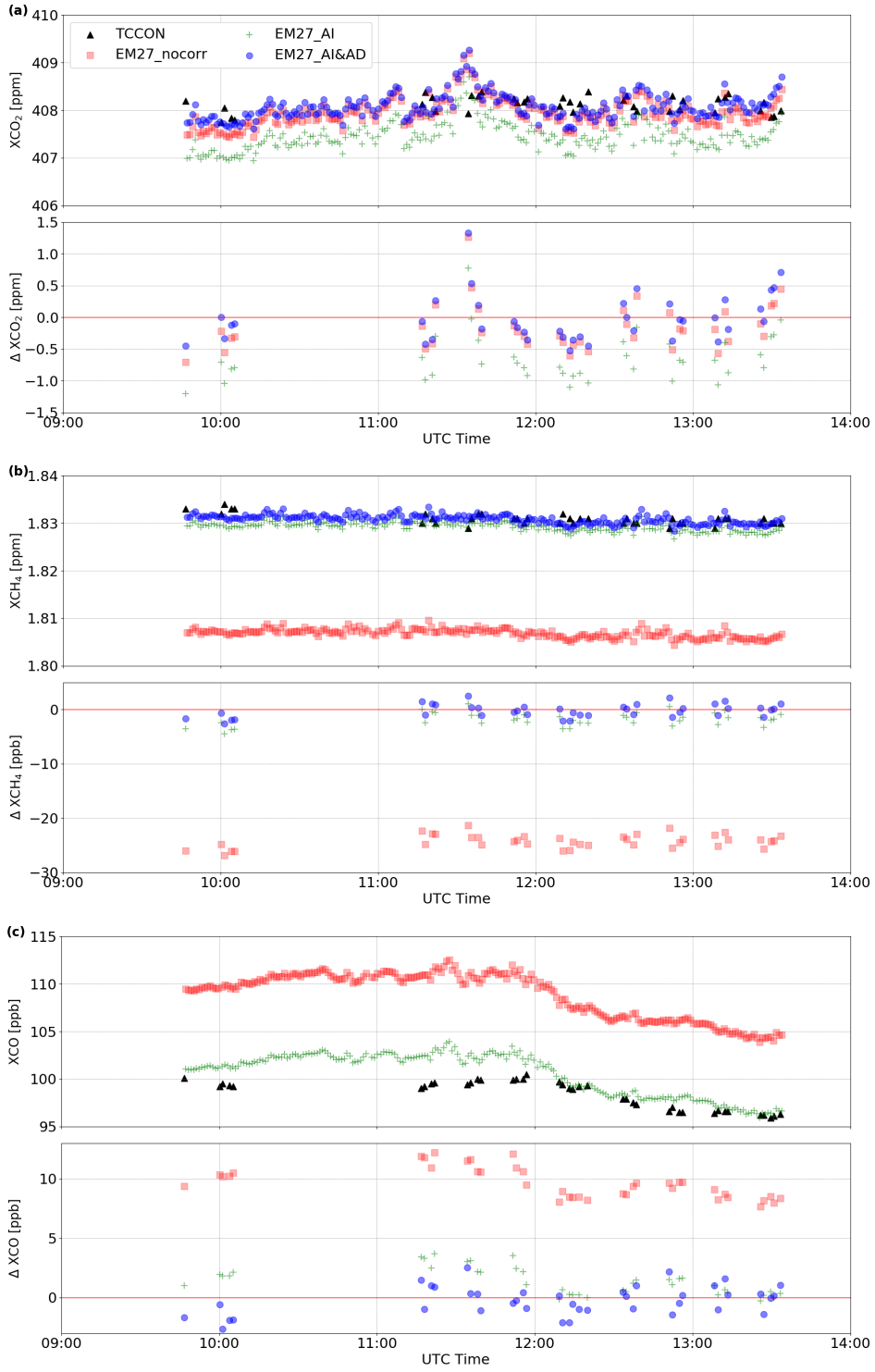

Figure 3.2: Time series of (a): XCO_2, (b): XCH_4 and (c): XCO measured with the EM27/SUN and TCCON spectrometers at KIT, Karlsruhe on February 15, 2017. The reference TCCON retrievals (black triangles) are presented for all target gases. Measurements of XCO_2 and XCH_4 with the AI correction ($X_{gas,AI}$) and with the subsequent AD correction ($X_{gas,AIAD}$) are shown. Only an AI correction was applied to XCO.

3.3 Intraday variable ground pressure and temperature

A good knowledge of pressure and temperature profiles is essential for deriving the DMFs of greenhouse gases. The same pressure and temperature (pT) profiles are used for evaluating the TCCON 125HR and EM27/SUN measurements to minimize the associated systemic errors. These pT profiles can be acquired from in-situ measurements (e.g. radiosonde balloon profile measurements). However, FTIR stations lack in-situ pT profiles nearby except for the ground-based pT measurements. Therefore, the pT vertical profiles that are used in this work for the analysis of the TCCON and the EM27/SUN measurements are obtained from model data, provided by the NCEP[1]/NCAR[2] analysis product [Kalnay et al., 1996]. A pT profile is generated every day for a certain location and interpolated to local noon. However, the retrievals are considerably affected by the intraday variable ground pressure and temperature [Gisi et al., 2012]. The single vertical pT profiles are not suitable for the evaluation of an entire measurement day without accounting for station surface pressure. In the next sections, the effects of intraday variable ground pressure and temperature are discussed.

3.3.1 Intraday variable ground pressure

To emphasize the effects of a intraday variable ground pressure on the retrieval process, measurements from one day (June 8, 2017) were analyzed. The covered time range extends approximately from 6:00 AM to 6:00 PM. Figure 3.3 shows the time series of the fixed and in-situ measured variable ground pressure used in the PROFFIT algorithm (the diurnal time series of O_2, CO_2, CH_4 and CO retrievals in terms of total columns and column-averaged DMFs are shown in Appendix A—Figure A.1, A.2). Within the day, the pressure decreases from ∼999 hPa in the early morning to ∼996 hPa later in the afternoon. The constant pressure line (red) corresponds to the observed pressure line (green) at noon. Therefore, the difference between these pressures is maximal in the morning and in the afternoon. We test the measured ground pressure and the constant value from UTC noon in the retrieval procedure. Small effect exists in XCO_2 and XCH_4 which are larger than effects on XCO, especially in the early morning and later in the afternoon. Figure 3.4 displays the relative difference between using the variable ground pressure and the fixed pressure in retrieving trace gases in terms of total columns (left panel) and X_{Gas} (right panel), different colors denoting different gases. Different species show different sensitivity to the ground pressure. The O_2 column reveals the highest sensitivity to pressure changes, compared to those of CO_2, CH_4 and CO in descending order. An increase of 1 hPa in the ground pressure leads to approximately an average 0.05 % decrease in the O_2 column. The relative reduction in of total column amounts for CO_2 and CH_4 is on the order of 0.019 % and 0.015 % on average when the pressure increases by 1 hPa, while the CO total column shows no significant

[1]National Centers for Environmental Prediction
[2]National Center for Atmospheric Research

variation ($\sim -0.0021\,\%$) with respect to the ground pressure. The O_2 total column has a much larger decrement than the other gases, which causes it to effect X_{Gas} values because it is the denominator in the DMF equation. This overcompensation effect occurs for the retrieved XCO_2, XCH_4 and XCO. A change of 1 hPa in the ground pressure causes an average increase of about $0.035\,\%$ in XCO_2, $0.039\,\%$ in XCH_4 and $0.052\,\%$ in XCO, respectively.

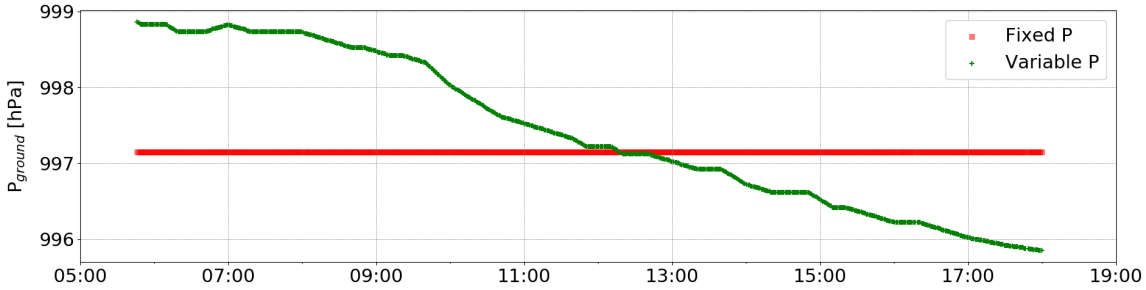

Figure 3.3: Diurnal time series of fixed and variable ground pressure used in the PROFFIT algorithm on June 8, 2017 in Sodankylä as an example.

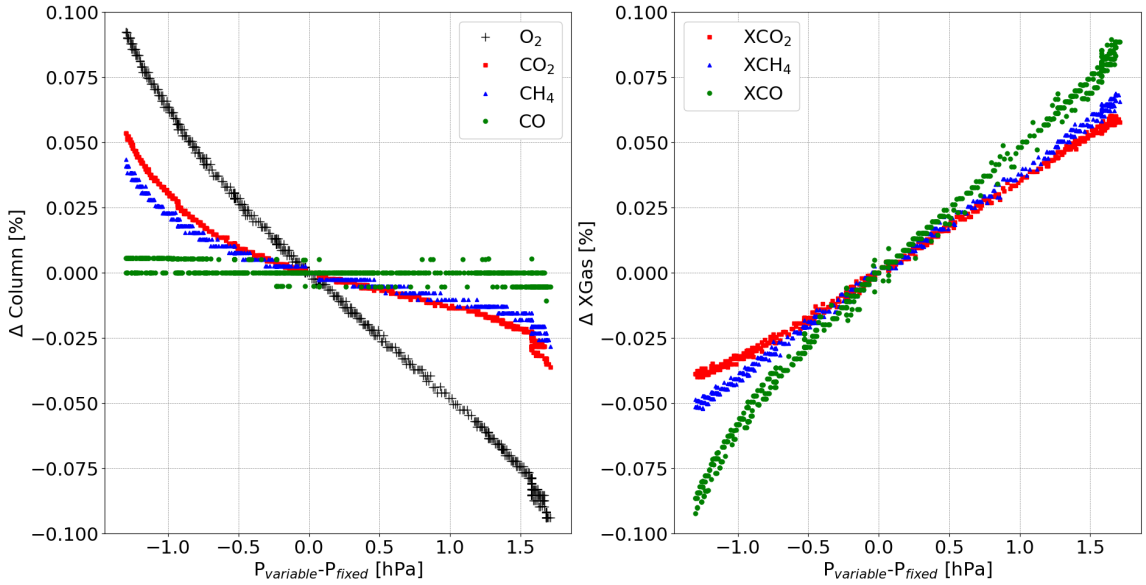

Figure 3.4: Relative difference of O_2, CO_2, CH_4 and CO retrievals with fixed and variable pressure used in the PROFFIT algorithm, left: in total columns; right: in X_{Gas}—using measurements performed in Sodankylä on June 8, 2017 as an example.

3.3.2 Temperature sensitivity

A slightly modified temperature profile was applied to study the temperature sensitivity for the retrievals. Since it is difficult to obtain the intraday variable temperature in the boundary layer, a systematic disturbance assuming a bias of 5 K in the temperature profile in lower

layers, up to an altitude level of 2 km, was assumed. The diurnal time series of O_2, CO_2, CH_4 and CO retrievals with the original temperature profile and the modified one in terms of total columns and column-averaged DMFs are shown in Appendix A—Figure A.3, A.4.

The total columns of trace gases enhance with increasing temperature without exception. The retrieved total columns of O_2, CO_2 and CH_4 within this selected measurement day change moderately by 0.23 %, 0.15 % and 0.04 %, respectively. The enhancement of the CO column, on the other hand, with a value of approximately 2.37 % is much higher. Due to the compensation by O_2, the resulting relative changes for XCO_2, XCH_4 and XCO show a different behavior. Both XCO_2 and XCH_4 are overcompensated with the approximate changes of −0.08 % and −0.18 %, respectively. XCO is undercompensated with a change of approximately 2.14 %. Therefore, an increase of 1 K in the temperature leads to a reduction of about 0.016 % (0.06 ppm) in XCO_2 and 0.036 % (0.66 ppb) in XCH_4, whereas XCO is increased by 0.428 % (0.34 ppb).

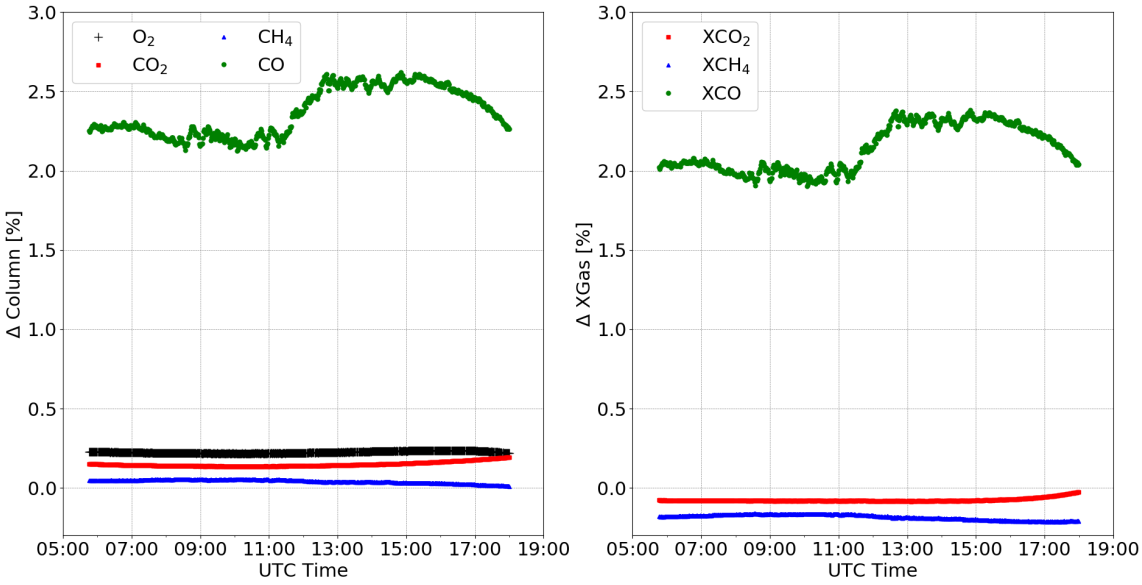

Figure 3.5: Time series of relative difference of O_2, CO_2, CH_4 and CO retrievals with original and modified temperature profile used in the PROFFIT algorithm, left: in total columns; right: in X_{Gas}—using measurements performed in Sodankylä on June 8, 2017 as an example.

To summarize, it can be stated that accurate intraday variable pressure values based on a local meteorological station or portable pressure datalogger are mandatory for accurate retrieval results. Different species show different sensitivities to the ground pressure and the temperature. The O_2 column amount is more sensitive to the pressure and the temperature than the CO_2 and CH_4 columns. Pressure change has no obvious effect on the CO column, while the temperature brings the highest effect on the CO column among all species. Thus, the column-averaged DMF method can only partly eliminate the effect of erroneous pressure and temperature values.

3.4 Instrumental line shape

The instrumental line shape (ILS) is an important indicator for assessing the instrumental performance. Misalignment and optical aberrations lead to a non-ideal ILS, which has to be taken into account in the retrieval procedure [Hase et al., 1999]. Two simplified ILS parameters are used to characterize the EM27/SUN spectrometer, including the modulation efficiency (ME) and the phase error (PE) at MOPD which ideally should be 1 and 0, respectively (for more details see section 2.2). In the TCCON network, a dedicated low-pressure (∼5 hPa) gas cell is used as the standard approach to derive the ILS. However, this method only works for the high-resolution spectrometer because a longer cell at the same pressure would be needed for the lower resolution instrument, for which there is no space internally. The ILS of the EM27/SUN instrument is derived from open-path measurements of H_2O performed in laboratory. This experiment can also be easily performed during campaigns since only an external light source is needed. To derive the ILS from the laboratory spectra, the LINEFIT retrieval software is used [Hase et al., 1999] (see section 2.2). Regular ILS measurements are necessary especially before the transportation of the EM27/SUN spectrometer to a field campaign and after the return. It should be noted that ILS effects are only considered in the PROFFIT retrieval algorithm but not in the current version of the GGG package that is widely used for retrieving the official TCCON data.

In this section, the sensitivities of the ME and PE on the retrievals are studied by using a set of solar measurements recorded in Sodankylä on June 8, 2017 as an example.

3.4.1 Modulation efficiency

The ME for EM27/SUN instruments is typically slightly below 1, which would be expected for an ideal FTS. Frey et al. [2018] has studied 30 EM27/SUN instruments and the ME at MOPD ensemble average is 0.9851 ± 0.0078.

Two different values of the ME (i.e. 1.00 and 0.99) are used within the PROFFIT software for retrievals, using a single measurement day (June 8, 2017) in Sodankylä as an example (the diurnal time series of target species retrievals with different ME values in terms of total columns and X_{Gas} are shown in Appendix A—Figure A.5, A.6). In general, the retrievals with different ME values have a similar tendency for each species throughout the day. The total column abundances increase with decreasing ME value. The time series of relative differences of these species in terms of total column are displayed in Figure 3.6, left panel. A decrease of 1 % in the ME value results in higher amount of O_2 column with an average value of $(0.37 \pm 0.01)\%$. CO_2 shows a higher sensitivity than O_2, with an average increase of $(0.55 \pm 0.03)\%$, while CH_4 is the least sensitive species, with an average change of $(0.27 \pm 0.01)\%$. Among all these species, CO shows the highest change and reveals the strongest intraday variability, with an average value of $(0.74 \pm 0.10)\%$, ranging from 0.42 % to 0.83 %. This is mainly because the absorption of CO within the selected spectral window

is much weaker than those of the other gases. The superimposition from the nearby strong interfering lines of CH_4 and H_2O makes it more sensitive to apparent variation. With the compensation of O_2 column, the relative changes of X_{Gas} are approximately $(0.18 \pm 0.02)\%$ in XCO_2, $(-0.100 \pm 0.002)\%$ in XCH_4, and $(0.36 \pm 0.11)\%$ in XCO, respectively.

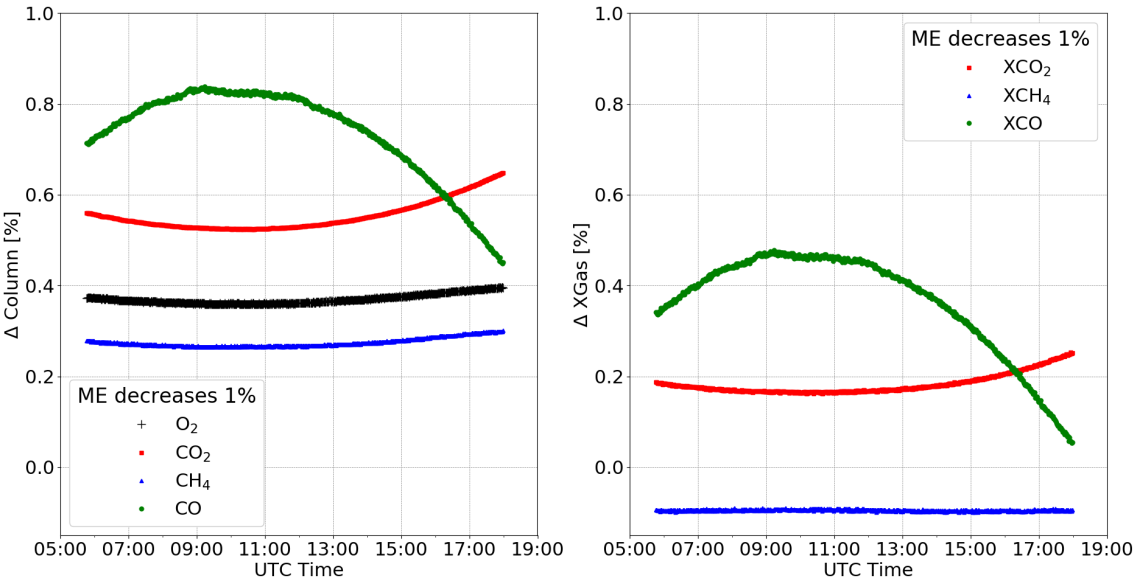

Figure 3.6: Time series of relative difference of O_2, CO_2, CH_4 and CO due to a 1 % decrease of the ME values, left: in total columns; right: in X_{Gas}—using measurements performed in Sodankylä on June 8, 2017 as an example.

The relative difference changes show an intraday variation, mainly due to the effects of SZA and different gases display different responses (see Figure 3.7). The O_2 and CH_4 columns show a similar and nearly linear positive correlation with SZA. This results in a non-significant correlation between XCH_4 relative change and SZA. Slightly higher correlation is found in CO_2, especially at higher SZA, while the SZA sensitivity decreases a little for XCO_2 with the compensation of O_2 column. On the other hand, the CO column is decreasing with increasing SZA and this effect is most strongly pronounced compared with the other gases and the SZA effect on XCO becomes slightly stronger due to the influence of O_2 column.

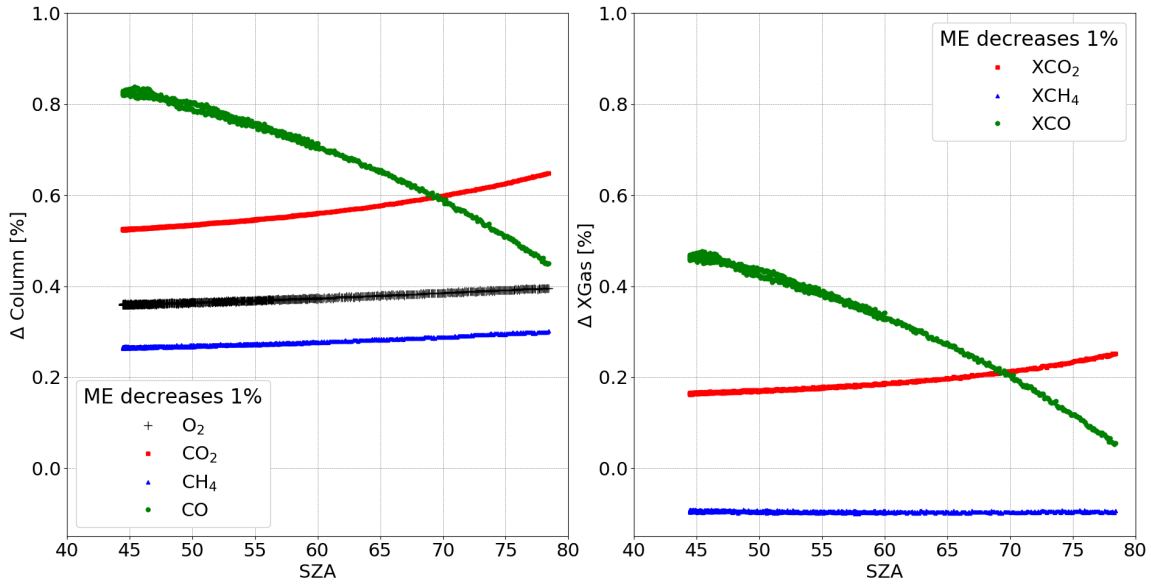

Figure 3.7: Relative difference of O_2, CO_2, CH_4 and CO with respect to SZA due to a 1 % decrease of the ME values, left: in total columns; right: in X_{Gas}—using measurements performed in Sodankylä on June 8, 2017 as an example.

3.4.2 Phase Error

The second ILS parameter is the phase error. For the large majority of the EM27/SUN instruments characterized at KIT, an average PE value of around ±0.002 rad was found, indicating a nearly symmetric ILS shape [Frey et al., 2018]. In contrast to the results of the ME sensitivity, the PE does not show an obvious impact on the target gases (the diurnal time series of target species retrievals with different PE values in terms of total columns and X_{Gas} are shown in Appendix A—Figure A.7, A.8). By decreasing the PE from 0 to −0.01 rad, the tendencies of change for both, CO_2 and CH_4 are mostly similar with average values of $(-0.0066 \pm 0.0048)\%$ and $(-0.020 \pm 0.002)\%$, respectively and both show a slightly positive correlation with SZA (see Figure 3.8, 3.9). The O_2 column amount shows a relatively higher sensitivity to the PE change by an approximate increase of $(0.052 \pm 0.006)\%$ and its relative difference shows a negative correlation with SZA. This change results in a slight overcompensation in the XCO_2 and XCH_4 retrievals, with average values of $(-0.058 \pm 0.011)\%$ and $(-0.072 \pm 0.007)\%$, respectively. The PE change affects the CO more strongly with an average relative difference of $(-0.11 \pm 0.10)\%$, ranging from −0.23 % to 0.06 %. The relative difference of CO column also shows an obvious sensitivity to SZA. This is because CO is a weak absorber within the selected spectral window, and there are strong interfering lines from the nearby H_2O and CH_4, which makes CO more sensible to apparent variation.

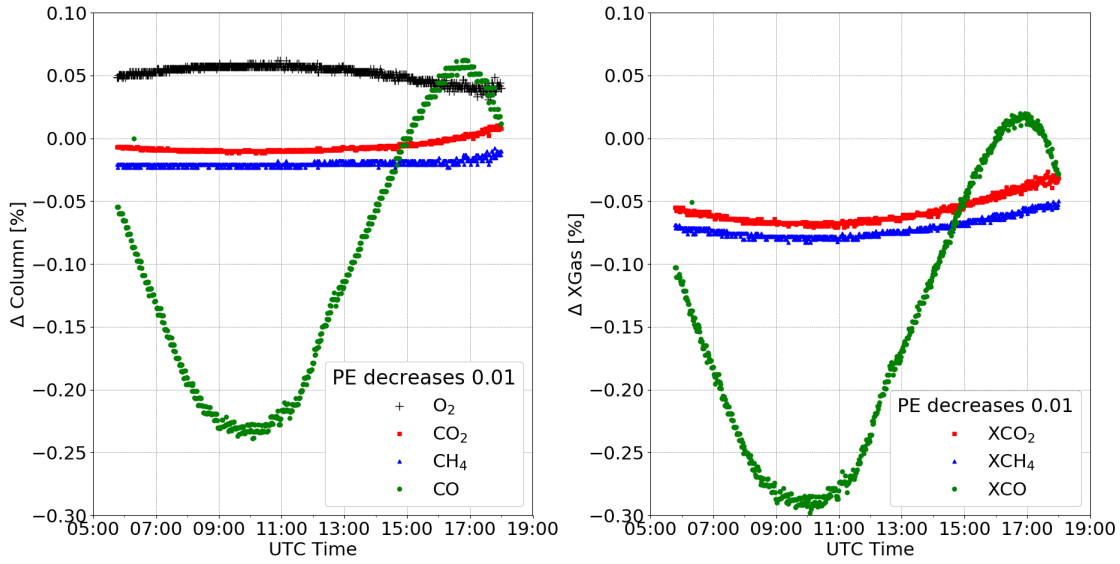

Figure 3.8: Time series of relative difference of O_2, CO_2, CH_4 and CO due to a 0.01 rad reduction of the PE values, left: in total columns; right: in X_{Gas}—using measurements performed in Sodankylä on June 8, 2017 as an example.

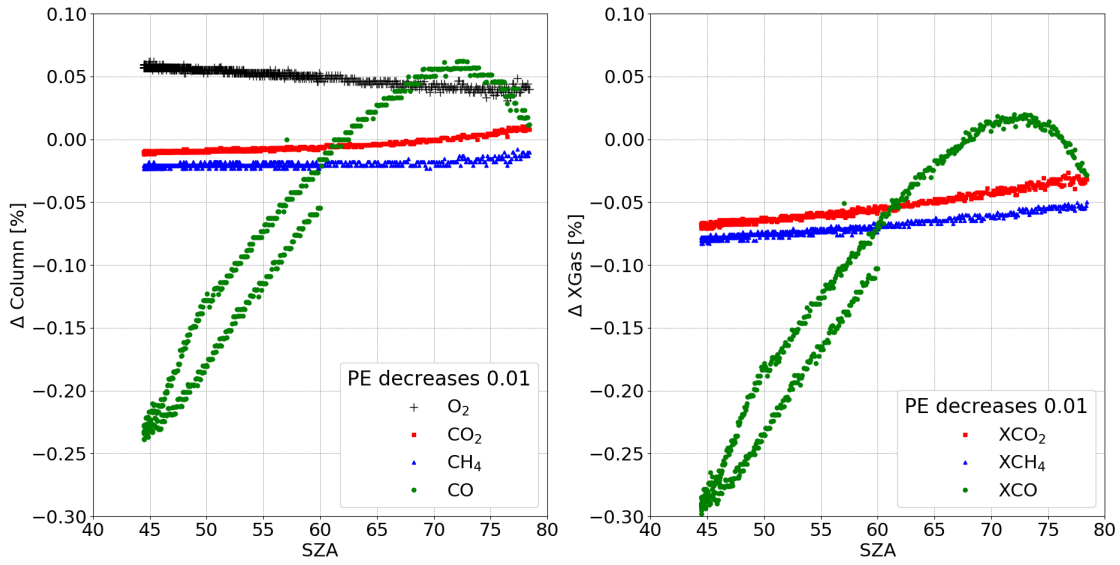

Figure 3.9: Relative difference of O_2, CO_2, CH_4 and CO with respect to SZA due to a 0.01 rad reduction of the PE values, left: in total columns; right: in X_{Gas}—using measurements performed in Sodankylä on June 8, 2017 as an example

To summarize, the ME value is the dominate affect on retrievals between the two ILS parameters. Additionally, the measured PE value is approximately ±0.002 rad based on the study of an ensemble of EM27/SUN spectrometers [Frey et al., 2018], which results in lesser change than the aforementioned errors.

3.5 A-priori profiles

For retrieving correct column abundances from ground-based FTIR spectra, the choice of a-priori VMR vertical profiles for the target gases is important. In the following section several different sets of a-priori profiles are used for investigating the sensitivity of the retrievals with respect to the choice of the a-priori profile. One set of profiles is derived from the Whole Atmosphere Community Climate Model (WACCM)[1]. These profiles are sampled on 49 levels from the observation altitude up to 120 km and stay constant over the year. Another set of a-priori VMR profiles are derived from the GGG algorithm and change with time. These empirical profiles are based on several kinds of model data up to 70 km and are sampled on an equidistant 1 km grid (see subsection 2.2.1).

Any practical choice of the a-priori VMR profiles is generally based on model data. To assess the quality of the model data, knowledge of the actual profiles is required and might be obtainable from in-situ AirCore balloon launches. The AirCore, which was an auxiliary activity in the Finland campaign, is a simple and viable atmospheric sampling system to measure vertical profiles of greenhouse gases [Karion et al., 2010]. The AirCore system that was used in Sodankylä was built at the University of Groningen (UG). It consists of a 100 m long coiled stainless steel tube, combing 40 m of 0.25 inch (6.35 mm) tube and 60 m of 0.125 inch (3.175 mm) tube, along with an automatic shut-off valve and home-made data logger to record temperature and pressure during the flight. A 3 kg balloon was used to launch the AirCore along with a radiosonde and an iridium transceiver (see Figure 3.10). The air is removed from the tube during ascent to an altitude of 30 km while ambient air flushes into the tube as it descends. A Cavity Ring-Down Spectrometer (CRDS) manufactured by Picarro Inc. is used afterwards to quantify the mole fractions of CO_2, CH_4 and CO in the AirCore sample.

(a) AirCore in package (b) AirCore launch

Figure 3.10: (a): The prepared AirCore in package (Photographs courtesy of FMI and UG); (b): the launching AirCore with balloon at FMI in March, 2017.

[1] https://www2.acom.ucar.edu/gcm/waccm

To determine the influence of the a-priori VMR profiles on the retrievals, these different profiles (1) the AirCore, (2) the fixed (WACCM), and (3) the daily-variable (MAP) VMR profiles were applied in the PROFFIT analysis, using the measurements performed in Sodankylä on August 28, 2017 as an example. Figure 3.11 shows the sets of vertical profiles (the AirCore in black, the invariable profiles of WACCM in red, and the daily-variable MAP profile in green) for CO_2, CH_4 and CO. Both the AirCore and the MAP profiles are from the same day. Throughout the available altitude levels, the MAP profiles for CO_2 and CH_4 are closer to the AirCore data, especially at lower altitudes. The tropospheric CO profiles from the WACCM and the MAP models are of similar shape, and the relative bias compared to the AirCore profile for both reaches up to 70 %.

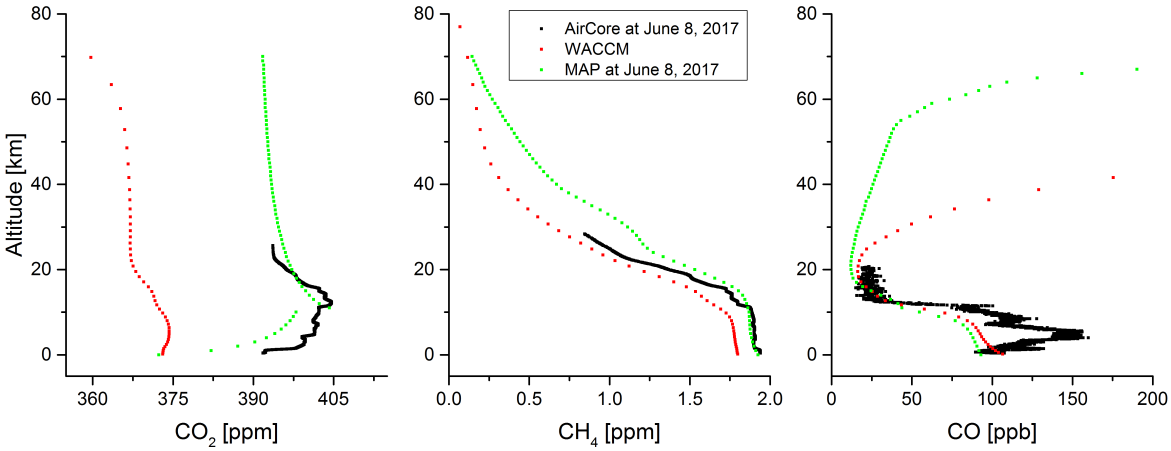

Figure 3.11: A-priori VMR profiles of CO_2, CH_4, CO from WACCM, MAP and AirCore.

Since the profile shape of O_2 is highly predictable and fairly constant in the troposphere, identical O_2 a-priori profiles are used for these three datasets. Thus, there is no obvious influence from the a-priori profiles on the O_2 retrievals (The effect of a-priori VMR profiles on other species in terms of total columns and X_{Gas} are presented in Appendix A—Figure A.9, A.10). Here, we use the AirCore profiles as the reference. For this measurement day, the use of MAP profiles results in higher deviations compared to those that use the WACCM profiles (see Figure 3.12). With respect to the AirCore-retrieved results, total columns are higher by $(0.23 \pm 0.02)\%$, $(0.35 \pm 0.04)\%$, $(0.99 \pm 0.04)\%$ for CO_2, CH_4 and CO, respectively, when the MAP profiles are used. Whereas total columns are lower by $(0.10 \pm 0.01)\%$ and $(0.26 \pm 0.03)\%$ for CO_2 and CH_4 on average by using the WACCM profiles. The total column of CO shows an opposite situation with on average about $(0.22 \pm 0.03)\%$ higher values than the reference.

The use of different a-priori VMR profiles shows different responses to the SZA. The airmass effects on trace gases retrieved with WACCM and MAP profiles with respect to the AirCore retrieved results are presented in Figure 3.13. The relative differences of CO_2 and CH_4 columns (WACCM-AirCore) show a negative correlation with SZA while a positive

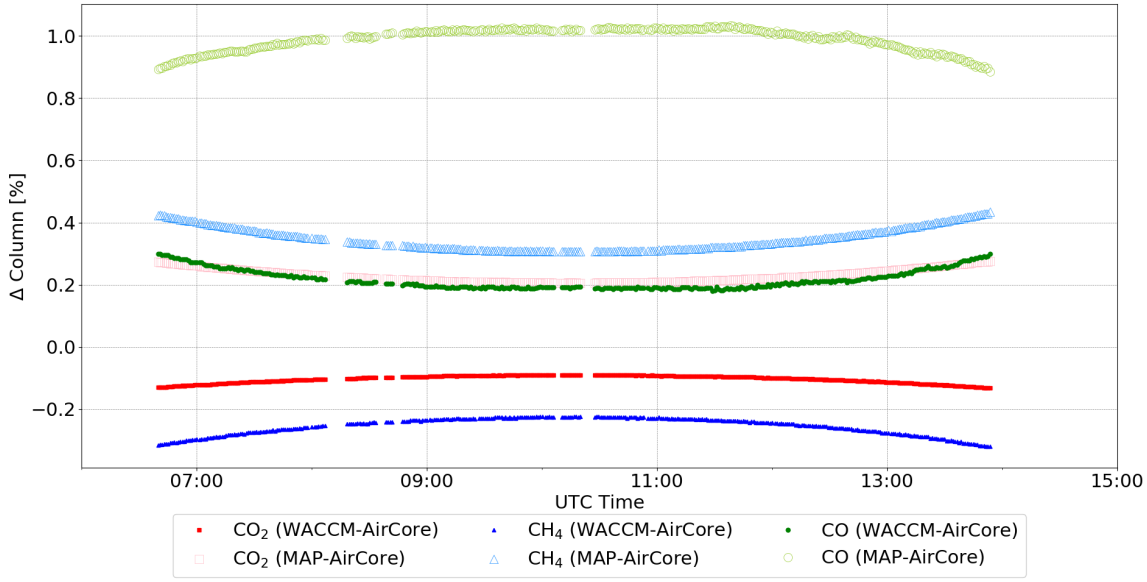

Figure 3.12: Time series of relative difference of CO_2, CH_4 and CO columns retrieved with WACCM and MAP a-priori VMR profiles with respect to the AirCore retrieved results, respectively. The results for WACCM-AirCore are denoted in solid symbols and the results for MAP-AirCore in hollow symbols.

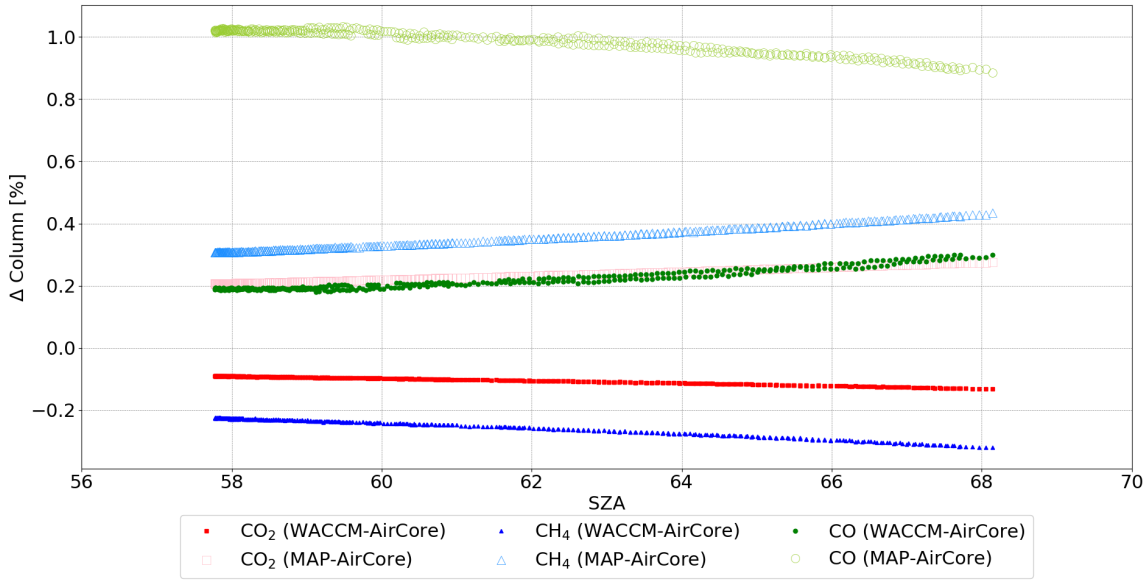

Figure 3.13: Relative difference of CO_2, CH_4 and CO columns retrieved with WACCM and MAP a-priori VMR profiles with respect to the AirCore retrieved results as a function of SZA. The results for WACCM-AirCore are denoted in solid symbols and the results for MAP-AirCore in hollow symbols.

tendency exists in the CO column. For retrievals using MAP profiles (MAP-AirCore), relative differences of both CO_2 and CH_4 columns increase with increasing SZA. Whereas, the CO column displays a negative correlation. The use of an identical O_2 profile in obtaining X_{Gas} dose not cause any differences in the different datasets. Therefore, relative differences in terms of X_{Gas} show similar patterns to those in terms of total columns (see Appendix A—Figure A.11).

To conclude, for investigating this sample day, the shape of the a-priori VMR profiles affects the retrievals to a certain extent. The use of a-priori VMR profiles has stronger impacts on XCO than XCO_2 and XCH_4 due to its larger difference between the modeled a-priori profile shapes (WACCM or MAP) with the measured AirCore profiles in the troposphere. Note that the retrieval differences caused by the a-priori VMR profiles can be different over the year, since the profiles change with season. AirCore launches were performed several times during the Finland campaign, which will be discussed in more detail in subsection 4.1.2.

3.6 Conclusions

Accurate a-priori information is a precondition to obtain high-precision retrievals from ground-based FTIR measurements. The approach of using column-averaged dry-air mole fractions instead of total columns for the target gases reduces the systematic errors. The compensation by using the O_2 column is expected to be better for XCO_2 and XCH_4 than XCO, since CO is a weak absorber within the selected spectral window as compared to the other two gases. The superimposition from the nearby strong interfering lines of CH_4 and H_2O makes XCO more sensitive to apparent variation.

To quantify the spectroscopic inadequacies, certain EM27/SUN retrievals are scaled to the TCCON results with corresponding airmass independent correction factor derived from in-situ side-by-side measurements. In summary, the XCO_2 correction factor is 0.99879 and 0.99871 for the EM27/SUN spectrometers operated at Sodankylä and Kiruna sites respectively; the scaling factors of XCH_4 are 1.01241 and 1.01250, and 0.92347 for XCO for the instrument in Sodankylä. Airmass dependent biases are taken into account in XCO_2 and XCH_4 by applying a polynomial function based on the studies of Klappenbach et al. [2015].

The use of an intraday variable ground pressure profile rather than a single fixed value on the measurement day turns out to be mandatory. For a sample day, a 1 hPa higher ground pressure leads to a reduction of 0.055 % in the O_2 total column, which also causes the increases of 0.035 % in XCO_2, 0.039 % in XCH_4 and 0.052 % in XCO, respectively. An increase of 1 K in temperature corresponds to a decrease of 0.015 % in XCO_2, 0.037 % in XCH_4 and an increase of 0.428 % in XCO, respectively.

Considering ILS parameters in the retrieval procedure also helps to reduce the systematic errors. The modulation efficiency (ME) parameter dominates the effect. The reduction of the ME value by 1 % induces changes of 0.18 % in XCO_2 and -0.01 % in XCH_4, respectively, for

a selected sample day. XCO is affected by the ME changes to a larger range (0.05 %–0.48 %) and suffers from asymmetry in the ILS due to the presence of strong interfering bands. The relative difference derived from different affects are summarized in Figure 3.14 (see Table 1 in the Appendix A for numerical values). It should be noted that the measured PE value changes on the order of 0.001 rad, resulting in much less impact on retrievals than the values listed here.

The choice of a-priori VMR profiles turns out to be important. The shape of the true atmospheric VMR profiles is not constant but changing over time. Thus, it is a better choice to use daily variable VMR profiles reflecting the meteorological structure rather than using invariable ones. The choice of identical a-priori VMR profiles simplifies the intercomparison between different FTIR instruments [Rodgers and Connor, 2003].

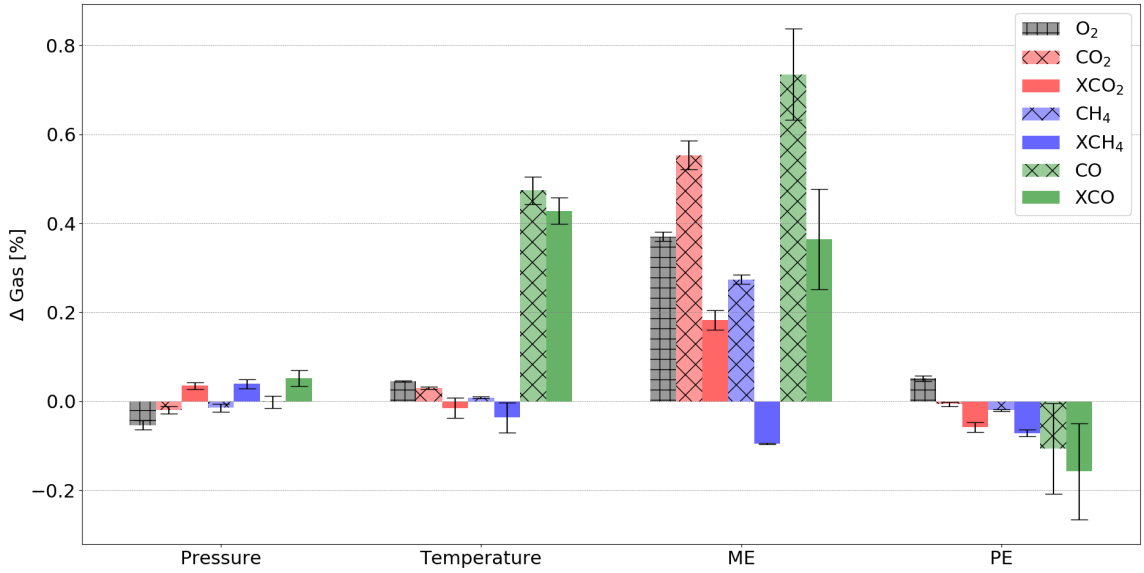

Figure 3.14: Daily average relative difference (%) in different species due to 1 hPa increase of ground pressure, 1 K increase of temperature, 1% decrease of modulation efficiency and 0.01 rad decrease of phase error. The results are derived from the measurements performed in Sodankylä on June 8, 2017 as an example.

Chapter 4

Ground-based GHG measurements in Sodankylä and Kiruna

In this chapter, I discuss how two EM27/SUN spectrometers located in Sodankylä and Kiruna are utilized to detect gradients and to determine the emission strength of trace gases (CO_2 and CH_4) from wetlands within the Arctic Circle. The observations with the EM27/SUN instrument at FMI, Sodankylä are performed in the framework of the FRM4GHG campaign. This campaign focused on the intercomparison of simultaneously measured column-averaged abundances of GHGs using several different portable low-cost ground-based remote sensing spectrometers. First, the EM27/SUN observations are retrieved with the PROFFIT algorithm using the optimized processing procedures described in Chapter 3, including the implementation of the measured ILS parameters and daily-variable a-priori VMR profiles (MAP) which are also used in retrievals for observations from the co-located 125HR. The impact of using measured a-priori VMR profiles from the AirCore balloon launches on the trace gas retrievals is also investigated. In addition, the optimized results are compared to in-situ tower observations in Sodankylä in the context of surface fluxes. Comparisons of the EM27/SUN measurements to the reference TCCON data and to the 125HR low-resolution data are provided, followed by another comparison to the data from the other portal low-resolution spectrometers participating in the campaign. Additionally, an investigation of the regional greenhouse gas emissions is discussed.

4.1 Optimization of EM27/SUN retrievals

4.1.1 Measured ILS implementation

An ILS sensitivity study for an example day has been presented in section 3.4 to demonstrate the effect of the ILS on the trace gas retrievals. The influence of the ILS indicates the necessity to characterize the ILS and to apply the parameters to the retrieval procedure. Regular ILS characterizations were performed during the FRM4GHG campaign and the

variation of the ME value is approximately within 0.1 % (for details see section 2.2). This value is within the uncertainty budget of the open-path measurement which is 0.29 % in total as derived by Frey et al. [2018]. The slight variation of the ILS parameters might be connected to carrying the spectrometer outside for measurements every day in spring, and due to unavoidable errors during the experiment (e.g. the uncertainty of the distance measurement between the lamp and the instrument). The absence of a significant change in the EM27/SUN instrumental performance demonstrates the highly stable characteristics of the spectrometer. The measurements were stable, even when the instrument was exposed to −15 °C. Note that no realignment of the instrument was performed during the whole campaign period.

Here, the average values of the ME and PE parameters are used, i.e. 0.9825 and -0.001, respectively, based on all the ILS measurements performed during the campaign (except the erroneous experiment on May 8, 2017 when the expected stable lab air was disturbed by the air conditioner). Note that the constant WACCM-derived a-priori profiles are used for the EM27/SUN retrievals in this subsection. The impacts of using MAP and AirCore as a priori profiles are explored in section 4.1.2. Additionally, the quality filter of SZA $< 80°$ is applied to the results to exclude retrievals with higher uncertainty at higher SZA.

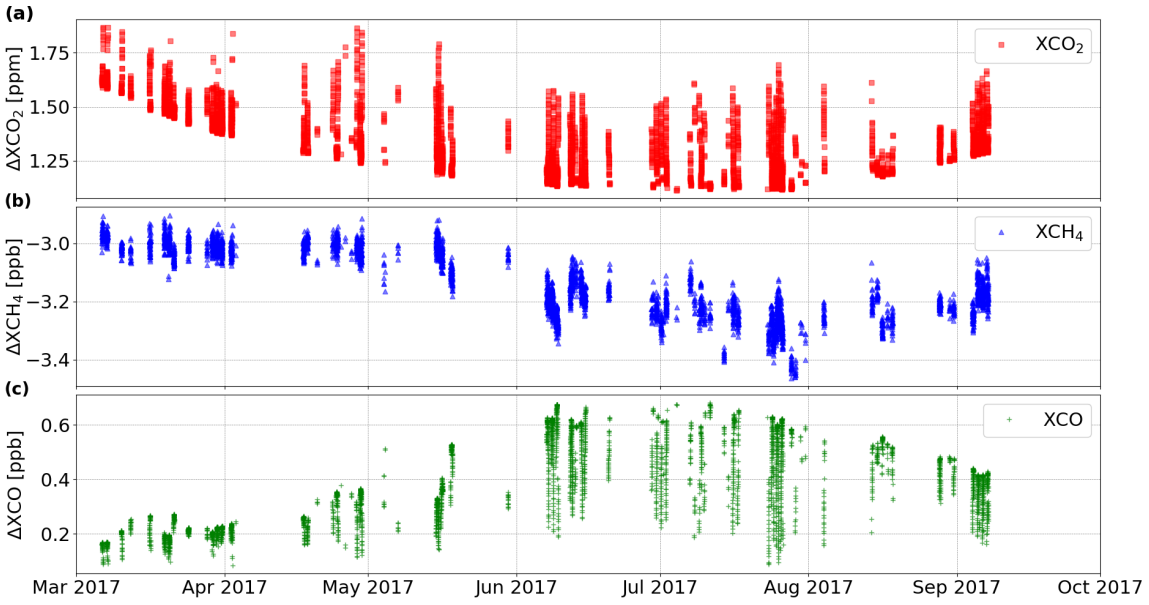

Figure 4.1: Time series of the difference between results with the measured ILS parameters and with the ideal ILS parameters in retrieving (a): XCO_2, (b): XCH_4 and (c): XCO measured with the EM27/SUN instrument.

The difference between the EM27/SUN data retrieved with the measured ILS parameters and with the ideal ILS parameters is presented in Figure 4.1. For XCO_2, higher changes are observed in spring, up to 1.9 ppm, while a maximum of 1.6 ppm is observed in summer. However, the difference in XCH_4 between the two EM27/SUN datasets shows a different

	ideal ILS		measured ILS	
	bias	relative bias	bias	relative bias
XCO_2	(-1.57 ± 0.95) ppm	(-0.39 ± 0.24)%	(-0.22 ± 1.04) ppm	(-0.06 ± 0.26)%
XCH_4	(-4.22 ± 5.77) ppb	(-0.23 ± 0.32)%	(-7.36 ± 5.85) ppb	(-0.40 ± 0.32)%
XCO	(-0.44 ± 1.98) ppb	(-0.39 ± 2.37)%	(-0.07 ± 2.1) ppb	(0.09 ± 2.55)%

Table 4.1: Sensitivity study on the effect of ILS changes. EM27/SUN data are retrieved with ideal and measured ILS parameters. Depicted is the annual average bias and relative bias of retrieved X_{Gas} with respect to the TCCON retrievals.

tendency. The effect of the measured ILS parameters causes a consistent negative offset during spring on the order of 3.0 ppb, while a slightly stronger negative offset and more variability are observed later during the year. XCO is offset by around 0.2 ppb in the early period of the measurements. After that, the difference increases gradually, peaks in summer and drops down afterwards, showing a seasonal variability.

The implementation of measured ILS parameters in retrieving EM27/SUN data helps to achieve a better agreement with the TCCON reference results (see Figure 4.2 in terms of correlation, time series of these three dataset are presented in Appendix A Figure A.12). XCO_2 shows a most obviously better agreement after using the measured ILS parameters among all the species. Most of the EM27/SUN data retrieved with the ideal ILS are lower than the TCCON data and the average bias between these two datasets is approximately -1.57 ppm. The bias is reduced by using the measured ILS parameters to -0.22 ppm. In contrast, using the measured ILS increases the bias of XCH_4 from -4.22 ppb to -7.36 ppb. This worse agreement is mainly due to the effect of polar vortex in early spring. Improved a-priori profiles will be discussed in next subsection. For XCO a slightly better agreement is achieved after the implementation of the measured ILS parameters, where an annual average bias of -0.07 ppb is obtained, while the bias before is -0.44 ppb. The annual mean value of the bias and relative bias for trace gases retrieved with different ILS parameters with respect to the TCCON data are summarized in Table 4.1. The changes in the relative differences do not fully correspond to the ILS sensitivity analysis for the example day shown in section 3.4 because the seasonal variability is affected by the airmass dependency. In addition, the constant WACCM-derived a-priori VMR profiles have been used for the EM27/SUN retrievals, which results in systematic errors when TCCON data is retrieved with MAP a-priori profiles.

To investigate the sensitivity of the ILS with SZA, the relative difference between the EM27/SUN retrieved with different ILS parameters as a function of SZA is presented in Figure 4.3. XCO_2 (red square) shows an obvious positive correlation with SZA and the tendency becomes stronger at higher SZA. Whereas there is no significant correlation in XCH_4 (blue triangle). XCO is most sensitive to SZA, with different layers of negative correlation which is mainly due to its weak absorption and interference from nearby CH_4 and H_2O

spectral lines.

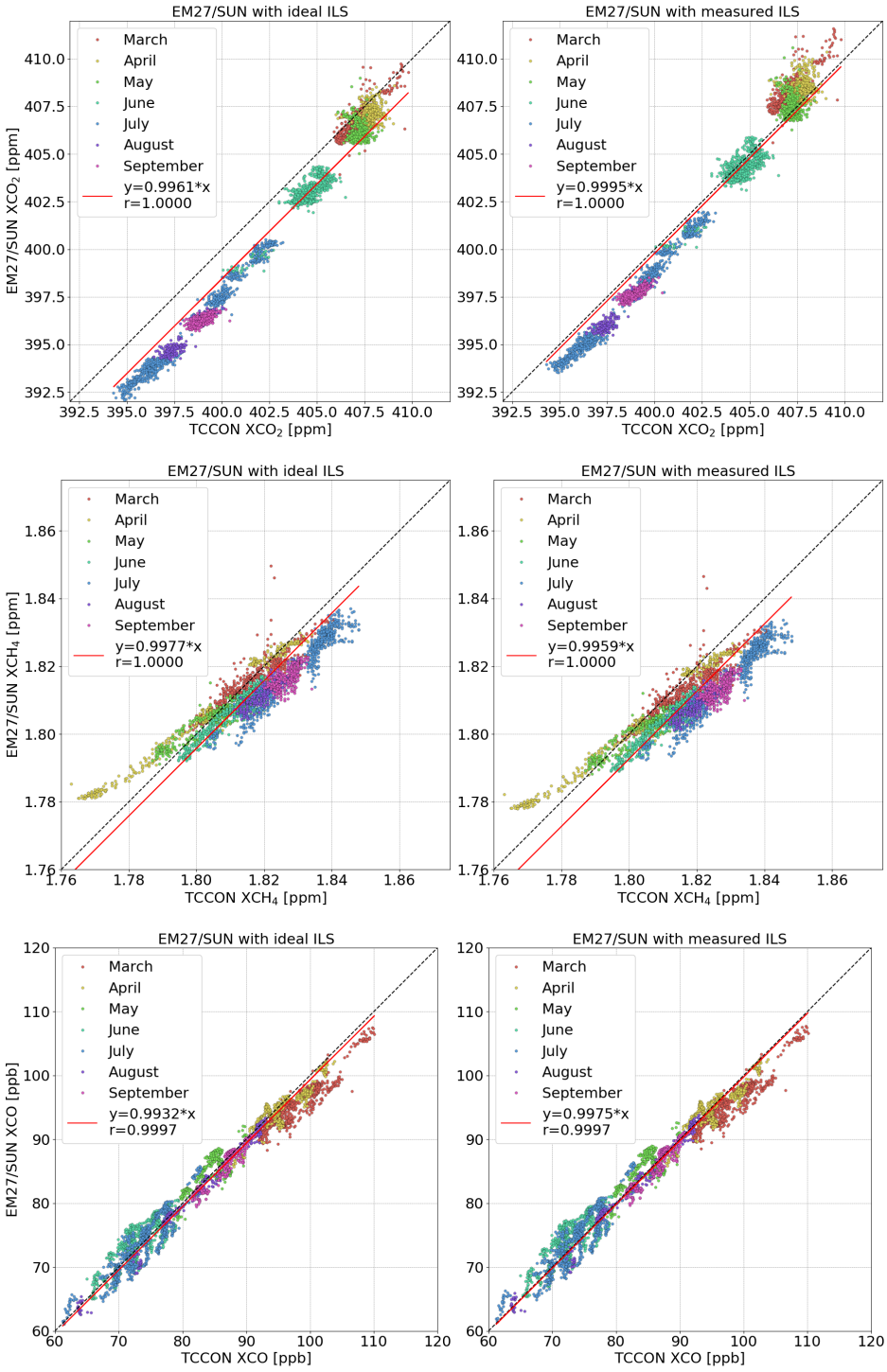

Figure 4.2: XCO_2, XCH_4 and XCO measured with the EM27/SUN instrument retrieved with ideal ILS (left panel) and measured ILS parameters (right panel) with respect to the TCCON results. Different colors denote the measurements recorded in different months.

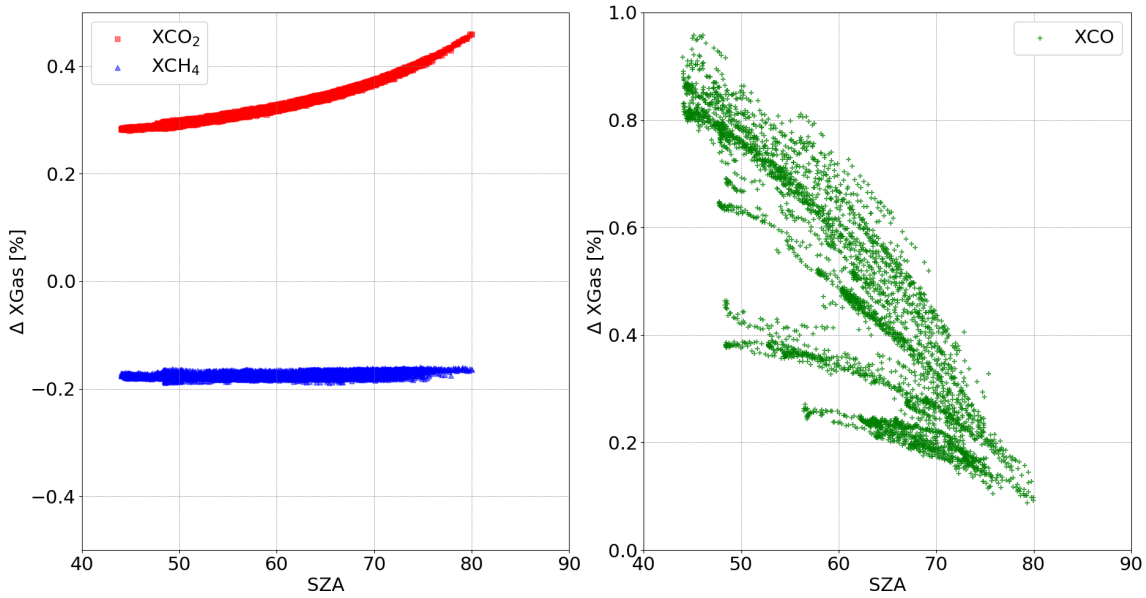

Figure 4.3: Relative differences of species between retrieved with measured ILS parameters and retrieved with ideal ILS parameters as a function of SZA. Left panel: XCO_2 and XCH_4; right panel: XCO.

4.1.2 A-priori VMR implementation

WACCM-derived and MAP a-priori profiles

In section 3.5 the influence of a-priori VMR profiles on trace gas retrievals has been discussed for a measurement day, and I found it impacted the retrievals by as much as 1 % for XCO. The atmospheric vertical profiles change with season, therefore, seasonal variations of the a-priori impact are expected. The EM27/SUN data during the whole campaign were retrieved with two different sets of a-priori profiles—the constant WACCM-derived and the daily-variable MAP profiles, as used by TCCON. Additionally, the impact of the measured AirCore a-priori profiles on the retrievals is also discussed for select days. It should be noted that the measured ILS parameters were used in the EM27/SUN retrievals and measurements with SZA $> 80°$ were discarded.

Figure 4.4 shows the constant WACCM-derived and daily variable MAP a-priori profiles (146 days in total, ranging from February 13, 2017 to November 7, 2017) for CO_2, CH_4 and CO. Compared with the constant WACCM-derived a-priori profiles, MAP profiles show obvious seasonal changing and different changing tendency for different species. A significant seasonal variability exists in the MAP profiles for CO_2, especially in the lower atmosphere. In the beginning of the year, the CO_2 concentrations tend to decrease with increasing height. The lower part of the profiles (below ∼10 km) changes dramatically around May, resulting in increasing concentrations with altitude and a higher rate of change. For CH_4 there is less seasonal variability than for CO_2 and mainly concentrates on the UTLS (upper troposphere

and lower stratosphere) region, likely related to the tropopause height. The profiles show similar shapes over the season and mostly shift to higher values with time. CO profiles change obviously with time below 20 km. Larger vertical change is found early in the year.

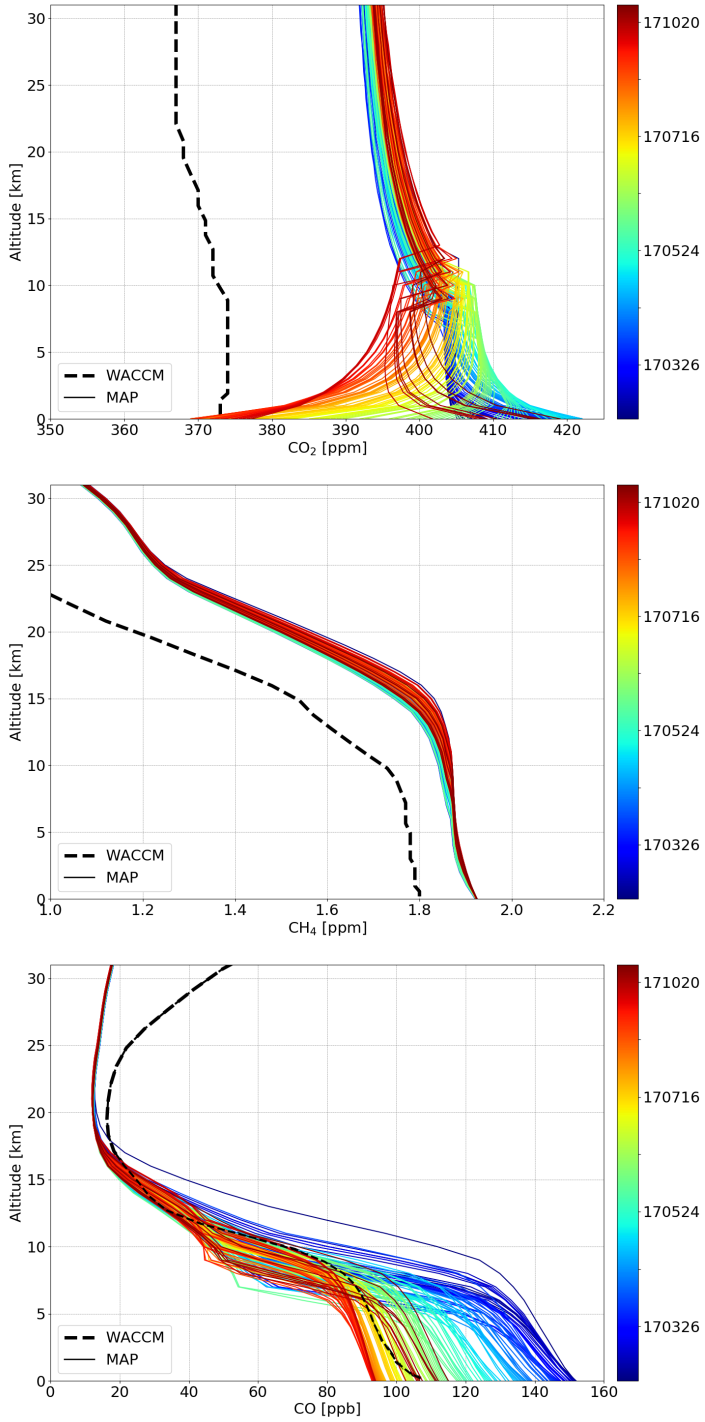

Figure 4.4: A-priori profiles of WACCM-derived (dash line in black) and MAP (solid line) for 146 days in 2017. Different colors represent different days for MAP profiles.

A-priori profiles are an important prerequisite in retrieving species concentrations, resulting in systematic errors when different profiles are used in retrievals. Figure 4.5 shows the time series of difference for the trace gases for the EM27/SUN measurements retrieved with the WACCM-derived a-priori profiles and with the MAP profiles. A difference of −0.4 ppm of XCO_2 between retrievals using the two datasets (MAP-WACCM) is seen in the beginning of the campaign. The difference becomes more negative with the largest value of −1.7 ppm around May. Afterwards, it becomes smaller and reaches zero around July. Later, the absolute difference increases up to about 2.1 ppm in early September (see Figure 4.5 (a)). For XCH_4 strong daily and seasonal variability is found when using different a-priori VMR profiles (see Figure 4.5 (b)). The difference is approximately 20.0 ppb in early March and starts to decrease, resulting in a minimum value of about 3.3 ppb in July. Afterwards, it increases gradually back to nearly 20.0 ppb. Using different priors has a much stronger diurnal impact on XCH_4 than XCO_2. The largest daily variation from 7.5 ppb to 21.1 ppb occurs on July 25, with a daily standard deviation of 3.7 ppb. Using different a-priori VMR profiles also changes the bias in XCO over time, with biases from −0.2 ppb to 3.6 ppb (see Figure 4.5 (c)). The bias increases gradually from March and reaches the maximum value in July, opposite of XCH_4. The seasonal variability found in the retrievals is due to seasonal variability in the MAP a-priori VMR profiles, while the WACCM-derived profile is constant for all seasons.

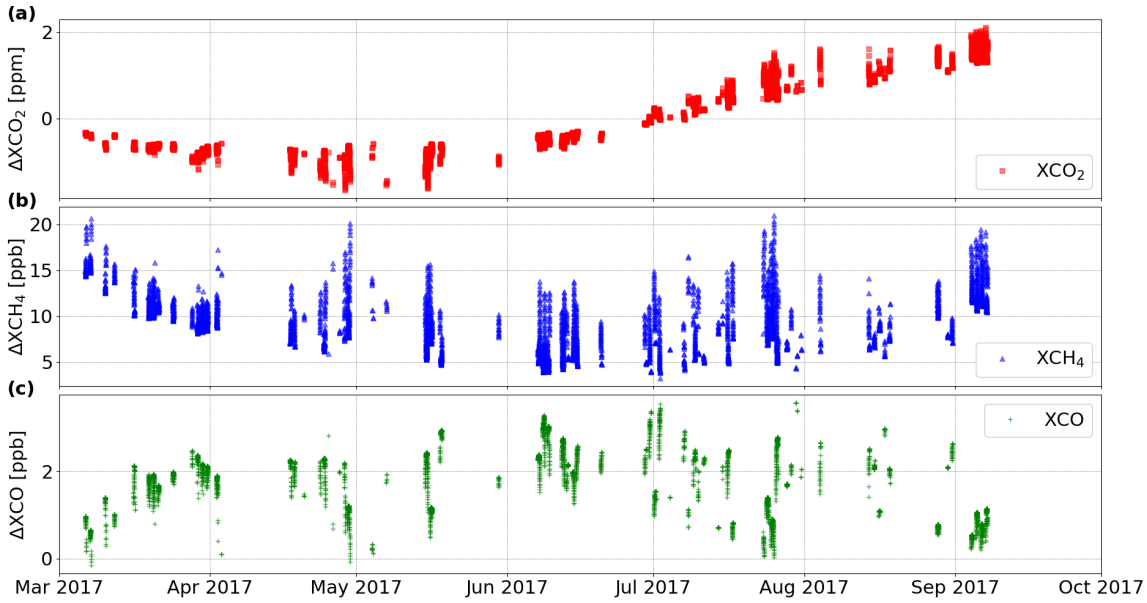

Figure 4.5: Time series of differences from retrieving XCO_2, XCH_4 and XCO with the fixed WACCM-derived a-priori and the daily-variable MAP a-priori VMR profiles, respectively (MAP-WACCM). Note that the WACCM-derived profile is a constant climatological profile, while MAP is a variable day-to-day adjusted profile.

The linear correlation of the two EM27/SUN datasets with respect to the TCCON reference results is presented in Figure 4.6 (see Appendix A—Figure A.13 in terms of time series) and the numerical values for the bias and relative bias are summerized in Table 4.2. In every panel, EM27/SUN data retrieved with the WACCM-derived a-priori profiles is presented on the left, and data retrieved with the MAP a-priori profiles is presented on the right. The fitting line is forced through the origin and different colors denote the measurements recorded in different months. It should be noted that the TCCON reference results are retrieved with the MAP profiles. For XCO_2 retrieved with the WACCM-derived profile, the best matched measurements occur in May and June. However, worse agreement is found in the beginning of and at the end of the campaign. EM27/SUN results are larger than the TCCON results in spring and early summer and are lower in late summer and autumn. When using the MAP profiles, the agreement is improved throughout the year. The EM27/SUN retrievals decrease in spring and increase in autumn. These changes reduce the bias compared to the TCCON data with an annual-average difference of 0.06 ppm ($\sim$0.01 %), resulting in an overall better agreement. The annual-average standard deviation is reduced by $\sim$0.40 ppm indicating a reduced seasonal variability. A more significant overall increase is found for XCH_4 with approximately 9.72 ppb ($\sim$0.51 %) on average after using the MAP a-priori VMR profiles. The significant change caused by the different profiles is also clearly visible here when the linearly dependent coefficient increases from 0.9959 to 1.0011, showing much better correlation with the reference TCCON data. The XCO correlation becomes slightly worse probably because the MAP profiles do not properly describe the actual atmospheric variability. Therefore, in order to reduce these systematic errors derived from different a-priori VMR profiles, ideally identical a-priori profiles should be used when comparing retrievals from different FTIR spectrometers with different sensitivities.

	WACCM		MAP	
	bias	relative bias	bias	relative bias
XCO_2	(-0.22 ± 1.04) ppm	(-0.06 ± 0.26)%	(-0.28 ± 0.64) ppm	(-0.07 ± 0.16)%
XCH_4	(-7.73 ± 5.85) ppb	(-0.40 ± 0.32)%	(1.99 ± 5.76) ppb	(0.11 ± 0.32)%
XCO	(-0.07 ± 2.1) ppb	(0.09 ± 2.55)%	(1.72 ± 2.48) ppb	(2.30 ± 3.2)%

Table 4.2: Sensitivity study of the effect of different a-priori VMR profiles on the EM27/SUN retrievals. EM27/SUN data are retrieved with the WACCM-derived and the MAP profiles, respectively. Depicted are the annual average bias and the relative bias of retrieved X_{Gas} with respect to the TCCON retrievals.

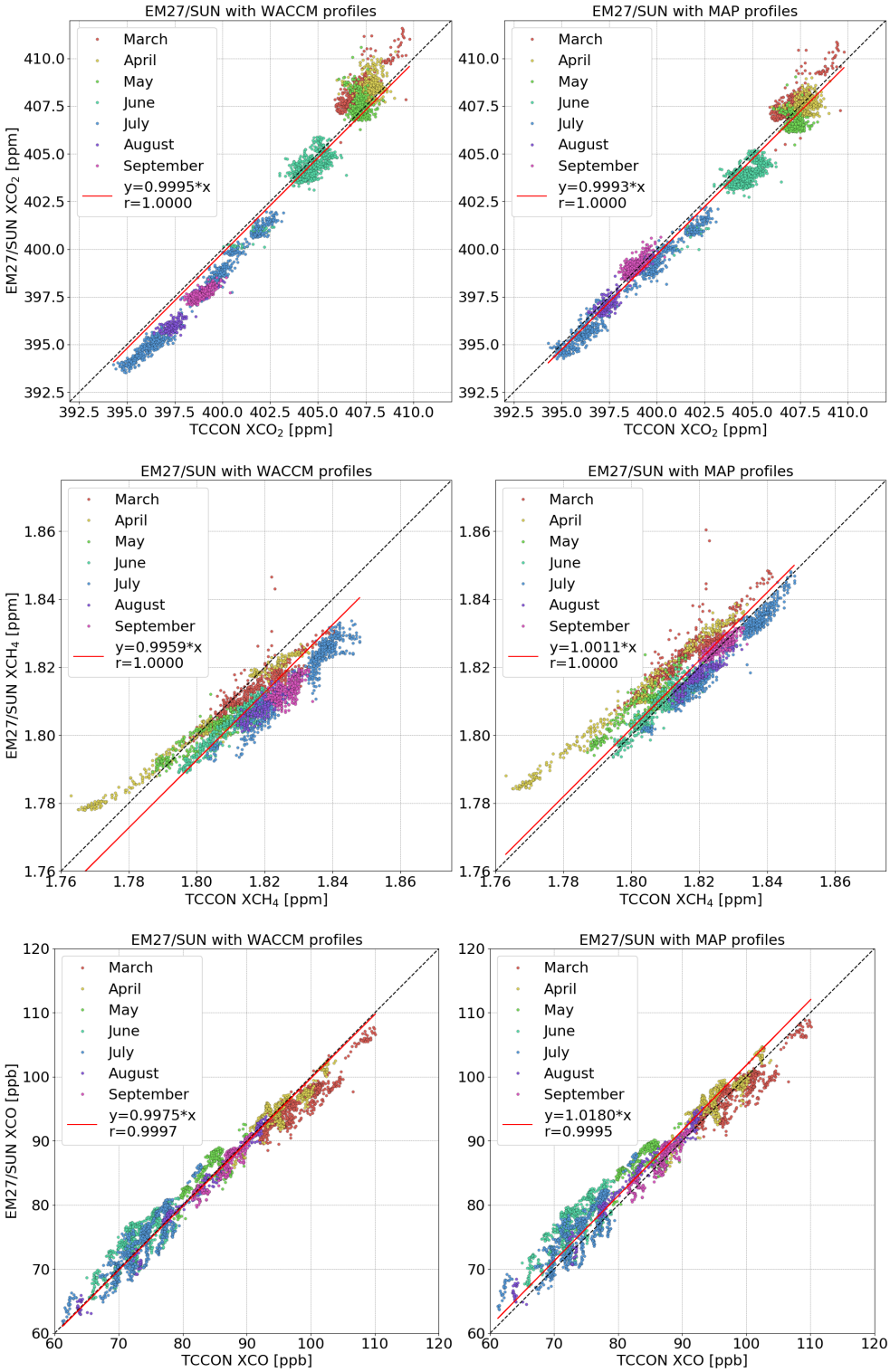

Figure 4.6: XCO_2, XCH_4 and XCO measured with the EM27/SUN instrument retrieved with different a-priori profiles with respect to the TCCON results. The EM27/SUN retrievals with the WACCM-derived profiles are depicted on the left side, while the retrievals with the MAP profiles are depicted on the right. Different colors denote the measurements recorded in different months.

AirCore a-priori profiles

The use of common a-priori VMR profiles is expected to improve the agreement between different remote sensing measurements. The balloon-based AirCore, as an innovative, simple and viable sampling system provides the possibility to measure the actual vertical distribution of CO_2 and CH_4 [Andersen et al., 2018; Karion et al., 2010; Membrive et al., 2017].

Ten AirCore soundings were launched co-located with the TCCON and EM27/SUN instruments during the FRM4GHG campaign between April and October, 2017. Figure 4.7 shows the three kinds of a-priori VMR profiles—the constant WACCM-derived profiles (dash line), the daily-variable MAP profiles (dot lines) and the measured AirCore profiles (solid lines) at 10 AirCore sounding days for CO_2, CH_4 and CO. Different colors denote different measurement days for the MAP and AirCore profiles.

For CO_2, less variation occurs in the higher altitude for all the three kinds of profiles, while the tropospheric slope of both MAP and AirCore profiles varies significantly over the year. The constant WACCM-derived profile shows a large difference compared to the other two profiles with approximately 30 ppm bias for all altitude levels. The shape of the WACCM-derived profile in lower layers is similar to the MAP and AirCore profiles in October but with less variation. In spring and early summer the CO_2 amounts in both MAP and AirCore profiles decreased with increasing height. The MAP profiles have larger slope change compared to the AirCore profiles but underestimate the absolute amounts in the troposphere. However, the amount of CO_2 in the MAP profiles is overestimated by approximately 10 ppm near the surface. The MAP profiles have similar shapes to the AirCore profiles in August and September, when the CO_2 concentration increased with altitude in general. However, the amount of CO_2 in the MAP profiles is underestimated by approximately 20 ppm in lower layers and a constant amount between 5 km to 10 km is observed in AirCore profiles. Both MAP and AirCore profiles in October were during the transition from summer/autumn to winter but higher variation and concentration are found in the AirCore profile.

The WACCM-derived CH_4 profile has a similar shape compared to the MAP profiles but is around 0.2 ppm lower in the troposphere. The bias is doubled in the intermediate altitude levels. The MAP profiles show less variability over time and altitude than the AirCore profiles. Good agreement is found below 8 km. There is no obvious change at the higher altitude for the MAP profiles throughout time. In the AirCore profiles, CH_4 is quite stable in the lower layer of the atmosphere but varies at higher altitudes over the year. The dominant variability occurs in the upper troposphere and in the stratosphere. An obvious decrease is found in April above 20 km which is approximately 75 % as much as in later seasons.

The WACCM-derived CO profile has a large bias compared to the MAP profile above the tropopause and the bias increases with higher altitude, while the lower part is similar to the MAP profiles in autumn. The MAP profiles have similar shapes to the AirCore profiles with slightly lower values. Strong variability is observed in the altitude range between 8–15 km

in the AirCore profiles when step changes happen at different altitudes in different seasons. The AirCore profiles show a high degree of variability up to 20 km and vary with season. There are lower concentrations of CO in spring and early summer near the surface, while the amounts are more steady at higher altitude in different seasons.

To quantify the effect of the AirCore a-priori VMR profiles on different species, new datasets are retrieved using these profiles in the PROFFIT algorithm. The new profiles combine the measured AirCore profiles, scaled MAP profiles and near-surface observations. The combination is necessary because the AirCore soundings mostly extend up to around 25 km (or 20 km for CO) and no data below 0.5 km are available from AirCore. These combined profiles include 71 levels at equally spaced altitudes, similar to the MAP profiles. The measurements from the in-situ tower mast at FMI are used for prescribing the ground concentration of the trace gases. Levels from 1 km up to around 25 km (slightly different for different days) for CO_2 and CH_4 or up to around 20 km for CO are derived from the AirCore results, using the average gas concentration between ± 0.5 km at each level. For each species measured with AirCore, the highest available altitude level is considered as the transition point. The distributions above this point are acquired from the MAP profiles scaled to the AirCore profiles. The scale ratio equals to the gas concentration in the AirCore profile divided by the MAP concentration at the transition altitude. Figure 4.8 shows four measurement days in different seasons for CO_2, CH_4 and CO. The profiles consisting of the green square (tower observations at surface) and red dots (AirCore at lower layers and scaled MAP profiles at higher layers) depict the new a-priori VMR profiles which are used in both the 125HR and the EM27/SUN retrievals.

Figure 4.9, 4.10, and 4.12 show the correlation of two kinds of retrievals between the EM27/SUN and the 125HR instruments (left panel). The dot symbols denote the values retrieved with TCCON-official MAP profiles and the cross symbols denote the values retrieved with the extended profiles based on the AirCore profiles. Different colors depict different measurement days when the AirCore profiles are available. The changes after applying new profiles for both instruments are shown in right panels.

For XCO_2 no significant change was observed in the agreement between the EM27/SUN and the reference 125HR measurements in spring and early summer. Both of them retrieved similar less amounts of XCO_2 (~ -0.3 ppm) after using the extended a-priori profiles based on the AirCore profiles in April and nearly no change was found for both datasets in May. However, stronger change occurred in late summer and autumn due to the larger difference between the two CO_2 a-priori profiles in the troposphere, resulting in better agreement between the EM27/SUN and the reference 125HR measurements (see Figure 4.8, CO_2 profiles in last two columns). Application of the extended AirCore profiles reduces the 125HR XCO_2 values by approximately (-0.47 ± 0.13) ppm on average and results in nearly double amount of decrease in EM27/SUN retrievals by (-0.92 ± 0.08) ppm on August 28, 2017. For the three AirCore launch days in September, the 125HR retrievals are reduced by approximately

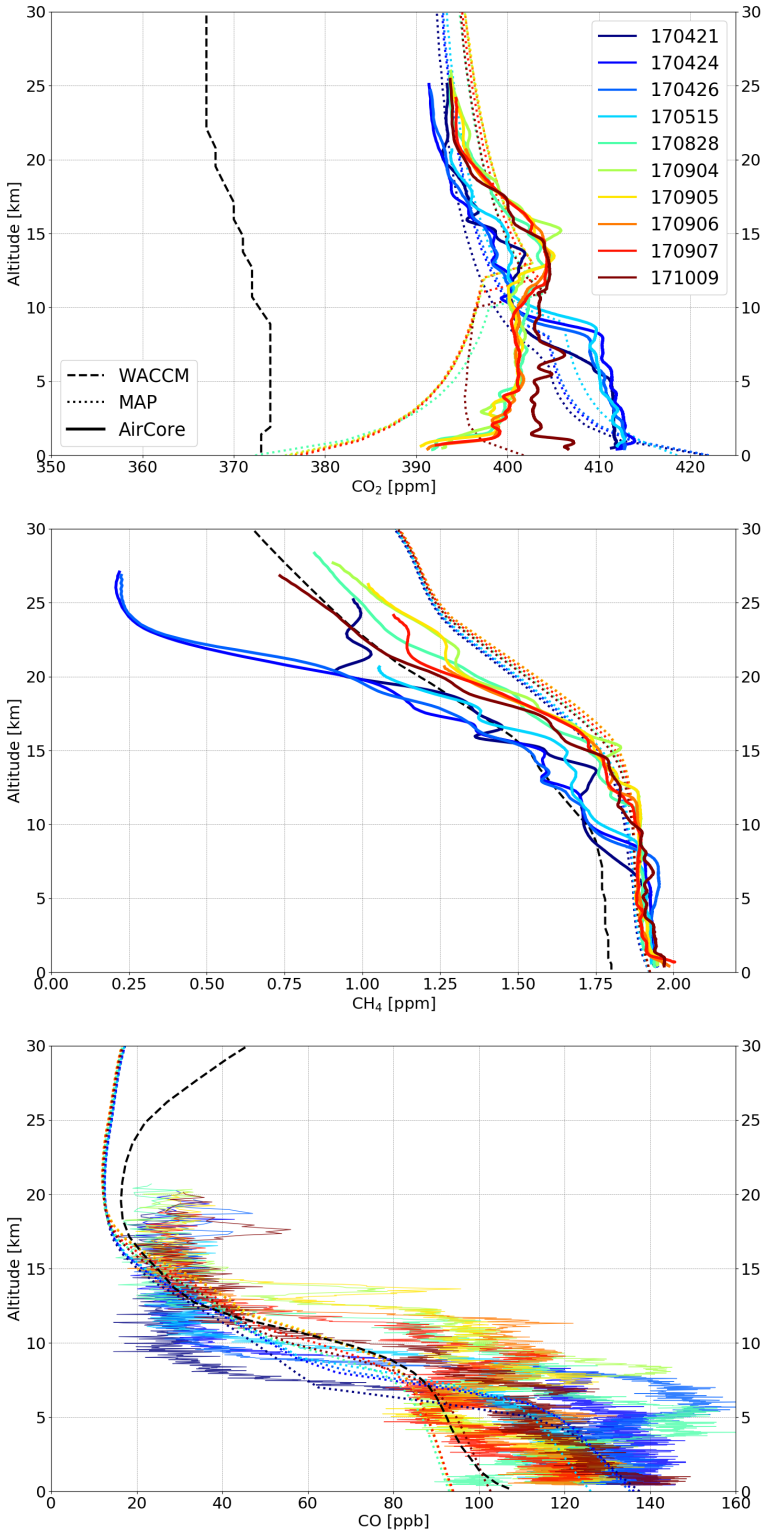

Figure 4.7: A-priori profiles of the WACCM-derived profile (dash line in black), MAP (dot line) and AirCore (solid line) at 10 AirCore launch days in 2017. Different colors represent different days for MAP and AirCore profiles. The figures on the left column show the profiles with an altitude up to 70 km, while figures on the right columns are zoomed in and with an altitude up to 30 km.

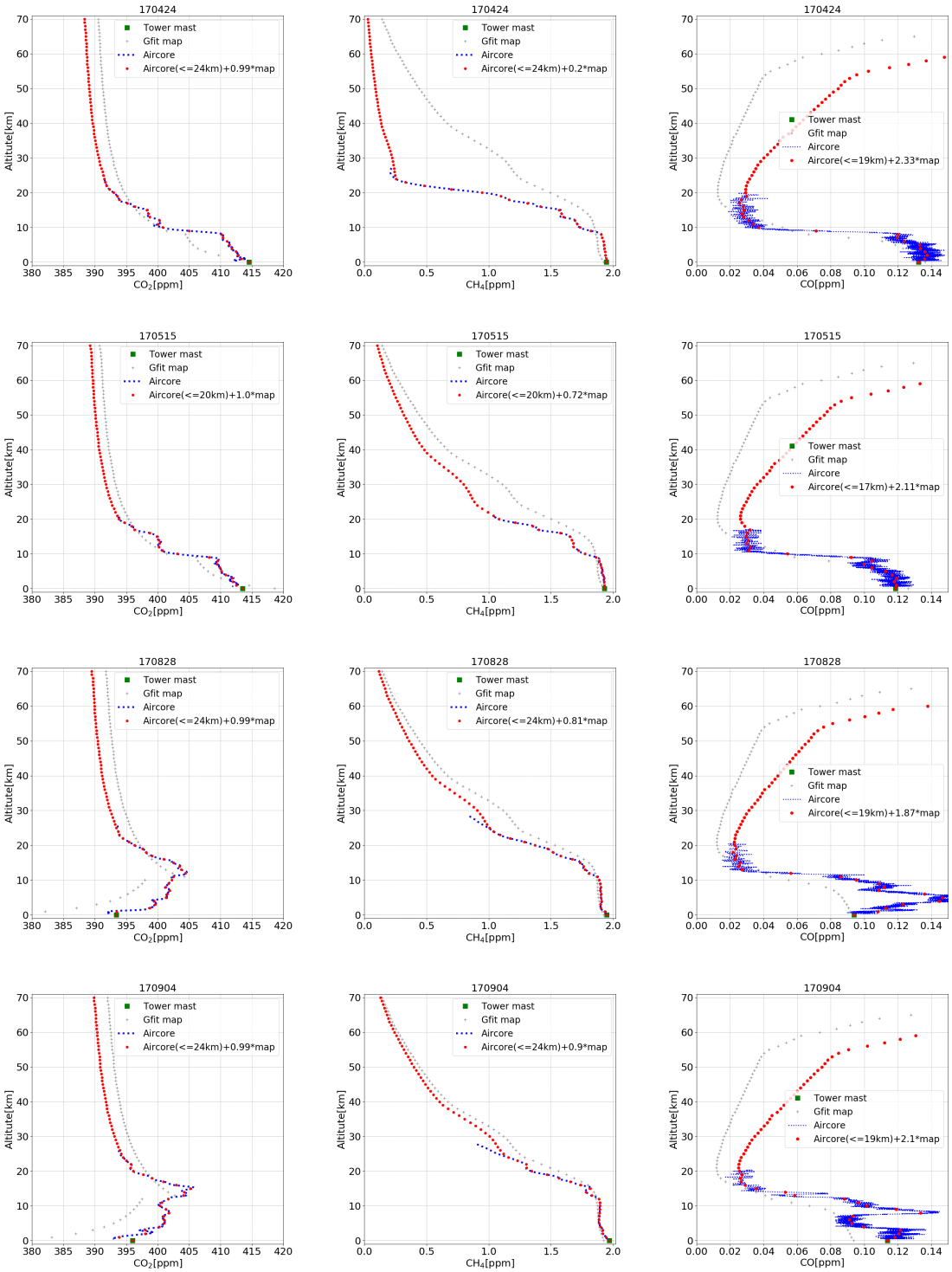

Figure 4.8: The MAP, Aircore and combined profiles for CO_2, CH_4 and CO at four measurement days in 2017. Red points denote the new profiles based on the in-situ tower measurements at ground, AirCore profiles and scaled MAP profiles.

(-0.66 ± 0.17) ppm, and (-0.99 ± 0.12) ppm in EM27/SUN retrievals. The effect of the combined profiles on the 125HR results is slightly less than on the EM27/SUN retrievals. This is mainly because the two instruments operate with different spectral resolutions.

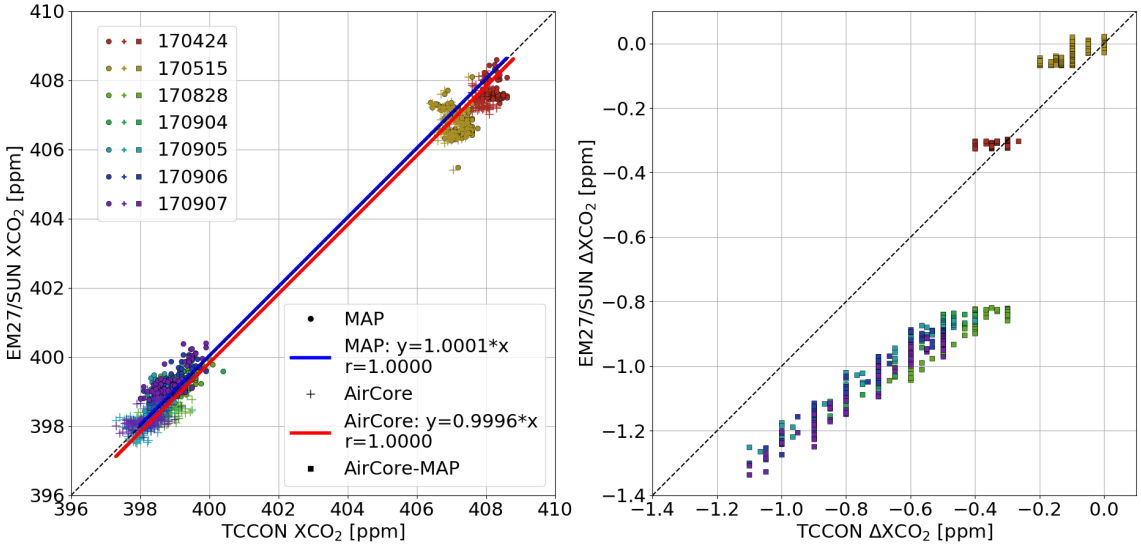

Figure 4.9: The left panel shows the CO_2 correlation between the TCCON and the EM27/SUN retrievals for all the AirCore launch days. The data retrieved using MAP profiles are denoted with dots, data retrieved using extended AirCore profiles are denoted with cross symbols. Different colors represent different measurement days. The right panel shows the difference between the retrievals with the MAP profiles and with the extended AirCore profiles for the TCCON and EM27/SUN measurements.

A significant change is observed in XCH_4 and the EM27/SUN measurements show a higher sensitivity than the TCCON 125HR measurements to the different a-priori profiles (see Figure 4.10). The highest change is observed on April 24, 2017, when an average decrease of (22.46 ± 5.44) ppb is obtained in EM27/SUN retrievals after using the extended AirCore a-priori VMR profiles. However, much less change is found in 125HR retrievals with approximately (2.06 ± 7.81) ppb on average. The change becomes smaller with approximately (-11.85 ± 3.32) ppb for EM27/SUN retrievals in May, while slight increase is found in the 125HR measurements by approximately (0.62 ± 4.72) ppb. In August and September the change continuously decreases for the both datasets, with approximately (-6.48 ± 1.34) ppb for EM27/SUN and (-0.92 ± 1.53) ppb for the 125HR observations. Besides the decreasing sensitivity of both EM27/SUN and 125HR measurements on different a-priori profiles, the diurnal variation of the changes is weaker in later year than earlier. The main reason is that the difference between the measured profiles and the modeled MAP profiles is larger in spring than in autumn. The significant bias in spring is mainly caused by the polar vortex. Ostler et al. [2014] investigated the stratospheric subsidence caused by the polar vortex and found different impacts on MIR and NIR retrievals because of the differing sensitivity depending

on the altitude, although the same a-priori VMR profiles were used. Due to this reason, the differences between the real atmospheric shapes of trace gases and the assumed profiles introduce differences in the retrieved column amounts. Similarly, the sensitivities of the EM27/SUN and TCCON instruments differ due to different spectral resolution. Figure 4.11 shows N_2O data from the Microwave Limb Sounder (MLS) on the Aura satellite for two days in April before the first AirCore launch and four more days when AirCore flights were performed. Because of its long life time, N_2O is a good tracer for estimating the position of the polar vortex. Therefore, N_2O concentrations on the 490 K potential temperature level, approximately at the height of 18 km, is used here to study the XCH_4 abnormal observations in April during the FRM4GHG campaign. In the beginning of April, 2017 the polar vortex is found in the Arctic and started to extend to lower latitudes. The polar vortex gradually disappeared at the end of April. The presence of the polar vortex in April explains the bias between the TCCON 125HR and the EM27/SUN retrievals in spring, while better agreement is found in summer and autumn. This hypothesis is also supported by a comparison of the MAP and the AirCore-measured CH_4 profiles in April, May, August and September (see Figure 4.8, CH_4 profiles in middle column). An obvious difference is found on April 24, 2017, while for the other days the profiles were quite similar and decreased with time.

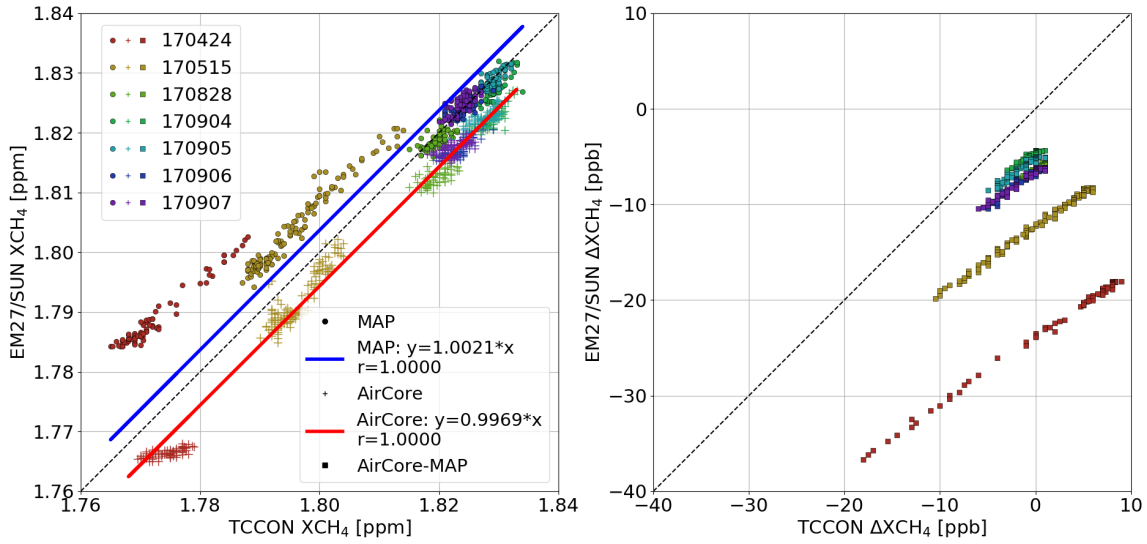

Figure 4.10: The left panel shows the CH_4 correlation between the TCCON and the EM27/SUN retrievals for all the AirCore launch days. The data retrieved using MAP profiles are denoted with dots, data retrieved using extended AirCore profiles are denoted with cross symbols. Different colors represent different measurement days. The right panel shows the difference between the retrievals with the MAP profiles and with the extended AirCore profiles for the TCCON and EM27/SUN measurements.

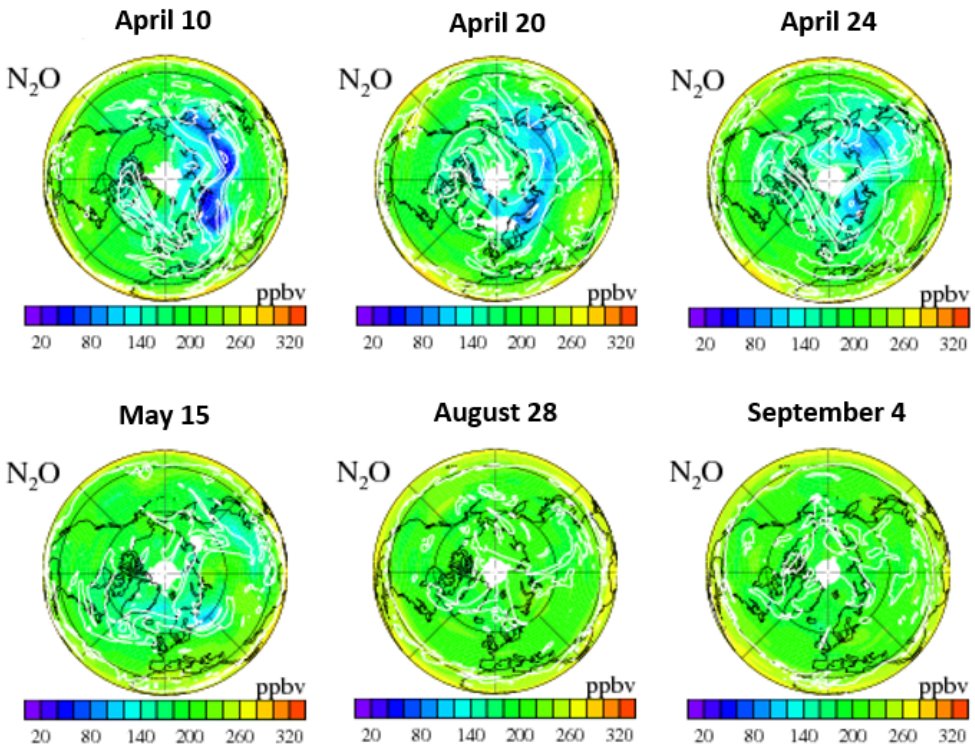

Figure 4.11: N_2O measurements from the MLS instrument on board the Aura satellite as an indicator for the position of the polar vortex in April, May and September. Data and plots courtesy of the NASA science team (https://mls.jpl.nasa.gov/).

The agreement between the EM27/SUN and TCCON retrievals does not show an obvious change in XCO when replacing the MAP a-priori profiles with the extended AirCore profiles. In April, the EM27/SUN retrievals show slightly higher sensitivity to the change of the a-priori profiles with approximately (-2.19 ± 0.28) ppb than the TCCON 125HR retrievals with approximately (-1.67 ± 0.11) ppb. However, the changes in 125HR retrievals are overall larger than those in EM27/SUN retrievals in the other days, except on September 6, 2017 when both changes are similar with approximately (-0.76 ± 0.04) ppb in TCCON and (-0.64 ± 0.07) ppb in EM27/SUN retrievals. The MAP a-priori profiles had a worse agreement with the AirCore profiles in August and September than the early year, which however, does not obviously influence the XCO retrieved from both instruments measurements when using different a-priori profiles. Hedelius et al. [2016] studied the differences in the averaging kernels of retrieved X_{Gas} measurements from EM27/SUN and TCCON instruments and the retrieved XCO from both instruments show no obvious sensitivity to altitude and SZA. This study indicates that the high-resolution instrument and low-resolution instrument are similarly sensitive to the CO profiles which later compensates the impact from the a-priori profiles.

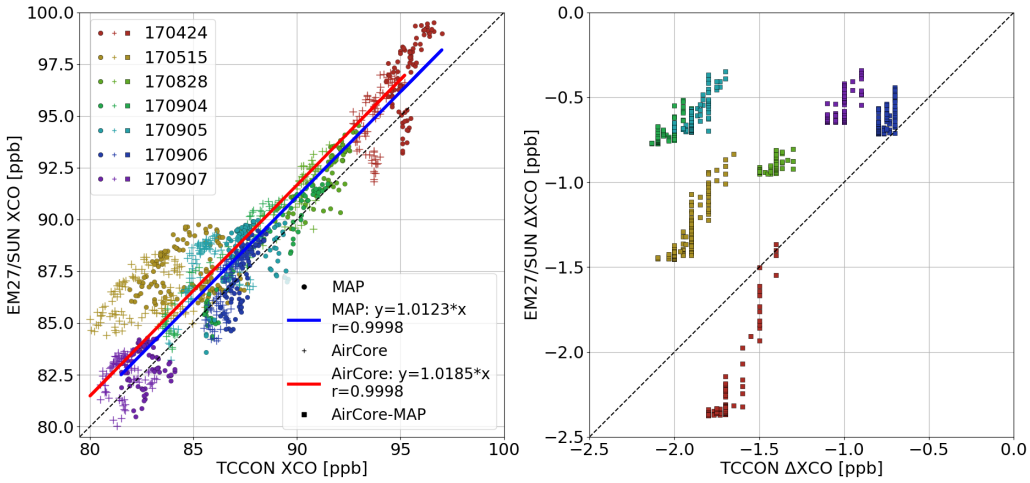

Figure 4.12: The left panel shows the CO correlation between the TCCON and the EM27/SUN retrievals for all the AirCore launch days. The data retrieved using MAP profiles are denoted with dots, data retrieved using extended AirCore profiles are denoted with cross symbols. Different colors represent different measurement days. The right panel shows the difference between the retrievals with the MAP profiles and with the extended AirCore profiles for the TCCON and EM27/SUN measurements.

4.2 Analysis of seasonal variations

4.2.1 EM27/SUN and in-situ observations

Boreal vegetation especially at high latitude experiences a clearly distinguishable evolution cycle between winter and summer seasons. The photosynthetic activity is more likely influenced by temperature than water availability [Suni et al., 2003]. Some studies have proven that air temperature is a very important factor for the commencement of photosynthesis in spring and considered as a good predictor for boreal forest growth at high latitudes [Suni et al., 2003]. Moreover, the beginning of snow melt is also another useful factor to predict the outset of the growing season [Thum et al., 2009]. Soil respiration increases in autumn because of the higher temperature, while the photosynthesis activity becomes weaker (Piao et al., 2008). Therefore, to support the measurements with the FTIR instruments, air/soil temperature, air pressure, snow depth and trace gases flux are analyzed in this section.

The FMI, Sodankylä hosts various scientific programs, exploring e.g. snow and soil hydrology, and the interaction between the biosphere and the atmosphere. Long-term measurements with different purposes are performed using a tower, masts and platforms assembled with versatile instruments. To support the measurements with the FTIR instruments, air/soil temperature, air pressure, snow depth and trace gases flux are analyzed in this section. The operative Automatic Weather Station (AWS: LUO0015)[1] has been measuring meteorological parameters since 2006, including the air temperature at 2 m height, the air pressure at station level, snow depth, etc. The pressure and temperature from this station are interpolated to the observation altitude. This diurnal-variation ground pressure and temperature are used as the official input files for retrieving the TCCON 125HR and the EM27/SUN measurements. A 48 m high meteorological mast (MET0002)[2] is located on site and measures wind speed/direction, snow depth, PPFD (Photosynthetic Photon Flux Density), net radiation, etc. every 10 minutes. The daily average values are used here. Additionally, the LI-COR LI-7000 Gas Analyzer installed at the micrometeorological mast (MET0006 station)[3] is a quick response sensor for measuring atmospheric water vapor and CO_2 concentration. Together with a simultaneously measuring sonic anemometer, it is possible to calculate the CO_2 flux from the CO_2 concentration and the wind information based on the eddy covariance (EC) method. The eddy covariance method provides continuous and direct measurements of net carbon dioxide (and water vapor) exchange across the interface between the terrestrial ecosystem and the atmosphere [Baldocchi, 2003]. The flux is defined by measuring the covariance between the vertical wind velocity and the volume mixing ratio of CO_2 in the atmosphere. A negative value of the covariance represents uptake when net CO_2 is absorbed by the plant canopy and a positive value denotes the release of CO_2 into the atmosphere [Baldocchi, 2003].

[1] http://litdb.fmi.fi//luo0015_data.php
[2] http://litdb.fmi.fi//met0002_data.php
[3] http://litdb.fmi.fi//met0006_data.php

The measurements recorded with the EM27/SUN spectrometer began from March 6, 2017 and lasted until September 7, 2017 (see Figure 4.13). The atmospheric CO_2 was quite stable from March to the end of April with an average value of (407.61 ± 0.59) ppm. It decreased gradually in May (monthly average: (406.60 ± 0.35) ppm and started to decrease more rapidly since June. A possible explanation is the change in snow cover and the soil temperature (see Figure 4.14, first panel with the snow depth (red line) and subsoil temperature (blue line)). The average of snow depth was (71.0 ± 2.3) cm in March and April. During this period the ground was totally covered by snow, keeping the soil temperature close to 0 °C. The snow cover and low temperature froze the subsurface soil, and hindered therefore the water uptake of plants. Subsequently, this slowed down the recovery of the photosynthesis, resulting in an constant CO_2 concentration in the atmosphere. The snow melting period started from May and lasted approximately one month. When the snow depth was reduced to around 15 cm, soil temperature started to increase. The first time temperature reached above 0 °C was on May 26, when a small decrease occurred in XCO_2. After the snow completely disappeared at the end of May, the subsoil temperature rapidly reached values above 10 °C in a few days and remained around 15 °C in July. The temperature started to decrease in August and gradually dropped to 0 °C in November. This variability of the soil temperature was inversely similar to the change of XCO_2, which supports the theory of temperature being a critical factor for the photosynthesis activity [Suni et al., 2003]. The change of XCO_2 shows a close correlation with the variability of the CO_2 flux (Figure 4.14 (c)). A negative CO_2 flux was detectable from the middle of May onwards, indicating that the CO_2 absorption is larger than the emission. CO_2 fluxes typically were less than $2\,\mu mol\,m^{-2}\,s^{-1}$ in June and July (nearly half of the data in July were missing due to a failure of the gas analyzer sensor) during which XCO_2 decreased rapidly. A higher CO_2 flux is observed since August with randomly dispersed values due to the weakening photosynthesis activity. The daily minimum CO_2 flux increased from August to the middle of September, when XCO_2 kept a stable level.

XCH_4 retrieved from the EM27/SUN measurements ranged between 1.77 and 1.85 ppm during the campaign (see Figure 4.13 (b)), showing higher variation than XCO_2. The concentration of XCH_4 in the atmosphere shows a positive correlation with the temperature. The highest amount of XCH_4 was observed in the end of July, when both subsoil and air temperature reached the highest value. This might be due to the warmer weather increasing the activity of methanogens [Macdonald et al., 1998], resulting in higher atmospheric XCH_4.

XCO shows a similar variation tendency to XCO_2 (see Figure 4.13 (c)). The highest atmospheric XCO concentration was observed in the beginning of the measurements. The concentration stayed around 100 ppb in March and April and started to decrease at the end of April. Nearly 30 % of XCO was reduced until July. These reduction is mainly due to reactions with OH radicals (85 %) and soils (10 %), and the diffusion into the stratosphere [Khalil and Rasmussen, 1990].

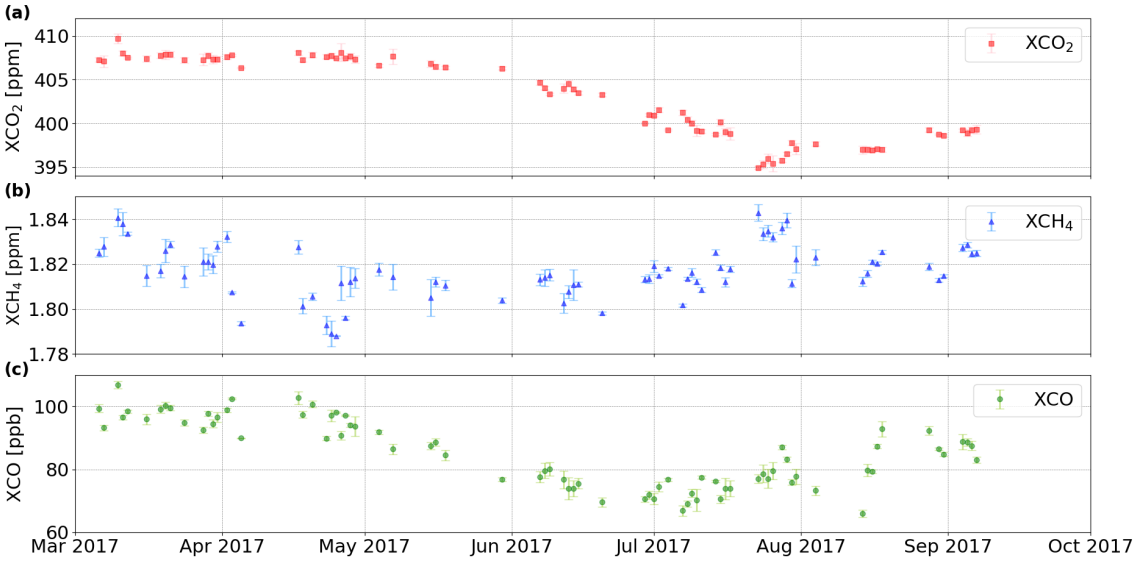

Figure 4.13: Time series of the daily mean of (a): XCO_2, (b): XCH_4 and (c): XCO observed with the EM27/SUN spectrometer at FMI, Sodankylä. Error bars represent the standard deviation of the daily average.

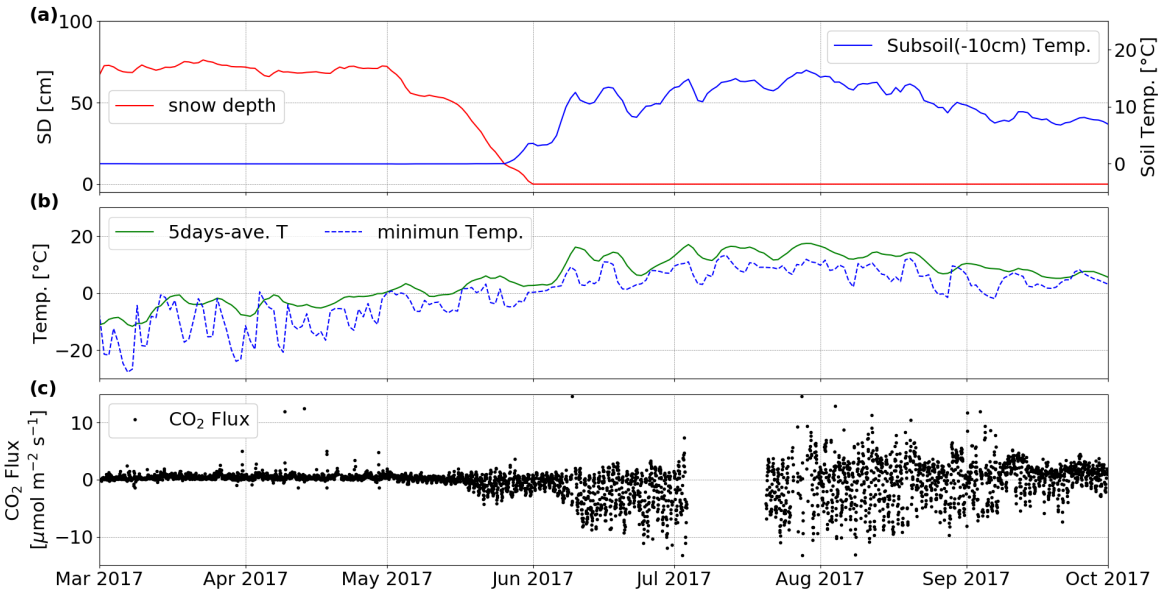

Figure 4.14: Time series of (a): snow depth and subsoil temperature, (b): 5-day average and daily minimum air temperature and (c): CO_2 flux observed at FMI, Sodankylä.

The X_{Gas} fluxes from the tower measurements show a similar annual variability for trace gases as compared to the EM27/SUN retrievals (Figure 4.15). The tower observed higher XCO_2 and XCO than the EM27/SUN spectrometer in spring and summer, while a similar amount of gases were observed in autumn for both instruments. However, XCH_4 presents a different situation that a steady offset existed between the tower observation and the FTIR measurements during the whole year. These two different situations are mainly because the tropospheric vertical profiles of CO_2 and CO present distinct shapes in early year and late year, whereas CH_4 has a similar shape during the whole campaign in the troposphere. The difference between the FTIR spectrometer and the tower observations is mainly because the spectrometer measures the total columns of trace gases in the atmosphere while the tower mast only observes the concentration near the ground level, and therefore higher values are expected in the tower observations. In addition, higher variability is found in tower observations, especially in late summer and autumn. This is because the in-situ observations are more sensitive to the local sinks and sources, while the total columns of trace gases are influenced by the atmospheric circulation which suppresses the variability.

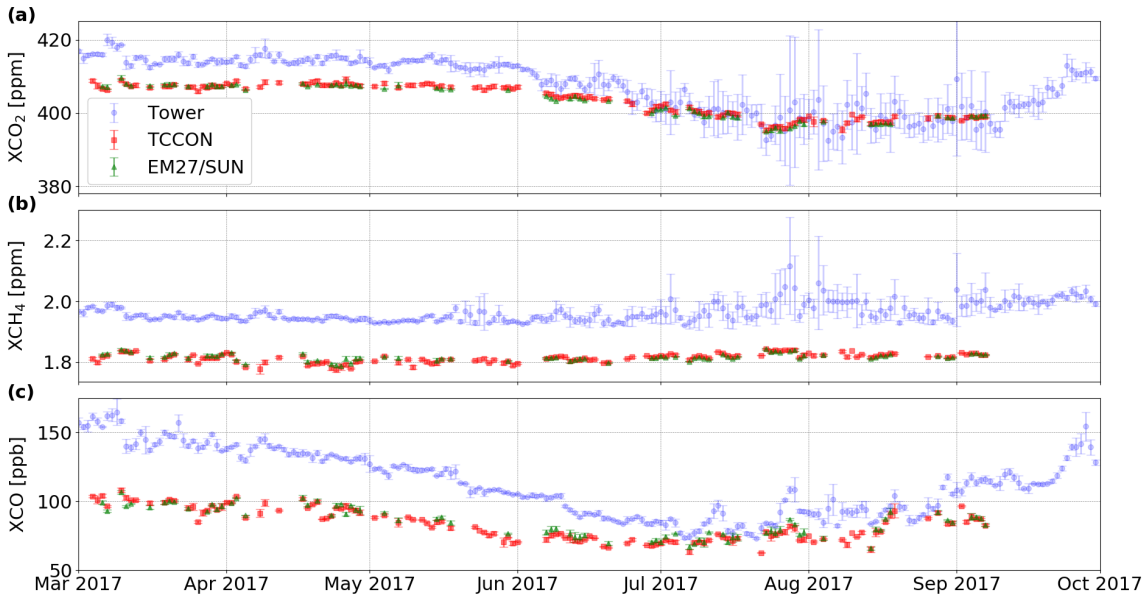

Figure 4.15: Time series of (a): XCO_2, (b): XCH_4 and (c): XCO from the in-situ tower, the TCCON 125HR and the EM27/SUN spectrometers. Error bars are obtained from the standard deviation of 5-minute average.

4.2.2 EM27/SUN and TCCON retrievals

XCO_2

Figure 4.16 shows the time series of XCO_2 from the EM27/SUN instrument and the TCCON 125HR instrument as a reference (upper panel). The difference between the two datasets (ΔXCO_2) is presented in the lower panel. 5-minute mean value is used here to reduce the random error. The measurement started in early March and lasted until September, 2017. Over the whole time series the atmospheric XCO_2 showed a strong seasonal variability. XCO_2 stayed around 405–410 ppm in the first few months and started to decrease at the end of May and finally dropped to ∼394 ppm at the end of August. Later, the CO_2 concentration in the atmosphere increased gradually. Approximately 12 ppm change of XCO_2 has been observed between early spring and summer. This decrease is mainly due to the photosynthesis and respiration of plants. Note that the data from September to November was missing because of bad weather and high solar zenith angle, as a data quality filter of SZA $< 80°$ is applied here.

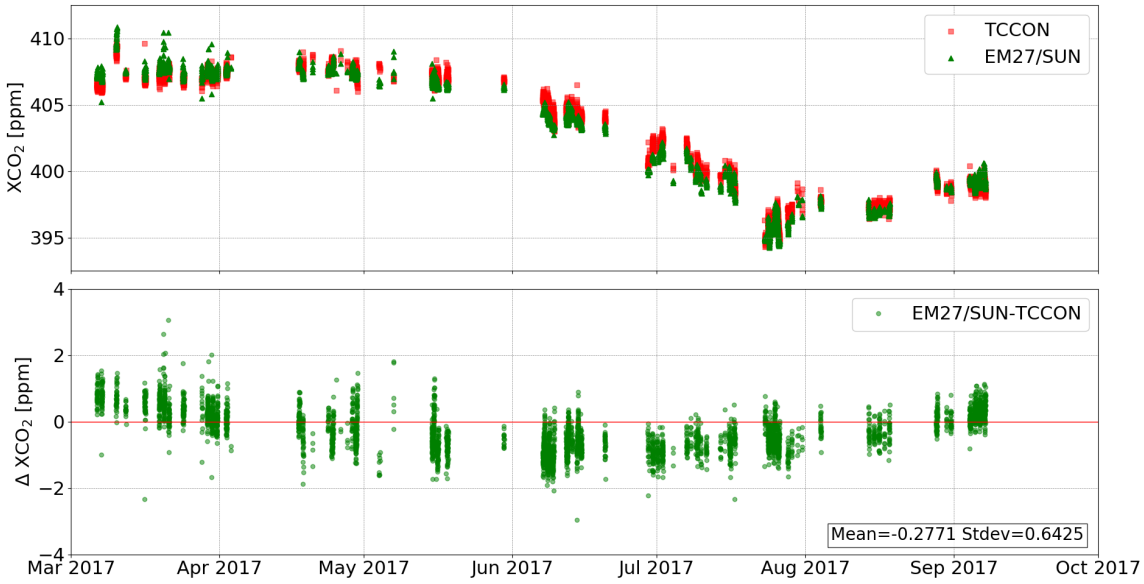

Figure 4.16: Time series of XCO_2 from the TCCON 125HR and the EM27/SUN spectrometers (upper panel) and the bias between them (lower panel).

Although its spectral resolution is only 0.5 cm^{-1}, the EM27/SUN instrument shows a good agreement with the high-resolution spectrometer 125HR used in TCCON. The difference between them is about (0.28 ± 0.64) ppm throughout the campaign. The slight U shape of the yearly difference indicates a seasonal variation mainly due to the effects of different airmass dependencies. The EM27/SUN spectrometer measured approximately 1 ppm higher XCO_2 than the TCCON 125HR instrument did in the beginning of March, then the bias decreased gradually. The results from the EM27/SUN instrument showed better agreement with the

reference TCCON instrument from April to May when the bias was around zero. The bias from June to August was mostly negative, reaching nearly -2 ppm. ΔXCO_2 increased back to positive values around September. Even though there were no data after the middle of September, it is likely that ΔXCO_2 would continue increasing because of the diminishing effect of photosynthesis.

Figure 4.17 upper panel shows the correlation of uncorrected and corrected EM27/SUN results (airmass independent (AI) and airmass dependent (AD) correction) with respect to the TCCON 125HR results. Different colors denote the results from measurements derived in different months. Both sets of measurements from the EM27/SUN spectrometer show very good agreement with the TCCON reference retrievals. The implementation of AI and AD correction helps to reduce the bias. However, when considering the SZA effect, an obvious positive correlation is found in the difference between the corrected EM27/SUN and the TCCON results (see Figure 4.17 lower panel). The SZA correction for XCO_2 based on previous work [Klappenbach et al., 2015] seems to slightly overestimate the effects. This is because a different a-priori profile modeled from the CAMS[1] was used in the ship campaign (34 °S – 54 °N), while the a-priori profiles used in the TCCON network are generated with the GGG package. Systematic differences caused by these two different models might be the main reason to cause this non-perfect correction.

[1]Copernicus Atmosphere Monitoring Service data assimilation and forecasting system

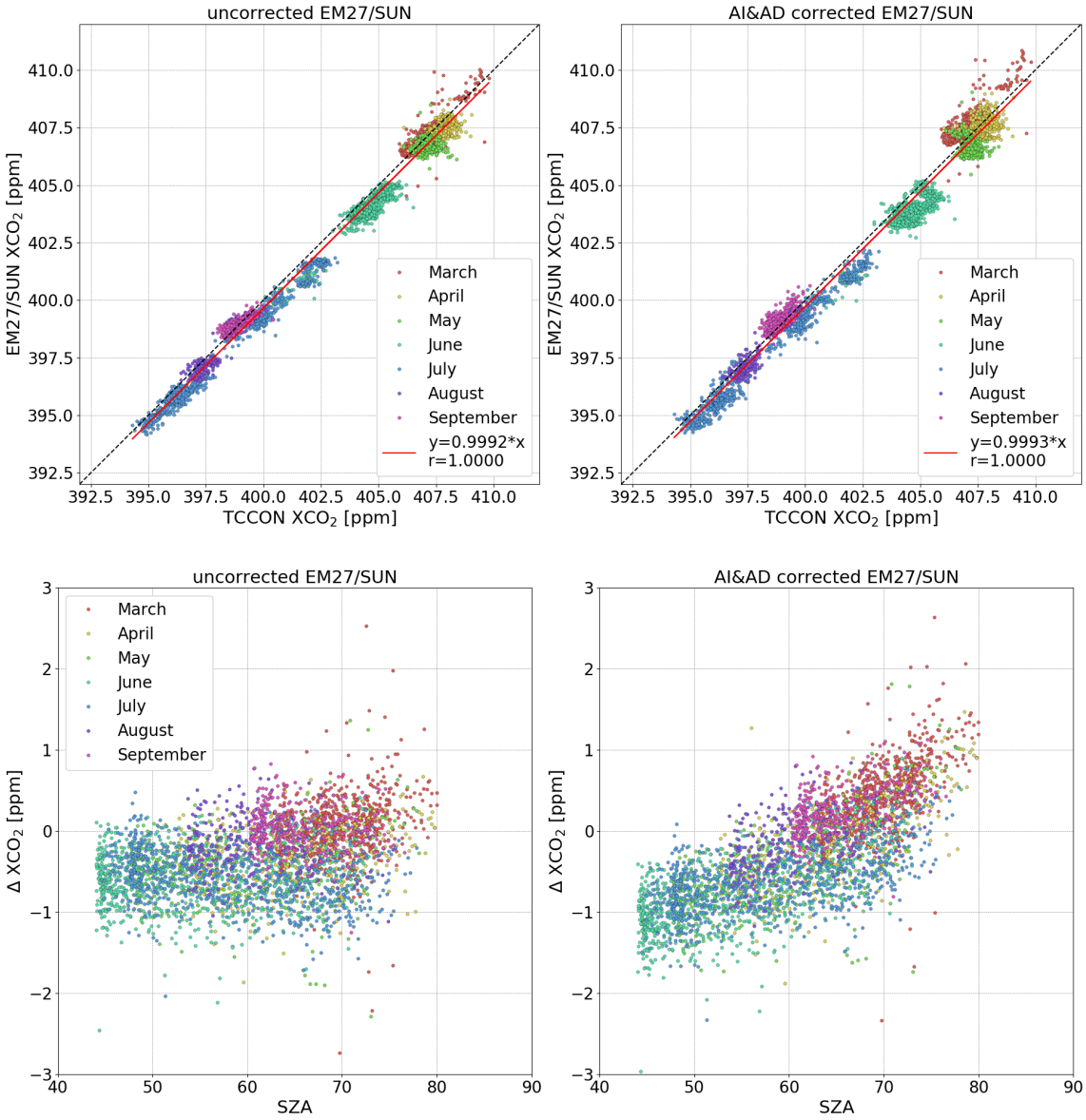

Figure 4.17: Correlation of XCO_2 between the EM27/SUN and the reference TCCON spectrometers (upper panel) and the bias as a function of SZA (lower panel). In each panel the EM27/SUN retrievals without correction are shown on the left, and retrievals with the AI and AD correction are shown on the right.

XCH_4

The time series of XCH_4 from the EM27/SUN and the reference TCCON observations are displayed in Figure 4.18 upper panel. The bias between the two datasets is presented in lower panel and shows a seasonal variability. The EM27/SUN instrument measured around 10 ppb higher XCH_4 than the TCCON instrument before June. Later, both instruments observed similar amounts of XCH_4. This seasonal variability is also seen in Figure 4.19, top right. Measurements in different months show obviously separated bands of data points. The large difference in March, April and May is mainly due to the improper modeled a-priori profiles in spring which has been discussed in subsection 4.1.2. To investigate the effect of the AI and AD corrections, the correlations of the two different EM27/SUN retrievals with respect to the TCCON results are shown in Figure 4.19 upper panel. The biases as a function of SZA are shown in the lower panel. The application of the AI and AD corrections decreased the biases by approximately 20 ppb. However, similar to XCO_2, the empirical AD correction developed by Klappenbach et al. [2015] seems to overestimate the effects, resulting in slightly higher sensitivity to the airmass.

Figure 4.18: Time series of XCH_4 from the TCCON 125HR and the EM27/SUN instruments (upper panel) and the bias between them (lower panel).

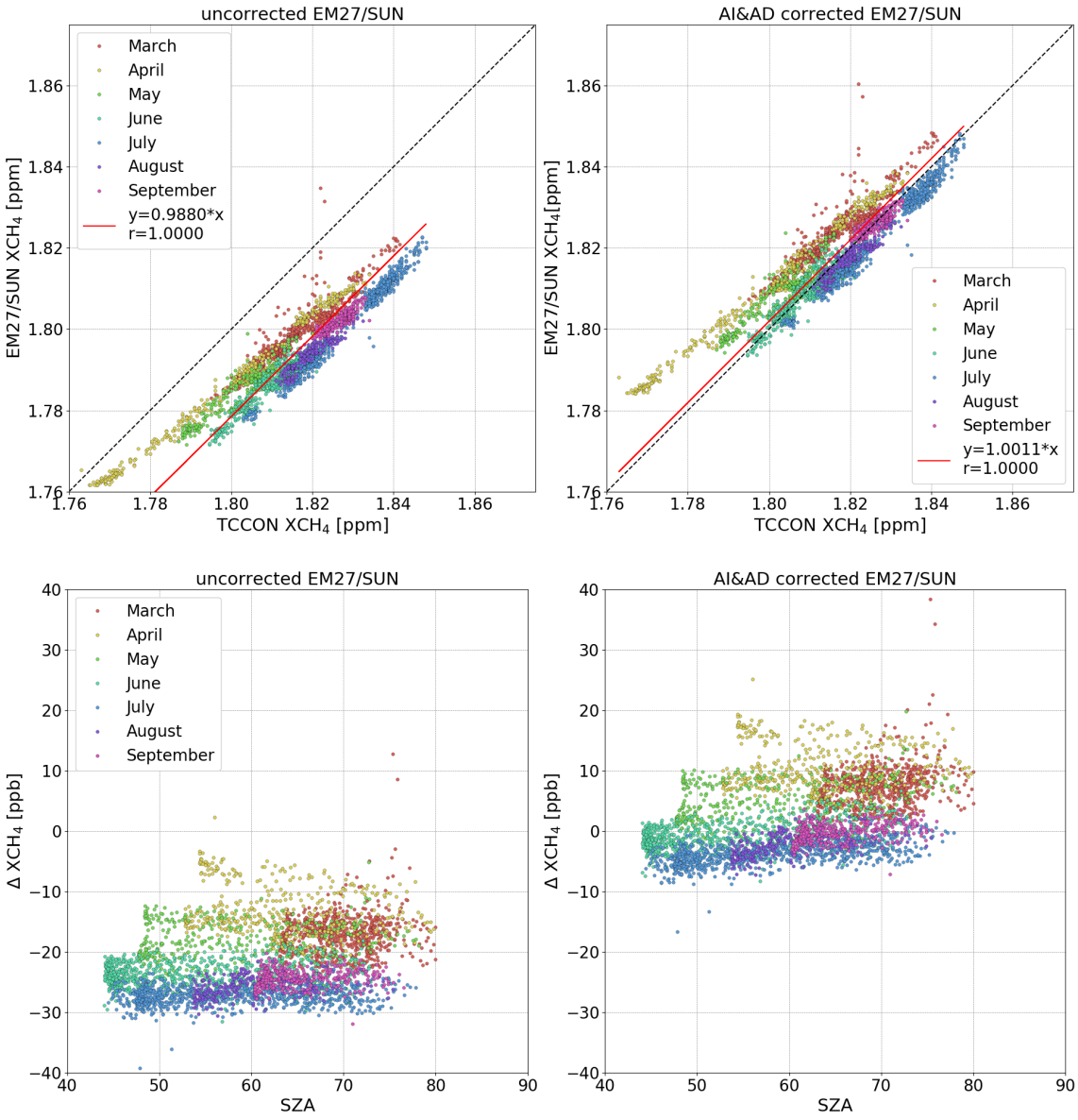

Figure 4.19: Correlation of XCH_4 between the EM27/SUN and the reference TCCON spectrometers (upper panel) and the bias as a function of SZA (lower panel). In each panel EM27/SUN retrievals without correction are shown on the left and retrievals with the AI and AD correction are shown on the right.

XCO

The time series of XCO recorded with the EM27/SUN and the TCCON instruments are presented in Figure 4.20. Throughout the year the bias between the low-resolution and the high-resolution retrievals ranged from −6 ppb to 8 ppb, showing roughly a concave parabolic shape. The yearly averaged bias is approximately 1.72 ppb with the lowest value in early March and the highest value in early June. A higher diurnal variability exists in XCO than in the other two species. The AI correction improves the agreement between the EM27/SUN and the TCCON retrievals (see Figure 4.21 upper panel). The significant SZA dependency can be seen in Figure 4.21 lower panel. The bias decreased with increasing SZA. This apparently negative correlation is mainly due to the lack of airmass dependent correction for XCO. Here, only an airmass independent calibration factor was applied to XCO without airmass dependent correction because it is not clear whether the large airmass dependent correction applied by TCCON is realistic [Kiel et al., 2016]. Therefore, further studies on the SZA dependency will be necessary to optimize the XCO results.

Figure 4.20: Time series of XCO from the TCCON 125HR and the EM27/SUN instruments (upper panel) and the bias between them (lower panel).

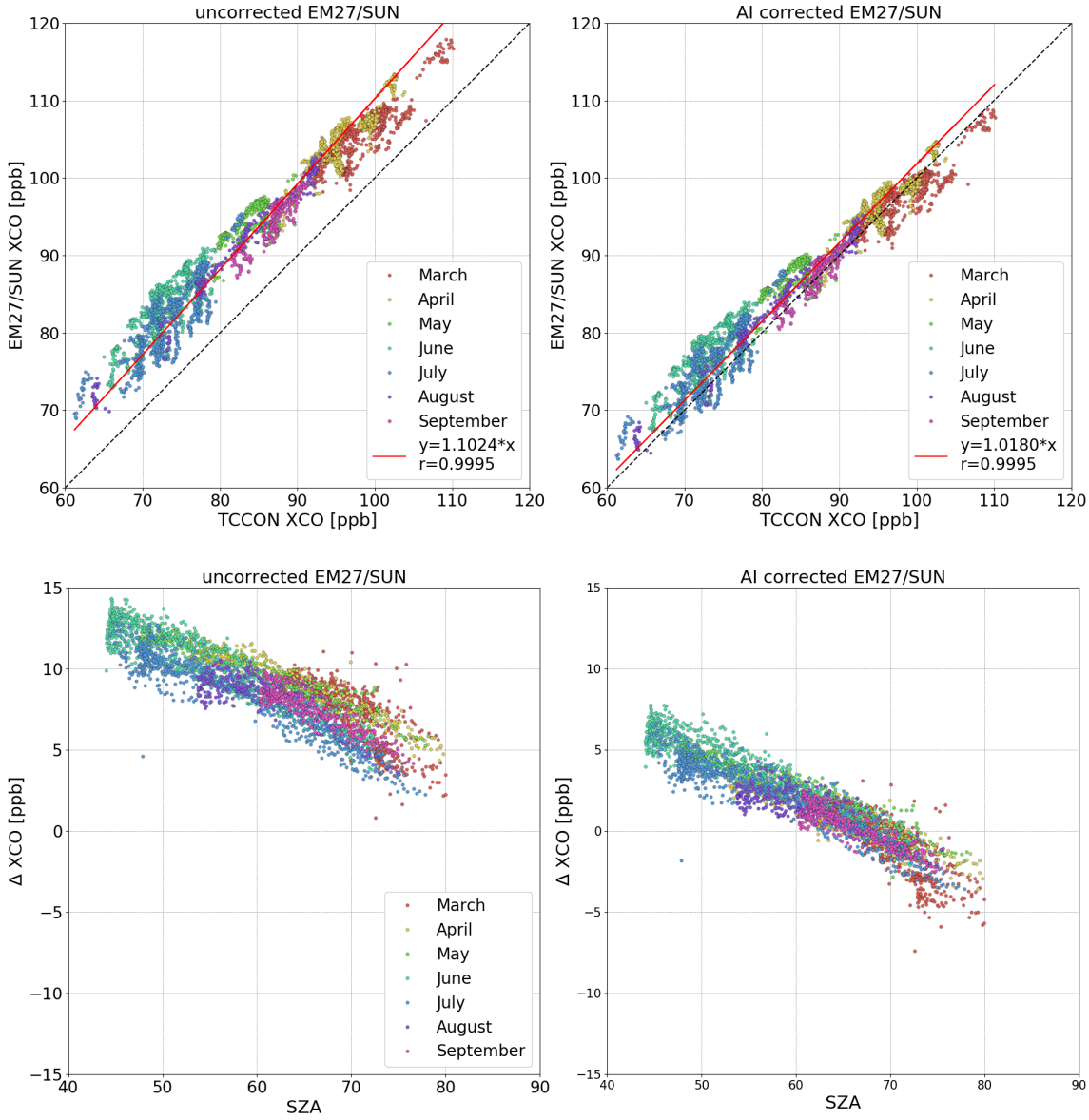

Figure 4.21: Correlation of XCO between the EM27/SUN and the reference TCCON spectrometers (upper panel) and the bias as a function of SZA (lower panel). In each panel EM27/SUN retrievals without correction are shown on the left and retrievals with the AI correction are shown on the right.

XAir

XAir (column-averaged amount of dry air) is a sensitive test of the integrity of measurements. It is used in the TCCON network to examine biases among different stations, and is derived from the ground pressure, the O_2 total column and the water vapor total column. It is also considered as a characteristic for diagnosing the systematic errors, such as erroneous ground pressure, wrong saving time for each spectrum and misalignment [Wunch et al., 2015]. XAir is defined as:

$$\mathrm{XAir} = \frac{\mathrm{Column_{air}}}{\mathrm{Column_{O_2}}} \cdot 0.2095 - \mathrm{X_{H_2O}} \cdot \frac{\mathrm{m_{H_2O}}}{\mathrm{m_{dryair}}} \tag{4.1}$$

here, $\mathrm{m_{H_2O}}$ and $\mathrm{m_{dryair}}$ are the mean molecular masses of water vapor and dry air. $\mathrm{Column_{O_2}}$ and $\mathrm{Column_{H_2O}}$ are the measured total columns of O_2 and H_2O. The total column of air can be assumed as:

$$\mathrm{Column_{air}} = \frac{\mathrm{P_{gr}}}{\mathrm{g_{air,lat}} \cdot \mathrm{m_{dryair}}/\mathrm{Na}} \tag{4.2}$$

where $\mathrm{P_{gr}}$ and Na denotes the in-situ measured ground pressure and Avogadro's constant. $\mathrm{g_{air,lat}}$ is the gravitational acceleration depending on latitude:

$$\mathrm{g_{air,lat}} = 9.780327 \cdot [1 + 5.5024 \cdot 10^{-3} \cdot \sin^2(\mathrm{lat}) - 5.8 \cdot 10^{-6} \cdot \sin^2(2 \cdot \mathrm{lat})] \tag{4.3}$$

Theoretically, the XAir should be a constant value of 1.0. However, the observed XAir values from the TCCON measurements are about 0.98 due to an approximate 2 % bias of spectroscopic line intensities of O_2 column [Wunch et al., 2015]. In addition, a diurnal variation exists because of the spurious airmass dependency. Wunch et al. [2015] also indicated that the maximal XAir error amounts to less than 0.5 % when the solar zenith angles are smaller than $\sim 78°$.

XAir from the two instruments' measurements is depicted in Figure 4.22. The upper panel shows the time series of XAir for the TCCON and the EM27/SUN instruments, and the lower panel shows the bias between the two datasets. The absolute values of XAir differ in the two instruments, with 0.9783 ± 0.0018 for the TCCON 125HR instrument and 0.9680 ± 0.0019 for the EM27/SUN instrument over the whole measurement record. This approximately 1 % bias and similar variability show the precision and stability of the EM27/SUN instrument. In spring and early summer (March to May), the XAir of the EM27/SUN instrument was around 0.9695 and the TCCON 125HR instrument was around 0.9768, leading to approximately 0.73 % difference. Later, the EM27/SUN XAir decreased to approximately 0.9670 after June while the TCCON XAir increased to about 0.9794, resulting in nearly 1.24 % bias between these two instruments. When plotting the XAir with respect to the solar zenith angle, the EM27/SUN instrument shows a weaker airmass dependency compared to the TCCON instrument (Figure 4.23). A small negative slope can be found in the TCCON retrievals, especially when SZA is larger than 60°. However, the XAir from the EM27/SUN measurements shows a pronounced spread with increasing SZA, which is not evident in the

TCCON instrument. The differing airmass dependent sensitivity is because the solar tracker used in TCCON has a higher accuracy than the one used in EM27/SUN, especially at high SZA. In addition, this is probably due to the different resolution of the spectrometers and the different retrieval algorithms—PROFFIT algorithm for the EM27/SUN measurements and the GFIT algorithm for the TCCON 125HR measurements. A known discrepancy in the determination of the EM27/SUN XAir exists due to a 20 % spectroscopic offset of retrieved H_2O in the near-infrared range [Casanova et al., 2006], which was not corrected for the calculation of XAir from the EM27/SUN observations.

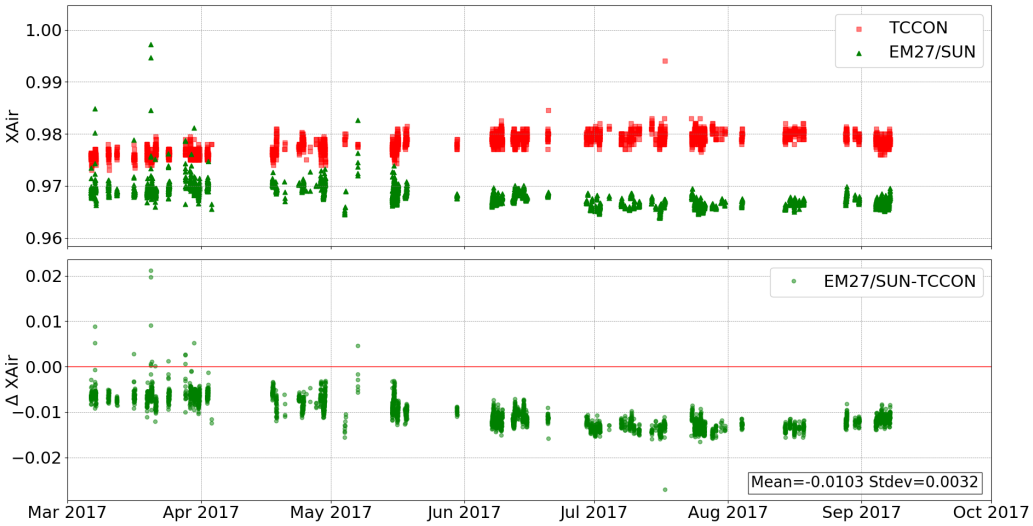

Figure 4.22: Time series of XAir from the TCCON 125HR and the EM27/SUN measurements (upper panel), and the bias between them (lower panel).

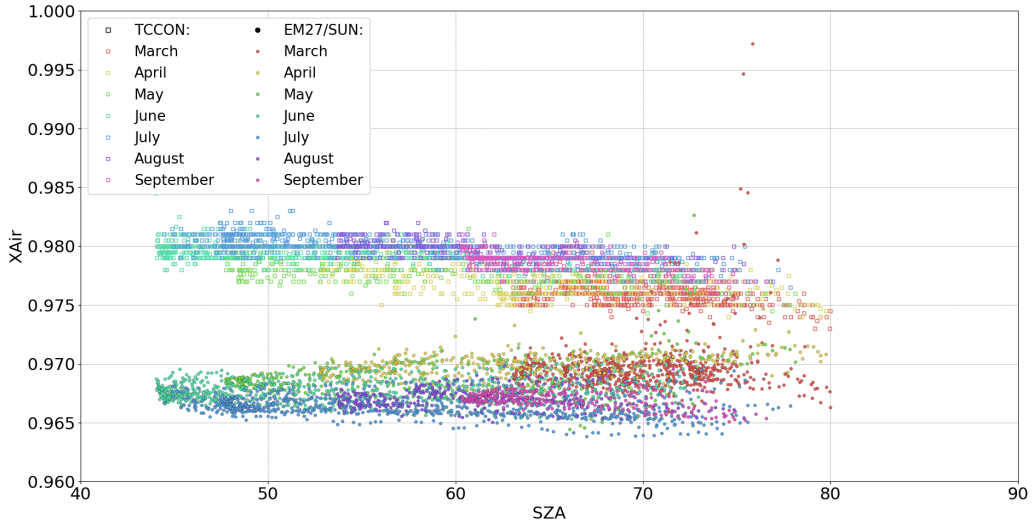

Figure 4.23: XAir from the TCCON 215HR and the EM27/SUN measurements with respect to SZA. Different colors denote different measurements recorded in different months.

4.2.3 EM27/SUN and 125HR LR retrievals

To better understand the precision and stability of the EM27/SUN spectrometer, an additional set of measurements with the 125HR spectrometer is discussed in this section, called 125HR LR dataset. Same to the setting used in the EM27/SUN instrument, the 125HR instrument uses the low-resolution of $0.5\,\mathrm{cm}^{-1}$ (double sided forward-and-backward scans) to record raw interferograms. The ILS of the 125HR is assumed to the same values as measured for the 125HR spectrometer in Karlsruhe, because measured ILS parameters from the Sodankylä instrument are not available. Additionally, the same analysis procedure and post processing are applied to the 125HR LR measurements. According to this identical instrumental settings and processing procedure, the differences between the EM27/SUN and the 125HR LR dataset are only ascribed to their own instrumental characteristics, rather than because of the different resolution, retrieval software, a-priori profiles, and airmass dependency correction.

$\mathbf{XCO_2}$

In Figure 4.24 time series of XCO_2 derived from the EM27/SUN and 125HR LR measurements, and the difference between them are presented, as well as their correlation. Both datasets show similar tendency throughout the campaign and a very good agreement between them. The XCO_2 derived from the EM27/SUN measurements is approximately 0.77 ppm ($\sim$0.19 %) higher than the 125HR LR retrievals, which is about -0.28 ppm when compared with the reference TCCON retrievals. This slightly positive offset was also observed in the long-term measurements in Karlsruhe [Frey et al., 2018]. The annual standard deviation of the ΔXCO_2 (EM27/SUN – 125HR LR) is approximately 0.36 ppm, showing less seasonal variability than the ΔXCO_2 between the EM27/SUN and the TCCON retrievals, which is 0.64 ppm.

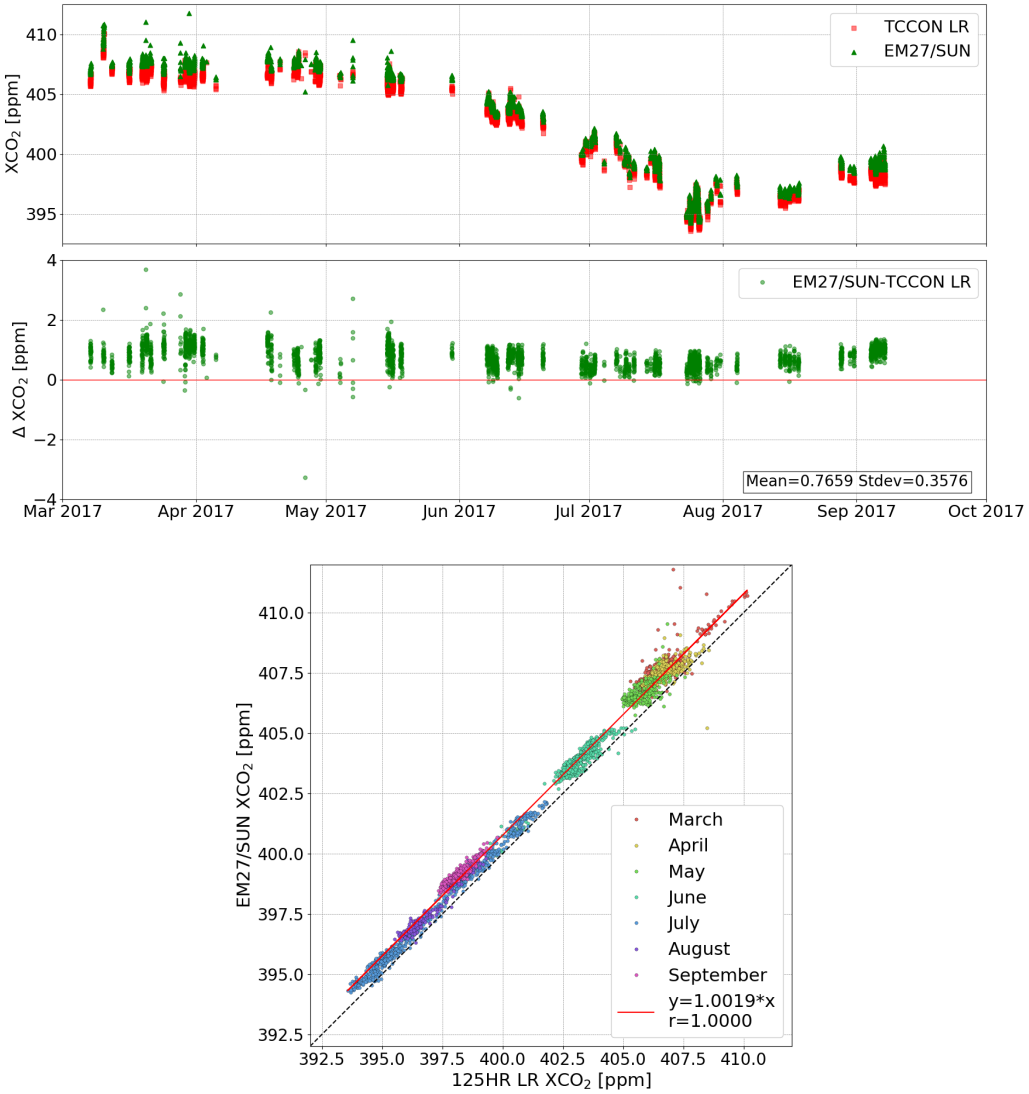

Figure 4.24: The upper two panels show the time series of the EM27/SUN and the 125HR LR XCO_2 measurements, and the bias between these two datasets. The lower panel shows the correlation between the two datasets and different colors denote different measurements recorded in different months.

XCH_4

Figure 4.25 shows the time series of XCH_4 derived from the two sets of measurements and the correlation plot. A much better agreement is observed than the one between the EM27/SUN and the TCCON retrievals. The bias between the EM27/SUN and the 125HR LR datasets is approximately 6.53 ppb, resulting in a ∼0.36 % higher XCH_4. A seasonal cycle is found with a variability of ∼2.84 ppb, which is nearly half of the value when comparing between the EM27/SUN and the TCCON retrievals (5.76 ppb). The impact of the polar vortex on the retrievals is less obvious here, while it is significant in the correlation plot between the EM27/SUN and the TCCON retrievals in April. This is because both datasets are retrieved from the instruments with same resolutions, showing similar sensitivity to the a-priori profiles.

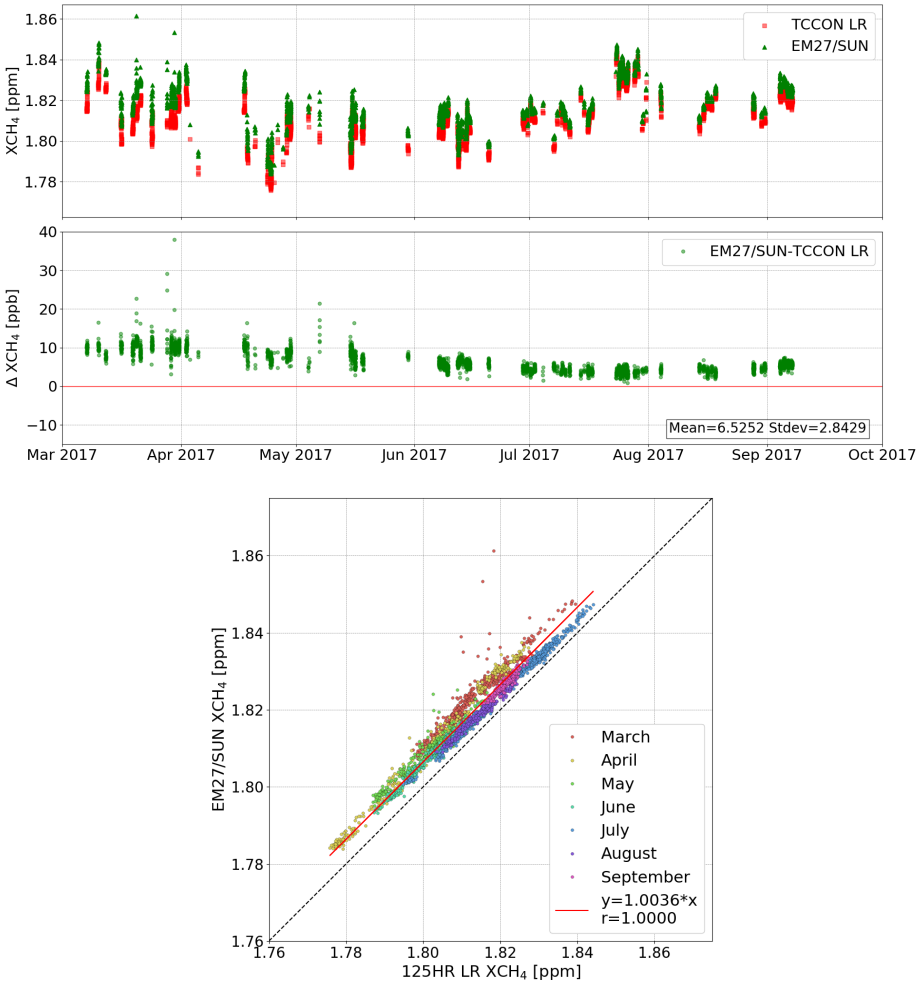

Figure 4.25: The upper two panels show the time series of XCH_4 derived from the EM27/SUN and the 125HR LR measurements, and the bias between these two datasets. The lower panel shows the correlation between the two datasets and different colors denote different measurements recorded in different months.

XCO

The EM27/SUN XCO retrievals show an overall higher value with respect to the 125HR LR dataset (see Figure 4.26). The bias ranges from 2 to 9 ppb with an annual average of ~4.62 ppb, showing a similar concave parabolic shape to the offset between the EM27/SUN and the TCCON retrievals. The seasonal variability is reduced approximately by half, from approximately 2.48 ppb (EM27/SUN–TCCON) to 1.31 ppb (EM27/SUN–125HR LR), resulting in a slightly better correlation here.

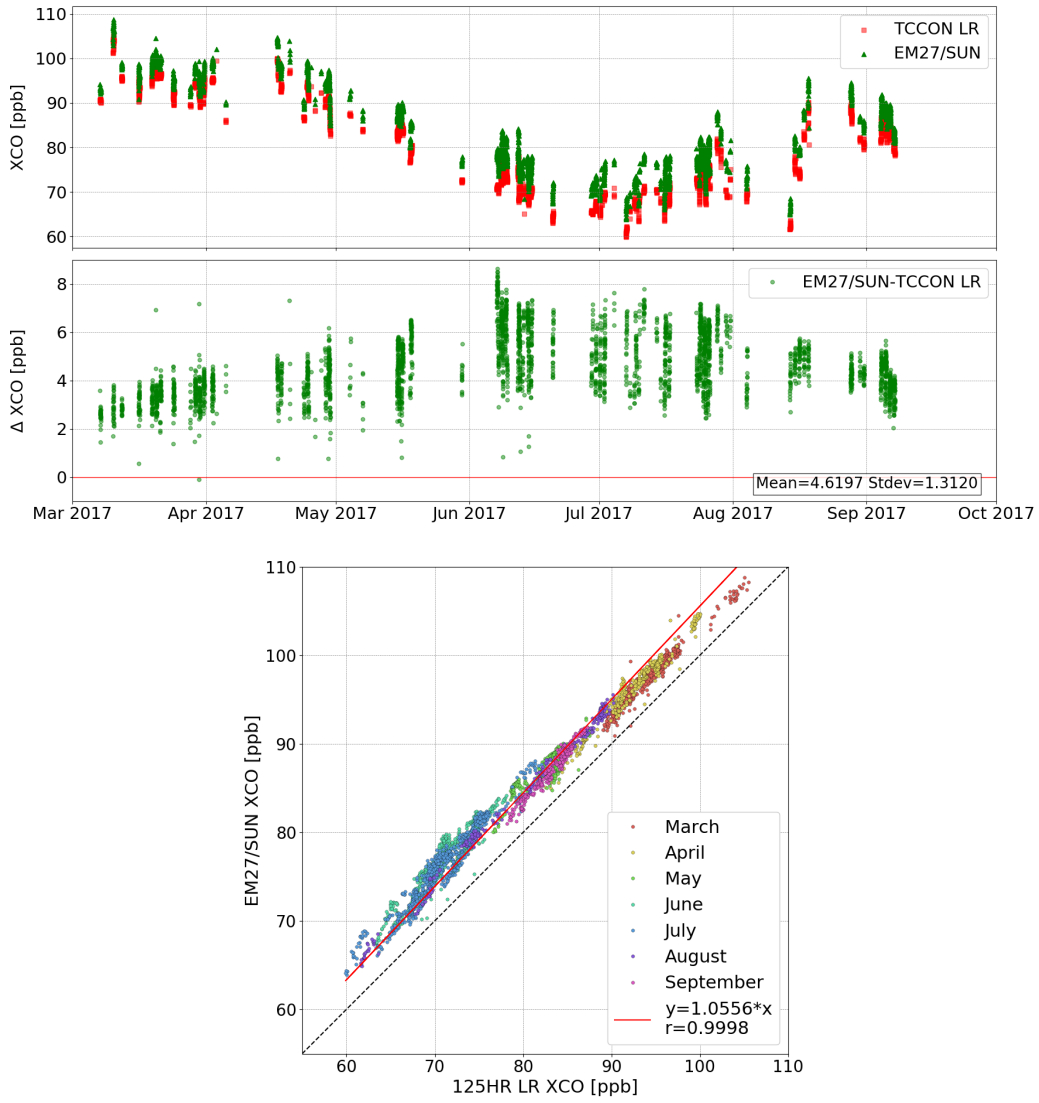

Figure 4.26: The upper two panels show the time series of XCO derived from the EM27/SUN and the 125HR LR measurements, and the bias between these two datasets. The lower panel shows the correlation between the two datasets and different colors denote different measurements recorded in different months.

4.2.4 Intercomparison of different portable low-resolution spectrometers

In addition to the EM27/SUN FTIR spectrometer, there are the other three portal low-resolution instruments participating in the FRM4GHG campaign—both Vertex70 and IRCube instruments are FTIR spectrometers, manufactured by Bruker, while the Laser Heterodyne Radiometer (LHR) is a homemade instrument. The Vertex70 instrument uses a resolution of $0.4\,\mathrm{cm}^{-1}$ and is operated by the University of Bremen and BIRA (Belgian Institute for Space Aeronomy). The University of Wollongong is responsible for the IRCube instrument with a same resolution of $0.5\,\mathrm{cm}^{-1}$ as used in the EM27/SUN instrument. LHR instrument is developed by the Laser Spectroscopy Group of the Space Science and Technology Department of the Rutherford Appleton Laboratory [Hoffmann et al., 2016; Tsai et al., 2012; Weidmann et al., 2007]. Its spectral resolution is determined by two different electronic filters, with $0.002\,\mathrm{cm}^{-1}$ and $0.02\,\mathrm{cm}^{-1}$.

XCO_2 measured from all the four portable low-resolution instruments with respect to the reference TCCON data is presented in Figure 4.27. A SZA filter quality (SZA $< 75°$) is applied to all the datasets. Two different correlations before and after July are presented in the Vertex70 measurements with respect to the TCCON measurements as a result of instrument modification. After this modification, the dataset shows an obviously better agreement with less bias and scatter. Higher measurement biases are observed in the correlation between the IRCube and TCCON data than in the EM27/SUN and Vertex70 measurements. A step change also occurs in March mainly due to the replacement of the fiber-optic cable which changes the alignment of the instrument. The LHR instrument is in its developmental phase and its measurements show larger biases than the other low-resolution instruments.

Compared with the other three datasets, EM27/SUN data shows the best agreement with respect to the reference TCCON measurements in the whole set of measurements in 2017. There are no significant biases or step change observed in the EM27/SUN measurements, showing impressively stable and consistent. No alignment was performed for the EM27/SUN instrument during the whole campaign. In addition, the EM27/SUN instrument also shows a robust characteristic as it was setup at the ambient temperature down to $-15\,°\mathrm{C}$, while the other low-resolution instruments were operated in the climate controlled campaign container.

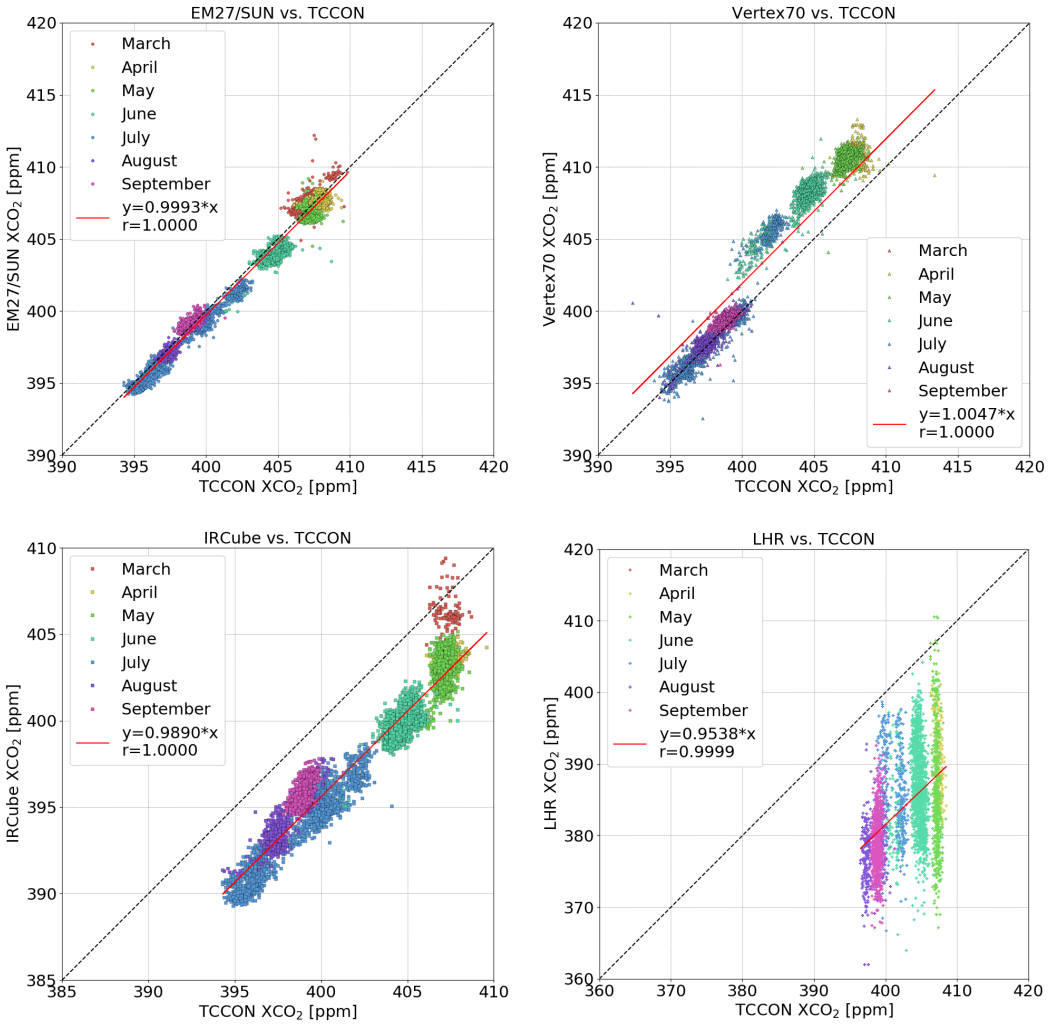

Figure 4.27: Correlations of XCO_2 from portal low-resolution instruments of EM27/SUN, Vertex70, IRCube and LHR with respect to the reference TCCON data. Different colors denote the measurements recorded in different months.

4.3 Gradient observations between Kiruna and Sodankylä

For enabling a study of GHG sources and sinks in the Arctic, a second calibrated EM27/SUN instrument was operated at IRF, Kiruna, besides the aforementioned EM27/SUN instrument at FMI, Sodankylä. The IRF is situated around 270 km to the west of Sodankylä (see Figure 4.28).

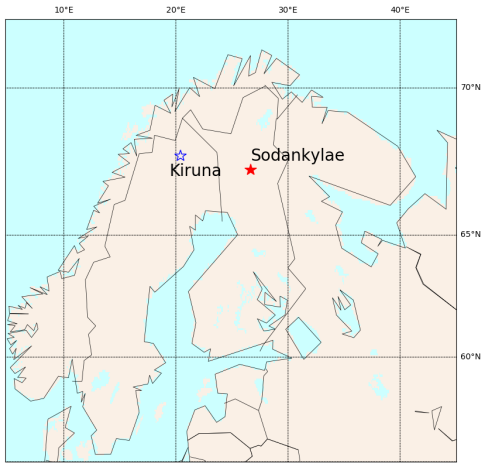

Figure 4.28: Map showing the measurement stations in Kiruna, Sweden and Sodankylä, Finland.

Similar in the forest coverage and climate, the trace gases measured at these two stations show very similar seasonal variability (see Figure 4.29). Measurements at IRF from the middle of June until the end of August, 2017 were not available due to a failure of the sun tracker on the roof.

Figure 4.30 shows one measurement day of the observations at both sites on March 16, 2017. Only coincident measurements within one minute from both instruments are shown. Obvious differences occurred at both sites after 10:30 UTC, when a nearly 0.86 ppm decrease of XCO_2 and a 11 ppb decrease of XCH_4 were observed in Sodankylä. To further study the sink/source of the target gases, the Hybrid Single-Particle Lagrangian Integrated Trajectory (HYSPLIT) model [Draxler and Hess, 1998] was used to compute the backward trajectories of air parcels between Kiruna and Sodankylä on March 16, 2017. The 7 h atmospheric trajectories were calculated for an arriving time of 12:00 UTC on this measurement day (Figure 4.30, lower panel). A very good match is found between these two stations at the lower layer. The two sites were connected roughly by a trajectory with 6 h transport time. Based on the emission formula (4.4) [Chen et al., 2016], local sources contributed on the order of -8.2×10^{18} molec. $m^{-2}\,s^{-1}$ for CO_2 and -1.0×10^{17} molec. $m^{-2}\,s^{-1}$ for CH_4 on this day. The negative values denote that the area between Kiruna and Sodankylä was likely to

be a sink for both CO_2 and CH_4.

$$X_{Gas,downwind} = t_{travel} \cdot \text{Emission} + X_{Gas,upwind} \tag{4.4}$$

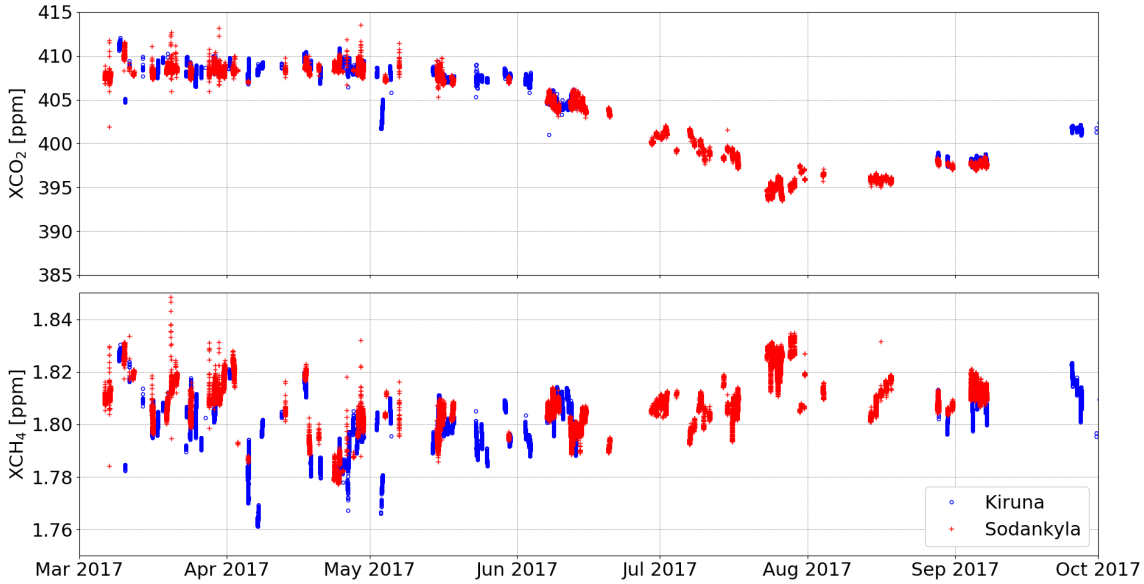

Figure 4.29: Time series of XCO_2 and XCH_4 recorded with the EM27/SUN instruments in Kiruna and Sodankylä.

Figure 4.31 shows another measurement day in March, when no obvious enhancement or reduction was observed for XCO_2. Nearly 5–10 ppb higher amounts of XCH_4 were observed in Sodankylä, which was roughly in the downwind direction. However, no connecting air parcel trajectories passed through the two sites during the measuring period due to the imperfect matching direction.

In general, it turns out to be quite difficult to deduce the strengths of weak distributed sources or sinks from paired FTS measurements. The weakness of the source requires a large distance between the spectrometers to create a measurable signal, but this choice in turn introduces problems due to dynamic effects and spoils the simple concept of a single connecting trajectory. Further modeling work will be necessary to support detection of emission signals.

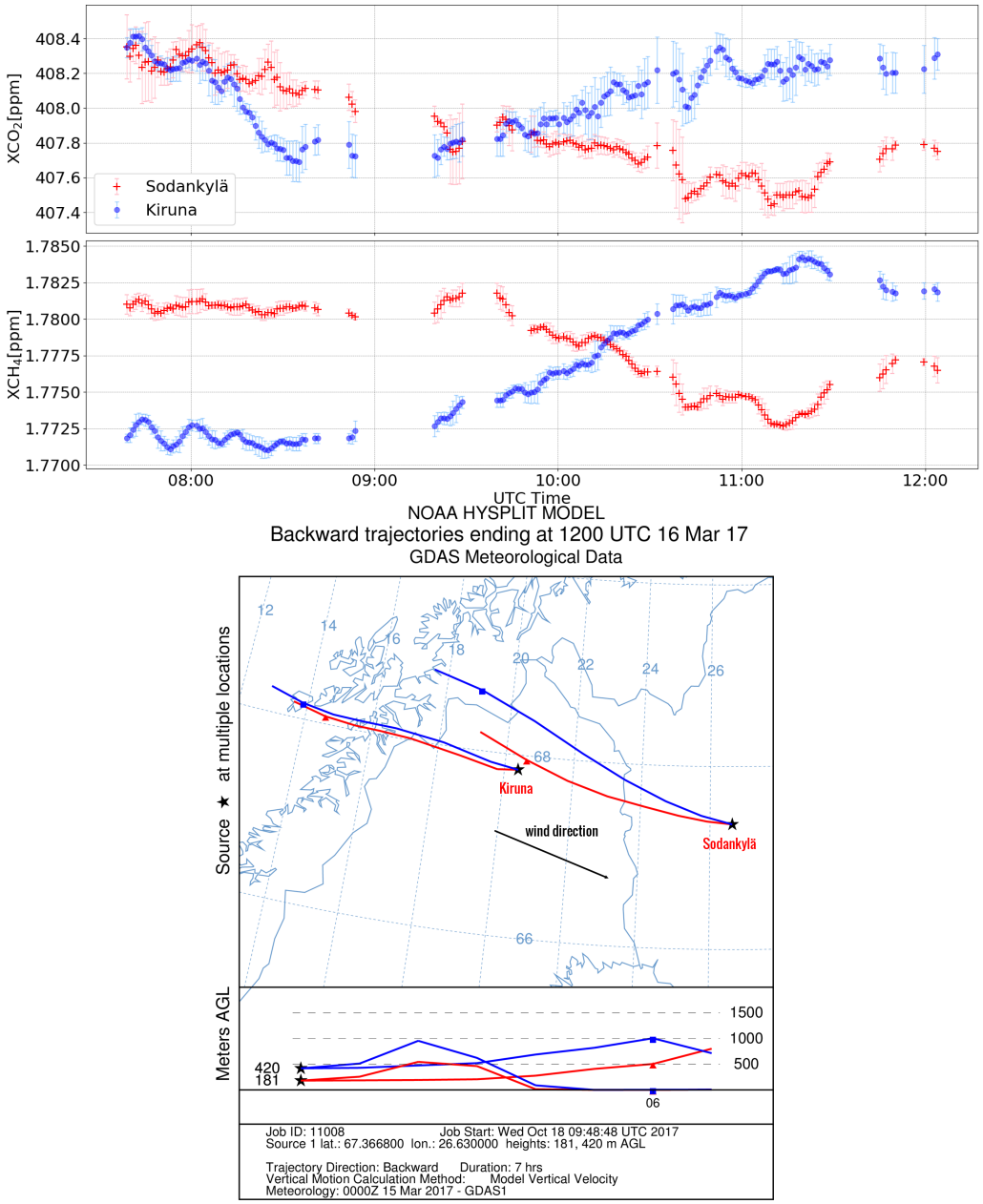

Figure 4.30: Time series of XCO_2 and XCH_4 measured in Kiruna and Sodankylä on March 16, 2017 (upper two panels). The error bars denote the standard deviation of the 5-minute moving average at each sites. A 7 h backward trajectory ended at both sites at 12:00 UTC time is presented in the lower panel. Nearly 6 h transported air parcel well connected the two stations at the lower layer. The wind direction was roughly west northwest, resulting in Sodankylä as a downwind station.

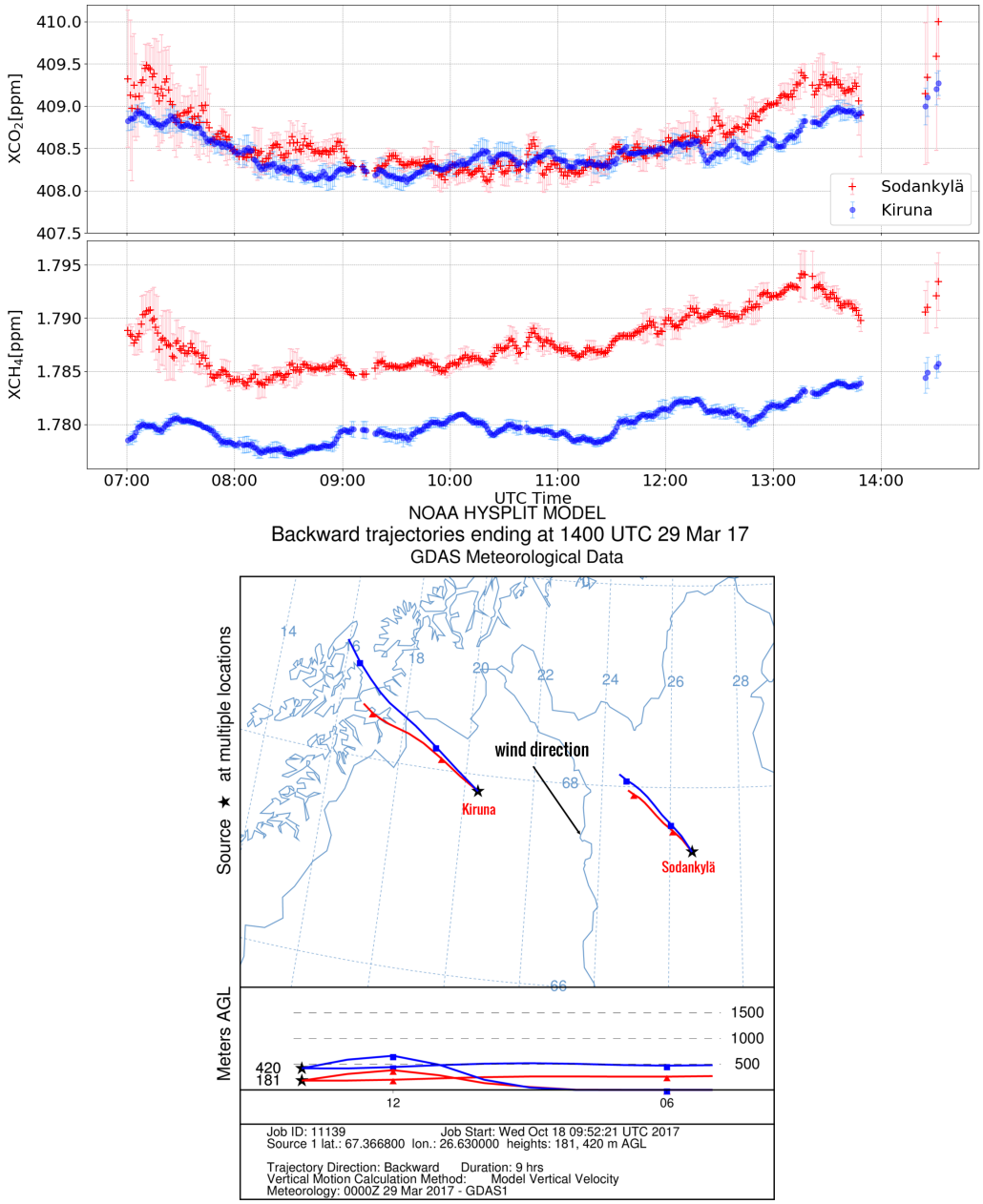

Figure 4.31: Time series of XCO_2 and XCH_4 measured in Kiruna and Sodankylä on March 29, 2017 (upper two panles). The error bars denote the standard deviation of the 5-minute moving average at each sites. A 9 h backward trajectory ended at 14:00 UTC time is presented in the right panel. Wind direction was roughly northwest, resulting no direct connection between the two stations (lower panel).

4.4 Conclusions

In this chapter, an EM27/SUN instrument was used to study the annual variability of the atmospheric trace gases (XCO_2, XCH_4 and XCO) in the Arctic circle. The investigated low-resolution EM27/SUN spectrometer shows the characteristics of outstanding accuracy, stabilization and reliability.

The optimization approaches of using the ILS parameters and the a-priori profiles were applied to the whole EM27/SUN dataset in sequence. The use of the measured ILS parameters reduces the annual average bias between the EM27/SUN and the reference TCCON retrievals by approximately 1.35 ppm in XCO_2 and 0.37 ppb in XCO, respectively, while it increased the bias by 3.14 ppb in XCH_4. The bias was slightly increased by 0.06 ppm in XCO_2 and 1.79 ppb in XCO when the daily-variable MAP profiles were applied in the retrievals instead of the constant WACCM-derived profiles. For XCH_4 a significant better agreement was seen with a decrease of 9.72 ppb.

The optimized EM27/SUN retrievals were first analyzed with respect to the in-situ meteorological observations. The column-average DMFs show a good agreement with the in-situ gas fluxes. The snow depth, the low subsoil temperature and the air temperature display impacts on the annual cycle of the atmospheric XCO_2 in the early period of the campaign. This is because the snow cover and the near zero soil temperature hindered the photosynthesis activity of plants. The stronger solar intensity, longer solar light duration and higher air temperature in summer increase the photosynthesis activity. This impact can be seen in terms of the decreasing XCO_2 concentration.

Additionally, the EM27/SUN data were compared to the reference TCCON data. All target gases (XCO_2, XCH_4 and XCO) show a very good agreement with yearly average biases of approximately (0.28 ± 0.64) ppm in XCO_2, (1.99 ± 5.76) ppb in XCH_4 and (1.72 ± 2.48) ppb in XCO. These differences are mainly due to the different spectral resolution and retrieval software. Higher discrepancies were found in XCH_4 observations in early spring. This is mostly caused by the inaccurate TCCON a-priori profiles affected by stratospheric intrusions when a relative strong polar vortex existed in April and gradually vanished afterwards. To reduce the aforementioned systematic errors, another dataset (125HR LR) is used in comparison to the EM27/SUN retrievals. The 125HR LR dataset was derived from the same instrumental setting, retrieving software and post processing procedure to the EM27/SUN dataset. Nearly half of the annual-average seasonal variability is reduced, resulting in ± 0.36 ppm in XCO_2, ± 2.48 ppb in XCH_4, and ± 1.31 ppb in XCO.

The intercomparison of different compact low-resolution instruments with respect to the reference TCCON observations were also discussed. Compared to the other low-resolution instruments, the EM27/SUN instrument is a promising FTIR spectrometer, with the characteristics of high stability and accuracy.

It has been shown that the usage of the improved a-priori VMR profiles reduced the observed difference between the high- and low-resolution spectrometers. The usage of the

empirical airmass dependent correction is not perfect for retrieving XCO_2 for this campaign performed at high latitude. This AD correction needs to be improved in future work.

Furthermore, different column measurements between Kiruna and Sodankylä were discussed. A significant decrease of XCO_2 and XCH_4 was observed at the downwind station in Sodankylä when two stations were well connected by air parcel transport. The area between the two places indicates a sink for the target gases on this measurement day. The emission between the two sites was on the order of 10^{18} molec. $m^{-2}\,s^{-1}$ for CO_2 and 10^{17} molec. $m^{-2}\,s^{-1}$ for CH_4. For another measurement day, similar observations in XCO_2 and a nearly constant offset in XCH_4 were seen at both sites when no direct connection existed between the two stations. Further modeling work is needed for in-depth interpretation of these measurements.

Chapter 5

Alaska campaign

In this chapter the Alaska campaign performed from August to October 2016, in cooperation with University of Alaska Fairbanks (UAF) and Los Alamos National Laboratory (LANL) is presented. Purpose of this campaign was to derive the CO_2 and CH_4 emissions from the observed gradients by using two EM27/SUN instruments, especially the CH_4 emission from the wetland surrounding Fairbanks, Alaska. For the precise observation with two instruments, lamp measurement for the instrumental line shape parameters were performed in the beginning of the campaign. Moreover, the inter-instrument calibration factors were obtained by performing side-by-side measurements in the beginning and during the campaign on the GI roof and at Poker Flat.

5.1 Instruments calibration

Every EM27/SUN instrument is aligned and calibrated at KIT before being handed over to users. Even though the EM27/SUN instrument has been proved as highly reliable and stable [Butz et al., 2017; Frey et al., 2015, 2018; Klappenbach et al., 2015], long-distance transport might cause changes in the instrumental performance. The precision requirements are demanding when investigating the gradients of a target area, as the local emission/absorption adds only a small contribution to the amounts of XCO_2 and XCH_4. Therefore, great care has to be taken for eliminating the bias caused by instruments. The calibration measurements comprised the ILS parameters measurements and side-by-side measurements.

The instrumental line shape parameters for the EM27/SUN spectrometer are obtained from open-path lamp measurement using the LINEFIT algorithm (for more details see section 2.2). The measurements were performed for both instruments in the beginning of the campaign (Figure 5.1). The retrieved ILS parameters (modulation efficiency and phase error) for the KIT and LANL instruments are collected in Table 5.1. Both instruments show slight modulation loss at maximum OPD and it is a little more pronounced in the LANL spectrometer. These obtained ILS parameters of each instrument were taken into account in the retrieving procedure with the PROFFIT algorithm.

Figure 5.1: ILS measurement in the laboratory, UAF, Fairbanks on August 5, 2016.

	Modulation efficiency	Phase error
KIT	0.9910	2.155E-03
LANL	0.9857	-1.395E-03

Table 5.1: ILS parameters at the MOPD for the KIT and LANL instruments.

Besides the lamp measurement, side-by-side calibration measurements were performed on the roof of the Geophysical Institute (GI roof), UAF and at Poker Flat which is about 35 km northeast of Fairbanks (see Figure 5.2). As discussed in Chapter 3, the intraday variable ground pressure and temperature and the a-priori VMR profiles show certain impacts on the retrievals. To eliminate these systematic errors, the ZENO3200 device provided by the LANL was used to record the intraday pressure and temperature. The a-priori VMR profiles were generated with the GGG package.

Figure 5.2: Side-by-side measurements on the GI roof, UAF (left) and at Poker flat (right) using the KIT and LANL EM27/SUN FTIR spectrometers.

Figure 5.3 presents the linear correlation of XCO_2 and XCH_4 measurements between the KIT and LANL EM27/SUN spectrometers at two different sites. Only coincident observations within one minute are shown in the figure. Only measurements with the solar zenith angle less than 70° are used here in order to avoid measurements with higher uncertainty. Additionally, 5-minute moving averages are used to reduce the random errors. It is obvious that these two instruments show a very good agreement in XCO_2 and XCH_4. Some abnormal observations are mostly due to the effect of clouds. For XCO_2, the LANL EM27/SUN measures approximately a 0.05 % (∼0.18 ppm) higher concentration than the KIT instrument on the GI roof, while an about 0.06 % (∼0.23 ppm) higher concentration is observed at Poker Flat. However, XCH_4 shows an opposite situation, here the KIT instrument measures higher concentrations. The differences are about 2.12 ppb on the GI roof and 2.0 ppb at Poker Flat.

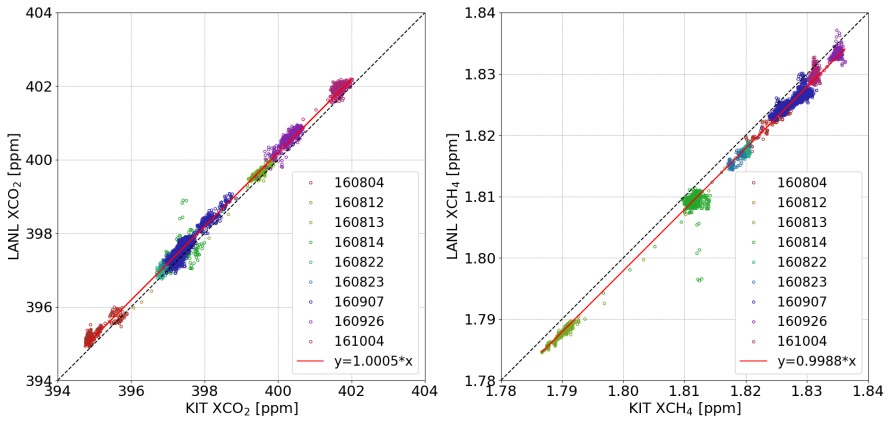

(a) GI roof

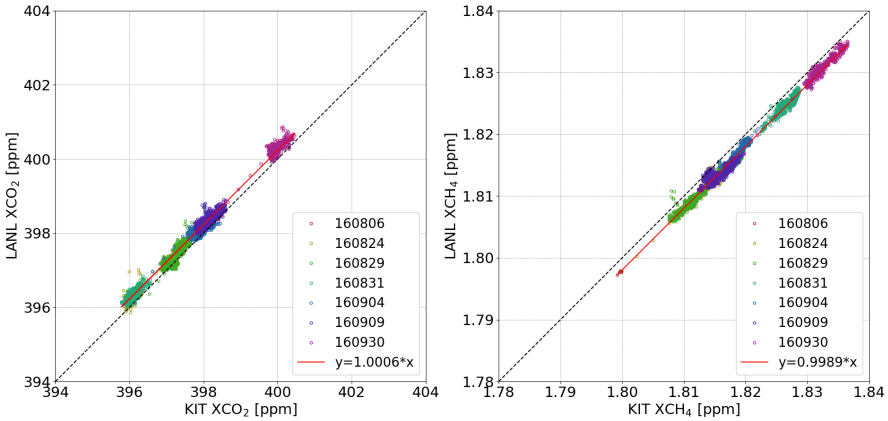

(b) Poker Flat

Figure 5.3: Linear correlation of XCO_2 (left) and XCH_4 (right) recorded with the KIT and LANL instruments on the (a): GI roof and at (b): Poker Flat. Different colors denote the measurements on different days and the red line denotes the fitting line through the origin.

To eliminate the systematic errors caused by the different instrumental characteristics, the empirical inter-calibration factors derived from the side-by-side measurements are applied for each species. The measurements performed with the KIT instrument are scaled to the LANL measurements by applying the corresponding scaling factors. The factor of a specific target gas at one station is the slope of the fitting line for the two datasets through the origin point (see Figure 5.3). The mean value of the slope derived from the two stations represents the final scaling factor for the related target gas, see table 5.2.

	GI roof	Poker Flat	$\text{factor}_{\text{calibration}}$
XCO_2	1.0005 (7.0E-4)	1.0006 (5.3E-4)	1.00055 (6.2E-4)
XCH_4	0.9988 (8.4E-4)	0.9989 (5.9E-4)	0.99885 (7.2E-4)

Table 5.2: Calibration factors for the KIT and LANL instruments (LANL/KIT). Values in the parentheses denote the 1σ empirical standard deviation of the ratio. The $\text{factor}_{\text{calibration}}$ of a specific trace gas is obtained by averaging the factors from two sites. These factors are used for calibrating the two spectrometers to a common scale.

As discussed in subsection 4.3.4, XAir is considered as a quality check parameter, derived only from the ground pressure and the spectroscopically acquired columns of O_2 and water vapor. Figure 5.4 shows the time series of XAir for each instrument at each site. Same to the data preparation of XCO_2 and XCH_4, the coincident 5-minute moving averaged XAir values are shown here for SZA lesser than 70°. Both spectrometers show similar characteristics and there is no obvious change in the ratio between them, showing the outstanding stability of the EM27/SUN instrument. Measurements performed at different sites do not show apparent differences. The averaged ratio of the XAir from the two instruments is approximately 1.0023 ± 0.0008 on the GI roof and 1.0028 ± 0.0006 at Poker Flat. The LANL instrument has slightly higher XAir value due to the higher recording of O_2 total columns than the KIT instrument at both measurement sites. Figure 5.5 shows the XAir ratio as a function of SZA. XAir ratios are distributed more dispersed at higher SZA and therefore measurements with SZA larger than 75° are discarded in the following section of gradient studies. Approximately 0.2 % difference is found between the forenoon and afternoon measurements, and is probably caused by the deviation in pointing of the solar position between the two solar trackers. When the SZA is around 70°, the solar tracker changes approximately 0.02° every 15 seconds, resulting in 0.1 % difference in XAir. Spectra are recorded together with the corresponding system time from the computer, and thus time differences between different computers might also lead to errors.

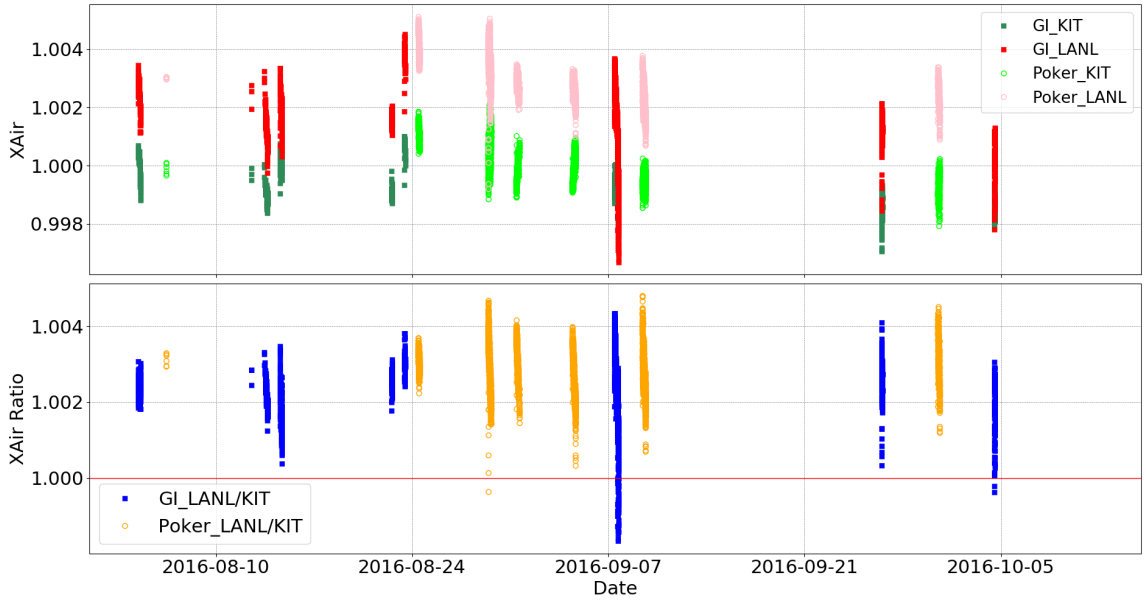

Figure 5.4: Time series of XAir (SZA $< 70°$) derived from the calibrated measurements on the GI roof (solid square) and at Poker Flat (empty circle) with the KIT and LANL spectrometers. Additionally, the ratio values between the two datasets is presented in the lower panel.

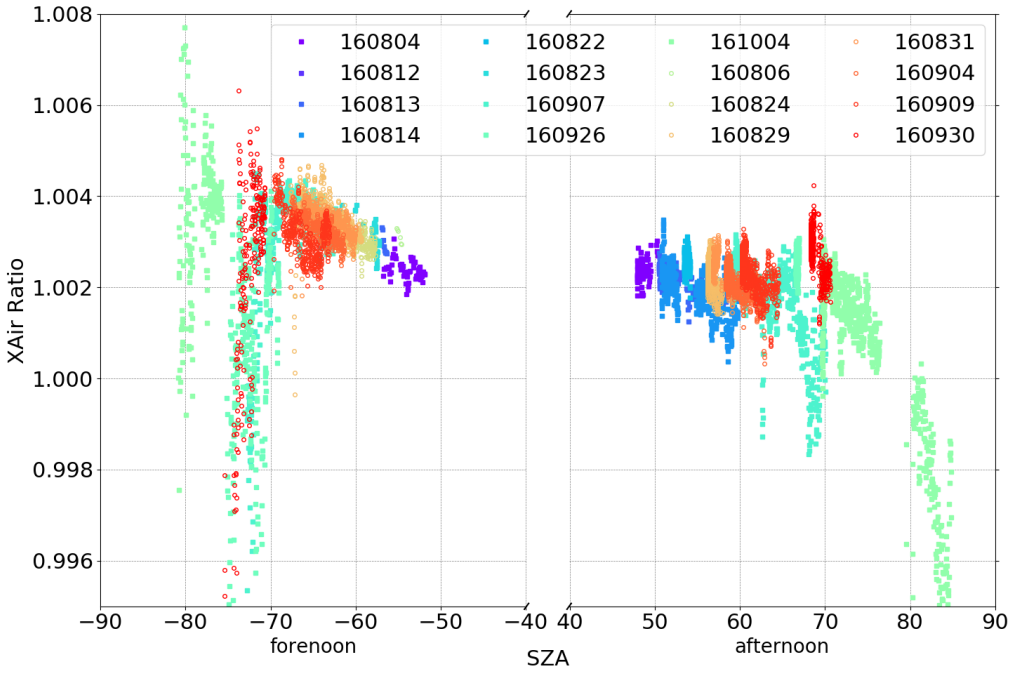

Figure 5.5: XAir ratio (LANL/KIT) as a function of SZA. Different colors denote the measurements on different days at GI roof (solid square) or at Poker Flat (empty circle). SZA < 0 correspond to the forenoon measurements

5.2 Detection of gradients

Wetlands occupy about 43 % area of the State of Alaska [Hall et al., 1994]. Fairbanks, located in the interior of Alaska, is covered mostly by taiga forests, also known as Boreal Forests. The Chena River flows through Fairbanks to the Tanana River which passes through the southern border of the city. The Tanana River emerges into the lowland swamp area known as the Tanana Valley, stretching south for more than 160 km up to the Alaska Range. The climate in Fairbanks is characterized as subarctic, with long cold winters and short warm summers.

Figure 5.6: Map showing the overview of the measurement sites in Fairbanks, Alaska. Blue markers represent the side-by-side measurements stations; when the KIT instrument was located on the GI roof, the LANL instrument was settled at the station denoted with the red markers near Fairbanks; the KIT and the LANL instruments were located at Nenana (black marker) and Anderson (red marker), respectively for the wetland emission study. (Map source: Google Map).

Two methods were applied to detect the gradients in XCO_2 and XCH_4 between two sites. The first one is settling the KIT instrument always on the GI roof, UAF and moving the LANL instruments to several places (Airport 1, Airport 2, all-terrain vehicles parking site (ATV land), Nenana and the downtown of Fairbanks). The other approach was to measure the wetland emissions between Nenana (KIT EM27/SUN) and Anderson (LANL

EM27/SUN). Figure 5.6 shows an overview map indicating the locations of the different stations. Table 5.3 shows more detailed information, including the measurement dates, coordinates and altitudes of the different stations, and the direct distance between two paired stations. To reduce the systematic errors when evaluating the emission/absorption rate of one area with these two instruments, the measured ILS parameters are used in the PROFFIT algorithm for the corresponding EM27/SUN measurements. Besides, calibration factors are applied to the KIT EM27/SUN retrievals for each species. Only coincident measurements from the two sites within one minute are selected to compute one-hour moving mean observations. This method reduces the random errors, e.g. caused by clouds.

	Date	KIT	LANL	Distance
GI-X	160808 160828 160908 161007 161012	GI (64.86°N, 147.85°W 223 m a.s.l.)	Airport 1 (64.80°N, 147.86°W, 131 m a.s.l.)	6.7 km
	160810		Airport 2 (64.79°N, 147.88°W, 144 m a.s.l.)	7.4 km
	160902 160903 160910		ATV land (64.77°N, 148.26°W, 405 m a.s.l.)	21.7 km
	160830 161001		Nenana (64.56°N, 149.09°W, 124 m a.s.l.)	67.6 km
	161005		Downtown (64.85°N, 147.71°W, 141 m a.s.l.)	7.0 km
Nenana - Anderson	160816 160817 160818	Nenana (64.56°N, 149.09°W, 124 m a.s.l)	Anderson (64.34°N, 149.20°W, 159 m a.s.l)	25.2 km

Table 5.3: Locations of the KIT and LANL instruments at different stations and their distances at different days in Fairbanks, Alaska.

5.2.1 GI roof - ATV land

In this experiment, the KIT instrument was operated on the GI roof. The LANL instrument was moved to the ATV land, about 22 km southwest away from the GI roof and surrounded by wetland areas. Observations were performed on three days when the wind direction was mostly northeast on September 2, northeast to east on September 3 and southwest on September 10, 2016. Connecting trajectories between two stations were found only on September 2 and 10 (Figure 5.7) while a poorer match of wind direction was found on September 3 (Figure 5.10).

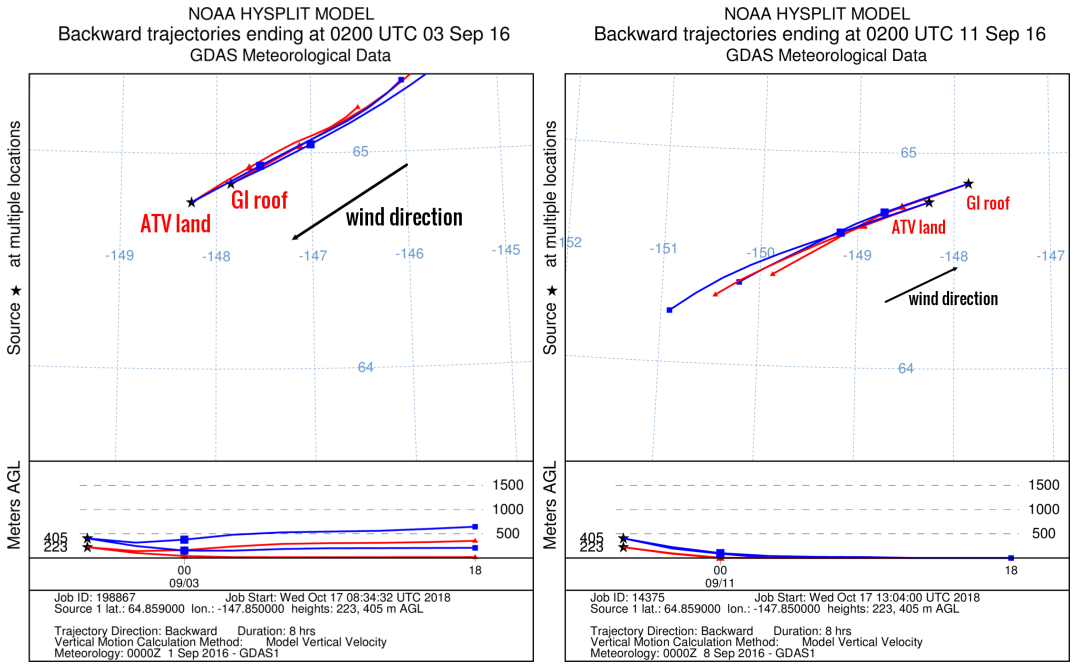

Figure 5.7: Eight-hour backward trajectories ending at 18:00 LT on September 2 and 10, 2016 (derived from GDAS Meteorological Data).

On September 2, the GI roof was mostly in the upwind direction. For XCO_2, both instrument observed similar amounts of concentration during most of the time, except the detection of elevated XCO_2 values at the ATV land (see Figure 5.8). This is probably due to the interaction of variable wind directions with local emissions, as the instrument was located at the parking lot and near the main road, where the emissions of passing-by cars generated a sudden enhancement. However, XCH_4 shows a different behavior. The upwind KIT instrument measured higher XCH_4 during most of the day. This is probably due to the complex terrain between the two stations. The ATV land is around 200 m higher than the GI roof. Both sites are located in the central Tanana Valley and to their west are the low valleys separated by ridges of hills with up to near 1 km a.s.l. altitude. This uneven terrain channels the air flow and probably makes the quality of the modeled trajectory poor. It is likely that the downwind LANL instrument measured different air parcels that did not pass through the GI roof.

The terrain impact was weaker on the measurements on September 10, when the wind direction was more parallel to the ridges. The downwind KIT instrument measured higher amounts of XCO_2 and XCH_4 on the most of the day (see Figure 5.9). The bias were up to 1.1 ppm for XCO_2 and 7.0 ppb for XCH_4, resulting in an emission rate of approximately 6.6×10^{19} molec. $m^{-2}\,s^{-1}$ and 4.3×10^{17} molec. $m^{-2}\,s^{-1}$, respectively. Since the LANL spectrometer stayed at the ATV land and the air flowing direction was mostly along the main road, the XCO_2 was very likely enhanced from the vehicles.

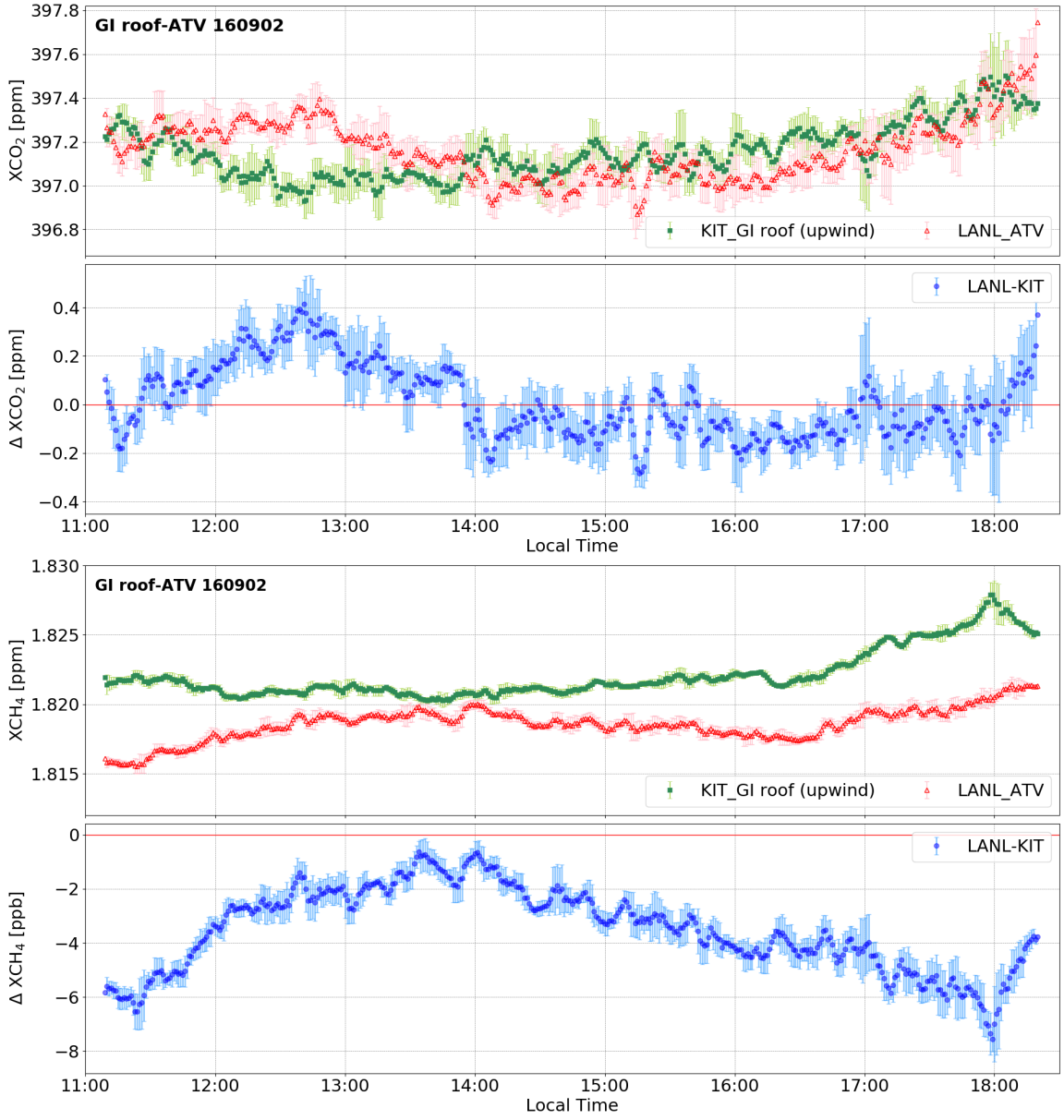

Figure 5.8: Time series of XCO_2 and XCH_4 recorded on the GI roof (KIT) and at the ATV land (LANL) on September 2, 2016. The wind on this day blew mostly from the northeast direction, resulting in the GI roof being the upwind station. Error bars represent the standard deviation of the 5-minute moving mean bias. Zero lines are marked in red.

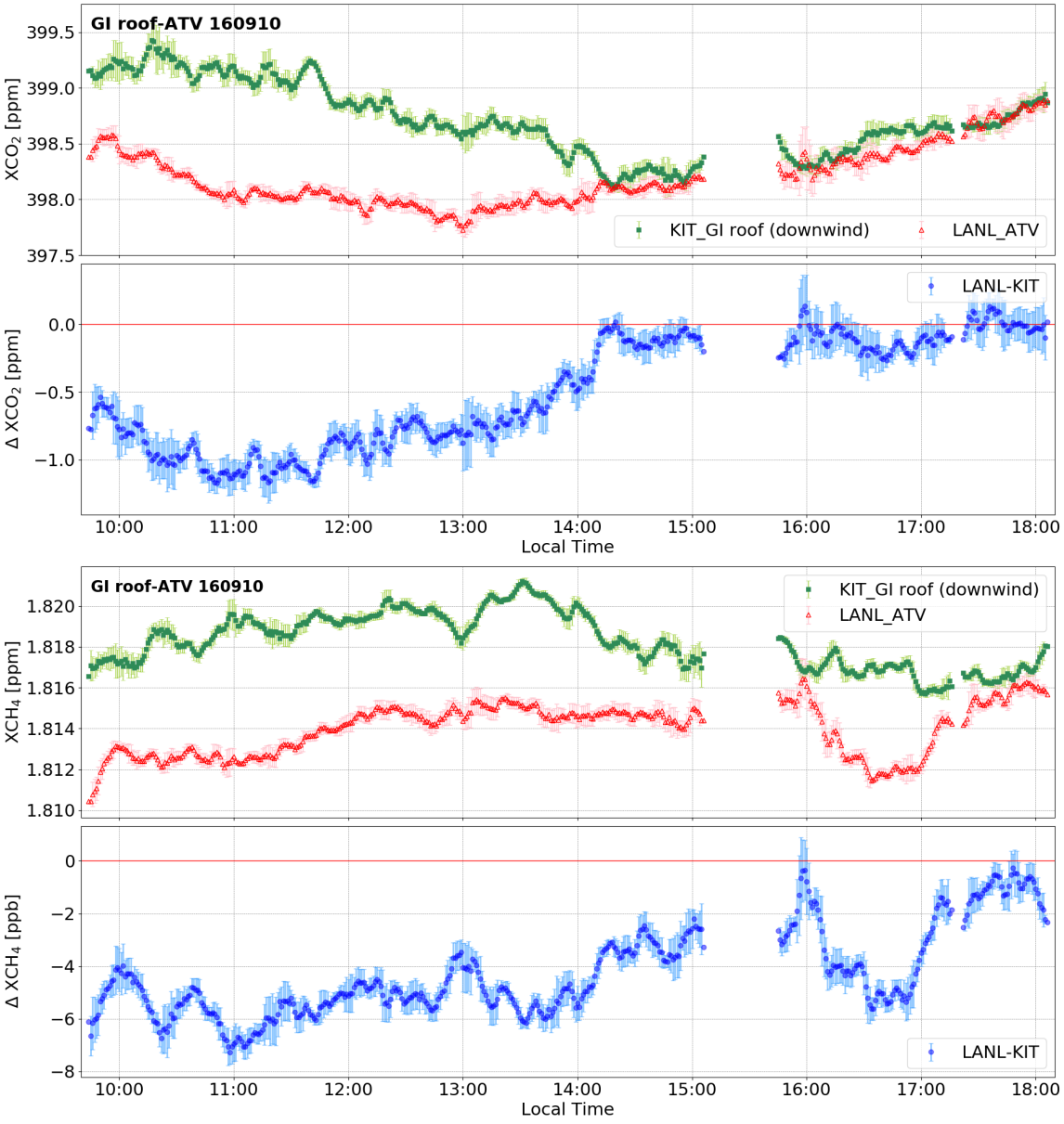

Figure 5.9: Time series of XCO_2 and XCH_4 recorded on the GI roof (KIT) and at the ATV land (LANL) on September 10, 2016. The wind on this day blew mostly from the southwest direction, resulting in the GI roof as the downwind station. Error bars represent the standard deviation of the 5-minute moving mean bias. Zero lines are marked in red.

The other measurement day was September 3, 2016 when the wind blew from east north-east to further north, resulting in no obvious connecting trajectory between the two sites before 22 UTC (local time (LT): 14:00) (Figure 5.10, left panel). Nearly 3-hour of well connected trajectory between the two sites was derived from 15:00 LT to 19:00 LT (Figure 5.10, right panel). The air parcel transportation is also observed in the measurements from the two stations (see Figure 5.11). The ΔXCO_2 and ΔXCH_4 stayed close to 0 ppm and 2 ppb respectively, when the wind direction was east north-east and two sites' backward trajectories were almost parallel. After the wind direction shifted to more north and the two sites were well connected, the downwind station (the LANL instrument at the ATV land) measured a slightly higher enhancement of up to 4.1 ppb. This small enhancement is much lower than the other day's measurements, because the north of Fairbanks is covered by chains of hills rather than wetland methane sources. The sudden increase of the amount of LANL XCH_4 is most probably due to a local source signal caused by the variable wind direction between 14:00 LT to 15:00 LT.

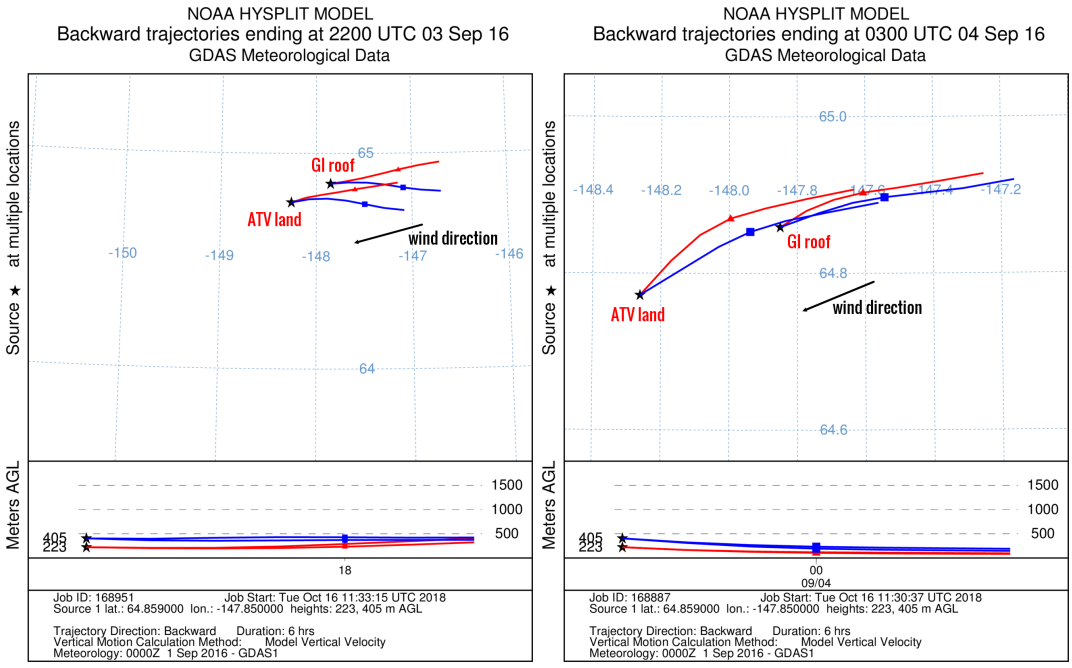

Figure 5.10: Backward trajectories ending at 14:00 LT (left) and 19:00 LT (right) on September 3, 2016 (derived from GDAS Meteorological Data).

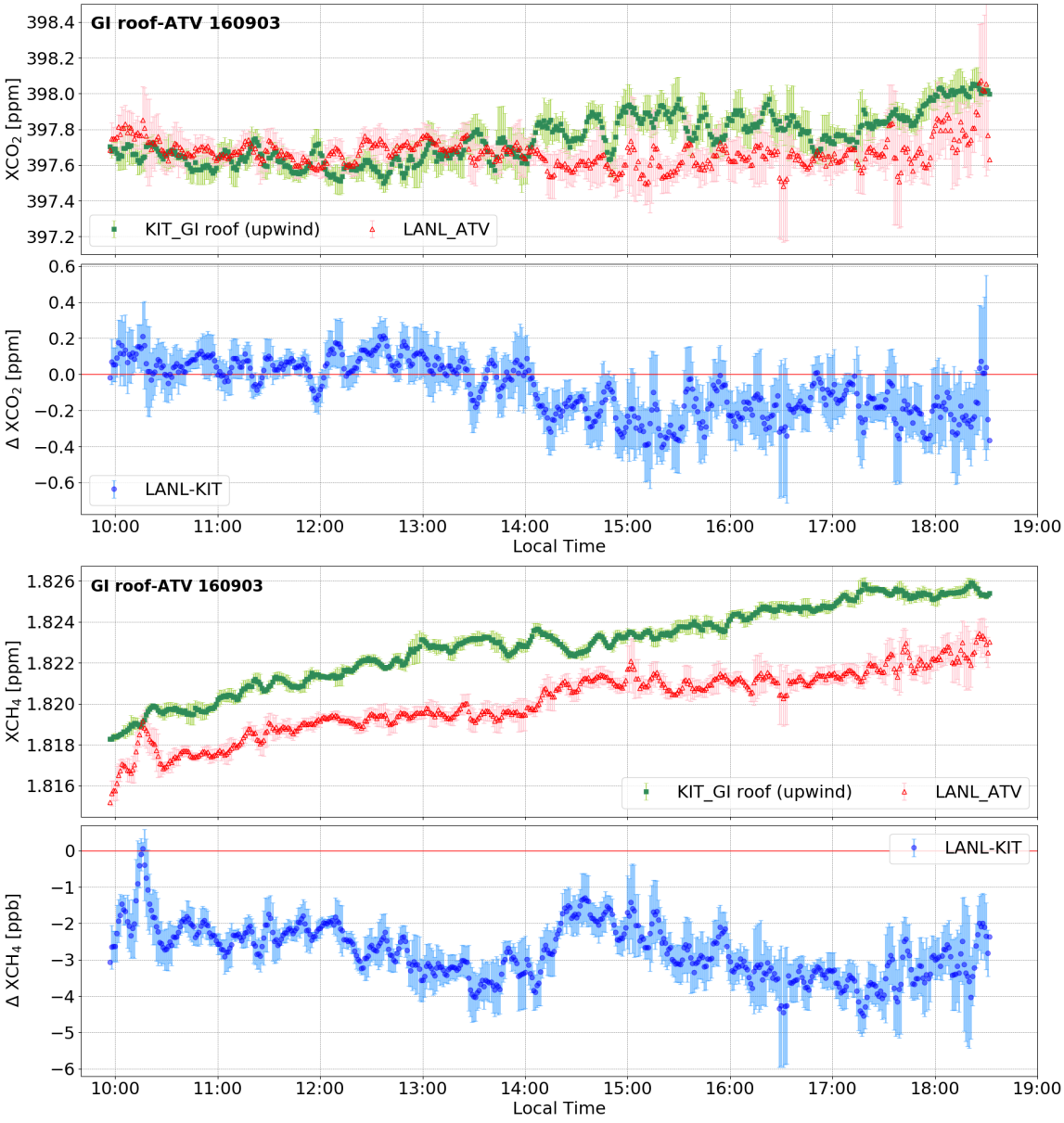

Figure 5.11: Time series of XCO_2 and XCH_4 recorded on the GI roof (KIT) and at the ATV land (LANL) on September 3, 2016. The wind direction on this day was from east north-east to north north-east. Error bars represent the standard deviation of the 5-minute moving mean bias. Zero lines are marked in red.

5.2.2 GI - Downtown

In this part, the KIT EM27/SUN instrument stayed on the GI roof while the LANL instrument was settled in downtown Fairbanks around 7 km to the southeast of the GI roof. East to northeast wind was the dominant wind direction during the observation day on October 5, 2016 (see the backward trajectories in Figure 5.12). No direct air transport between the two sites occurred. In the beginning of the measurement the LANL instrument observed approximately 1 ppm higher XCO_2 than the downwind KIT EM27/SUN spectrometer. This was probably due to the local source, like the anthropogenic activities in downtown Fairbanks. The different amounts of XCO_2 between the two sites became smaller when the wind direction changed to the northeast in the afternoon. Less variability was observed by the LANL instrument after noon and by the KIT instrument later in the day. The peak observed on the GI roof between 13:00 LT and 15:00 LT is probably due to local sources. For XCH_4, both instruments measured similar variability over the whole day. The LANL spectrometer observed approximately a 2 ppb higher amount in the beginning of the measurement. The difference slightly decreased to around 1.5 ppb after 13:00 LT because the source of the air changed. Different from XCO_2, no sudden increase of XCH_4 was observed in the afternoon. However, a stronger increase occurred around 12:30 LT on the GI roof than at the downtown site, resulting in a slight decrease of the bias. This is mostly due to the varying wind direction.

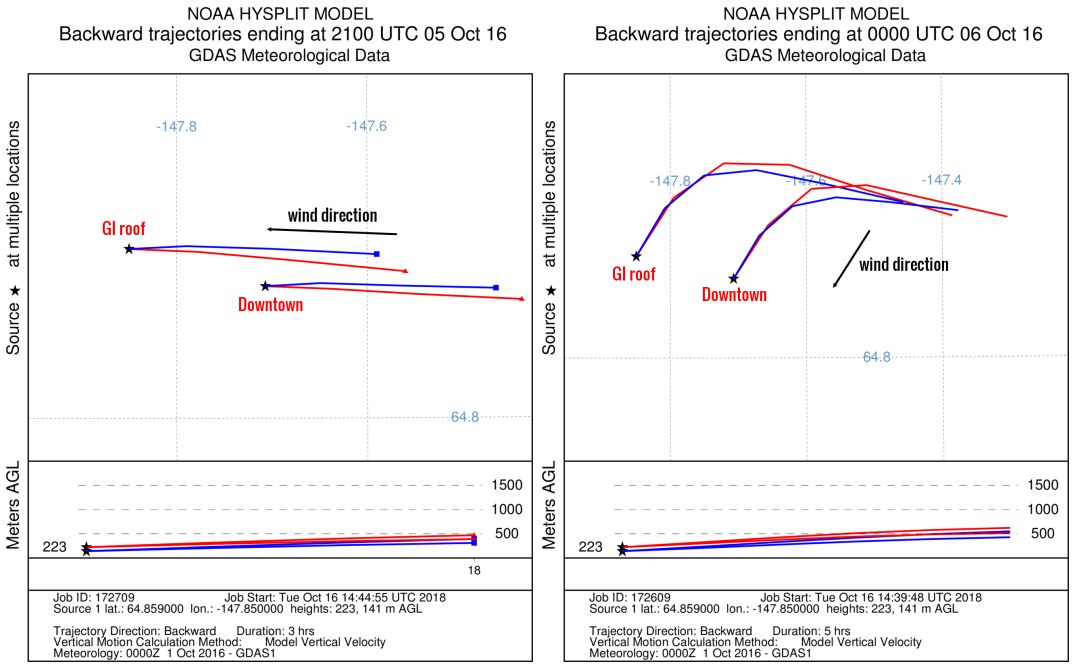

Figure 5.12: Backward trajectories ending at 13:00 LT (left) and at 16:00 LT (right) on October 5, 2016 (derived from GDAS Meteorological Data).

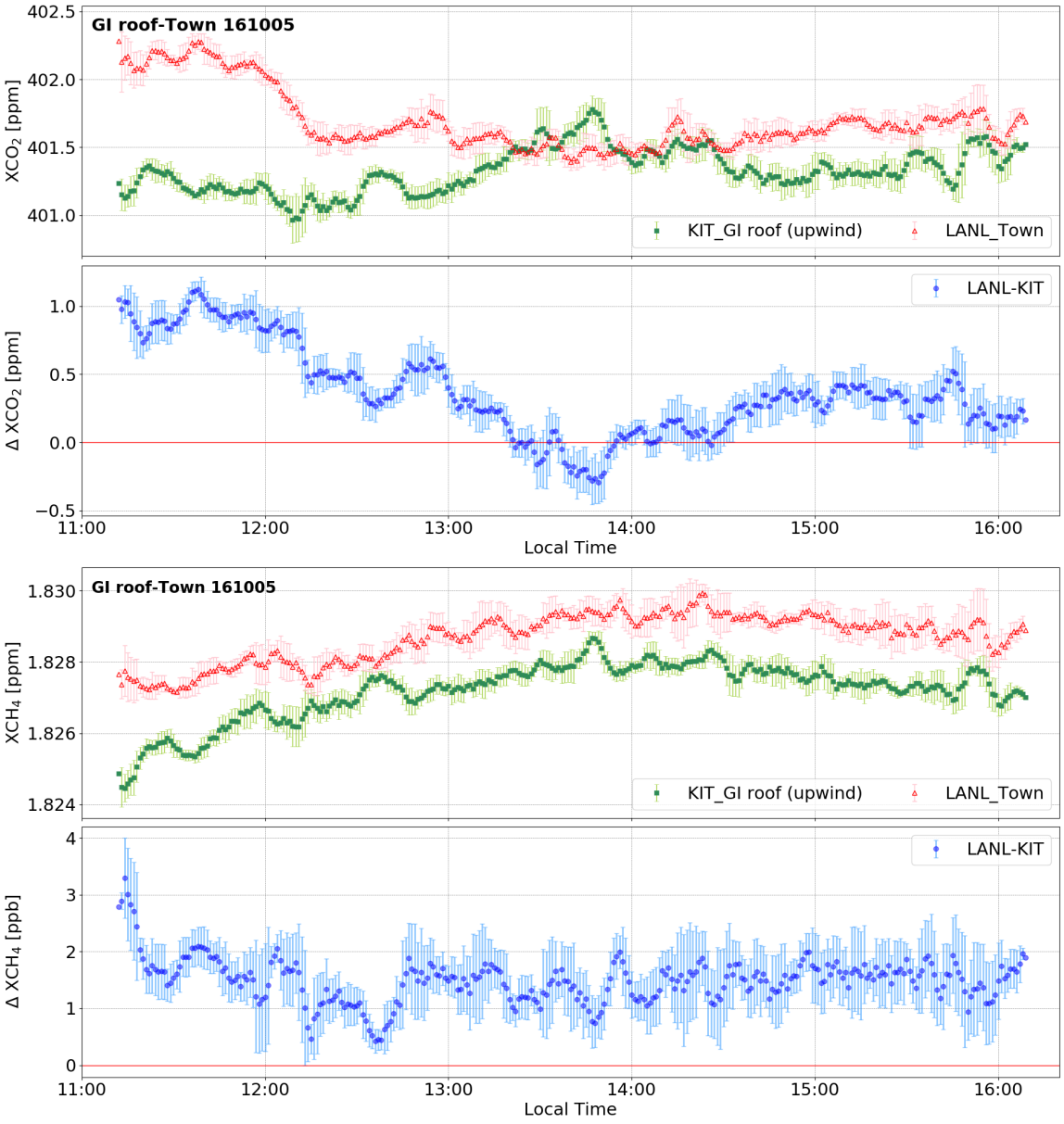

Figure 5.13: Time series of XCO_2 and XCH_4 recorded at Nenana (KIT) and Anderson (LANL) on October 5, 2016. The wind direction on this day was east before 13:00 LT and northeast in the afternoon. Error bars represent the standard deviation of the 5-minute moving mean bias. Zero lines are marked in red.

5.2.3 Nenana - Anderson

For achieving a better suited configuration for detecting wetland emissions, two sites named Nenana and Anderson were chosen to settle the two EM27/SUN instruments. These two sites are located in the middle of the wetland area with a distance of 25.2 km. The KIT EM27/SUN instrument was settled in the parking place in front of the Cyberlynx Correspondence Program office, Nenana. The Nenana city is located in the southwest of Fairbanks and is at the confluence where the tributary Nenana River flows into the Tanana River. The LANL instrument was settled in the Anderson City Camp Ground in the southwest of the Anderson townsite and was quite near to the Nenana River in the west. Here two-day measurements are discussed.

For both days the wind mostly came from southwest and the backward trajectories on these two days also show the airmass as transport from southwest (see Figure 5.14). The KIT instrument in Nenana was located in the downwind direction.

On August 17 XCO_2 shows quite variable measurements at both sites and no obvious enhancement in the downwind direction. The ΔXCO_2 was steady with the daily-mean value of ± 0.08 ppm ($\sim 0.05\,\%$ in term of the relative difference) on this measurement day. Some suddenly increased or decreased measurements occurred within certain periods (i.e. the peak measurements at around 15:00 LT at the Nenana station) probably due to the variable wind direction or other unknown local sources.

XCH_4 shows a different behavior with a continuous increase at both sites. An obvious enhancement is found in the downwind measurements recorded with the KIT EM27/SUN instrument. The peak measurements are also caused by the varying wind direction and local sources. However, the different shapes of the peaks and different occurrence times between the two set of measurements indicate different local sources for XCH_4 and XCO_2. The average difference of XCH_4 is around 3.2 ppb between these two sites (relative difference: $\sim 0.25\,\%$), five times higher than the difference in XCO_2, indicating a source predominantly emitting methane rather than carbon dioxide. In addition, an approximate 2-hour trajectory almost connected Nenana and Anderson, suggesting a local emission of methane on the order of 1.4×10^{17} molec. $m^{-2}\,s^{-1}$.

During the next day (August 18), the wind direction was nearly southwest (see the backward trajectory in Figure 5.14, right panel), but no direct connecting air transport existed between the two stations. Similar to the measurements on August 17, no significant change occurred in XCO_2 and the bias between the two sites was around 0.11 ppm. XCH_4 concentration measured with the KIT and LANL instruments were quite stable due to the calm air during this observing period. However, about 5.7 ppb higher XCH_4 was observed at KIT station, indicating the presence of a methane source near Nenana.

To conclude, the area around Nenana and Anderson is found to be a XCH_4 source rather than a XCO_2 source. The methane emission rate is on the order of 10^{17} molec. $m^{-2}\,s^{-1}$ for the measurement day.

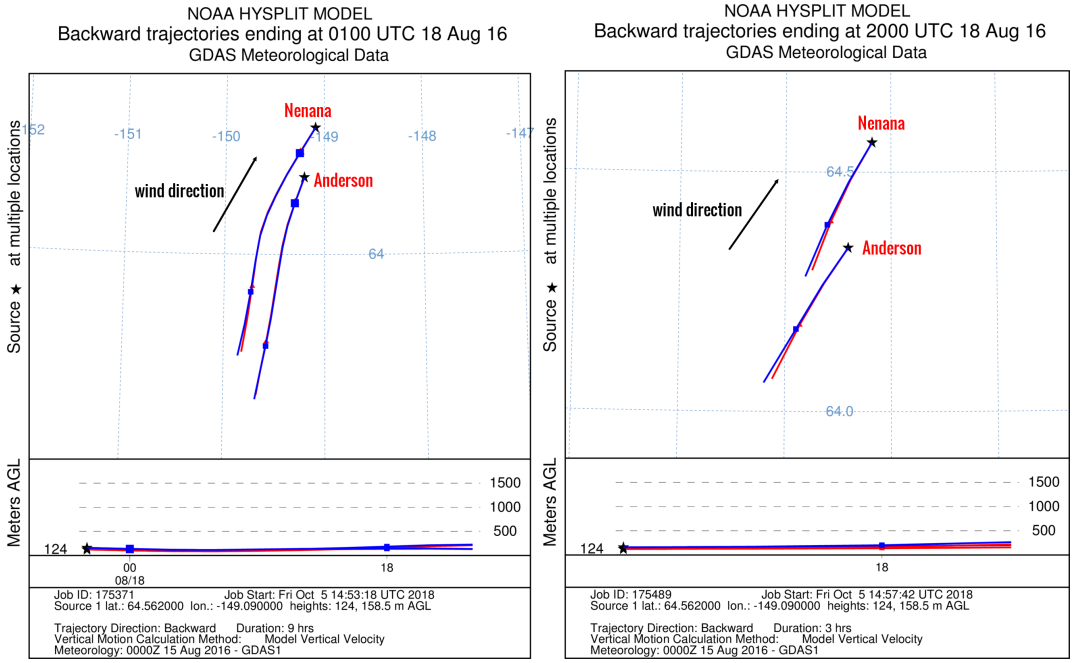

Figure 5.14: Backward trajectories ending at 17:00 LT on August 17, 2016 (left) and at 12:00 LT on August 18, 2016 (right) (derived from GDAS Meteorological Data).

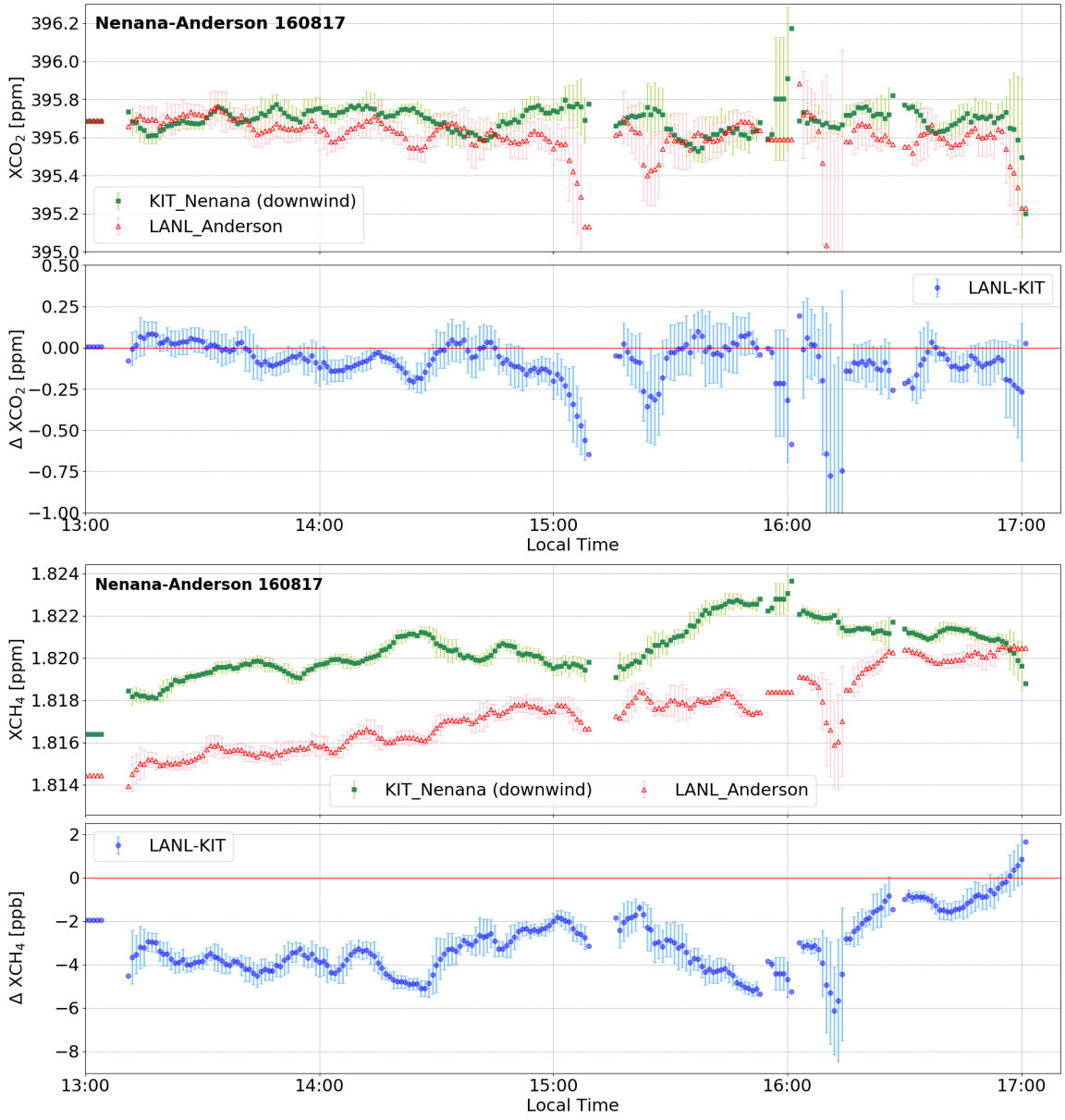

Figure 5.15: Time series of XCO_2 and XCH_4 recorded at Nenana (KIT) and Anderson (LANL) on August 17, 2016. Error bars represent the standard deviation of the 5-minute moving mean bias. Zero lines are marked in red.

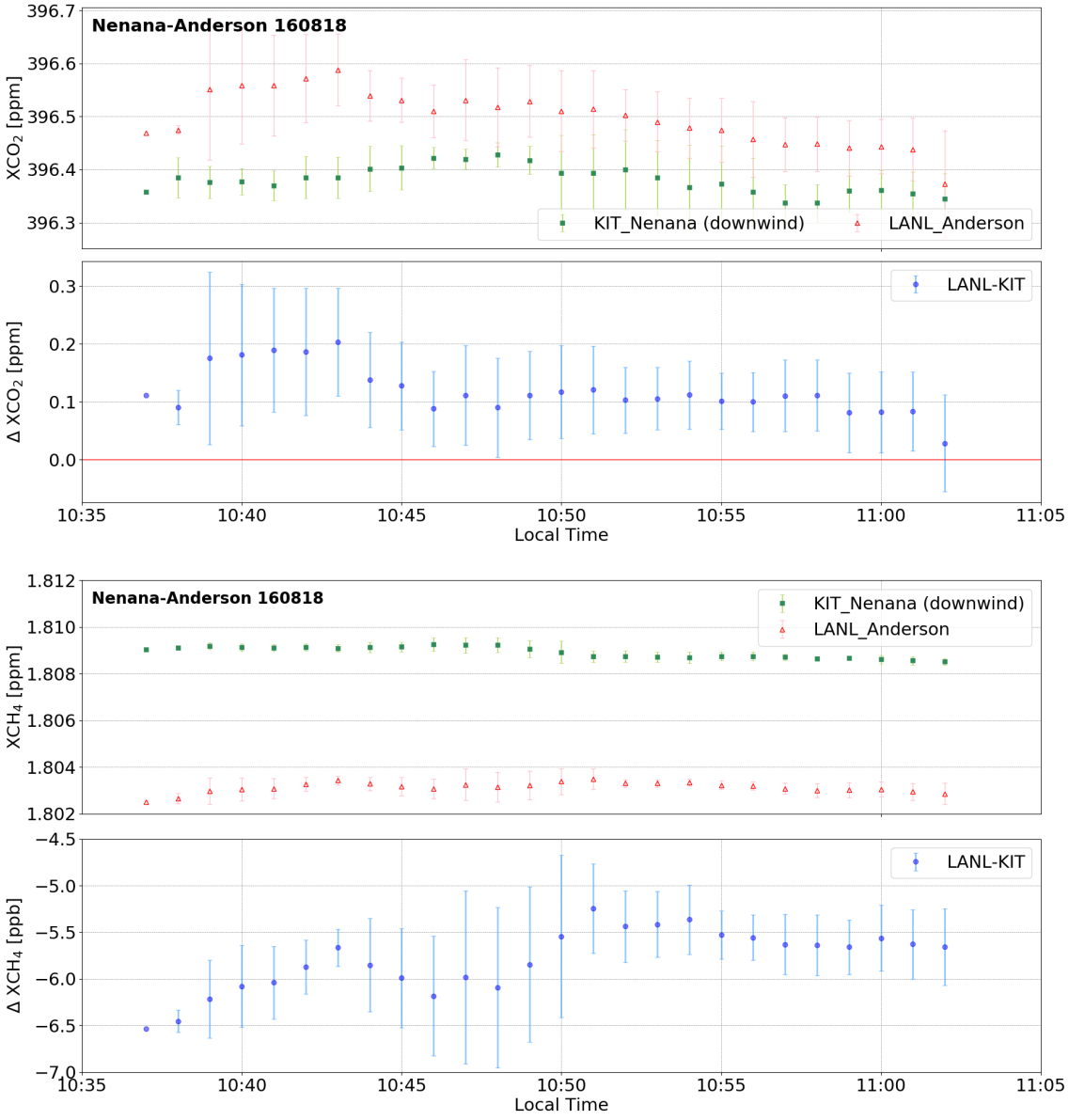

Figure 5.16: Time series of XCO_2 and XCH_4 recorded at Nenana (KIT) and Anderson (LANL) on August 18, 2016. Error bars represent the standard deviation of the 5-minute moving mean bias. Zero lines are marked in red.

5.3 Conclusions

In this chapter two instruments, one from KIT and one from LANL were used to investigate the GHG emissions from wetlands near Fairbanks, Alaska. Before the gradient study, side-by-side measurements were performed in several days for the inter calibration on the GI roof and at Poker Flat. The two different EM27/SUN spectrometers show stable characteristics and excellent accuracy and reliability even after the long-distance shipment from Karlsruhe to Fairbanks, and the frequent transport within the campaign. On average, the bias between these two instruments was approximately 0.06 % in XCO_2 and 0.11 % in XCH_4. These differences have been taken into account when attempting the detection of gradients.

To study the sources and sinks near Fairbanks, several paired stations were chosen for operating the two instruments. When studying the area between the ATV land and Fairbanks downtown, a short period of peak XCO_2 was observed near the ATV land and downtown because of the anthropogenic activities, e.g. car traffic. For the gradients study between the GI roof and the ATV land, it is difficult to investigate the CH_4 emission from the measurements in most of these days. This is mainly due to the complex terrain situation that hinders wind flow, and consequently hinders the air parcel transport. It was only when the measurements on September 10, 2016 were little influenced by the hills that the CH_4 emission rate was observed on the order of 10^{17} molec. m^{-2} s^{-1}. The wetland between the Nenana and Anderson stations is likely to be a CH_4 source, when an obvious CH_4 emission was observed at the downwind station. The estimated CH_4 emission from this area is on the order of 10^{17} molec. m^{-2} s^{-1} according to the measurements on August 17, 2016.

Chapter 6

Summary and Outlook

In this work, the sources and sinks for the atmospheric GHGs CO_2 and CH_4 on a regional scale were analyzed. Compared to in-situ and satellite measurement techniques, the applied ground-based remote sensing technique is advantageous due to its ability to measure column averaged abundances with high precision and accuracy with high temporal resolution. The TCCON network provides accurate total column abundances of trace gases globally. However, the costs and logistical requirements hinder its further expansion, and consequently limit the study of GHGs sources and sinks in interesting places. A new prototype of a mobile and compact solar absorption spectrometer (EM27/SUN) was recently developed at KIT in cooperation with Bruker Optics [Gisi et al., 2012; Hase et al., 2016]. EM27/SUN instruments have been successfully operated in several field campaigns [Butz et al., 2017; Frey et al., 2015; Klappenbach et al., 2015] and support the TCCON network by providing a travel standard [Hedelius et al., 2017]. In my work I used a pair of EM27/SUN spectrometers to study the sources and sinks of GHGs in the boreal region. The characterization and correction of error sources to improve the precision of the retrievals are also presented in this work, as these are prerequisites for detecting small signals.

Systematic errors are reduced by using the column-averaged dry-air mole fraction (DMF) method instead of the total columns for the target gases. Errors induced by differing instruments are calibrated out by side-by-side measurements. An airmass dependent empirical correction is investigated and applied to the results. A special focus is put on the instrumental line shape (ILS), as a 1 % reduction of the modulation efficiency induces change of 0.18 % and −0.01 % in XCO_2 and XCH_4, respectively. Measured ILS parameters are used for the retrievals within the PROFFIT algorithm for achieving better accuracy. The effects of intraday-variable ground pressure and temperature profiles are also discussed. A 1 hPa change of pressure and 1 K change of temperature cause errors in the O_2 columns of about 0.054 % and 0.045 %, respectively. CO_2 and CH_4 show a similar tendency to the pressure change with around −0.019 % and −0.015 %, respectively when the pressure increases by 1 hPa and much lesser change exists in CO total columns with approximately 0.002 %. The use of the DMF method partly compensates the systematic errors affecting both O_2 column

and CO_2 and CH_4 columns for a 1 hPa change in surface pressure, resulting in approximate changes of 0.035 % in XCO_2, 0.039 % in XCH_4, respectively, while XCO is overcompensated with around 0.052 %. However, CO_2, CH_4 and CO show larger different sensitivity to temperature changes. A 1 K increase contributes to about 0.03 % and 0.008 % higher total column abundances for CO_2 and CH_4, respectively, while CO shows a higher increase of 0.47 %. Therefore, a 1 K change in temperature up to 2 km results in ∼0.015 % decrease in XCO_2, a 0.037 % decrease in XCH_4 and a 0.43 % increase in XCO.

The aforementioned optimization methods are used for evaluating the measurements from the Sodankylä campaign in Finland. The measured ILS parameters are applied within the PROFFIT algorithm, reducing the relative bias compared to the TCCON measurements by approximately 0.33 % and 0.30 % in XCO_2 and XCO, respectively over the whole year. The XCH_4 bias is slightly different with an increase of ∼0.17 % which is mainly due to the imperfect choice of the a-priori VMR profiles.

Three kinds of vertical a-priori VMR profiles used in the retrievals are discussed. The use of the daily-variable MAP profiles results in a better correlation with respect to the TCCON observations than using constant climatologic a-priori profiles derived from the WACCM model. The application of the measured AirCore as a-priori profiles is also presented and emphasizes the importance of using a realistic a-priori profile. Significant improvements are found in XCH_4 during spring time by using the AirCore profiles. This is mainly because the polar vortex strongly influences the vertical profiles in the stratosphere, which consequently results in the differences in the retrievals. The slope of the linear correlation between the EM27/SUN and the TCCON retrievals through the origin point improves from 0.71 to 1.01.

The optimized EM27/SUN results are compared to local meteorological observations at FMI. The target gas abundances derived from the EM27/SUN observations show a reasonable agreement with the corresponding in-situ gas fluxes. Additionally, snow depth, soil and air temperature show certain impacts on the photosynthesis activity of plants, which consequently influence the atmospheric XCO_2 concentrations.

By means of an intercomparison of column-averaged DMFs measured with the EM27/SUN and co-located 125HR FTIR spectrometers, the EM27/SUN instrument turns out to be highly precise and stable. The yearly average biases are approximately (0.28 ± 0.64) ppm in XCO_2, (1.99 ± 5.76) ppb in XCH_4 and (1.72 ± 2.48) ppb in XCO. The average XAir derived from the EM27/SUN retrievals amounts to 0.9680 and is about 0.01 lower than the TCCON XAir. EM27/SUN XAir shows a slightly higher sensitivity to high solar zenith angles than the TCCON XAir does. The differences between these two datasets are mainly due to the retrieval software and instrumental characteristics (e.g. ILS parameters and spectral resolution). To eliminate these systematic errors, an additional dataset (125HR LR) is introduced here, which was recorded with the 125HR spectrometer using the same instrumental setting parameters, retrieval software (PROFFIT) and post processing as to the EM27/SUN dataset. The correlations between the EM27/SUN with respect to the 125HR LR retrievals show better agree-

ment for all species than with respect to the TCCON retrievals. Nearly half of the seasonal variability is reduced—from 0.64 ppm to 0.36 ppm in XCO_2, from 5.76 ppb to 2.84 ppb in XCH_4, and from 2.48 ppb to 1.31 ppb in XCO. The absolute differences (EM27/SUN-125HR LR) increase for all X_{Gas} because no scaling factors are applied in this comparison.

To study the sources and sinks from boreal areas, two sets of GHG gradient experiments were performed: one between Sodankylä and Kiruna; the other one in the Fairbanks region in Alaska. Local source contributions on the order of -8.2×10^{18} molec. $m^{-2}\,s^{-1}$ for CO_2 and -1.0×10^{17} molec. $m^{-2}\,s^{-1}$ for CH_4 were locally derived from the measurements on March 16, 2017, indicating sinks for CO_2 and CH_4 in this area. However, the Fairbanks campaign results in different GHGs emission rates. The boreal wetland between Nenana and Anderson is very likely a CH_4 source, which emitted CH_4 on the order of 10^{17} molec. $m^{-2}\,s^{-1}$. Moreover, the instrumental intercomparison of the two EM27/SUN (one from KIT and one from LANL) proves very stable characteristics and excellent accuracy and reliability in measuring trace gas abundances. The average bias between these two instruments was found to be on the order of 0.06 % in XCO_2 and 0.11 % in XCH_4.

The excellent performance and high accuracy of the EM27/SUN spectrometer distinguish the device as a promising candidate to reduce gaps in the TCCON network. Besides, after calibration, its advantages of compactness, portability and robustness make it an optimal device for field campaigns to investigate local GHGs sources and sinks. Moreover, this spectrometer is a valuable tool for the validation of satellite soundings. Retrievals from the dual-channel EM27/SUN instrument may be used to validate the XCH_4 and XCO from the recently launched Sentinel-5P satellite.

Finally, some ideas for the future are listed here. Cooperation between the modeling working groups and the provision of observational GHG data should be intensified, because connecting two sites with direct, stable and sufficiently enough wind is difficult to plan. Improved a-priori VMR profiles will help to improve the accuracy of the retrievals.

An automated enclosure developed by the Technical University of Munich (TUM) [Heinle and Chen, 2018] was used for the EM27/SUN instrument in Sodankylä in summer, 2018 and has proved to be very useful. The instrument is stored in a robust case with cooling fan and heater inside and a rain sensor on top, which protects the instrument from harmful environment and poor weather conditions. Its remote-control feature reduces the cost of human effort since no personnel is needed on site after settling down the instrument. In addition, this automated shelter improves the practicability in long-term field campaigns.

Appendix A

Pressure sensitivity

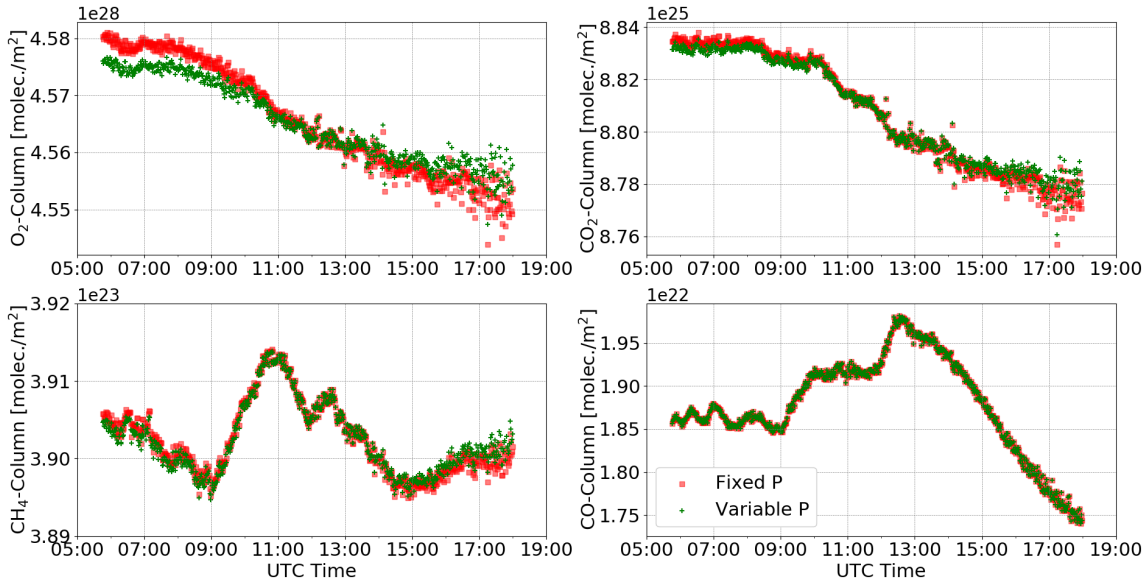

Figure A.1: Time series of total columns of O_2, CO_2, CH_4 and CO retrievals with fixed and variable ground pressure used in the PROFFIT algorithm—using measurements performed in Sodankylä on June 8, 2017 as an example.

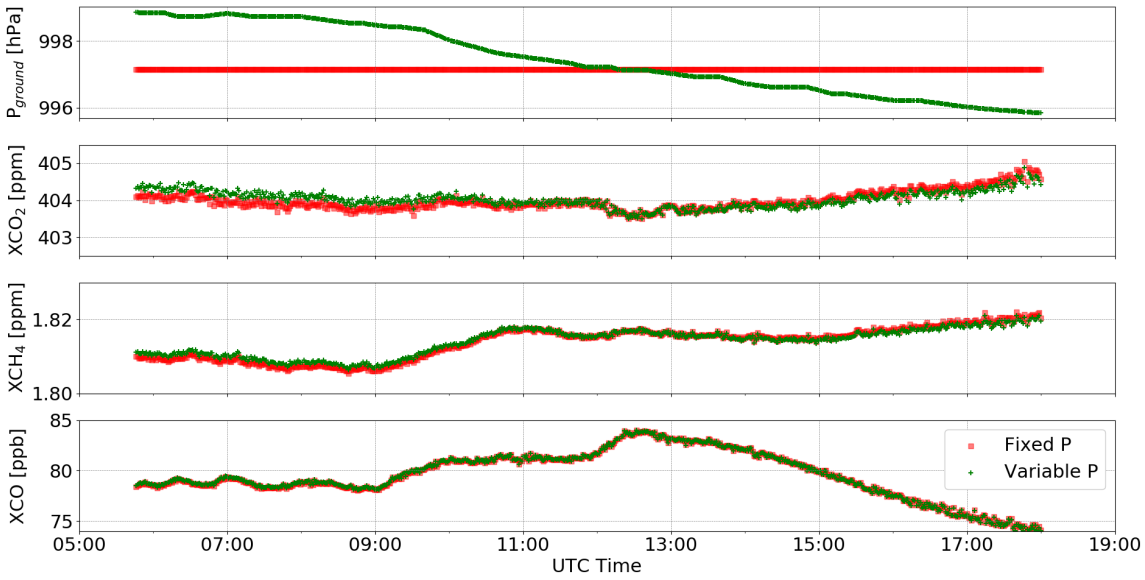

Figure A.2: Time series of XCO_2, XCH_4 and XCO retrievals with fixed and variable ground pressure used in the PROFFIT algorithm—using measurements performed in Sodankylä on June 8, 2017 as an example.

Temperature sensitivity

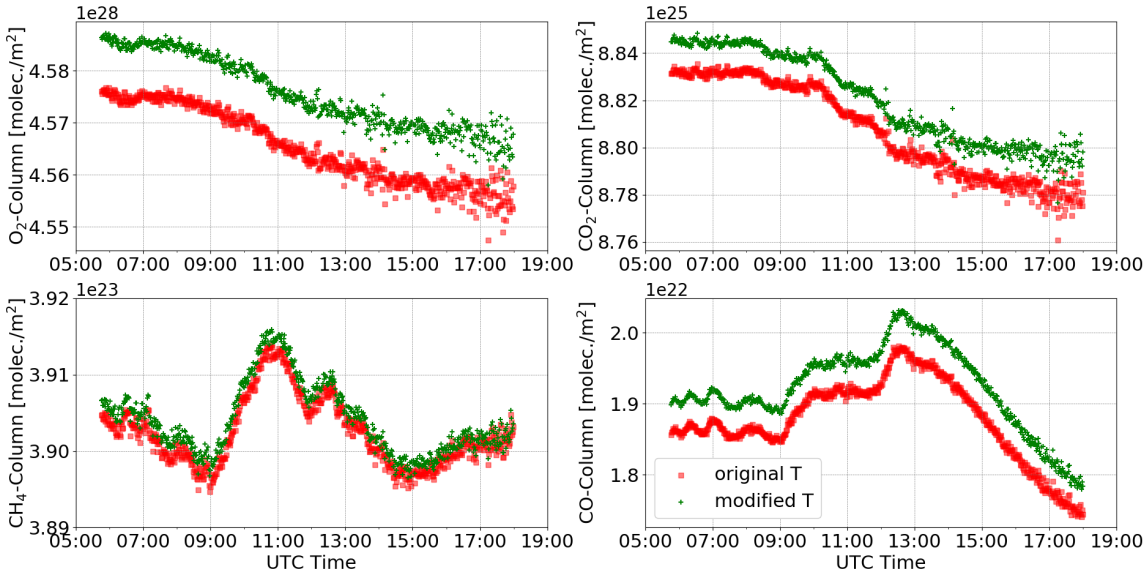

Figure A.3: Time series of total columns of O_2, CO_2, CH_4 and CO retrievals with the original and modified temperature profile used in the PROFFIT algorithm—using measurements performed in Sodankylä on June 8, 2017 as an example.

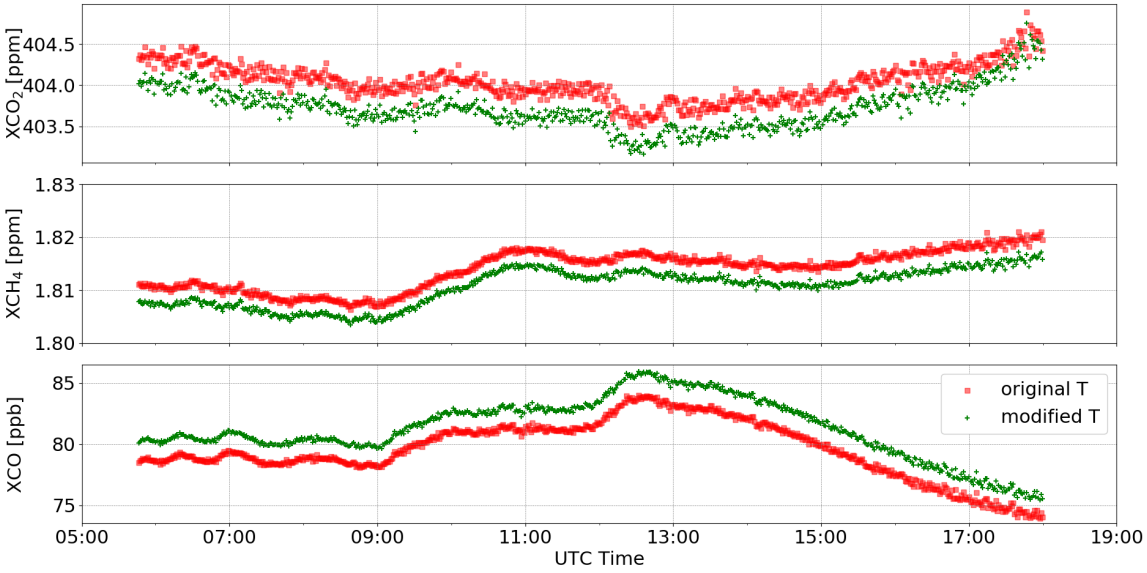

Figure A.4: Time series of XCO_2, XCH_4 and XCO retrievals with the original and modified temperature profile used in the PROFFIT algorithm—using measurements performed in Sodankylä on June 8, 2017 as an example.

Instrumental line shape

Modulation efficiency

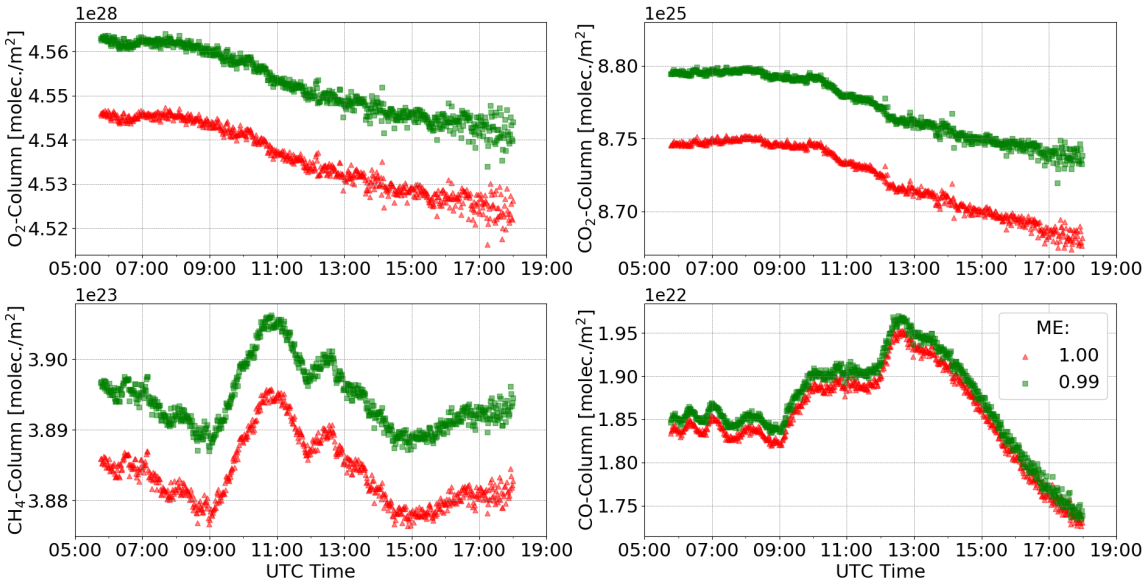

Figure A.5: Time series of total columns of O_2, CO_2, CH_4 and CO retrievals with different ME values used in the PROFFIT software—using measurements performed in Sodankylä on June 8, 2017 as an example.

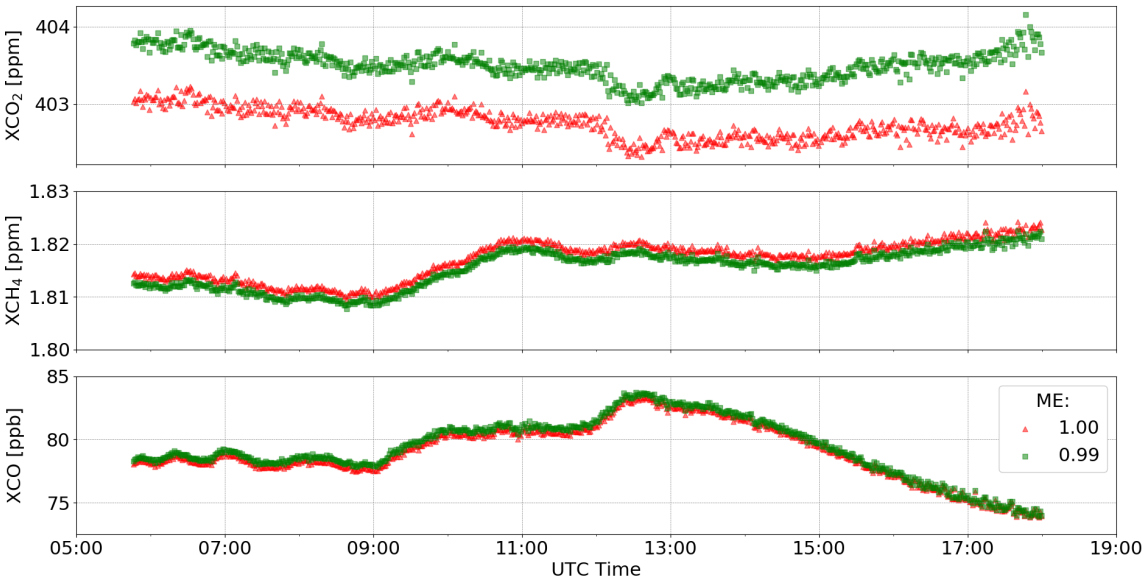

Figure A.6: Time series of XCO_2, XCH_4 and XCO retrievals with different ME values used in the PROFFIT software—using measurements performed in Sodankylä on June 8, 2017 as an example.

Phase error

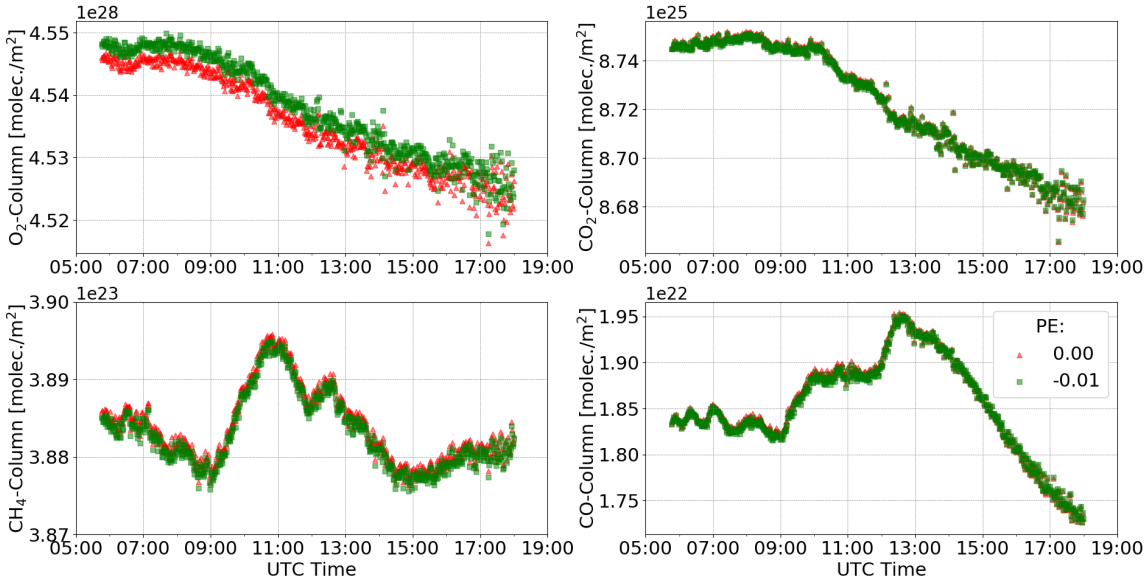

Figure A.7: Time series of total columns of O_2, CO_2, CH_4 and CO retrievals with two different PE values used in the PROFFIT software—using measurements performed in Sodankylä on June 8, 2017 as an example.

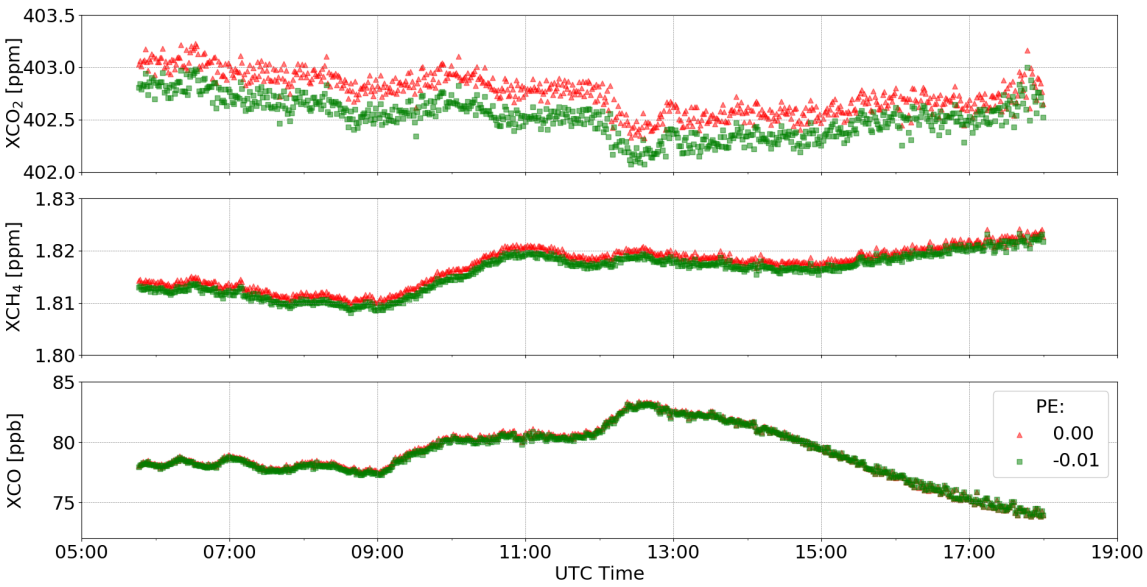

Figure A.8: Time series of XCO_2, XCH_4 and XCO retrievals with different PE values used in the PROFFIT software—using measurements performed in Sodankylä on June 8, 2017 as an example.

A-priori VMR profiles

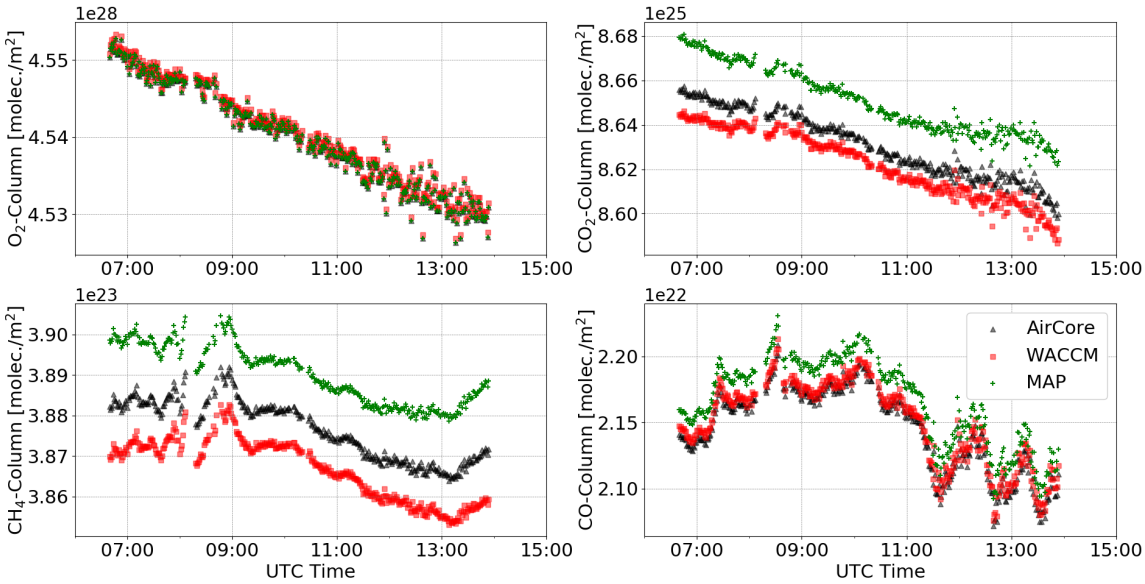

Figure A.9: Time series of total columns of O_2, CO_2, CH_4 and CO retrieved with three different a-priori VMR profiles.

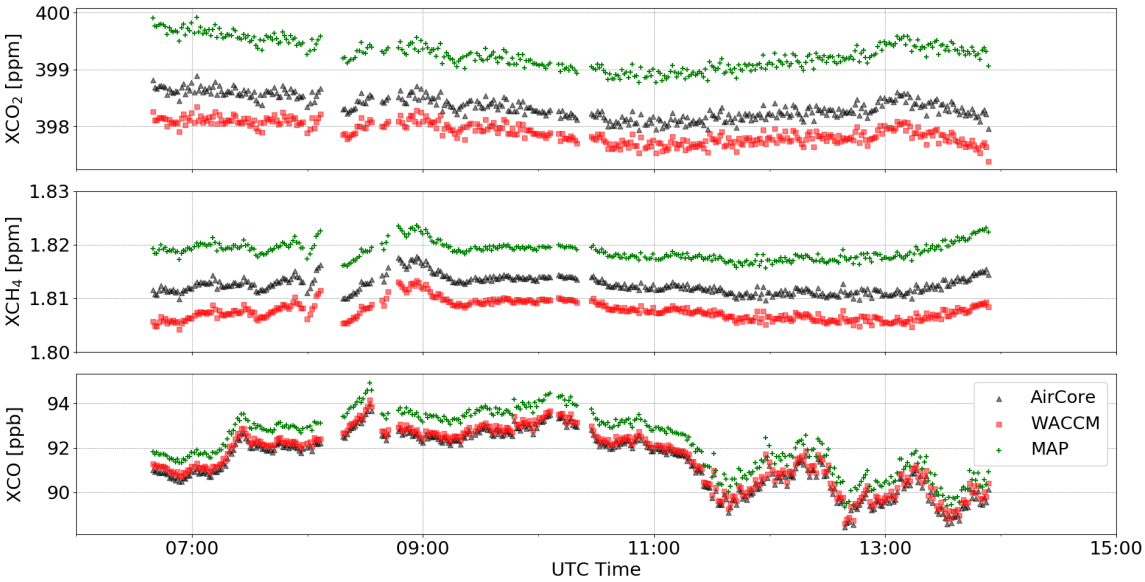

Figure A.10: Time series of XCO_2, XCH_4 and XCO retrievals with fixed a-priori VMR profiles (WACCM, in black), daily varying a-priori profiles (MAP, in red) and measured AirCore profiles in green.

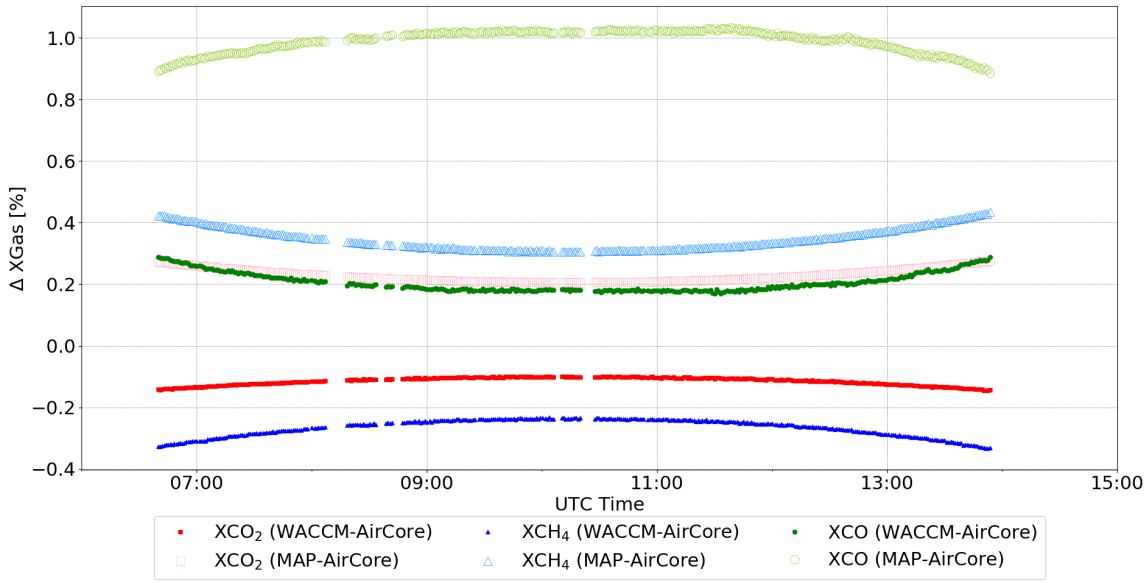

Figure A.11: Time series of relative difference for XCO_2, XCH_4 and XCO retrievals with different a-priori VMR profiles. Retrievals with MAP profiles w.r.t. WACCM profiles are denoted in solid symbols while AirCore w.r.t. WACCM are denoted in hollow symbols.

	O_2	CO_2	CH_4	CO
Pressure 1 hPa increase	-5.38E-02±1.01E-02	-1.91E-02±8.30E-03 3.47E-02±8.13E-03	-1.48E-02±9.00E-03 3.91E-02±1.07E-02	-2.12E-03±1.39E-02 5.17E-02±1.77E-02
Temperature increase 1 K	4.51E-02±1.32E-03	2.98E-02±2.87E-03 -1.52E-02±2.235E-02	8.30E-03±2.32E-03 -3.67E-02±3.40E-02	0.474±3.09E-02 0.428±0.0297
ME 1% decrease	3.70E-01±1.04E-02	5.53E-01±3.23E-02 1.83E-01±2.20E-02	2.74E-01±9.85E-03 -9.51E-02±1.72E-03	7.35E-01±1.03E-01 3.64E-01±1.13E-01
PE 0.01 rad decrease	5.18E-02±6.16E-03	-6.61E-03±4.79E-03 -5.84E-02±1.06E-02	-2.00E-02±2.35E-03 -7.17E-02±7.70E-03	-1.06E-01±1.02E-01 -1.58E-01±1.08E-01

Table 1: Relative difference (%) in different species due to different effects. For each species the first row represents the change in total column and the second row in X_{Gas}. The results are derived from the measurements performed in Sodankylä on June 8, 2017 as an example.

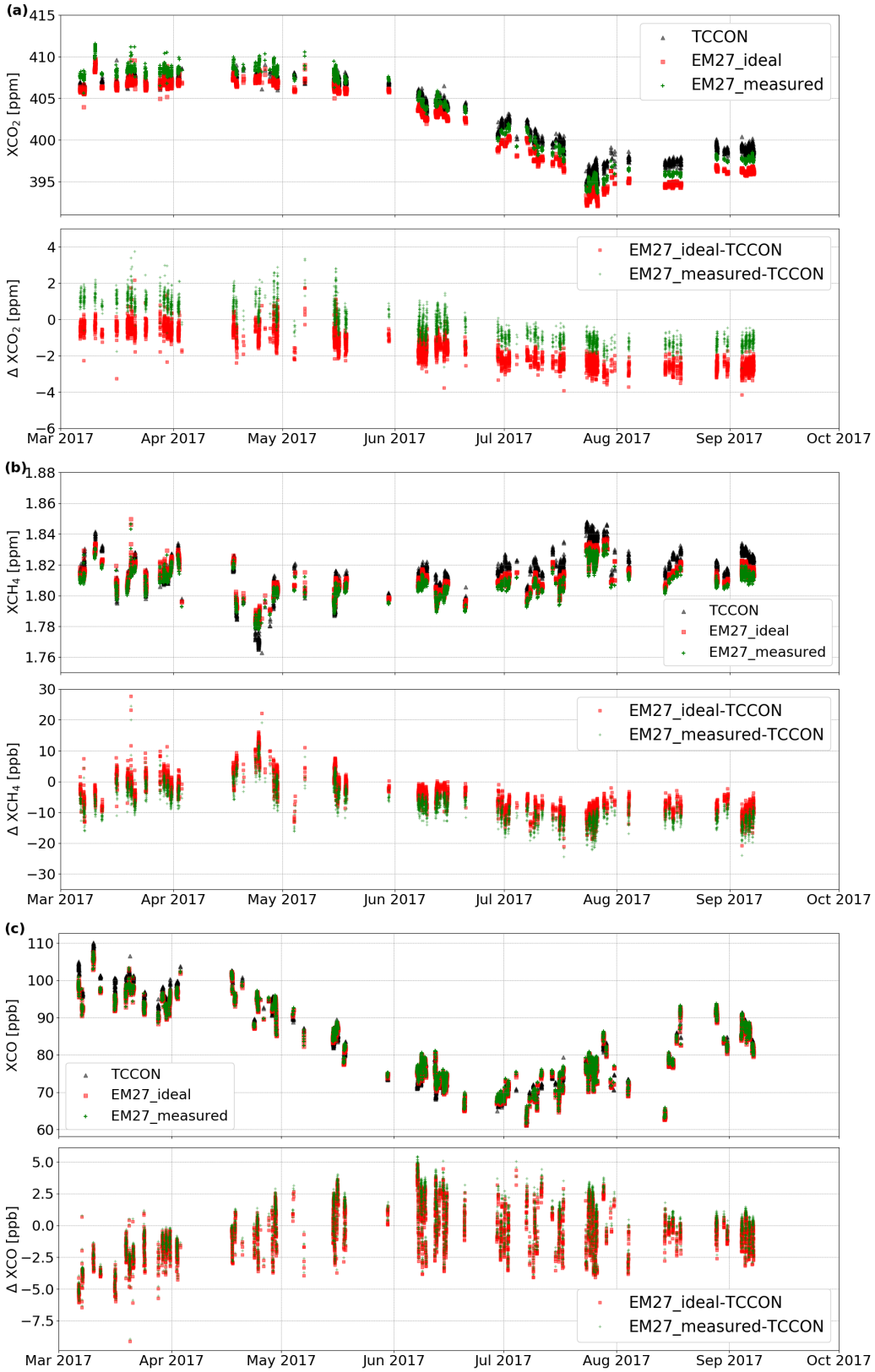

Figure A.12: Time series of (a): XCO_2, (b): XCH_4 and (c): XCO results. EM27/SUN data retrieved with ideal and measured ILS parameters are shown as red squares and green crosses, respectively. TCCON results (black triangles) are shown as a reference.

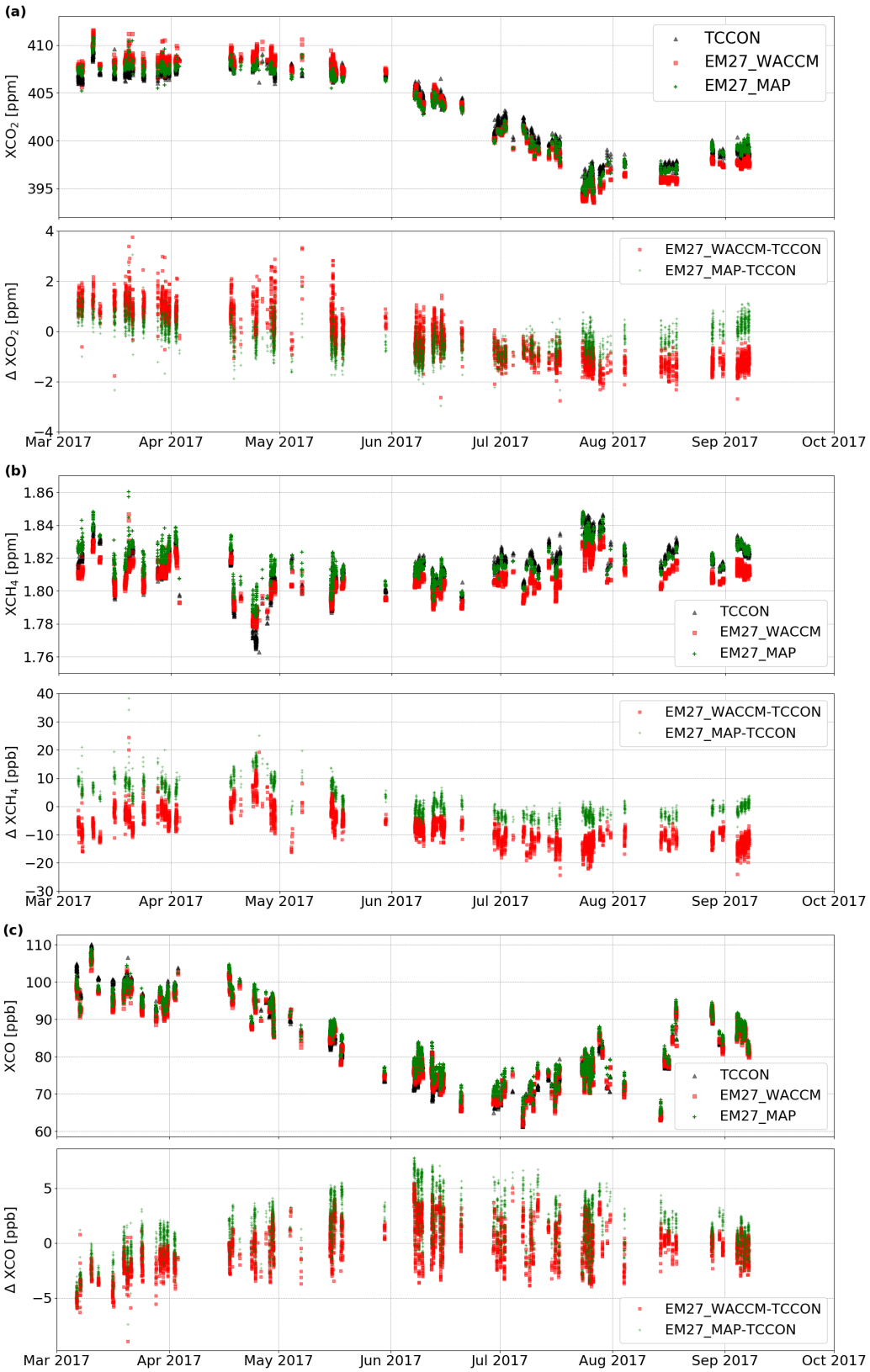

Figure A.13: Time series of XCO_2, XCH_4 and XCO results, retrieved with the fixed WACCM-derived a-priori and the daily-variable MAP a-priori VMR profiles, respectively. Both datasets are compared to the TCCON retrievals.

References

Andersen, T., Scheeren, B., Peters, W., and Chen, H.: A UAV-based active AirCore system for measurements of greenhouse gases, Atmospheric Measurement Techniques, 11, 2683–2699, https://doi.org/10.5194/amt-11-2683-2018, URL https://www.atmos-meas-tech.net/11/2683/2018/, 2018. 72

Andrews, A. E., Boering, K. A., Daube, B. C., Wofsy, S. C., Loewenstein, M., Jost, H., Podolske, J. R., Webster, C. R., Herman, R. L., Scott, D. C., Flesch, G. J., Moyer, E. J., Elkins, J. W., Dutton, G. S., Hurst, D. F., Moore, F. L., Ray, E. A., Romashkin, P. A., and Strahan, S. E.: Mean ages of stratospheric air derived from in situ observations of CO_2, CH_4, and N_2O, Journal of Geophysical Research: Atmospheres, 106, 32 295–32 314, https://doi.org/10.1029/2001JD000465, URL https://agupubs.onlinelibrary.wiley.com/doi/abs/10.1029/2001JD000465, 2001. 37

Archer, D.: Global warming understanding the forecast, Hoboken, N.J John Wiley & Sons, 2nd edn., URL http://openlibrary.org/books/OL25263898M, 2012. 5

Atkins, P. W. and De Paula, J.: Atkins Physical chemistry, Oxford University Press, Oxford [u.a.], 8. ed. edn., 2006. 16, 151

Baldocchi, D. D.: Assessing the eddy covariance technique for evaluating carbon dioxide exchange rates of ecosystems: past, present and future, Global Change Biology, 9, 479–492, https://doi.org/10.1046/j.1365-2486.2003.00629.x, URL https://onlinelibrary.wiley.com/doi/abs/10.1046/j.1365-2486.2003.00629.x, 2003. 80

Bengtsson, L.: The global atmospheric water cycle, Environmental Research Letters, 5, 025202, https://doi.org/10.1088/1748-9326/5/2/025202, 2010. 5

Bernath, P. F., McElroy, C. T., Abrams, M. C., Boone, C. D., Butler, M., Camy-Peyret, C., Carleer, M., Clerbaux, C., Coheur, P.-F., Colin, R., DeCola, P., DeMazière, M., Drummond, J. R., Dufour, D., Evans, W. F. J., Fast, H., Fussen, D., Gilbert, K., Jennings, D. E., Llewellyn, E. J., Lowe, R. P., Mahieu, E., McConnell, J. C., McHugh, M., McLeod, S. D., Michaud, R., Midwinter, C., Nassar, R., Nichitiu, F., Nowlan, C., Rinsland, C. P., Rochon, Y. J., Rowlands, N., Semeniuk, K., Simon, P., Skelton, R., Sloan, J. J., Souc, y. M.-A.,

Strong, K., Tremblay, P., Turnbull, D., Walker, K. A., Walkty, I., Wardle, D. A., Wehrle, V., Zander, R., and Zou, J.: Atmospheric Chemistry Experiment (ACE): Mission overview, Geophysical Research Letters, 32, https://doi.org/10.1029/2005GL022386, URL https://agupubs.onlinelibrary.wiley.com/doi/abs/10.1029/2005GL022386, 2005. 37

Butz, A., Dinger, A. S., Bobrowski, N., Kostinek, J., Fieber, L., Fischerkeller, C., Giuffrida, G. B., Hase, F., Klappenbach, F., Kuhn, J., Lübcke, P., Tirpitz, L., and Tu, Q.: Remote sensing of volcanic CO_2, HF, HCl, SO_2, and BrO in the downwind plume of Mt. Etna, Atmospheric Measurement Techniques, 10, 1–14, https://doi.org/10.5194/amt-10-1-2017, URL https://www.atmos-meas-tech.net/10/1/2017/, 2017. 2, 31, 105, 125

Casanova, S. E. B., Shine, K. P., Gardiner, T., Coleman, M., and Pegrum, H.: Assessment of the consistency of near-infrared water vapor line intensities using high-spectral-resolution ground-based Fourier transform measurements of solar radiation, Journal of Geophysical Research: Atmospheres, 111, https://doi.org/10.1029/2005JD006583, URL https://agupubs.onlinelibrary.wiley.com/doi/abs/10.1029/2005JD006583, 2006. 92

Chen, J., Viatte, C., Hedelius, J. K., Jones, T., Franklin, J. E., Parker, H., Gottlieb, E. W., Wennberg, P. O., Dubey, M. K., and Wofsy, S. C.: Differential column measurements using compact solar-tracking spectrometers, Atmospheric Chemistry and Physics, 16, 8479–8498, https://doi.org/10.5194/acp-16-8479-2016, URL https://www.atmos-chem-phys.net/16/8479/2016/, 2016. 99

Daniel, J. S. and Solomon, S.: On the climate forcing of carbon monoxide, Journal of Geophysical Research: Atmospheres, 103, 13 249–13 260, https://doi.org/10.1029/98JD00822, URL https://agupubs.onlinelibrary.wiley.com/doi/abs/10.1029/98JD00822, 1998. 12

Davis, S. P., Abrams, M. C., and Brault, J. W.: 3 - Theory of the ideal instrument, in: Fourier Transform Spectrometry, edited by Davis, S. P., Abrams, M. C., and Brault, J. W., pp. 29 – 39, Academic Press, San Diego, https://doi.org/https://doi.org/10.1016/B978-012042510-5/50003-2, URL http://www.sciencedirect.com/science/article/pii/B9780120425105500032, 2001. 5

Deutscher, N. M., Griffith, D. W. T., Bryant, G. W., Wennberg, P. O., Toon, G. C., Washenfelder, R. A., Keppel-Aleks, G., Wunch, D., Yavin, Y., Allen, N. T., Blavier, J.-F., Jiménez, R., Daube, B. C., Bright, A. V., Matross, D. M., Wofsy, S. C., and Park, S.: Total column CO_2 measurements at Darwin, Australia - site description and calibration against in situ aircraft profiles, Atmospheric Measurement Techniques, 3, 947–958, https://doi.org/10.5194/amt-3-947-2010, URL https://www.atmos-meas-tech.net/3/947/2010/, 2010. 38

Dlugokencky, E. J., Nisbet, E. G., Fisher, R., and Lowry, D.: Global atmospheric methane: budget, changes and dangers, Philosophical Transactions of the Royal Society of London A: Mathematical, Physical and Engineering Sciences, 369, 2058–2072, https://doi.org/10.1098/rsta.2010.0341, URL http://rsta.royalsocietypublishing.org/content/369/1943/2058, 2011. 1

Draxler, R. and Hess, G.: An overview of the HYSPLIT 4 modelling system for trajectories, dispersion, and deposition, Australian Meteorological Magazine, 47, 295–308, 1998. 99

Etheridge, D. M., Steele, L. P., Francey, R. J., and Langenfelds, R. L.: Atmospheric methane between 1000 A.D. and present: Evidence of anthropogenic emissions and climatic variability, Journal of Geophysical Research: Atmospheres, 103, 15 979–15 993, https://doi.org/10.1029/98JD00923, URL https://agupubs.onlinelibrary.wiley.com/doi/abs/10.1029/98JD00923, 1998. 1

Frey, M., Hase, F., Blumenstock, T., Groß, J., Kiel, M., Mengistu Tsidu, G., Schäfer, K., Sha, M. K., and Orphal, J.: Calibration and instrumental line shape characterization of a set of portable FTIR spectrometers for detecting greenhouse gas emissions, Atmospheric Measurement Techniques, 8, 3047–3057, https://doi.org/10.5194/amt-8-3047-2015, URL https://www.atmos-meas-tech.net/8/3047/2015/, 2015. 2, 31, 32, 33, 38, 39, 41, 105, 125

Frey, M., Sha, M. K., Hase, F., Kiel, M., Blumenstock, T., Harig, R., Surawicz, G., Deutscher, N. M., Shiomi, K., Franklin, J., Bösch, H., Chen, J., Grutter, M., Ohyama, H., Sun, Y., Butz, A., Mengistu Tsidu, G., Ene, D., Wunch, D., Cao, Z., Garcia, O., Ramonet, M., Vogel, F., and Orphal, J.: Building the COllaborative Carbon Column Observing Network (COCCON): Long term stability and ensemble performance of the EM27/SUN Fourier transform spectrometer, Atmospheric Measurement Techniques Discussions, 2018, 1–34, https://doi.org/10.5194/amt-2018-146, URL https://www.atmos-meas-tech-discuss.net/amt-2018-146/, 2018. 45, 53, 55, 56, 64, 93, 105

Frey, M. M.: Characterisation and application of portable solar absorption spectrometers for the detection of greenhouse gas emissions from regional anthropogenic sources, Ph.D. thesis, Karlsruher Institut für Technologie (KIT), URL http://dx.doi.org/10.5445/IR/1000088312, 2018. 30, 36, 151, 159

Geibel, M. C., Messerschmidt, J., Gerbig, C., Blumenstock, T., Chen, H., Hase, F., Kolle, O., Lavrič, J. V., Notholt, J., Palm, M., Rettinger, M., Schmidt, M., Sussmann, R., Warneke, T., and Feist, D. G.: Calibration of column-averaged CH_4 over European TCCON FTS sites with airborne in-situ measurements, Atmospheric Chemistry and Physics, 12, 8763–8775, https://doi.org/10.5194/acp-12-8763-2012, 2012. 38

Gisi, M.: Setup of precise camera based solar tracker systems and greenhouse gas measurements using a modified portable spectrometer, Ph.D. thesis, Karlsruher Institut für Technologie (KIT), URL http://digbib.ubka.uni-karlsruhe.de/volltexte/1000031248, 2012. 20, 151

Gisi, M., Hase, F., Dohe, S., Blumenstock, T., Simon, A., and Keens, A.: XCO_2-measurements with a tabletop FTS using solar absorption spectroscopy, Atmospheric Measurement Techniques, 5, 2969–2980, https://doi.org/10.5194/amt-5-2969-2012, URL https://www.atmos-meas-tech.net/5/2969/2012/, 2012. 2, 29, 38, 50, 125

GLOBALVIEW-CO_2: Cooperative Global Atmospheric Data Integration Project - Carbon dioxide, URL http://dx.doi.org/10.3334/OBSPACK/1002, compiled by NOAA Global Monitoring Division: Boulder, Colorado, U.S.A, 2013. 37

Gurney, K. R., Law, R. M., Denning, A. S., Rayner, P. J., Pak, B. C., Baker, D., Bousquet, P., Bruhwiler, L., Chen, Y.-H., Ciais, P., Fung, I. Y., Heimann, M., John, J., Maki, T., Maksyutov, S., Peylin, P., Prather, M., and Taguchi, S.: Transcom 3 inversion intercomparison: Model mean results for the estimation of seasonal carbon sources and sinks, Global Biogeochemical Cycles, 18, https://doi.org/10.1029/2003GB002111, URL https://agupubs.onlinelibrary.wiley.com/doi/abs/10.1029/2003GB002111, 2004. 2

Hall, J. V., Frayer, W., and Wilen, B. O.: Status of Alaska wetlands, US Fish and Wildlife Service, Alaska Region, URL http://hdl.handle.net/2027/uc1.31210024953653, 1994. 110

Hansen, J., Ruedy, R., Sato, M., and Lo, K.: Global Surface Temperature Change, Reviews of Geophysics, 48, https://doi.org/10.1029/2010RG000345, URL https://agupubs.onlinelibrary.wiley.com/doi/abs/10.1029/2010RG000345, 2010. 1, 10

Hase, F.: Inversion von Spurengasprofilen aus hochaufgelösten bodengebundenen FTIR-Messungen in Absorption, Ph.D. thesis, Karlsruher Institut für Technologie (KIT), URL http://swbplus.bsz-bw.de/bsz086717057abs.htm, 2000. 17

Hase, F.: Improved instrumental line shape monitoring for the ground-based, high-resolution FTIR spectrometers of the Network for the Detection of Atmospheric Composition Change, Atmospheric Measurement Techniques, 5, 603–610, https://doi.org/10.5194/amt-5-603-2012, URL https://www.atmos-meas-tech.net/5/603/2012/, 2012. 32

Hase, F., Blumenstock, T., and Paton-Walsh, C.: Analysis of the instrumental line shape of high-resolution Fourier transform IR spectrometers with gas cell measurements and new retrieval software, Appl. Opt., 38, 3417–3422, https://doi.org/10.1364/AO.38.003417, URL http://ao.osa.org/abstract.cfm?URI=ao-38-15-3417, 1999. 32, 53

Hase, F., Hannigan, J., Coffey, M., Goldman, A., Höpfner, M., Jones, N., Rinsland, C., and Wood, S.: Intercomparison of retrieval codes used for the analysis of high-resolution, ground-based FTIR measurements, Journal of Quantitative Spectroscopy and Radiative Transfer, 87, 25 – 52, https://doi.org/https://doi.org/10.1016/j.jqsrt.2003.12.008, URL http://www.sciencedirect.com/science/article/pii/S0022407303003765, 2004. 3, 38

Hase, F., Drouin, B. J., Roehl, C. M., Toon, G. C., Wennberg, P. O., Wunch, D., Blumenstock, T., Desmet, F., Feist, D. G., Heikkinen, P., De Mazière, M., Rettinger, M., Robinson, J., Schneider, M., Sherlock, V., Sussmann, R., Té, Y., Warneke, T., and Weinzierl, C.: Calibration of sealed HCl cells used for TCCON instrumental line shape monitoring, Atmospheric Measurement Techniques, 6, 3527–3537, https://doi.org/10.5194/amt-6-3527-2013, URL https://www.atmos-meas-tech.net/6/3527/2013/, 2013. 32

Hase, F., Frey, M., Kiel, M., Blumenstock, T., Harig, R., Keens, A., and Orphal, J.: Addition of a channel for XCO observations to a portable FTIR spectrometer for greenhouse gas measurements, Atmospheric Measurement Techniques, 9, 2303–2313, https://doi.org/10.5194/amt-9-2303-2016, URL https://www.atmos-meas-tech.net/9/2303/2016/, 2016. 2, 29, 30, 40, 125, 151

Hedelius, J. K., Viatte, C., Wunch, D., Roehl, C. M., Toon, G. C., Chen, J., Jones, T., Wofsy, S. C., Franklin, J. E., Parker, H., Dubey, M. K., and Wennberg, P. O.: Assessment of errors and biases in retrievals of X_{CO_2}, X_{CH_4}, X_{CO}, and X_{N_2O} from a $0.5\,cm^{-1}$ resolution solar-viewing spectrometer, Atmospheric Measurement Techniques, 9, 3527–3546, https://doi.org/10.5194/amt-9-3527-2016, URL https://www.atmos-meas-tech.net/9/3527/2016/, 2016. 21, 79

Hedelius, J. K., Parker, H., Wunch, D., Roehl, C. M., Viatte, C., Newman, S., Toon, G. C., Podolske, J. R., Hillyard, P. W., Iraci, L. T., Dubey, M. K., and Wennberg, P. O.: Intercomparability of X_{CO_2} and X_{CH_4} from the United States TCCON sites, Atmospheric Measurement Techniques, 10, 1481–1493, https://doi.org/10.5194/amt-10-1481-2017, URL https://www.atmos-meas-tech.net/10/1481/2017/, 2017. 2, 125

Heinle, L. and Chen, J.: Automated enclosure and protection system for compact solar-tracking spectrometers, Atmospheric Measurement Techniques, 11, 2173–2185, https://doi.org/10.5194/amt-11-2173-2018, URL https://www.atmos-meas-tech.net/11/2173/2018/, 2018. 127

Hoffmann, A., Macleod, N. A., Huebner, M., and Weidmann, D.: Thermal infrared laser heterodyne spectroradiometry for solar occultation atmospheric CO_2 measurements, Atmospheric Measurement Techniques, 9, 5975–5996, https://doi.org/10.5194/amt-9-5975-2016, URL https://www.atmos-meas-tech.net/9/5975/2016/, 2016. 97

IPCC: Climate Change 2013: The Physical Science Basis. Contribution of Working Group I to the Fifth Assessment Report of the Intergovernmental Panel on Climate Change, Cambridge University Press, Cambridge, United Kingdom and New York, NY, USA, https://doi.org/10.1017/CBO9781107415324, URL www.climatechange2013.org, 2013. 5, 8, 11, 12, 150

Joos, F. and Spahni, R.: Rates of change in natural and anthropogenic radiative forcing over the past 20,000 years, Proceedings of the National Academy of Sciences, 105, 1425–1430, https://doi.org/10.1073/pnas.0707386105, URL http://www.pnas.org/content/105/5/1425, 2008. 1

Kalnay, E., Kanamitsu, M., Kistler, R., Collins, W., Deaven, D., Gandin, L., Iredell, M., Saha, S., White, G., Woollen, J., Zhu, Y., Leetmaa, A., Reynolds, B., Chelliah, M., Ebisuzaki, W., Higgins, W., Janowiak, J., Mo, K. C., Ropelewski, C., Wang, J., Jenne, R., and Joseph, D.: The NCEP/NCAR 40-Year Reanalysis Project, Bulletin of the American Meteorological Society, 77, 437–472, https://doi.org/10.1175/1520-0477(1996)077⟨0437:TNYRP⟩2.0.CO;2, 1996. 37, 50

Karion, A., Sweeney, C., Tans, P., and Newberger, T.: AirCore: An Innovative Atmospheric Sampling System, Journal of Atmospheric and Oceanic Technology, 27, 1839–1853, https://doi.org/10.1175/2010JTECHA1448.1, URL https://doi.org/10.1175/2010JTECHA1448.1, 2010. 57, 72

Keppel-Aleks, G., Toon, G. C., Wennberg, P. O., and Deutscher, N. M.: Reducing the impact of source brightness fluctuations on spectra obtained by Fourier-transform spectrometry, Appl. Opt., 46, 4774–4779, https://doi.org/10.1364/AO.46.004774, URL http://ao.osa.org/abstract.cfm?URI=ao-46-21-4774, 2007. 38

Khalil, M. and Rasmussen, R.: The global cycle of carbon monoxide: Trends and mass balance, Chemosphere, 20, 227 – 242, https://doi.org/https://doi.org/10.1016/0045-6535(90)90098-E, URL http://www.sciencedirect.com/science/article/pii/004565359090098E, 1990. 81

Kiel, M.: Trace gas measurements from different spectral regions using FTIR spectroscopy, Ph.D. thesis, Karlsruher Institut für Technologie (KIT), URL http://dx.doi.org/10.5445/IR/1000056859, 2016. 27, 38, 39

Kiel, M., Hase, F., Blumenstock, T., and Kirner, O.: Comparison of XCO abundances from the Total Carbon Column Observing Network and the Network for the Detection of Atmospheric Composition Change measured in Karlsruhe, Atmospheric Measurement Techniques, 9, 2223–2239, https://doi.org/10.5194/amt-9-2223-2016, URL https://www.atmos-meas-tech.net/9/2223/2016/, 2016. 38, 89

Kivi, R. and Heikkinen, P.: Fourier transform spectrometer measurements of column CO_2 at Sodankylä, Finland, Geoscientific Instrumentation, Methods and Data Systems, 5, 271–279, https://doi.org/10.5194/gi-5-271-2016, URL https://www.geosci-instrum-method-data-syst.net/5/271/2016/, 2016. 28

Klappenbach, F., Bertleff, M., Kostinek, J., Hase, F., Blumenstock, T., Agusti-Panareda, A., Razinger, M., and Butz, A.: Accurate mobile remote sensing of XCO_2 and XCH_4 latitudinal transects from aboard a research vessel, Atmospheric Measurement Techniques, 8, 5023–5038, https://doi.org/10.5194/amt-8-5023-2015, URL https://www.atmos-meas-tech.net/8/5023/2015/, 2015. 2, 31, 38, 41, 47, 60, 85, 87, 105, 125

Kulawik, S., Wunch, D., O'Dell, C., Frankenberg, C., Reuter, M., Oda, T., Chevallier, F., Sherlock, V., Buchwitz, M., Osterman, G., Miller, C. E., Wennberg, P. O., Griffith, D., Morino, I., Dubey, M. K., Deutscher, N. M., Notholt, J., Hase, F., Warneke, T., Sussmann, R., Robinson, J., Strong, K., Schneider, M., De Mazière, M., Shiomi, K., Feist, D. G., Iraci, L. T., and Wolf, J.: Consistent evaluation of ACOS-GOSAT, BESD-SCIAMACHY, CarbonTracker, and MACC through comparisons to TCCON, Atmospheric Measurement Techniques, 9, 683–709, https://doi.org/10.5194/amt-9-683-2016, URL https://www.atmos-meas-tech.net/9/683/2016/, 2016. 26

Lamouroux, J., Tran, H., Laraia, A., Gamache, R., Rothman, L., Gordon, I., and Hartmann, J.-M.: Updated database plus software for line-mixing in CO_2 infrared spectra and their test using laboratory spectra in the 1.5–2.3μm region, Journal of Quantitative Spectroscopy and Radiative Transfer, 111, 2321–2331, https://doi.org/10.1016/j.jqsrt.2010.03.006, 2010. 40

Le Quéré, C., Moriarty, R., Andrew, R. M., Canadell, J. G., Sitch, S., Korsbakken, J. I., Friedlingstein, P., Peters, G. P., Andres, R. J., Boden, T. A., Houghton, R. A., House, J. I., Keeling, R. F., Tans, P., Arneth, A., Bakker, D. C. E., Barbero, L., Bopp, L., Chang, J., Chevallier, F., Chini, L. P., Ciais, P., Fader, M., Feely, R. A., Gkritzalis, T., Harris, I., Hauck, J., Ilyina, T., Jain, A. K., Kato, E., Kitidis, V., Klein Goldewijk, K., Koven, C., Landschützer, P., Lauvset, S. K., Lefèvre, N., Lenton, A., Lima, I. D., Metzl, N., Millero, F., Munro, D. R., Murata, A., Nabel, J. E. M. S., Nakaoka, S., Nojiri, Y., O'Brien, K., Olsen, A., Ono, T., Pérez, F. F., Pfeil, B., Pierrot, D., Poulter, B., Rehder, G., Rödenbeck, C., Saito, S., Schuster, U., Schwinger, J., Séférian, R., Steinhoff, T., Stocker, B. D., Sutton, A. J., Takahashi, T., Tilbrook, B., van der Laan-Luijkx, I. T., van der Werf, G. R., van Heuven, S., Vandemark, D., Viovy, N., Wiltshire, A., Zaehle, S., and Zeng, N.: Global Carbon Budget 2015, Earth System Science Data, 7, 349–396, https://doi.org/10.5194/essd-7-349-2015, URL https://www.earth-syst-sci-data.net/7/349/2015/, 2015. 5

Liu, Y., Lin, J., Huang, G., Guo, Y., and Duan, C.: Simple empirical analytical approxima-

tion to the Voigt profile, J. Opt. Soc. Am. B, 18, 666–672, https://doi.org/10.1364/JOSAB.18.000666, URL http://josab.osa.org/abstract.cfm?URI=josab-18-5-666, 2001. 19

Lu, D., Liu, Y., and TanSat Science Team: Early phase achievement and scientific plan of TanSat Mission, in: EGU General Assembly Conference Abstracts, vol. 19 of *EGU General Assembly Conference Abstracts*, p. 11709, 2017. 26

Luo, M., Cicerone, R. J., and Russell, J. M.: Analysis of Halogen Occultation Experiment HF versus CH_4 correlation plots: Chemistry and transport implications, Journal of Geophysical Research: Atmospheres, 100, 13 927–13 937, https://doi.org/10.1029/95JD00621, URL https://agupubs.onlinelibrary.wiley.com/doi/abs/10.1029/95JD00621, 1996. 37

Macdonald, J., Fowler, D., Hargreaves, K., Skiba, U., Leith, I., and Murray, M.: Methane emission rates from a northern wetland; response to temperature, water table and transport, Atmospheric Environment, 32, 3219 – 3227, https://doi.org/https://doi.org/10.1016/S1352-2310(97)00464-0, URL http://www.sciencedirect.com/science/article/pii/S1352231097004640, 1998. 81

Marsh, D. R., Mills, M. J., Kinnison, D. E., Lamarque, J.-F., Calvo, N., and Polvani, L. M.: Climate Change from 1850 to 2005 Simulated in CESM1(WACCM), Journal of Climate, 26, 7372–7391, https://doi.org/10.1175/JCLI-D-12-00558.1, URL https://doi.org/10.1175/JCLI-D-12-00558.1, 2013. 39

Membrive, O., Crevoisier, C., Sweeney, C., Danis, F., Hertzog, A., Engel, A., Bönisch, H., and Picon, L.: AirCore-HR: a high-resolution column sampling to enhance the vertical description of CH_4 and CO_2, Atmospheric Measurement Techniques, 10, 2163–2181, https://doi.org/10.5194/amt-10-2163-2017, URL https://www.atmos-meas-tech.net/10/2163/2017/, 2017. 72

Messerschmidt, J., Geibel, M. C., Blumenstock, T., Chen, H., Deutscher, N. M., Engel, A., Feist, D. G., Gerbig, C., Gisi, M., Hase, F., Katrynski, K., Kolle, O., Lavrič, J. V., Notholt, J., Palm, M., Ramonet, M., Rettinger, M., Schmidt, M., Sussmann, R., Toon, G. C., Truong, F., Warneke, T., Wennberg, P. O., Wunch, D., and Xueref-Remy, I.: Calibration of TCCON column-averaged CO_2: the first aircraft campaign over European TCCON sites, Atmospheric Chemistry and Physics, 11, 10 765–10 777, https://doi.org/10.5194/acp-11-10765-2011, URL https://www.atmos-chem-phys.net/11/10765/2011/, 2011. 38

Nicholls, D., Barnes, F., Acrea, F., Chen, C., Buluç, L. Y., and Parker, M. M.: Top-down and bottom-up approaches to greenhouse gas inventory methods—a comparison between national-and forest-scale reporting methods, Gen. Tech. Rep. PNW-GTR-906. Portland, OR: US Department of Agriculture, Forest Service, Pacific Northwest Research Station. 30 p., 906, 2015. 2

Oshchepkov, S., Bril, A., Yokota, T., Yoshida, Y., Blumenstock, T., Deutscher, N. M., Dohe, S., Macatangay, R., Morino, I., Notholt, J., Rettinger, M., Petri, C., Schneider, M., Sussman, R., Uchino, O., Velazco, V., Wunch, D., and Belikov, D.: Simultaneous retrieval of atmospheric CO_2 and light path modification from space-based spectroscopic observations of greenhouse gases: methodology and application to GOSAT measurements over TCCON sites, Appl. Opt., 52, 1339–1350, https://doi.org/10.1364/AO.52.001339, URL http://ao.osa.org/abstract.cfm?URI=ao-52-6-1339, 2013. 2

Ostler, A., Sussmann, R., Rettinger, M., Deutscher, N. M., Dohe, S., Hase, F., Jones, N., Palm, M., and Sinnhuber, B.-M.: Multistation intercomparison of column-averaged methane from NDACC and TCCON: impact of dynamical variability, Atmospheric Measurement Techniques, 7, 4081–4101, https://doi.org/10.5194/amt-7-4081-2014, URL https://www.atmos-meas-tech.net/7/4081/2014/, 2014. 76

Phillips, D. L.: A Technique for the Numerical Solution of Certain Integral Equations of the First Kind, J. ACM, 9, 84–97, https://doi.org/10.1145/321105.321114, URL http://doi.acm.org/10.1145/321105.321114, 1962. 23

Ridder, T., Warneke, T., and Notholt, J.: Source brightness fluctuation correction of solar absorption fourier transform mid infrared spectra, Atmospheric Measurement Techniques, 4, 1045–1051, https://doi.org/10.5194/amt-4-1045-2011, URL https://www.atmos-meas-tech.net/4/1045/2011/, 2011. 39

Rodgers, C. D. and Connor, B. J.: Intercomparison of remote sounding instruments, Journal of Geophysical Research: Atmospheres, 108, https://doi.org/10.1029/2002JD002299, URL https://agupubs.onlinelibrary.wiley.com/doi/abs/10.1029/2002JD002299, 2003. 61

Rothman, L. S., Gordon, I. E., Babikov, Y., Barbe, A., Chris Benner, D., Bernath, P. F., Birk, M., Bizzocchi, L., Boudon, V., Brown, L. R., Campargue, A., Chance, K., Cohen, E. A., Coudert, L. H., Devi, V. M., Drouin, B. J., Fayt, A., Flaud, J.-M., Gamache, R. R., Harrison, J. J., Hartmann, J.-M., Hill, C., Hodges, J. T., Jacquemart, D., Jolly, A., Lamouroux, J., Le Roy, R. J., Li, G., Long, D. A., Lyulin, O. M., Mackie, C. J., Massie, S. T., Mikhailenko, S., Müller, H. S. P., Naumenko, O. V., Nikitin, A. V., Orphal, J., Perevalov, V., Perrin, A., Polovtseva, E. R., Richard, C., Smith, M. A. H., Starikova, E., Sung, K., Tashkun, S., Tennyson, J., Toon, G. C., Tyuterev, V. G., and Wagner, G.: The HITRAN2012 molecular spectroscopic database, Journal of Quantitative Spectroscopy and Radiative Transfer, 130, 4–50, https://doi.org/10.1016/J.JQSRT.2013.07.002, URL https://hal.archives-ouvertes.fr/hal-01005779, 2013. 37

Saad, K. M., Wunch, D., Toon, G. C., Bernath, P., Boone, C., Connor, B., Deutscher, N. M., Griffith, D. W. T., Kivi, R., Notholt, J., Roehl, C., Schneider, M., Sherlock,

V., and Wennberg, P. O.: Derivation of tropospheric methane from TCCON CH_4 and HF total column observations, Atmospheric Measurement Techniques, 7, 2907–2918, https://doi.org/10.5194/amt-7-2907-2014, URL https://www.atmos-meas-tech.net/7/2907/2014/, 2014. 37

Schlager, H., Grewe, V., and Roiger, A.: Chemical Composition of the Atmosphere, pp. 17–35, Springer Berlin Heidelberg, Berlin, Heidelberg, https://doi.org/10.1007/978-3-642-30183-4_2, URL https://doi.org/10.1007/978-3-642-30183-4_2, 2012. 5

Schmidt, G. A., Ruedy, R. A., Miller, R. L., and Lacis, A. A.: Attribution of the present-day total greenhouse effect, Journal of Geophysical Research: Atmospheres, 115, https://doi.org/10.1029/2010JD014287, URL https://agupubs.onlinelibrary.wiley.com/doi/abs/10.1029/2010JD014287, 2010. 12

Schneider, M., Hase, F., Blumenstock, T., Redondas, A., and Cuevas, E.: Quality assessment of O_3 profiles measured by a state-of-the-art ground-based FTIR observing system, Atmospheric Chemistry and Physics, 8, 5579–5588, https://doi.org/10.5194/acp-8-5579-2008, URL https://www.atmos-chem-phys.net/8/5579/2008/, 2008. 38

Schneider, M., Romero, P. M., Hase, F., Blumenstock, T., Cuevas, E., and Ramos, R.: Continuous quality assessment of atmospheric water vapour measurement techniques: FTIR, Cimel, MFRSR, GPS, and Vaisala RS92, Atmospheric Measurement Techniques, 3, 323–338, https://doi.org/10.5194/amt-3-323-2010, URL https://www.atmos-meas-tech.net/3/323/2010/, 2010. 38

Suni, T., Berninger, F., Vesala, T., Markkanen, T., Hari, P., Mäkelä, A., Ilvesniemi, H., Hänninen, H., Nikinmaa, E., Huttula, T., Laurila, T., Aurela, M., Grelle, A., Lindroth, A., Arneth, A., Shibistova, O., and Lloyd, J.: Air temperature triggers the recovery of evergreen boreal forest photosynthesis in spring, Global Change Biology, 9, 1410 – 1426, https://doi.org/10.1046/j.1365-2486.2003.00597.x, URL https://onlinelibrary.wiley.com/doi/abs/10.1046/j.1365-2486.2003.00597.x, 2003. 80, 81

Thum, T., Aalto, T., Laurila, T., Aurela, M., Hatakka, J., Lindroth, A., and Vesala, T.: Spring initiation and autumn cessation of boreal coniferous forest CO_2 exchange assessed by meteorological and biological variables, Tellus B: Chemical and Physical Meteorology, 61, 701–717, https://doi.org/10.1111/j.1600-0889.2009.00441.x, URL https://doi.org/10.1111/j.1600-0889.2009.00441.x, 2009. 80

Tikhonov, A. N.: On the solution of ill-posed problems and the method of regularization, Doklady Akademii Nauk SSSR, 151, 501–504, 1963. 23

Toon, G. C.: The JPL MkIV interferometer, Opt. Photon. News, 2, 19–21, https://doi.org/10.1364/OPN.2.10.000019, URL http://www.osa-opn.org/abstract.cfm?URI=opn-2-10-19, 1991. 37

Tsai, T. R., Rose, R. A., Weidmann, D., and Wysocki, G.: Atmospheric vertical profiles of O_3, N_2O, CH_4, CCl_2F_2, and H_2O retrieved from external-cavity quantum-cascade laser heterodyne radiometer measurements, Appl. Opt., 51, 8779–8792, https://doi.org/10.1364/AO.51.008779, URL http://ao.osa.org/abstract.cfm?URI=ao-51-36-8779, 2012. 97

Washenfelder, R. A., Wennberg, P. O., and Toon, G. C.: Tropospheric methane retrieved from ground-based near-IR solar absorption spectra, Geophysical Research Letters, 30, https://doi.org/10.1029/2003GL017969, URL https://agupubs.onlinelibrary.wiley.com/doi/abs/10.1029/2003GL017969, 2003. 37

Weidmann, D., Reburn, W. J., and Smith, K. M.: Ground-based prototype quantum cascade laser heterodyne radiometer for atmospheric studies, Review of Scientific Instruments, 78, 073 107, https://doi.org/10.1063/1.2753141, URL https://doi.org/10.1063/1.2753141, 2007. 97

Wunch, D., Toon, G. C., Wennberg, P. O., Wofsy, S. C., Stephens, B. B., Fischer, M. L., Uchino, O., Abshire, J. B., Bernath, P., Biraud, S. C., Blavier, J.-F. L., Boone, C., Bowman, K. P., Browell, E. V., Campos, T., Connor, B. J., Daube, B. C., Deutscher, N. M., Diao, M., Elkins, J. W., Gerbig, C., Gottlieb, E., Griffith, D. W. T., Hurst, D. F., Jiménez, R., Keppel-Aleks, G., Kort, E. A., Macatangay, R., Machida, T., Matsueda, H., Moore, F., Morino, I., Park, S., Robinson, J., Roehl, C. M., Sawa, Y., Sherlock, V., Sweeney, C., Tanaka, T., and Zondlo, M. A.: Calibration of the Total Carbon Column Observing Network using aircraft profile data, Atmospheric Measurement Techniques, 3, 1351–1362, https://doi.org/10.5194/amt-3-1351-2010, URL https://www.atmos-meas-tech.net/3/1351/2010/, 2010. 38, 40

Wunch, D., Toon, G. C., Blavier, J.-F. L., Washenfelder, R. A., Notholt, J., Connor, B. J., Griffith, D. W. T., Sherlock, V., and Wennberg, P. O.: The Total Carbon Column Observing Network, Philosophical Transactions of the Royal Society A: Mathematical, Physical and Engineering Sciences, 369, 2087–2112, https://doi.org/10.1098/rsta.2010.0240, 2011. 2, 25, 36, 37, 38, 44, 45, 46

Wunch, D., Toon, G. C., Sherlock, V., Deutscher, N. M., Liu, C., Feist, D. G., and Wennberg, P. O.: The Total Carbon Column Observing Network's GGG2014 Data Version, Tech. rep., Carbon Dioxide Information Analysis Center, Oak Ridge National Laboratory, Oak Ridge, Tennessee, U.S.A. doi: 10.14291/tccon.ggg2014.documentation.R0/1221662, https://doi.org/10.14291/tccon.ggg2014.documentation.R0/1221662, URL http://dx.doi.org/10.14291/tccon.ggg2014.documentation.R0/1221662, 2015. 3, 28, 36, 37, 91

Wunch, D., Wennberg, P. O., Osterman, G., Fisher, B., Naylor, B., Roehl, C. M., O'Dell, C., Mandrake, L., Viatte, C., Kiel, M., Griffith, D. W. T., Deutscher, N. M., Velazco,

V. A., Notholt, J., Warneke, T., Petri, C., De Maziere, M., Sha, M. K., Sussmann, R., Rettinger, M., Pollard, D., Robinson, J., Morino, I., Uchino, O., Hase, F., Blumenstock, T., Feist, D. G., Arnold, S. G., Strong, K., Mendonca, J., Kivi, R., Heikkinen, P., Iraci, L., Podolske, J., Hillyard, P. W., Kawakami, S., Dubey, M. K., Parker, H. A., Sepulveda, E., García, O. E., Te, Y., Jeseck, P., Gunson, M. R., Crisp, D., and Eldering, A.: Comparisons of the Orbiting Carbon Observatory-2 (OCO-2) X_{CO_2} measurements with TCCON, Atmospheric Measurement Techniques, 10, 2209–2238, https://doi.org/10.5194/amt-10-2209-2017, URL https://www.atmos-meas-tech.net/10/2209/2017/, 2017. 26

Yang, Z., Washenfelder, R. A., Keppel-Aleks, G., Krakauer, N. Y., Randerson, J. T., Tans, P. P., Sweeney, C., and Wennberg, P. O.: New constraints on Northern Hemisphere growing season net flux, Geophysical Research Letters, 34, https://doi.org/10.1029/2007GL029742, URL https://agupubs.onlinelibrary.wiley.com/doi/abs/10.1029/2007GL029742, 2007. 2

List of Figures

List of Tables

Nomenclature

ACE	Atmospheric Chemistry Experiment
AD	Airmass dependent
AI	Airmass independent
AWS	Automatic Weather Station
BIRA	Belgian Institute for Space Aeronomy
BOD	Ground-based Remote Sensing
CAMS	Copernicus Atmosphere Monitoring Service
CDS	Carbon Dioxide Spectrometer
CRDS	Cavity Ring-Down Spectroscopy
DMF	column-averaged dry-air mole fraction
EC	Eddy Covariance
ESA	European Space Agency
FMI	Finnish Meteorology Institute
FOV	Field of view
FRM4GHG	Ground-Based Infrared Greenhouse Gas Observations
FTIR	Fourier-Transform Infrared
FTS	Fourier transform spectrometer
FWHM	full width at half maximum
GHG	Greenhouse gas

GOSAT	Greenhouse Gases Observing Satellite
GWP	global warming potential
HITRAN	High Resolution Transmission Molecular Absorption Database
ILS	Instrumental line shape
IMECC	Infrastructure for Measurement of the European Carbon Cycle
IMK	Institute of Meteorology and Climate Research
InGaAs	Indium gallium arsenide
InSb	Indium antimonide
IPCC	Intergovernmental Panel on Climate Change
IRF	Swedish Institute of Space Physics
KIT	Karlsruhe Institute of Technology
LANL	Los Alamos National Laboratory
LANL	Los Alamos National Laboratory
LHR	Laser Heterodyne Radiometer
MACC	Monitoring Atmospheric Composition and Climate
ME	Modulation efficiency
MIR	Mid-infrared
MOPD	Maximum optical path difference
NCAR	National Center for Atmospheric Research
NCEP	National Centers for Environmental Prediction
NDACC	Network for the Detection of Atmospheric Composition Change
NIR	Near-infrared
OCO-2	Orbiting Carbon Observatory 2
OPD	Optical path difference
PE	Phase error
ppb	parts per billion

PPFD	Photosynthetic Photon Flux Density
ppm	parts per million
ppt	parts per trillion
pT	pressure and temperature
RF	radiative forcing
SBF	source brightness fluctuations
SCIAMACHY	Scanning Imaging Absorption Spectrometer for Atmospheric Chartography
SZA	Solar zenith angle
TanSat	Chinese Carbon Dioxide Observation Satellite Mission
TCCON	Total Carbon Column Observing Network
TROPOMI	TROPOspheric Monitoring Instrument
UAF	University of Alaska Fairbanks
UG	University of Groningen
UTLS	upper troposphere and lower stratosphere
VMR	volume mixing ratio
WACCM	Whole Atmospheric Chemistry Climate Model
WMO	World Meteorological Organization
XAir	column-averaged amount of dry air

Acknowledgements

It has been an unforgettable and extraordinary experience of my Ph.D. years at Karlsruhe Institute of Technology, not only from the scientific perspective, but also from personal willpower. Here, I would like to take the opportunity to sincerely acknowledge all the people who helped and supported me in different ways. I would not have done it without them.

First of all, I sincerely thank Prof. Dr. Thomas von Clarmann for giving me the opportunity to write this thesis. He gave me the freedom to play with my topic, continued supporting my work and was interested in the developments. He is also an excellent teacher, since I learned a lot from his lectures, like "What is probability?" and "Statistics". I would like to thank him for the valuable suggestions on my thesis.

My special thanks go to Prof. Dr.-Ing. Stefan Hinz who agreed to be my second referee. Thanks to him for the beneficial discussion and for giving his time generously and shepherding this thesis through many necessary changes.

I would like to thank Prof. Dr. rer. nat. André Butz from Heidelberg University who kindly agreed to be my external referee. It is appreciated that I got the chance to participate in his previous work of the Etna campaign, from which I have learned much. I also would like to thank him for the valuable discussions, patient guidance, strong encouragements and for proofreading my thesis.

I am very grateful to Dr. Thomas Blumenstock for accepting me as a member in his group (Ground-based FTIR Remote Sensing). Thanks so much for his continuous encouragements, strong support during my Ph.D. period, and for his helpful recommendations for proofreading my thesis. Meanwhile, I owe much to Dr. Frank Hase who is my scientific supervisor. Thank so much for his excellent and patient support and supervision throughout these four-year Ph.D. study. His wide range of knowledge about physics and instruments, outstanding willingness

to engage in answering and discussing questions were of great importance to the success. Thank so much to guide me in the science and also in my personal development. His attitude and devotion to the science encourages me all the time, and will continue inspiring me and be a role model for me in the rest of our lives.

Next, I would like to profusely acknowledge the other members in the BOD group and other colleagues at IMK-ASF. I appreciate the good atmosphere at the institute. A lot of thanks to Dr. Matthias Frey for showing me the ropes at the beginning, for his continuous support to my work and his helpful comments on my thesis. I would like to thank Jochen Gross for the invaluable help with all the technical problems and my office-sharing colleague Ugur Cayoglu for helping me with Python programming. Special thanks also go to Dr. Farahnaz Khosrawi, Dr. Darko Dubravica and Dr. Florian Hänel for tremendously proofreading my thesis. I would like to thank our institute secretaries Astrud Wiessner, Sandra Leist and Derya Cayiroglu with the official paper works.

I would like to thank Dr. Rigel Kivi, Pauli Heikkinen and other colleagues at FMI for their all support and help when I was in Finland. I also would like to thank PD. Dr. Uwe Raffalski at IRF for operating the EM27/SUN spectrometer. Thanks also go to other colleagues in the FRM4GHG projects. I also thank Prof. William Simpson and Niki Jacobs at UAF, Fairbanks for organizing the Alaska campaign and their warmly hospitality. Additional thanks to Niki for critical comments and suggestions on my thesis. Also, special thanks go to Dr. Jacob Hedelius at the University of Toronto for his kindness to proofread my thesis. His scholarly insight substantially improved the content.

I give my gratitude to the China Scholarship Council (CSC) for financially supporting my first two years' Ph.D. work. I also thank the Karlsruhe House of Young Scientists (KHYS) that funded me with my stay in Finland under the Research Travel Grant. And this work is partly funded by European Space Agency's FRM Programme under grant agreement no. ESA-IPL-POE-LG-cl-LE-2015-1129[1].

I also would like to take it as an honor to express my thanks to my friends for their supportive influences in my life all the way. I thank them very much for

[1] http://frm4ghg.aeronomie.be/index.php

coming to my life and helping me in any way: Mengting, my close friend since high school, continuously encourages me and I share a lot of cheerful and bad moments with her; Xin who is near to finish her Ph.D. study in Paris, helps me in numerous ways through these years abroad and I can exchange my joyous and stressful feelings with her about the Ph.D. study; Chang, Lei and Qiuyu who are my college friends and started their postgraduate in the same year, always give me a helping hand when I am plagued by troubles; Han, who has a glowing personality, can easily cheer me up when I am depressed and it is as if the sun came to shine on my life, making it brighter and happier; and a lot of others whose name I have not mentioned here and forgive me for not being able to list all of them.

Finally I would like to express my deep sense of gratitude to my ever loving big family. My grandparents, parents, aunts, uncles and cousins have given me numerous encouragement and support. My dearest mother Xiufeng who is strong and brave to support our family and has been educating, encouraging and supporting me all the time, and my ever beloved father, Xiaoyan would have been proud with me. I could not have done this work without them and I will remain their selfless dedication throughout my whole life. Thank you so much, my dearest families.